



José Nuno dos Santos Gomes

**Polaritonics in nanostructures  
with 2D materials and  
point emitters**

Universidade do Minho  
Escola de Ciências





**Universidade do Minho**  
Escola de Ciências

José Nuno dos Santos Gomes

**Polaritonics in nanostructures  
with 2D materials and  
point emitters**

Masters' Thesis  
Master in Physics

Thesis supervised by

**Professor Mikhail Igorevich Vasilevskiy**  
**Professor Nuno Miguel Machado**  
**Reis Peres**

July 2020

# Declaration

Name: José Nuno dos Santos Gomes

E-mail: nunobg93@hotmail.com

Phone: (M) (+351) 924384788

Civil ID number: 14304052

Thesis title: Polaritonics in nanostructures with 2D materials and point emitters

Supervisors: Professor Mikhail Vasilevskiy and Professor Nuno Peres

Year of conclusion: 2020

Masters in Physics

THE FULL REPRODUCTION OF THIS THESIS IS AUTHORIZED ONLY FOR INVESTIGATION PURPOSES, WITH A WRITTEN DECLARATION FROM THE INVESTIGATOR, WHO COMMITS TO SUCH.

*Universidade do Minho, May 2020*

Signature:

## **Declaration of Integrity**

I declare to have acted with integrity while performing the present academic work and I confirm that I did not incur in any plagiarising practices or any undue usage or falsification of informations or results in any of the steps of this work. I also declare that I know and have respected the Code for Ethical Conduct of the University of Minho.



## Acknowledgements

I am extremely grateful to Professor Mikhail Vasilevskiy for all the guidance provided along the course of not only this thesis, but since my Bachelors degree and in all the academic work that I have done since then. The ability to provide challenging but attainable goals, step by step, has been a driver for much of my learning process. I am also very grateful to Professor Nuno Peres for guiding me in the first chapter of the thesis, for being calm and also giving me valuable guidance to become a more organized and efficient investigator. I would like to thank Dr. Yuliy Bludov for accepting my collaboration on the studies of hybrid plasmon-magnon polaritons and being available to share results and compare calculations. I am thankful for the help provided by my friend and colleague Bruno Alexandre, who has always been available to listen to me talk about this work, providing valuable advice and helping me to get out of some dead ends. My family is also responsible for my successes, not only because of the obvious monetary support but also because they have always celebrated my achievements and helped me through my doubts and fears. I hope this work makes them proud, as well as all the future works I will be involved in. Funding from the European Commission, within the project "Graphene-Driven Revolutions in ICT and Beyond" (Ref. No. 696656), and from the Portuguese Foundation for Science and Technology (FCT) in the framework of the PTDC/NAN-OPT/29265/2017 "Towards high speed optical devices by exploiting the unique electronic properties of engineered 2D materials" project the Strategic Funding UID/FIS/04650/2019 is gratefully acknowledged.





# Abstract

This thesis presents results of theoretical consideration of three distinct problems of light interaction with solid-state nanostructures. Each of these problems is related to the concept of polaritons, mixed excitations resulting from coupling of photons to certain quasiparticles in the condensed matter. This concept is described in the Introduction and each of the specific problems considered is presented in a separate chapter.

In the first of these chapters, polaritonic effects in a structure containing an antiferromagnet ( $\text{MnF}_2$ ) and a graphene sheet are studied. The dispersion relations are studied both for TE and TM polarizations. Comparisons are made between the system with only antiferromagnet, only graphene sheet and the full system, in order to study the effect of each part of the system on the dispersion relation. The variations of the absorbance, reflectance and transmittance with the angle of incidence of a plane wave are also studied. A perfect metal is added to the system in order to study the effect of the extra confinement on the dispersion relations.

In the following chapter, a system consisting of a 2D transition metal dichalcogenide (TMD) layer, namely a monolayer of  $\text{MoS}_2$ , embedded in a cylindrical microcavity made of  $\text{Si}_3\text{N}_4$ , is studied. The focus is on studying the formation of exciton-polariton modes and their effect on the dispersion relation, as well as on the local density of states. A study of the enhancement of the total and local density of states is conducted with respect to both the frequency and the position in the cylinder. A point-emitter can then be placed at the spots of maximum intensity to take advantage of the distribution of energy inside the cavity.

In the last part of this work, the eigenmodes of a microsphere are studied in order to predict the distribution of energy from external excitation of these modes by incidence of plane waves on the microsphere. For this, the effect of the local density of states is combined with the distribution of the incident rays as their travel inside the sphere in order to estimate the distribution of light on the microcavity. As in the previous chapter, a point-emitter can be placed in the position of higher enhancement to take advantage of the distribution of energy inside the cavity.

The last chapter of the thesis is devoted to discussion of some physical aspects and potential applications of the solved problems.



## Resumo

Esta tese apresenta resultados teóricos de três problemas distintos de interação de luz com nanoestruturas de matéria condensada. Cada um destes problemas está relacionado com o conceito de polaritões, excitações mistas resultantes do acoplamento de fótons a determinadas quasi-partículas na matéria condensada, e este conceito é abordado na introdução e cada um dos problemas estudado tem um capítulo dedicado ao mesmo.

No primeiro destes capítulos, são estudados os efeitos polaritônicos numa estrutura que contém um antiferromagnete ( $\text{MnF}_2$ ) e uma folha de grafeno. As relações de dispersão são estudadas para ambas as polarizações possíveis, 'transverse magnetic' (TM) e 'transverse electric' (TE). Comparam-se os sistemas com apenas o antiferromagnete, apenas a folha de grafeno e o sistema completo, de forma a estudar o efeito que cada componente tem na relação de dispersão. Também é estudada a variação da absorbância, refletância e transmitância com o ângulo de incidência de uma onda plana. É adicionado um metal perfeito ao sistema de forma a estudar o efeito do confinamento adicional nas relações de dispersão.

No capítulo seguinte, é estudado um sistema com uma monocamada de um metal de transição dicalcogeneto (TMD), nomeadamente  $\text{MoS}_2$ , embutido numa microcavidade cilíndrica de  $\text{Si}_3\text{N}_4$ . O foco está no estudo da formação de polaritões excitónicos e os seus efeitos na relação de dispersão do sistema, assim como na densidade local de estados. É levado a cabo um estudo do aprimoramento das densidades de estado totais e locais com a variação da frequência eletromagnética e da zona do cilindro. Sabendo os resultados destas variações é possível colocar um emissor pontual num dos locais de máxima intensidade para tomar partido da distribuição de energia dentro da cavidade.

Na parte final deste trabalho, estudam-se os modos próprios eletromagnéticos de uma microesfera de forma a prever a distribuição de energia resultante da excitação externa destes modos por incidência de ondas planas. Para tal, o efeito da densidade local de estados tem de ser combinado com a distribuição de raios incidentes dentro da esfera à medida que os mesmos se propagam no interior. Tal como no capítulo anterior, é possível colocar um emissor pontual no interior da esfera na posição de maior aprimoramento para tomar partido da distribuição de energia dentro da cavidade.

O capítulo final desta tese é dedicado à discussão de alguns aspetos físicos e potenciais aplicações dos problemas resolvidos.



# Contents

<b>Abstract</b>	<b>ii</b>
<b>Abstract</b>	<b>iii</b>
<b>List of Figures</b>	<b>vi</b>
<b>1 Introduction</b>	<b>1</b>
1.1 Scope of this thesis . . . . .	1
1.2 Materials used in the systems studied . . . . .	3
1.2.1 Uniaxial antiferromagnets . . . . .	4
1.2.2 Transition metal dichalcogenides . . . . .	5
1.3 Plasmon-polaritons and Magnon-polaritons . . . . .	7
1.4 Microcavity polaritons . . . . .	8
<b>2 Polaritonics of antiferromagnets with graphene</b>	<b>10</b>
2.1 Magneto-optic response of an easy-axis antiferromagnet with no static field . . . . .	10
2.2 Magneto-optic response of an easy-axis antiferromagnet in the presence of a static field . .	14
2.3 Optical conductivity of graphene . . . . .	15
2.4 Antiferromagnet-graphene system - Dispersion relations, transmittance, reflectance and absorbance . . . . .	17
2.4.1 TE modes . . . . .	17
2.4.2 TM modes . . . . .	24
2.5 Adding a perfect metal . . . . .	31
2.5.1 TE modes . . . . .	31
2.5.2 TM modes . . . . .	37
<b>3 Exciton-Polaritons of a 2D TMD layer embedded in a cylindrical microcavity</b>	<b>45</b>
3.1 Excitonic susceptibility of the 2D semiconductor layer on the cavity . . . . .	46
3.1.1 Exciton confinement . . . . .	46
3.1.2 Empty cavity photon modes . . . . .	48
3.1.3 Susceptibility and optical conductivity . . . . .	53
3.2 Microcavity exciton-polaritons . . . . .	56
3.2.1 Semiclassical theory . . . . .	56
3.2.2 Quantum picture . . . . .	58
3.3 Polariton Densities of States . . . . .	61

3.3.1	Total and Projected Densities of States . . . . .	61
3.3.2	Local Density of States . . . . .	62
3.4	Point Emitter Attached to the TMD Layer: the Purcell effect . . . . .	62
<b>4</b>	<b>Photonic states confined to a spherical microcavity</b>	<b>66</b>
4.1	Determination of the eigenmodes . . . . .	67
4.1.1	Scalar Helmholtz equation . . . . .	67
4.1.2	Vectorial Helmholtz equation . . . . .	68
4.1.3	Components of the electromagnetic fields . . . . .	69
4.1.4	TM-type and TE-type modes . . . . .	69
4.2	Ideal cavity modes . . . . .	70
4.2.1	Dispersion relations . . . . .	70
4.2.2	Local density of states . . . . .	72
4.3	Modes for a real cavity with dielectric interface . . . . .	75
4.3.1	Dispersion relations . . . . .	76
4.3.2	Local density of states . . . . .	79
4.4	Microsphere with incorporated point emitters . . . . .	81
4.4.1	Geometrical optics model for weakly absorbing sphere . . . . .	81
4.4.2	Concentration of rays with respect to position . . . . .	82
4.4.3	Emission distribution inside the sphere . . . . .	86
4.4.4	Local emission rate . . . . .	86
4.5	Continuous regime . . . . .	90
4.5.1	Total density of states . . . . .	91
4.5.2	Local density of states . . . . .	92
<b>5</b>	<b>Conclusion</b>	<b>95</b>
	<b>Bibliography</b>	<b>113</b>
	<b>Bibliography</b>	<b>114</b>

# List of Figures

1.1	Electronic band structure of graphene showing the linear dispersion relation that characterizes Dirac electrons at the Dirac points, as given by (1.1). The Dirac points are the points where the upper band touches the lower band. The electrons' effective mass is zero, near these points. Because their effective mass is zero, the Dirac electrons all must behave like light inside the graphene layer, having a constant fixed velocity. The dispersion is shown in units of $t$ with numerical values of $t = 2.7$ eV and $t' = -0.2t$ . . . . .	4
1.2	Depiction of the precession of the spin of a particle that takes place in the presence of an external magnetic field. . . . .	5
1.3	Structure of a transition metal dichalcogenide (TMD) monolayer. The black spheres represent the transition metal atoms (Mo, W, etc) and the blue spheres the smaller chalcogen atoms (S, Se, or Te). A single layer of this material consists in a triangular lattice of a transition metal in the middle of two triangular lattices of a chalcogen atom (S, Se or Te). (a) Side view, a layer with a thickness of only three atoms. (b) Top view, the repeating pattern of the monolayer on the plane with which it is aligned. . . . .	6
1.4	'Pillar microcavity from an etched planar DBR semiconductor microcavity (left), with emission mode spectrum (right), from Gérard et al. (1996).' . . . .	9
2.1	Scheme of the system under study, with the antiferromagnet a distance $d$ away from the graphene sheet. Medium 1 is the AFM, medium 2 is below the graphene sheet, and medium 3 is above the graphene sheet. Evanescent waves decaying in the $z$ direction, and propagating parallel to the graphene sheet will be studied, as well as propagating waves incident from medium 3, which generally is the vacuum or air. . . . .	11
2.2	Crystalline structure of $\text{MnF}_2$ with overlapping lattices. For temperatures under the Néel temperature, this material can be treated as a set of alternating spin lattices. . . . .	11

2.3 Dispersion relation for evanescent TE waves generated by surface magnon-plasmon polaritons, for different values of the Fermi energy  $E_F$ .  $\Omega_0$  is the antiferromagnet resonance frequency (2.29).  $q_c$  is the corresponding wavenumber in vacuum  $q_c = \frac{\Omega_0}{c}$ . The level of doping of the graphene sheet affects the nature of the dispersion. The group velocity is negative for  $E_F = 0.4$  eV, shifting from the positive group velocity associated with lower  $E_F$ . These are the solutions to equation (2.79). The value of  $d$ , the separation between the graphene sheet and the antiferromagnet, is  $0.5 \mu\text{m}$ . For the antiferromagnet permeability function given by (2.27)-(2.29), the values of the quantities that determine it can also be consulted in equations (2.33)-(2.35). The value of the loss coefficient in (2.59) is  $\gamma_e = 0$  eV. Ignoring losses at the graphene sheet is valid when dealing with low temperatures. . . . . 19

2.4 Comparison between the loss function ( $\Im(r)$ ) from (2.100) for propagating TE modes and the dispersion relation from (2.79) for evanescent TE waves generated by surface magnon-plasmon polaritons. The loss function is higher close to the energies of the evanescent modes.  $\Omega_0$  is the antiferromagnet resonance frequency (2.29).  $q_c$  is the corresponding wavenumber in vacuum  $q_c = \frac{\Omega_0}{c}$ . The value of  $d$ , the separation between the graphene sheet and the antiferromagnet, is  $0.5 \mu\text{m}$ . For the antiferromagnet permeability function given by (2.27)-(2.29), the values of the quantities that determine it can also be consulted in equations (2.33)-(2.35). The value of the loss coefficient in (2.59) is  $\gamma_e = 0$  eV. Ignoring losses at the graphene sheet is valid when dealing with low temperatures. . . . . 22

2.5 Reflectance, Transmittance and Absorbance, as defined by equations (2.109), (2.108) and  $A = 1 - R - T$  for propagating TE waves incident from medium 3 on the system depicted in figure 2.1, for the frequency  $\omega = 0.90 \Omega_0$ . For the antiferromagnet permeability function given by (2.27)-(2.29), the values of the quantities that determine it can also be consulted in equations (2.33)-(2.35). The loss coefficient used in (2.59) was  $\gamma_e = 0.1$  eV. . . . . 23

2.6 Reflectance, Transmittance and Absorbance, as defined by equations (2.109), (2.108) and  $A = 1 - R - T$  for propagating TE waves incident from medium 3 on the system depicted in figure 2.1, for the frequency  $\omega = 1.10 \Omega_0$ . For the antiferromagnet permeability function given by (2.27)-(2.29), the values of the quantities that determine it can also be consulted in equations (2.33)-(2.35). The loss coefficient used in (2.59) was  $\gamma_e = 0.1$  eV. When the angle of incidence is higher than about 75 degrees, the value of  $q$ , the  $x$  component of the wave-vector, becomes so high that the wave cannot propagate inside the antiferromagnet, thus the sharp decline of the transmittance. . . . . 24

2.7 Dispersion relation for evanescent TM waves generated by surface magnon-plasmon polaritons, for the Fermi energy  $E_F = 0.03$  eV.  $\Omega_0$  is the antiferromagnet resonance frequency (2.29).  $q_c$  is the corresponding wavenumber in vacuum  $q_c = \frac{\Omega_0}{c}$ . The presence of the antiferromagnet splits the dispersion into a lower and upper branch. These are solutions to equation (2.128). The value of  $d$ , the separation between the graphene sheet and the antiferromagnet, is  $0.5 \mu\text{m}$ . For the antiferromagnet permeability function given by (2.27)-(2.29), the values of the quantities that determine it can also be consulted in equations (2.33)-(2.35). The value of the loss coefficient in (2.59) is  $\gamma_e = 0$  eV. Ignoring losses at the graphene sheet is valid when dealing with low temperatures. . . . . 26

2.8 Comparison between the loss function ( $\Im(r)$ ) from (2.148) and the dispersion relation from (2.128) for TM modes generated by surface magnon-plasmon polaritons.  $\Omega_0$  is the antiferromagnet resonance frequency (2.29).  $q_c$  is the corresponding wavenumber in vacuum  $q_c = \frac{\Omega_0}{c}$ . The value of  $d$ , the separation between the graphene sheet and the antiferromagnet, is  $0.5 \mu\text{m}$ . For the antiferromagnet permeability function given by (2.27)-(2.29), the values of the quantities that determine it can also be consulted in equations (2.33)-(2.35). The value of the loss coefficient in (2.59) is  $\gamma_e = 0 \text{ eV}$ . Ignoring losses at the graphene sheet is valid when dealing with low temperatures. . . . . 28

2.9 Reflectance, Transmittance and Absorbance, as defined by equations (2.158), (2.157) and  $A = 1 - T - R$  for propagating TM waves incident from medium 3 on the system depicted in figure 2.1.  $q_{lim} = \omega/c$  is the maximum value of  $q$  that maintains  $k_3$  real, for which we can say we have incident light from medium 3.  $k_1$  is always real for  $\omega < \Omega_0$  since  $\mu_1 > 1$ , which means the transmittance only goes to zero at the limit  $q = q_{lim}$  where  $k_3 = 0$ . The loss coefficient used in (2.59) was  $\gamma_e = 0.1 \text{ eV}$ . . . . . 30

2.10 Reflectance, Transmittance and Absorbance, as defined by equations (2.109), (2.108) and  $A = 1 - T - R$  for propagating TM waves incident from medium 3 on the system depicted in figure 2.1.  $q_{lim} = \omega/c$  is the maximum value of  $q$  that maintains  $k_3$  real, for which we can say we have incident light from medium 3.  $k_1$  becomes zero when  $q = \omega/c\sqrt{\mu_1}$  and imaginary for higher values of  $q$ . From that point on the transmittance is zero since there is no propagating light in medium 1. The loss coefficient used in (2.59) was  $\gamma_e = 0.1 \text{ eV}$ . . . . . 30

2.11 Scheme of the system with a graphene sheet a distance  $d$  from the antiferromagnet, of thickness  $a$  over a perfect metal. Evanescent waves decaying in the  $z$  direction, and propagating parallel to the graphene sheet will be studied, as well as propagating waves incident from medium 3, which generally is the vacuum or air. . . . . 31

2.12 Plot of the result of (2.185), which measures the overall difference between the energies of the modes with a graphene sheet of Fermi energy  $E_F = 0.4 \text{ eV}$  and the energies of modes with a graphene sheet of Fermi energy  $E_F = 0 \text{ eV}$ . The distance between the graphene sheet and the antiferromagnet is  $d = 0.05 \mu\text{m}$ . The 'mode distances' between the modes are measured as a function of  $a$ , the width of the antiferromagnet. This is a way to find the value of  $a$  which maximizes the effect of the graphene sheet on the energies of the modes of the system.  $\Omega_0$  is the antiferromagnet resonance frequency (2.29). For the antiferromagnet permeability function given by (2.27)-(2.29), the values of the quantities that determine it can also be consulted in equations (2.33)-(2.35). The value of the loss coefficient in (2.59) is  $\gamma_e = 0 \text{ eV}$ . Ignoring losses at the graphene sheet is valid when dealing with low temperatures. . . . . 34

2.13 Dispersion relation for TE modes (2.184) solved for the values of  $a$  and  $d$  that maximize the 'mode distance' between the  $E_F = 0$  eV scenario and the  $E_F = 0.4$  eV scenario. The definition of 'mode difference' used was  $\sum_n \Delta\omega_n$  where  $\Delta\omega_n$  is the difference between the solution number  $n$  with  $E_F = 0.4$  and the solution number  $n$  with  $E_F = 0$ , and the sum is over all solutions plotted. For these values of  $a$  and  $d$ , the effect of the graphene sheet on the dispersion relation is maximized.  $\Omega_0$  is the antiferromagnet resonance frequency (2.29).  $q_c$  is the corresponding wavenumber in vacuum  $q_c = \frac{\Omega_0}{c}$ . For the antiferromagnet permeability function given by (2.27)-(2.29), the values of the quantities that determine it can also be consulted in equations (2.33)-(2.35). The value of the loss coefficient in (2.59) is  $\gamma_e = 0$  eV. Ignoring losses at the graphene sheet is valid when dealing with low temperatures. 35

2.14 Comparison between the loss function ( $\Im(r)$ ) from (2.209) and the dispersion relation from (2.184) for TE modes generated by surface magnon-plasmon polaritons.  $\Omega_0$  is the antiferromagnet resonance frequency (2.29).  $q_c$  is the corresponding wavenumber in vacuum  $q_c = \frac{\Omega_0}{c}$ . The value of  $d$ , the separation between the graphene sheet and the antiferromagnet, is  $0.5 \mu\text{m}$ . The value of  $a$ , the thickness of the antiferromagnet, is  $50 \mu\text{m}$ . For the antiferromagnet permeability function given by (2.27)-(2.29), the values of the quantities that determine it can also be consulted in equations (2.33)-(2.35). The value of the loss coefficient in (2.59) is  $\gamma_e = 0$  eV. Ignoring losses at the graphene sheet is valid when dealing with low temperatures. . . . . 38

2.15 Values of the gap  $\Delta$  between between the lower and upper bands of TM modes for a separation between the antiferromagnet and the graphene sheet of  $d = 0.05 \mu\text{m}$ , as a function of  $a$ , for Fermi energies of  $E_F = 0.03$  eV and  $E_F = 0.07$  eV.  $\Omega_0$  is the antiferromagnet resonance frequency (2.29). For the antiferromagnet permeability function given by (2.27)-(2.29), the values of the quantities that determine it can also be consulted in equations (2.33)-(2.35). The value of the loss coefficient in (2.59) is  $\gamma_e = 0$  eV. Ignoring losses at the graphene sheet is valid when dealing with low temperatures. . . . . 40

2.16 Dispersion relation for TM modes (2.184) solved for different values of AFM width  $a$ , different metal distances  $d$  and Fermi energy of the graphene sheet  $E_F = 0.03$  eV. The values of  $a$  are chosen to maximize the splitting energy  $\Delta$ .  $\Omega_0$  is the antiferromagnet resonance frequency (2.29).  $q_c$  is the corresponding wavenumber in vacuum  $q_c = \frac{\Omega_0}{c}$ . For the antiferromagnet permeability function given by (2.27)-(2.29), the values of the quantities that determine it can also be consulted in equations (2.33)-(2.35). The value of the loss coefficient in (2.59) is  $\gamma_e = 0$  eV. Ignoring losses at the graphene sheet is valid when dealing with low temperatures. . . . . 41



2.17	Comparing the imaginary part of the reflectivity (2.258) (Loss function) with the dispersion relation for evanescent TM modes calculated in the previous section (2.234) generated by surface magnon-plasmon polaritons. $\Omega_0$ is the antiferromagnet resonance frequency (2.29). $q_c$ is the corresponding wavenumber in vacuum $q_c = \frac{\Omega_0}{c}$ . The value of $d$ , the separation between the graphene sheet and the antiferromagnet, is $0.5 \mu\text{m}$ . The value of $a$ , the thickness of the antiferromagnet, is $346 \mu\text{m}$ . The Fermi energy of the graphene sheet is $E_F = 0.07 \text{ eV}$ . The value of the loss coefficient in (2.59) is $\gamma_e = 0 \text{ eV}$ . Ignoring losses at the graphene sheet is valid when dealing with low temperatures. The loss function peaks at energies corresponding to the evanescent modes. . . . .	44
3.1	Sketch of the system under study in chapter 3: a TMD monolayer inserted in a dielectric cylindrical cavity of length $L$ with relative permittivity $\epsilon$ . The electrical permittivities of the materials in the cavity and their dimensions, as well as the TMD layer conductivity caused mainly by the formation of exciton-polaritons, will determine the optical spectra. .	46
3.2	Mode volume (3.58) as a function of the energies of the modes for $\mu = 0, 10$ . It is clear that for higher energy modes the angular momentum number $\mu$ does not influence the mode volume as much as for lower energy modes. The cylinder radius is $R = 3 \mu\text{m}$ and height $L = 0.3 \mu\text{m}$ . Furthermore, these values are much smaller than for a planar cavity due to the field confinement in all directions. . . . .	53
3.4	(Color online) Separations between the upper and lower polariton modes calculated within the classical picture, corresponding to Fig. 3.3(red balls) and using the quantum formalism (blue squares), for $\mu = 0$ (connected by solid lines) and 10 (connected by dashed lines). The parameters are the same as in Fig. 3.3. . . . .	57
3.3	(Color online) Uncoupled exciton (dashed line), MC photon (dashed line with black balls) and polariton dispersion curves for $\mu = 0$ and 10 (red balls and blue squares, respectively). The radial index takes only integer values but the points are connected to improve visibility. The parameters are: cylinder radius $R = 2 \mu\text{m}$ , height $L = 0.235 \mu\text{m}$ , dielectric constant of the MC material $\epsilon = 3.4$ , Fermi velocity $v_F = 5.5 \times 10^5 \text{ m/s}$ , exciton energy $E_{ex} = 1.9 \text{ eV}$ , and Bohr radius $a_{ex} = 0.8 \text{ nm}$ . . . . .	58
3.5	(Color online) Hopfield coefficients corresponding to the MC photon (red symbols and dash-lines) and two excitons ( $\mu \pm 1$ ) (green and blue symbols and dash-lines) for the upper and lower polariton modes with $\mu = 0$ and 10. The parameters are the same as in Fig. 3.3.	60
3.6	(Color online) Dependence of the DOS, $\rho^{(\mu)}$ , for empty cavity (defined similar to Eq. (3.101) but without sum over $i$ , red curve) and DOS for cavity with TMD layer projected over photonic ( $\rho_{ph}^{(\mu)}$ , Eq. (3.102), blue curve) and excitonic (green curve) subspaces for $\mu = 0$ . Also shown is the uncoupled exciton peak. All densities of states are shown normalized to unity, i.e. divided by $\int \rho^{(\mu)}(E)dE$ . The inset shows a zoom into the energy interval near the avoided crossing. . . . .	61
3.7	(Color online) Dependence of the local density of states, $\rho_{loc}^{(\mu)}(E; r, z = 0) \times V$ (where $V = \pi R^2 L$ ), on the normalized radius $r/R$ , for empty cavity and for cavity with TMD [where it is the polariton photon-projected LDOS, Eq. (3.103)], for $\mu = 0$ (left) and 10 (right). The lower panels highlight the redistribution of LDOS due to the TMD layer for the energies near the avoided crossing point. The parameters are the same as in Fig. 3.3.	63

3.8	(Color online) Energy and position dependence of the local emission rate of a point emitter located in the $z = 0$ plane calculated for empty cavity and for cavity with TMD. The right panel highlights the region near 1.87 eV where the Purcell effect enhancement due to the TMD layer is seen. We assumed $\bar{p}^{-1} = 1$ and other parameters are the same as in Fig. 3.3.	65
4.1	Photoluminescence of ZnO microspheres uniformly doped with point emitters (dye molecules Rhodamine B) under uniform illumination.	67
4.2	Solutions (for an ideal cavity) of equation (4.30) for TM-type modes and equation (4.34) for TE-type modes, with energy $\hbar\omega$ in eV for different $l$ . The energies presented correspond to the visible spectrum (1.65 to 3.1 eV). The radius of the sphere is $R = 3 \mu m$ . The dielectric constant of the sphere's material is $\epsilon = 3.4$ .	72
4.3	Evolution with respect to $m$ of local densities of states for TM-type modes, given by the first equation in (4.48). The $l$ value used is $l = 15$ and the $m$ values shown are, from left to right, $m = 0, m = 5, m = 10$ and $m = 15$ . The circle $(x', z)$ is any constant $\phi$ cross-section of the sphere. The radius used was $R = 2 \mu m$ , the energy at which the LDOS is calculated is 2 eV and only modes with $0 < \hbar\omega < 4$ (eV) were considered.	74
4.4	Evolution with relation to $m$ of local densities of states for TE-type modes, given by the second equation in (4.48). The $l$ value used is $l = 15$ and the $m$ values shown are, from left to right, $m = 0, m = 5, m = 10$ and $m = 15$ . The circle $(x', z)$ is any constant $\phi$ cross-section of the sphere. The radius used was $R = 2 \mu m$ , the energy at which the LDOS is calculated is 2 eV and only modes with $0 < E < 4$ (eV) were considered.	75
4.5	Real part of the solutions to equations for TM-type modes (4.53) and TE-type modes (4.55). The radius of the sphere is $R = 2 \mu m$ , $\epsilon_1 = 3.4$ and $\epsilon_2 = 1$ .	78
4.6	Imaginary parts of the solutions to the equation for TM-type modes (4.53) on the left and TE-type modes (4.55) on the right. Modes outside the visible range (1.65 to 3.1 eV) have been painted black. Note that the higher the angular momentum $l$ of a mode, the higher its lifetime. The radius of the sphere is $R = 2 \mu m$ , $\epsilon_1 = 3.4$ and $\epsilon_2 = 1$ .	78
4.7	Evolution with respect to $m$ of local densities of states for TM-type modes, real cavity with $\epsilon_1 = 3.4$ inside the sphere and $\epsilon_2 = 1$ outside. The local density of states ( $\rho_{l,m}$ ) is calculated according to equations (4.57)-(4.62) and using the electric field for real modes from equations (4.50). The $l$ value used is $l = 15$ and the $m$ values shown are, from left to right, $m = 0, m = 5, m = 10$ and $m = 15$ . The circle $(x', z)$ is any constant $\phi$ cross-section of the sphere. The radius used was $R = 2 \mu m$ , the energy at which the LDOS is calculated is 2 eV and only modes with $0 < \hbar\omega < 4$ (eV) were considered.	80
4.8	Evolution with respect to $m$ of local densities of states for TE-type modes, real cavity with $\epsilon_1 = 3.4$ inside the sphere and $\epsilon_2 = 1$ outside. The local density of states ( $\rho_{l,m}$ ) is calculated according to equations (4.57)-(4.62) and using the electric field for real modes from equations (4.51). The $l$ value used is $l = 15$ and the $m$ values shown are, from left to right, $m = 0, m = 5, m = 10$ and $m = 15$ . The circle $(x', z)$ is any constant $\phi$ cross-section of the sphere. $x'$ is the value on the $x$ axis rotated by the angle $\phi$ . The radius used was $R = 2 \mu m$ , the energy at which the LDOS is calculated is 2 eV and only modes with $0 < \hbar\omega < 6$ (eV) were considered.	81

4.9	(a) Cross-section of a sphere with incident radiation of intensity $I_i$ . The first two reflections are depicted, (but there are more). Equation (4.66) takes into account all reflections. (b) Side view of the sphere, showing projections of different diametric cross-sections onto zOx plane. All circles obeying equation $\phi = const$ are similar and will exhibit the same distribution of transmitted radiation. This symmetry means that it is only necessary to study one of these circles. . . . .	83
4.10	Schematic of the coordinate system used to determine the positions along the ray path. . . . .	83
4.11	Plot of the density distribution of energy absorbed, per unit time and unit length, from equation (4.84) for two different $n$ values. The point of maximum density occurs at $r/R = 1/n$ . So, the index of refraction of the sphere determines this point. However, the value of this peak goes with $1/n^2$ . . . . .	86
4.12	Evolution with relation to $l$ of the sums of local densities of states multiplied by the intensity distribution $\mathcal{W}_{abs}(r)$ for TE modes on the left and TM modes on the right. The $l$ values shown are, from top to bottom, $l = 1$ , $l = 10$ and $l = 30$ . The circle $(x', z)$ is any constant $\phi$ cross-section of the sphere. $x'$ is the value on the $x$ axis rotated by the angle $\phi$ . The radius used was $R = 2 \mu\text{m}$ , the energy at which the LDOS is calculated is 2 eV and only modes with $0 < \hbar\omega < 6$ (eV) were considered. . . . .	89
4.13	On the left, the normalized Purcell factor from (4.89), and on the right, the same factor multiplied by the intensity distribution $\mathcal{W}_{abs}(r)$ . The $l$ values used ranged from $l = 1$ to $l_{max} = 40$ . The criterion applied was to only use modes whose energies were smaller than $\hbar\omega = 6$ eV. The radius used was $R = 2 \mu\text{m}$ , the energies at which the LDOS is calculated are 2 and 2.5 eV. . . . .	90
4.14	Variation of the Purcell factor defined by (4.89), which is a multiple of the complete local density of states, with the distance from the center of the sphere, in the approximation of a large sphere (4.120), for a constant $E$ value of 2 eV. The total local density of states will be the sum of all possible $n$ values, in this case, all 428 possible values. The radius of the sphere is $R = 100\mu\text{m}$ . The refractive index is $n = \sqrt{\epsilon} = 1.33$ . . . . .	93
4.15	Variation of the Purcell factor defined by (4.89), multiplied by the incident ray distribution factor (4.84), with the distance from the center of the sphere, in the approximation of a large sphere (4.120), for a constant $E$ value of 2 eV. The total local density of states will be the sum of all possible $n$ values, in this case, all 428 possible values. The radius of the sphere is $R = 100\mu\text{m}$ . The permittivity is $\epsilon = 1.33$ . . . . .	94
5.1	Comparison of the field components' profiles $E_z$ and $D_r$ from exact solution, Eq. (5.65) (dashed lines) and from the ideal cavity model, Eq. (5.66) (full red lines) for $ck_z = 4$ eV. The radius of the cylinder $R = 3 \mu\text{m}$ , $\epsilon_1 = 1$ , $\epsilon_2 = 3.4$ , and the height $L = 0.3 \mu\text{m}$ . . . . .	103

# 1

## Introduction

---

### 1.1 Scope of this thesis

Light-matter interaction is responsible for a broad variety of phenomena and is in the heart of important fields of applications, such as microscopy, optoelectronics, photonics and renewable energy production. The development of materials technology led to new possibilities of using and controlling light, making optoelectronic devices that are much smaller than the wavelength of the light they work with, and the emergence of new areas of research, such as nanophotonics [1]. For example, in a recently published work [2], almost total light absorption in a nearly-atomic thick semiconductor layer incorporated in a specially designed photonic structure was demonstrated. This thesis work was inspired by such achievements. It is devoted to theory and modelling of several photonic structures where strong light-matter interaction leads to the formation of composite excitations called polaritons and strongly influences the optical properties of these structures.

The two most important particles in electromagnetism are the photon and the electron. [3] This work will explore two physically distinct ways in which the electron can be affected by a photon. To be more precise, ways in which a collective excitation of a system with multiple electrons can be created with the energy gained from absorbing a single photon. The interaction of the electromagnetic field of a photon with charged particles in any crystalline structure is called a polariton. [4, 5] Graphene is a material where this interaction can occur. In graphene, the charged particles that interacts with photons are electrons, but collective excitations of larger charged particles can occur in solids, specially at high temperatures. These excitations are called phonons because they are the basis of sound waves, and when the particles that oscillate are charged, these phonons can interact with electromagnetic waves to form phonon-polaritons (Sec 4.6., [6]). A graphene layer is a one atom thick layer of carbon atoms arranged in an hexagonal lattice. [7] In a graphene layer, electrons can oscillate when excited by an oscillating electromagnetic wave. [8] These charge oscillations generate their own electromagnetic field. This state of interaction can be considered as a collective excitation of the graphene electrons, normally called plasmon. [9] Graphene plasmons create an evanescent electromagnetic field, which decays exponentially with distance to the graphene sheet. The combination of the charge oscillations and the evanescent EM field is called the surface plasmon polariton (SPP). SPPs have their own dispersion relations, different

from those of any of the single electrons, plasmons or of the original photons. [9]

An analogous phenomenon can happen with spin carriers, such as atoms with total spin in an antiferromagnet. These spin carriers are affected by the magnetic field and when their spin changes direction it generates another magnetic field which influences the neighbouring spin carriers. These spin oscillations are called magnons and they too have their dispersion relations and act as particles, having properties that can be derived from dispersion relations such as effective mass (which is defined as the inverse of the second derivative of the energy with respect to the momentum, and its value indicates the effect that the other particles in the material are having on the response of a given particle to the application of a force [10]). [11] These oscillations, of electrical or magnetic nature, are a way in which electrons can be affected by a photon in a system with more than one medium. Such a system will be studied in chapter 2.

In chapter 3 the discussion will shift to a different system, a micro-cavity with an embedded 2D semiconductor layer. [12] An optical micro-cavity is any closed cavity with partially or totally reflecting boundaries, with dimensions of the order of micro-meters, hence the name micro-cavity. [13] And a semiconductor is a material that has a small gap between the valence band, which is the highest energy band within the material where electrons will still be present, which is completely filled with electrons, at zero temperature, and the conduction band, which is the band immediately above where electrons can travel across the material. [10] The conventional definition of a semiconductor is a material whose valence-conduction band gap is larger than 0 eV but smaller than 4 eV. [14] In chapter 3, the interaction studied is physically different. It involves a semiconductor material with essentially two energy bands, where the electron can go from the valence band to the conduction band if it absorbs a photon with a sufficient energy. The collective effect of all but one electron present in the valence band is equivalent to the presence of a positive charge in the place of the hole the electron leaves in the valence band. [15] This electron will 'attract' the hole (in reality, it is repelling all the electrons left in the valence band). Nevertheless, this electron-hole system can be treated as a particle similar to an hydrogen atom, although the masses of its charged particles are the same. This electron-hole pair is called an exciton (because it comes from the excitation of the electron from the valence to the conduction band) and it has bound states that have some similarity with the hydrogen atom states. [16] The effect of exciton-photon interaction studied in chapter 3 is not the physical oscillations of these excitons, but rather their oscillations in and out of existence, successively creating and destroying photons. These oscillations are made possible within the micro-cavity if the energies of the photons allowed within it are similar to the energies of the gaps between the valence and conduction bands of the semiconductor material inserted. [15] This process of successive creation and destruction of an exciton can be referred to as an exciton-polariton and it too can be thought of as a particle ('pseudo-particle') with its own dispersion relation and associated properties. [15] It is therefore interesting to study how these dispersion relations differ from the dispersions of the empty micro-cavity and if the effect of the exciton-polaritons can be used to control the emission properties of said cavity. [4]

Finally, in chapter 4, pure photonic states in a spherical micro-cavity will be studied. The goal will be to present the spatial distribution of intensity of the combined electromagnetic field of all the possible states of the system. The system of interest consists of point emitters embedded in a relatively large (micrometric) sphere made of a transparent dielectric material, which acts as a spherical cavity and influences the point emitters. This is known as the Purcell effect [17]. The Purcell factor is calculated

for the cavities of chapters 3 and 4. The Purcell factor is a measure of the level of enhancement of the spontaneous emission rate of a material when it is part of a given cavity or system, compared to the spontaneous emission rate it would display in an homogeneous isotropic environment. [17] In both these chapters the Purcell factor is calculated as a function of the local density of states of electromagnetic cavity modes. Calculation of the Purcell factor and its spatial variation allows to predict where the most intense spots of radiation will occur if photons of a particular energy reside in the micro-cavity or an emitter is placed at a given spot. [18] The study mentioned so far is only focused on the eigenstates of the system and not on the means of excitation of these states. Furthermore, a simple model of geometrical optics will be applied in order to deduce the effect of an incidence of plane waves on the cavity and mathematically account for the radial probabilistic distribution of incident photons that enter the cavity in a similar fashion to the rainbow theory. [19] The main results obtained in this work are summarized in chapter 5. Some of these results have been published [12, 20].

## 1.2 Materials used in the systems studied

The first two systems under study incorporate three different materials that allow for the creation of different types of polaritons. These materials will be introduced in this section.

### Graphene

As previously mentioned, graphene sheets are one atom thick layers of carbon atoms arranged on a hexagonal lattice. Graphene is a semi-metal with a zero band gap. [21] Graphite, which is what pencils are made of, is a collection of stacked graphene layers bound by weak van der Waals forces. [22] Creating graphene is simply a matter of isolating a single layer from these stacks. This material is extremely interesting because it exhibits Dirac electrons. These electrons have a linear dispersion relation (close to the Dirac points [9]) and therefore their effective mass is zero. The Dirac points are those where the upper band touches the lower band. [23] Because their effective mass is zero, the Dirac electrons all must behave like light inside the graphene layer, having a constant fixed velocity. This characteristic is common of all Dirac semimetals, but graphene has the longest mean free path at room temperature, features clear quantum Hall effects (half integral and fractional) and has the highest mobility. [24] These characteristics, along with its' light weight, make it a very intriguing material to study for a range of technological applications. [9] However, electronics applications are difficult to accomplish with pure graphene. For pure graphene, the bandgap is zero and therefore it is very difficult to build transistors out of this material. [9] The Fermi energy is defined as the energy range of the electrons at absolute zero temperature. By changing this energy, the bandgap can be controlled. Graphene can be doped in various ways to change the Fermi energy, creating either p-type graphene, which has the Fermi level below zero acting similar to a semiconductor, or n-type graphene, which has the Fermi level above zero acting similar to a metal. [9, 24] The band structure of graphene has been calculated with a tight-binding model resulting in the expression [25]:

$$E_{\pm}(\mathbf{k}) = \pm t\sqrt{3 + f(\mathbf{k})} - t'f(\mathbf{k}). \quad (1.1)$$

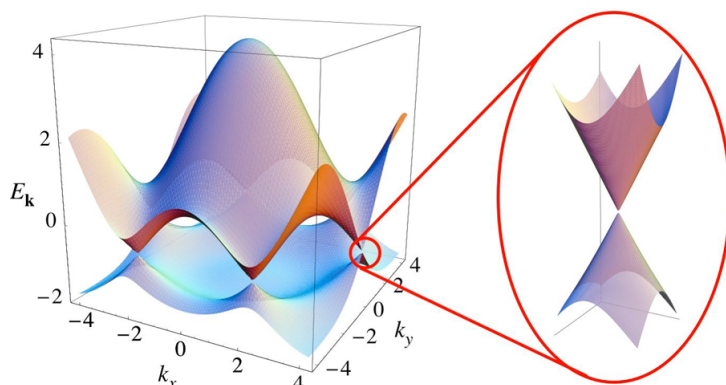


Figure 1.1: Electronic band structure of graphene showing the linear dispersion relation that characterizes Dirac electrons at the Dirac points, as given by (1.1). The Dirac points are the points where the upper band touches the lower band. [23] The electrons' effective mass is zero, near these points. [9] Because their effective mass is zero, the Dirac electrons all must behave like light inside the graphene layer, having a constant fixed velocity. The dispersion is shown in units of  $t$  with numerical values of  $t = 2.7$  eV and  $t' = -0.2t$ . [21]

Graphene can support surface plasmon polaritons when the density of Dirac electrons oscillates along with an oscillating electromagnetic field. [9] This field is exponentially decaying away from the graphene sheet. For the same frequency, the wave number of the polariton is much larger than that of the free-space photon, which leads to the aforementioned exponential decay. [8] The SPPs in graphene are localized on a scale lower than its wavelength and this is generally referred to as subwavelength optical confinement. [26] This precise localization is very alluring for optical devices and it is the property sought after in various fields such as optical data storage, spectroscopy, microscopy, integrated photonics, lithography, biological photonics, chemical studies, etc... [27] The conductivity of graphene under typical doping levels can be modelled by the Drude-like expression [9]:

$$\sigma(\omega) = \frac{e^2}{\pi \hbar} \frac{E_F}{\hbar \gamma - i \hbar \omega}, \quad (1.2)$$

where  $\gamma$  is a damping rate. This expression is used throughout chapter 2 as the graphene optical conductivity. Equation (1.2) is valid with both temperature and nonlocal effects can be ignored.

### 1.2.1 Uniaxial antiferromagnets

The second material featured in the system studied in chapter 2 is an uniaxial antiferromagnet, namely  $\text{MnF}_2$ . This material features antiferromagnetism in a single direction, that is, it contains layers of spins in which all the spins in the layer are aligned with each other but anti-aligned with the spins in the layers above and below. [20, 28] Figure 2.1 illustrates this arrangement. When acted upon by a magnetic field, the spins will precess around it as shown in figure 1.2, and their collective behaviour can form an excited state called the magnon. [11] Magnons are quantized spin waves, and they can occur both in ferromagnets and antiferromagnets. Without the magnetic field, the ground state of a layer of spins in an antiferromagnet consists of the spins all oriented in the same direction. The first excited state corresponds

to the inversion of one of the spins, and it is this inversion that creates a magnon because the effect of this inversion will spread as a wave around the original inverted spin. [11] The precession frequency of the individual spins is what determines the energy of a single magnon:

$$E_{magnon} = \hbar\omega_{prec}. \quad (1.3)$$

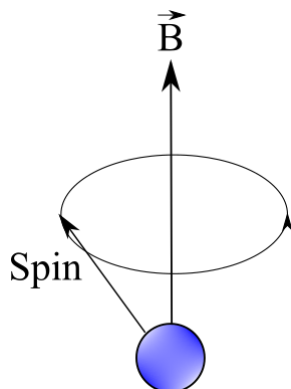


Figure 1.2: Depiction of the precession of the spin of a particle that takes place in the presence of an external magnetic field.

However, in ferromagnets the only factor at play is the magnetic anisotropy, which is much smaller than the interplay of exchange and anisotropy that occurs in antiferromagnets. [20] The choice for an uniaxial antiferromagnet to interact with the graphene layer is due to the fact that these magnons caused by the interplay of exchange and anisotropy have energies in the same spectral range as the energies of the SPPs in graphene (THz). [29] Spintronics, as opposed to electronics, is the manipulation of spin transport instead of charge transport in order to create devices for communication of information. [30] Antiferromagnets are also more useful for spintronic applications than ferromagnets. This is mainly because antiferromagnets have zero net angular momentum, which means they are much less affected by external electromagnetic fields. The spin transport in antiferromagnet as only been found to be reliable over a few nanometres [31] However, exploitation of the Hall effect allows for long-distance spin transport. [32] These uniaxial antiferromagnets can host surface and bulk magnon polaritons, which can be described as the result of interactions of photons with magnons. This is possible because the photon's magnetic field can couple to the spins in the antiferromagnets and generate magnons. However, the magnon's oscillating spins generate a magnetic field which corresponds to new photons. This back and forth creations of magnons and photons is what is described as a magnon-polariton. [29] Bulk magnon polaritons occur inside the antiferromagnetic material, where the boundary with the dielectric material is sufficiently far away. However, close to this boundary we have surface polaritons, whose electromagnetic fields decay exponentially away from the interface. [28]

### 1.2.2 Transition metal dichalcogenides

Transition metal dichalcogenides (TMD) are semiconductor materials that allow for some strong light-matter coupling. [33] A single layer of this material consists in a triangular lattice of a transition metal in



the middle of two triangular lattices of a chalcogen atom (S, Se or Te). [34] This structure is illustrated in figure 1.3. There are many photoelectronic applications of TMDs (for example, photodetection and lasing) [34–36]. The strong light-matter coupling that takes place is through the possibility of the formation of excitons. [15, 33]

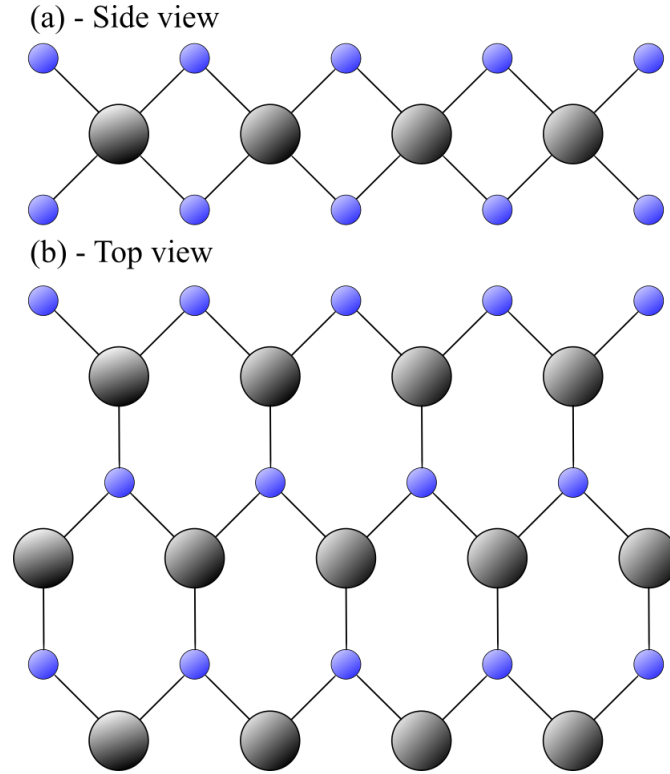


Figure 1.3: Structure of a transition metal dichalcogenide (TMD) monolayer. The black spheres represent the transition metal atoms (Mo, W, etc) and the blue spheres the smaller chalcogen atoms (S, Se, or Te) [37]. A single layer of this material consists in a triangular lattice of a transition metal in the middle of two triangular lattices of a chalcogen atom (S, Se or Te). (a) Side view, a layer with a thickness of only three atoms. (b) Top view, the repeating pattern of the monolayer on the plane with which it is aligned.

An exciton is a quasiparticle that arises from the combination of an electron on the conduction band of the semiconductor and the hole that it leaves behind in the valence band. [13] In TMDs, the excitons are very robust, with binding energy of the order of 0.5 eV and a very small effective Bohr radius. [33] Bound excitons can therefore be found at room temperature and 3D confinement of the exciton is possible. At the  $K$  and  $K'$  points of the Brillouin zone there are strong dipole optical transitions, for these are the points with the smallest gaps between the conduction and valence bands. [33] The electronic states are nearly two dimensional and this results in highly anisotropic emission. Furthermore, there are specific selection rules with (circular-) polarization-valley correlation. Compared to traditional semiconductor quantum wells, mono- or few-layer TMDs can more easily be combined with other 2D materials such as graphene and h-BN to make van der Waals heterostructures, [38] as well as be coupled to other quantum emitters [39–41] or plasmonic nanostructures. [42–45]. Recently, integration of an electroluminescent van

der Walls heterostructure containing a TMD layer cladded by h-BN and graphene layers into a monolithic optical micro-cavity was demonstrated, leading to a strong increase and a modification of the angular distribution of the electrically pumped emission from the TMD layer. [46]

### **TMD layer interacting with microcavity EM modes**

The combination of the TMD layer exciton with the electromagnetic eigenmodes of a microcavity is the exciton-polariton. [13, 15] Inserting the TMD layer in the microcavity greatly enhances the light-matter coupling as compared to having the layer interact with incident radiation in free space. [13, 15] In the strong coupling regime, the exchange of energy between excitons and photons becomes reversible, yielding a number of interesting and potentially useful effects owing to the formation of collective excitations called exciton-polaritons. [13, 15] It has been possible to modify the energy spectrum of these cavities with the light-matter coupling. This has been done for a variety of structure including Fabry-Perot cavities with Bragg reflectors as mirrors, micropillars, photonic crystals and plasmonic surfaces and nanostructures [47]. The strong coupling regime was studied theoretically and demonstrated experimentally for usual Fabry-Perot [35, 48–50] and the so called Tamm-type micro-cavities, [51] and also for a cylindrical whispering gallery mode (WGM) resonator. [52] Integrating van der Waals heterostructures with optical waveguides has recently been reviewed. [53]

The encouraging results obtained in these experimental work include high Rabi splittings (comparable to the best GaAs and II-VI MCs), the existence of exciton-polaritons at room temperature, and 2D-exciton-mediated lasing. The latter was achieved with a WGM microdisk resonator containing an embedded WS<sub>2</sub> monolayer. [52] Such a closed geometry ensures better confinement of light (smaller mode volume) and, potentially, can provide a stronger exciton-photon coupling compared to the traditional Fabry-Perot type of cavity.

## **1.3 Plasmon-polaritons and Magnon-polaritons**

The system studied in chapter 2 is a composite system made of a semi-infinite antiferromagnet and a graphene layer placed above at a certain distance. As discussed above, the antiferromagnet supports the creation of magnon-polaritons and the graphene layer supports the creation of plamon-polaritons. In this system, hybrid modes are possible, where the plasmons interact with the magnons to create stable eigenmodes of the system. [20] The graphene sheet therefore allows for tunability of the properties of the antiferromagnet, mainly the dispersion relation of the electromagnetic modes present in the system. The dispersion relations for TE and TM modes will be calculated for evanescent waves propagating parallel to both the graphene sheet and the antiferromagnet. This is accomplished by application of electromagnetic boundary conditions derived from Maxwell's equations and appropriate constitutive relations. [54] The scattering of incident plane waves is also studied, where there is an incident wave, and the boundary conditions are used to determine the reflectance and transmittance of the system. The results from these two calculations are related and this relation will be shown by comparing the loss functions (imaginary part of the reflectivity) of the propagating modes to the dispersion relations of the evanescent modes. Since the loss function should display peaks along the dispersion relation curves, [9] this comparison helps to confirm the validity of the calculations. Finally, the study is repeated for a system where a perfect metal is placed at the bottom of the antiferromagnet, effectively introducing another distance parameter:

the thickness of the antiferromagnet. In this case, it is possible to create a slightly larger gap between the first two bands of the TM modes. This distance parameter is another way to control the dispersion relation of these hybrid modes.

## 1.4 Microcavity polaritons

Polaritons arising in microcavities are also studied, as mentioned before, in chapters 3 and 4. These polaritons and their properties can be studied theoretically with linear optics by applying macroscopic Maxwell's equations. [55] The electrical permittivities of the materials in the cavity and their dimensions determine the optical spectra. Experimentally, these modes can be studied with an array of techniques such as infrared spectroscopy or Raman scattering. [55] Polaritons arise in these structures as interactions of the vibrations of the transient dipoles associated with certain particles (for example semiconductor excitons or phonons) with electromagnetic fields that can be either external or generated by the vibrations of said particles. A simple example of a system displaying polaritons is given in [55]. This system is a 'diatomic isotropic crystal with an ion-covalent type of the interatomic bond (of the cubic ZnS type)', and the permittivity of this material can be written as:

$$\epsilon(\omega) = \epsilon_\infty + (\epsilon_0 - \epsilon_\infty) \frac{\omega_{TO}^2}{\omega_{TO}^2 - \omega^2}, \quad (1.4)$$

where  $\omega_{TO}$  stands for the frequency of transverse optical phonons and  $\epsilon_\infty$  and  $\epsilon_0$  are just the high and low frequency limits, respectively. This model allows for bulk polaritons obeying the dispersion relation

$$\frac{k^2 c^2}{\omega^2} = \epsilon(\omega). \quad (1.5)$$

Each different type of polariton will have a different dielectric permittivity function  $\epsilon(\omega)$ . As such, the dispersion relation is determined by calculating the correct  $\epsilon(\omega)$  dependency for the polariton in question. In this work, the problems of determining the conductivity of a graphene sheet (caused by plasmons) and of a sheet of 2D semiconductor material (caused by excitons) will be tackled and these conductivities will be used to determine the dispersion relations of systems where these materials are embedded. Theoretically, bulk polaritons are described by propagating electromagnetic fields in the direction perpendicular to the surface of the materials and surface polaritons are characterised by evanescent fields. However, this distinction is not available to an experimentalist that simply analyses the spectrum results. As such, it is a considerable challenge for experimentalists to separate the contributions of surface modes from those of bulk modes [55]. The most typical Fabry-Perot cavities use dielectric Bragg mirrors, also referred to as Distribution Bragg Reflectors (DBR). These are pairwise layers of materials with alternating refractive index. The higher the contrast of the refractive index and the higher the number of pairs, the higher the finesse of the cavity. [13] Microcavities with a semiconductor-metal interface can have a significant Schottky barrier height. The Schottky barrier height is the potential energy above which the interface can conduct electricity. For metal/n-type interface, this will correspond to the difference between the conduction band minimum and the Fermi level of the metal. And for a metal/p-type interface, this will correspond to the difference between the valence band maximum and the Fermi level. [56] It is possible to take advantage of this barrier for photodetection and laser control. [55] Surface polaritons can be turned from non-radiative to radiative by the insertion of an attenuated total internal reflection prism

(ATR) above the crystal. [57] The function  $\epsilon(\omega)$  of some systems can be modelled theoretically, and from that function the observable properties like the reflectance  $R(\omega)$ , transmittance  $T(\omega)$  and absorbance  $A(\omega)$  can be determined. Conversely, when experimentalists measure the response of a system they can place the system on a metal, making  $T(\omega) = 0$ , and obtain values for  $A(\omega)$ , which uniquely determines  $R(\omega) = 1 - A(\omega)$  (ignoring scattering) and then from the integral Kramers-Kronig relations they can use the reflectance spectrum  $R(\omega)$  to obtain an estimate for the function  $\epsilon(\omega)$ . [55] Alternatively, the thermal emission spectrum of the system can be measured and compared to the blackbody spectrum at that temperature. [55] The difference between them allows to determine the polariton spectrum of the system being studied, if there is no significant process other than polariton formation at that temperature. Approximately cylindrical shape cavities can be obtained by etching a planar one with Bragg reflectors. In these structures the lateral confinement is provided by planar microcavities whereas DBR mirrors provide the vertical confinement. Such a structure (shown in Fig. 1.4) is called a pillar micro-cavity. A cavity like this is suitable for incorporating a 2D semiconductor layer [35]. A similar pillar micro-cavity with one dielectric material and a 2D semiconductor layer is studied in chapter 3.

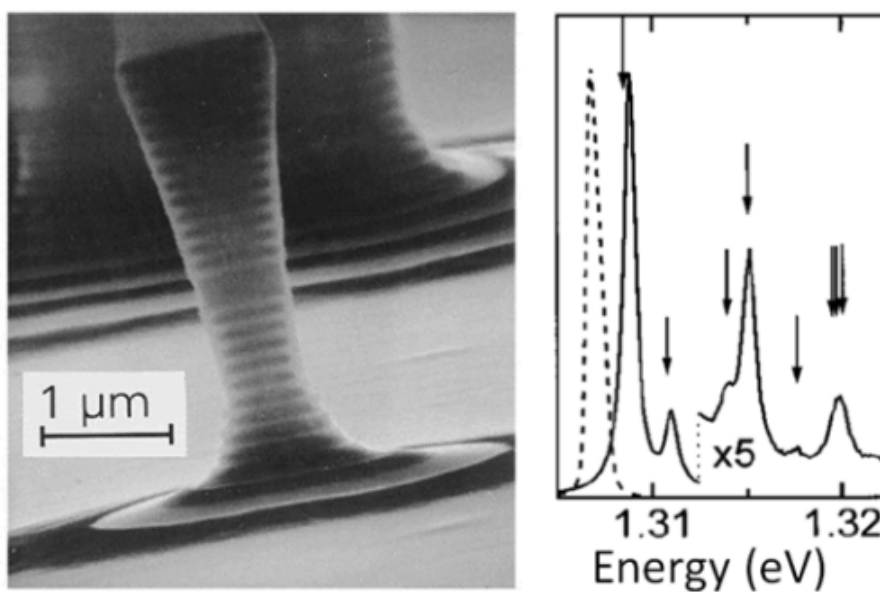


Figure 1.4: 'Pillar microcavity from an etched planar DBR semiconductor microcavity (left), with emission mode spectrum (right), from Gérard et al. (1996).' Figure 1.10 from [13].

# 2

## Polaritonics of antiferromagnets with graphene

---

Uniaxial antiferromagnets typically exhibit resonant frequencies in the THz range, which is much higher than the GHz range of ferromagnetic materials. [20] These higher frequencies are much closer to the spectral range of graphene surface plasmon polaritons, and thus a coupling between magnon-polaritons at the antiferromagnet and plasmons in the graphene sheet can lead to hybrid polaritons. [20] Our goal is to study these hybrid polaritons by calculating the dispersion relations of a system consisting of a graphene sheet placed a distance  $d$  from a semi-infinite antiferromagnet. Figure (2.1) illustrates the system under consideration. The goal is to study the effect of the graphene sheet on the polaritonic modes of the antiferromagnet. To achieve this, one needs to model the magnetic permeability of the antiferromagnet first.

### 2.1 Magneto-optic response of an easy-axis antiferromagnet with no static field

An antiferromagnetic medium exhibits a relative magnetic permeability tensor  $\overleftrightarrow{\mu}_r$  which characterizes its interaction with the magnetic fields through

$$\mathbf{B} = \overleftrightarrow{\mu}_r \cdot \mathbf{H}. \quad (2.1)$$

This tensor must be determined in order to correctly calculate the response fields  $\mathbf{B}$  in the system. The antiferromagnetic material considered will be  $\text{MnF}_2$ . Below the Néel temperature, this material can be treated as a set of alternating spin lattices [58], as figure 2.2 illustrates. Hence, each Mn point in the lattice can be modelled as a point magnetic dipole and the total magnetization (with no external field) is zero.

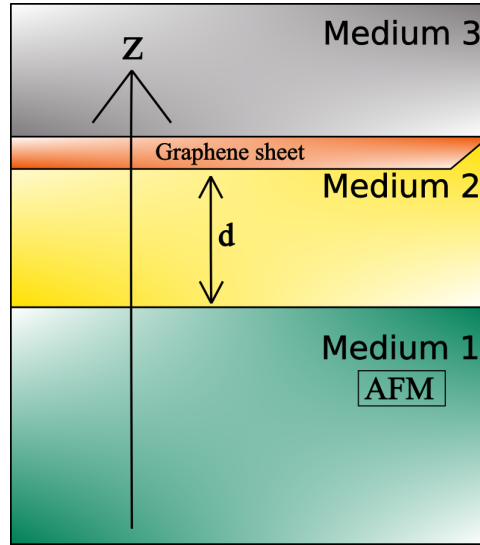


Figure 2.1: Scheme of the system under study, with the antiferromagnet a distance  $d$  away from the graphene sheet. Medium 1 is the AFM, medium 2 is below the graphene sheet, and medium 3 is above the graphene sheet. Evanescent waves decaying in the  $z$  direction, and propagating parallel to the graphene sheet will be studied, as well as propagating waves incident from medium 3, which generally is the vacuum or air.

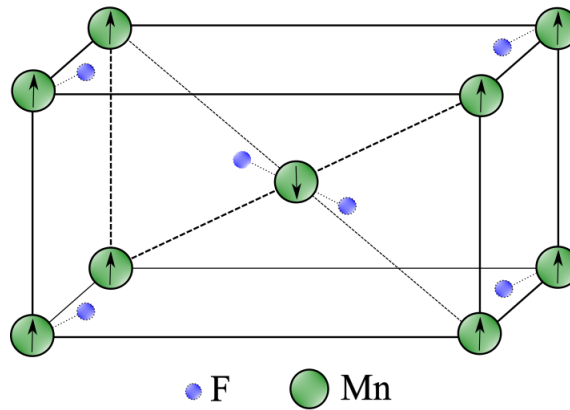


Figure 2.2: Crystalline structure of  $\text{MnF}_2$  with overlapping lattices. For temperatures under the Néel temperature, this material can be treated as a set of alternating spin lattices. [58]

The magnetization  $\mathbf{M}$  must obey the relation:

$$\mathbf{B} = \mathbf{H} + 4\pi\mathbf{M}. \quad (2.2)$$

A semi-classical approach will be used to determine the magnetization. An oscillating magnetic field induces spin precession, and this precession occurs in the positive direction for positive spins and negative direction for negative spins, as shown in figure 1.2. Firstly, one writes the torque applied to a magnetic

dipole  $\mathbf{m}$  in the presence of an external field:

$$\boldsymbol{\tau} = \mathbf{m} \times \mathbf{H}_{ext}. \quad (2.3)$$

Considering the wavelength is much larger than the distance between the lattice dipoles, the torque equation for the sublattice  $i$  (2D) reads:

$$\boldsymbol{\tau}_i = \mathbf{M}_i \times \mathbf{H}_{ef}, \quad (2.4)$$

where  $\mathbf{H}_{ef}$  is the applied effective field felt by the sublattice and  $M_i$  is its magnetization. Classically, the torque is defined as [59]

$$\boldsymbol{\tau} = \frac{d\mathbf{L}}{dt}, \quad (2.5)$$

where  $\mathbf{L}$  is the angular momentum. The gyromagnetic ratio  $\gamma$  relates the angular momentum to the magnetization by  $\gamma\mathbf{L} = \mathbf{M}$ . This means that for the sublattice:

$$\boldsymbol{\tau}_i = \frac{1}{\gamma} \frac{d\mathbf{M}_i}{dt}. \quad (2.6)$$

The gyromagnetic ratio for electrons is given by [54]

$$\gamma = \frac{q}{2m}, \quad (2.7)$$

with  $q$  and  $m$  being the charge and mass of the electron. The magnetization is determined by:

$$\frac{1}{\gamma} \frac{d\mathbf{M}_i}{dt} = \mathbf{M}_i \times \mathbf{H}_{ef}. \quad (2.8)$$

In the absence of an external static field, the effective field  $\mathbf{H}_{ef}$  will be modelled by three terms:

1. The anisotropy field, which aligns the spins in the preferential direction of the antiferromagnet -  $\mathbf{B}_A$ ,
2. An exchange field, which models the interaction between the sublattices of opposing spins and drives the spins in opposite directions -  $\mathbf{B}_E$ ,
3. And finally the external oscillating fields -  $\mathbf{H}$ .

The anisotropy fields field by sublattices 1 and 2 will thus take the form:

$$\begin{cases} \mathbf{H}_A^{(1)} = B_A \hat{z} \\ \mathbf{H}_A^{(2)} = -B_A \hat{z} \end{cases}. \quad (2.9)$$

Furthermore, the exchange fields will be:

$$\begin{cases} \mathbf{H}_E^{(1)} = -B_E \frac{\mathbf{M}_2}{|\mathbf{M}_2|} \\ \mathbf{H}_E^{(2)} = -B_E \frac{\mathbf{M}_1}{|\mathbf{M}_1|} \end{cases}. \quad (2.10)$$

If the external field is small compared with the other fields, one can assume the magnetization on the easy-axis of the sublattices to be unaffected, which means for the easy-axis aligned with  $z$ ,  $\mu_{zz} = 1$ . It

is also known the components of the magnetization along this axis for the different sublattices must be symmetric. Thus, we define:

$$M_S = M_{1z} = -M_{2z}, \quad (2.11)$$

where the sublattice 1 is the one whose spins are oriented in the  $+z$  direction and the sublattice 2 in  $-z$  direction. Following the assumption of small external field, it is also possible to write, approximately, the exchange fields as:

$$\begin{cases} \mathbf{H}_E^{(1)} = -B_E \frac{\mathbf{M}_2}{M_S} \\ \mathbf{H}_E^{(2)} = -B_E \frac{\mathbf{M}_1}{M_S} \end{cases}. \quad (2.12)$$

Due to the symmetry in  $xy$ , it suffices to consider only the component  $H_x$  of the external field. Thus, the effective field becomes:

$$\mathbf{H}_{ef}^{(1)} = \hat{x} \left( H_x - B_E \frac{M_{2x}}{M_S} \right) - \hat{y} \left( B_E \frac{M_{2y}}{M_S} \right) + \hat{z} (B_A + B_E). \quad (2.13)$$

$$\mathbf{H}_{ef}^{(2)} = \hat{x} \left( H_x - B_E \frac{M_{1x}}{M_S} \right) - \hat{y} \left( B_E \frac{M_{1y}}{M_S} \right) - \hat{z} (B_A + B_E). \quad (2.14)$$

One can now write the components of equation (2.8) considering a harmonic field with time dependence  $e^{-i\omega t}$  and using (2.11):

$$\frac{-i\omega}{\gamma} M_{1x} = M_{1y} (B_A + B_E) + B_E M_{2y}, \quad (2.15)$$

$$\frac{-i\omega}{\gamma} M_{1y} = M_S H_x - M_{2x} B_E - M_{1x} (B_A + B_E), \quad (2.16)$$

$$\frac{-i\omega}{\gamma} M_{2x} = -M_{2y} (B_E + B_A) - B_E M_{1y}, \quad (2.17)$$

$$\frac{-i\omega}{\gamma} M_{2y} = -M_S H_x + M_{1x} B_E + M_{2x} (B_A + B_E), \quad (2.18)$$

where  $A \equiv \frac{-i\omega}{\gamma}$ . Now we reduce the system to only two equations, summing equations (2.15) and (2.17) and subtracting equations (2.16) and (2.18), yielding:

$$AM_x = B_A (M_{1y} - M_{2y}), \quad (2.19)$$

$$A (M_{1y} - M_{2y}) = -M_x (B_A + 2B_E), \quad (2.20)$$

where  $M_x = M_{1x} + M_{2x}$ . The next step is to multiply (2.19) by  $A$  and (2.20) by  $B_A$  and subtract the two equations to obtain:

$$M_x = M_{1x} + M_{2x} = \frac{2B_A M_S H_x}{A^2 + B_A^2 + 2B_A B_E}. \quad (2.21)$$

Now we go back to the system of equations (2.15)-(2.18) and subtract equations (2.15) and (2.17) and sum equations (2.16) and (2.18), yielding:

$$A (M_{1x} - M_{2x}) = M_y (2B_E + B_A), \quad (2.22)$$

$$AM_y = - (M_{1x} - M_{2x}) B_A, \quad (2.23)$$

where  $M_y = M_{1y} + M_{2y}$ . Now we multiply (2.22) by  $B_A$  and (2.23) by  $A$  and subtract the two equations to obtain:

$$M_y = 0. \quad (2.24)$$



Replacing  $A \equiv \frac{-i\omega}{\gamma}$  in equation (2.21):

$$M_x = M_{1x} + M_{2x} = \frac{2B_A M_S H_x}{B_A^2 + 2B_A B_E - \omega^2/\gamma^2}. \quad (2.25)$$

Equation (2.24) shows that the non-diagonal elements of the permeability are zero ( $\mu_{xz} = 0$ ). From equation (2.25) we can write:

$$\mu_{xx}(\omega) = 1 + 4\pi \frac{M_x}{H_x} = 1 + \frac{8\pi M_S B_A}{2B_E B_A + B_A^2 - \omega^2/\gamma^2}, \quad (2.26)$$

which is equivalent to:

$$\mu_{xx}(\omega) = 1 + \frac{8\pi\Omega_S^2}{\Omega_0^2 - \omega^2}, \quad (2.27)$$

where  $\Omega_S$  is the frequency given by:

$$\Omega_S = \gamma\sqrt{M_S B_A}, \quad (2.28)$$

$\Omega_0$  is the magnon resonance frequency:

$$\Omega_0 = \gamma\sqrt{2B_E B_A + B_A^2}. \quad (2.29)$$

Relation (2.27) can be used to model the permeability of an antiferromagnet in any system with an oscillating electromagnetic field and no constant external magnetic field. This formula will be applied in sections 2.3 and 2.4 to study the system depicted in figure 2.1. For the permeability function given by (2.27)-(2.29), the values of the quantities that determine it were given by Table I of [60]. These values are:

$$B_E = 55 \times 10^4 \text{ G}, \quad (2.30)$$

$$B_A = 7.87 \times 10^3 \text{ G}, \quad (2.31)$$

$$M_S = 6.0 \times 10^2 \text{ emu/cm}^3. \quad (2.32)$$

Or, in SI units:

$$B_E = 55 \text{ T}, \quad (2.33)$$

$$B_A = 0.787 \text{ T}, \quad (2.34)$$

$$M_S = 6.0 \times 10^5 \text{ A/m}. \quad (2.35)$$

## 2.2 Magneto-optic response of an easy-axis antiferromagnet in the presence of a static field

In the presence of a static magnetic field aligned with the easy-axis, ( $z$ ) the effective fields become:

$$\mathbf{H}_{ef}^{(1)} = \hat{x} \left( H_x - B_E \frac{M_{2x}}{M_S} \right) - \hat{y} \left( B_E \frac{M_{2y}}{M_S} \right) + \hat{z} (B_A + B_E + H_0), \quad (2.36)$$

$$\mathbf{H}_{ef}^{(2)} = \hat{x} \left( H_x - B_E \frac{M_{1x}}{M_S} \right) - \hat{y} \left( B_E \frac{M_{1y}}{M_S} \right) - \hat{z} (B_A + B_E - H_0). \quad (2.37)$$

With this external field of modulus  $H_0$ , the  $z$  component of the effective field is no longer symmetric with respect to the two sublattices of opposing spins. This symmetry break leads to non-diagonal terms in the magnetic permeability of the crystal. For this case, one solves again the components of equation (2.8):

$$\frac{-i\omega}{\gamma}M_{1x} = M_{1y}(B_A + B_E + H_0) + M_{2y}B_E, \quad (2.38)$$

$$\frac{-i\omega}{\gamma}M_{1y} = M_S H_x - M_{2x}B_E - M_{1x}(B_A + B_E + H_0), \quad (2.39)$$

$$\frac{-i\omega}{\gamma}M_{2x} = -M_{2y}(B_A + B_E - H_0) - M_{1y}B_E, \quad (2.40)$$

$$\frac{-i\omega}{\gamma}M_{2y} = -M_S H_x + M_{1x}B_E + M_{2x}(B_A + B_E - H_0). \quad (2.41)$$

Since the external oscillating field is chosen to be in  $x$ , the component  $M_y$  must be determined in order to calculate  $\mu_{xy}$  and the component  $M_x$  determines the diagonal element  $\mu_{xx}$ . In appendix A, equations (2.38)-(2.41) are manipulated to obtain:

$$M_y = iH_x\Omega_S^2 \left( \frac{1}{\Omega_0^2 - (\omega + \gamma B_0)^2} - \frac{1}{\Omega_0^2 - (\omega - \gamma B_0)^2} \right) \quad (2.42)$$

and

$$M_x = H_x\Omega_S^2 \left( \frac{1}{\Omega_0^2 - (\omega + \gamma B_0)^2} + \frac{1}{\Omega_0^2 - (\omega - \gamma B_0)^2} \right). \quad (2.43)$$

Hence, the non-diagonal term of the permeability is:

$$\mu_{yx} = 4\pi \frac{M_y}{H_x} = 4\pi i\Omega_S^2 \left( \frac{1}{\Omega_0^2 - (\omega + \gamma B_0)^2} + \frac{1}{\Omega_0^2 - (\omega - \gamma B_0)^2} \right) \quad (2.44)$$

and the diagonal term is:

$$\mu_{xx} = 1 + 4\pi \frac{M_x}{H_x} = 1 + 4\pi\Omega_S^2 \left( \frac{1}{\Omega_0^2 - (\omega + \gamma B_0)^2} + \frac{1}{\Omega_0^2 - (\omega - \gamma B_0)^2} \right). \quad (2.45)$$

Since the medium is symmetrical in  $xy$  the matrix must be hermitian.

$$\mu = \begin{bmatrix} \mu_{xx} & i\mu_{yx} & 0 \\ -i\mu_{yx} & \mu_{xx} & 0 \\ 0 & 0 & 1 \end{bmatrix}, \quad (2.46)$$

## 2.3 Optical conductivity of graphene

In this section, we deduce the optical conductivity of graphene semi-classically from the Boltzmann transport equation. The result will then be used for the graphene conductivity in the remainder of this thesis. The Boltzmann equation reads [10]:

$$\frac{\partial f}{\partial t} + \nabla_k f \cdot \frac{\partial \mathbf{k}}{\partial t} + \nabla f \cdot \frac{\partial \mathbf{r}}{\partial t} = \frac{\partial f}{\partial t} |_{\text{col}} \quad (2.47)$$

where  $f$  stands for the distribution function of the system, which can be written as  $f = f_0 + g_k$  where  $f_0$  stands for the Fermi-Dirac distribution.  $\nabla_k$  is the gradient with respect to the wave vector  $\mathbf{k}$ . The second term of (2.47) is

$$\nabla_k f \cdot \frac{\partial \mathbf{k}}{\partial t} = \frac{\mathbf{F}}{\hbar} \cdot \nabla_k f = \frac{-e\mathbf{E}}{\hbar} \cdot \nabla_k f_0 \quad (2.48)$$

where  $\mathbf{F}$  is the force the system is subject to and  $\mathbf{E}$  is the electric field. Also,

$$\frac{\nabla_k f_0}{\hbar} = \mathbf{v}_k \frac{\partial f_0}{\partial \epsilon} \quad (2.49)$$

where  $\mathbf{v}_k = v_F(\cos \theta, \sin \theta)$  is the velocity of the electrons. The collision term of (2.47) must cause the distribution  $g$  to relax toward thermal equilibrium. The relaxation time approximation [10] consists on considering the simplest collision term with this property:

$$\left. \frac{\partial f}{\partial t} \right|_{\text{coll}} = -\frac{g_k}{\tau} \quad (2.50)$$

where  $\tau$  is the relaxation time. Assuming  $f$  is homogeneous in the real space, equation (2.47) yields

$$-\frac{\partial g_k}{\partial t} + e\mathbf{E} \cdot \mathbf{v}_k \frac{\partial f_0}{\partial \epsilon} = \frac{g_k}{\tau}. \quad (2.51)$$

Now we write  $g_k = e^{-i\omega t} \mathbf{k} \cdot \mathbf{A}$ , where  $\mathbf{A}$  is an auxiliary field, and (2.51) becomes

$$\mathbf{v}_k \cdot \left( e\mathbf{E} \frac{\partial f_0}{\partial \epsilon} + i\omega \frac{k}{v_F} \mathbf{A} \right) = \mathbf{v}_k \cdot \left( \frac{k}{\tau v_F} \mathbf{A} \right). \quad (2.52)$$

From this system we have to determine  $A_x$  and  $A_y$ . Doing so yields:

$$A_x = \frac{E_x^{(f)}}{k(1 - i\omega\tau)} v_F \tau \quad (2.53)$$

$$A_y = \frac{E_y^{(f)}}{k(1 - i\omega\tau)} v_F \tau \quad (2.54)$$

where  $E_F = v_F \hbar k_F$  the Fermi energy. Also,  $E_{x(y)}^{(f)} = e E_{x(y)} \frac{\partial f_0}{\partial \epsilon}$ . We can now obtain  $g_k$  from:

$$g_k = e^{-i\omega t} \mathbf{k} \cdot \mathbf{A}, \quad (2.55)$$

$$g_k = \frac{e^{-i\omega t} v_F \tau}{1 - i\omega\tau} [\cos \theta E_x^{(f)} + \sin \theta E_y^{(f)}] \quad (2.56)$$

The current density vector is given by

$$\mathbf{J} = -\frac{e}{\pi^2} \int \mathbf{v}_k g_k(\mathbf{k}, \omega) d\mathbf{k} \quad (2.57)$$

where  $\mathbf{v}_k = v_F(\cos \theta, \sin \theta)$ . The degeneracy factor is 4, due to the two possible spin orientations and two valleys of the Brillouin zone K and K'. At  $T = 0$ ,  $\frac{\partial f_0}{\partial \epsilon} = -\delta(E - E_F)$ . Solving for the  $x$  component of the current density yields

$$J_x = \frac{e^2 \tau v_F k_F}{\pi \hbar} \frac{e^{-i\omega t}}{1 - i\omega\tau} E_x. \quad (2.58)$$

Since  $\mathbf{J} = \overleftrightarrow{\sigma} \mathbf{E}$ , the conductivity  $xx$  element will be

$$\sigma_{xx} = \frac{e^2 E_F}{\pi \hbar^2} \frac{1}{\gamma_e - i\omega}, \quad (2.59)$$

Here,  $\gamma_e$  is the mean collision rate given by  $\frac{1}{\tau}$ . This expression describes the intra-brand conductivity of graphene in the THZ and mid-IR range and for typical values of doping ( $E_F \sim 0.2 - 0.5$  eV). (Sec 2.3.2. of [9])

## 2.4 Antiferromagnet-graphene system - Dispersion relations, transmittance, reflectance and absorbance

### 2.4.1 TE modes

#### Evanescent waves

Transverse electric evanescent wave solutions to Maxwell's equations can be written in the form:

$$\begin{cases} \mathbf{E}^{(1)} = E_1 e^{\beta_1 z} e^{iqx} \hat{y} \\ \mathbf{E}^{(2)} = [E^+ e^{\beta_2 z} + E^- e^{-\beta_2 z}] e^{iqx} \hat{y} \\ \mathbf{E}^{(3)} = E_3 e^{-\beta_3(z-d)} e^{iqx} \hat{y} \end{cases} \quad (2.60)$$

The superscripts refer to the media 1,2 and 3 in figure 2.1. All the wavenumber components have to obey the dispersion relations in each media:

$$\begin{cases} \omega^2 = \frac{c^2}{\mu_1} (q^2 - \beta_1^2) \\ \omega^2 = c^2 (q^2 - \beta_2^2) = c^2 (q^2 - \beta_3^2) \end{cases} \quad (2.61)$$

To obtain the magnetic fields, we need to apply the relevant Maxwell equation (Faraday's law of induction):

$$-\frac{1}{c} \partial_t \mathbf{B} = \nabla \times \mathbf{E}, \quad (2.62)$$

$$i \frac{\omega}{c} \mathbf{B} = -\partial_z E_y \hat{x} + \partial_x E_y \hat{z}. \quad (2.63)$$

This means the magnetic field can be written as:

$$\begin{cases} \mathbf{B}^{(1)} = E_1 e^{\beta_1 z} e^{iqx} \frac{c}{\omega} [i\beta_1 \hat{x} + q\hat{z}] \\ \mathbf{B}^{(2)} = e^{iqx} \frac{c}{\omega} [i\beta_2 (E^+ e^{\beta_2 z} - E^- e^{-\beta_2 z}) \hat{x} + q (E^+ e^{\beta_2 z} + E^- e^{-\beta_2 z}) \hat{z}] \\ \mathbf{B}^{(3)} = E_3 e^{-\beta_3(z-d)} e^{iqx} \frac{c}{\omega} [-i\beta_3 \hat{x} + q\hat{z}] \end{cases} \quad (2.64)$$

To obtain the dispersion relation we apply boundary conditions at  $z = 0$  and  $z = d$ . Starting by  $z = 0$ , these conditions read [61]:

$$\hat{z} \cdot (\mathbf{B}^{(2)} - \mathbf{B}^{(1)})|_{z=0} = 0, \quad (2.65)$$

$$\hat{z} \times (\mathbf{E}^{(2)} - \mathbf{E}^{(1)})|_{z=0} = 0, \quad (2.66)$$

$$\hat{z} \times \left( \mathbf{B}^{(2)} - \frac{\mathbf{B}^{(1)}}{\mu_1} \right) |_{z=0} = 0. \quad (2.67)$$

Equations (2.65) and (2.66) both become:

$$E_1 = E^+ + E^-, \quad (2.68)$$

and equation (2.67) becomes:

$$\frac{\beta_1}{\mu_1} E_1 = \beta_2 (E^+ - E^-). \quad (2.69)$$

Cancelling  $E_1$  from these equations yields:

$$\frac{\beta_1}{\mu_1}(E^+ + E^-) = \beta_2(E^+ - E^-) \quad (2.70)$$

$$\left(\beta_2 + \frac{\beta_1}{\mu_1}\right)E^- = \left(\beta_2 - \frac{\beta_1}{\mu_1}\right)E^+. \quad (2.71)$$

On the other hand, the boundary conditions at  $z = d$  read:

$$\hat{z} \cdot (\mathbf{B}^{(3)} - \mathbf{B}^{(2)})|_{z=d} = 0, \quad (2.72)$$

$$\hat{z} \times (\mathbf{E}^{(3)} - \mathbf{E}^{(2)})|_{z=d} = 0, \quad (2.73)$$

$$\hat{z} \times (\mathbf{B}^{(3)} - \mathbf{B}^{(2)})|_{z=d} = \frac{4\pi}{c}\sigma(\omega)\mathbf{E}^{\parallel}|_{z=d}, \quad (2.74)$$

where  $\sigma(\omega)$  is the conductivity of the graphene sheet, given by (2.59). Equations (2.72) and (2.73) both become:

$$E_3 = E^+ e^{\beta_2 d} + E^- e^{-\beta_2 d}, \quad (2.75)$$

and equation (2.74) becomes:

$$\beta_3 E_3 + \beta_2(E^+ e^{\beta_2 d} - E^- e^{-\beta_2 d}) = i\omega \frac{4\pi}{c^2}\sigma(\omega)E_3. \quad (2.76)$$

Cancelling  $E_3$  from these equations we obtain:

$$\beta_2(E^+ e^{\beta_2 d} - E^- e^{-\beta_2 d}) = \left(i\omega \frac{4\pi}{c^2}\sigma(\omega) - \beta_3\right)(E^+ e^{\beta_2 d} + E^- e^{-\beta_2 d}) \quad (2.77)$$

$$E^+ e^{2\beta_2 d}(\beta_2 + \beta_3 - i\omega \frac{4\pi}{c^2}\sigma(\omega)) = E^-(\beta_2 - \beta_3 + i\omega \frac{4\pi}{c^2}\sigma(\omega)). \quad (2.78)$$

Combining equations (2.71) and (2.78) the dispersion relation is obtained:

$$e^{2\beta_2 d} \left(\beta_2 + \beta_3 - i\omega \frac{4\pi}{c^2}\sigma(\omega)\right) \left(\beta_2 + \frac{\beta_1}{\mu_1}\right) = \left(\beta_2 - \beta_3 + i\omega \frac{4\pi}{c^2}\sigma(\omega)\right) \left(\beta_2 - \frac{\beta_1}{\mu_1}\right). \quad (2.79)$$

In figure 2.3 the results of calculating this dispersion relation are shown with the graphene conductivity  $\sigma(\omega)$  being modelled by the Drude model and the permeability of the antiferromagnet  $\mu_1(\omega)$  being modelled by equation (2.27). Equations (2.81) are also used. It is noticeable that for a high enough Fermi energy of the doped graphene sheet, the group velocity of these hybrid polaritons becomes negative and their energies become higher than the resonant frequency of the antiferromagnet.

### Propagating waves

It is also of interest to study the scattering of propagating waves incident on the system depicted in figure 2.1. For transverse electric propagating modes, the electric field can be written as:

$$\begin{cases} \mathbf{E}^{(1)} = t e^{-ik_1 z} e^{iqx} \hat{y} \\ \mathbf{E}^{(2)} = [E^+ e^{ik_2 z} + E^- e^{-ik_2 z}] e^{iqx} \hat{y} \\ \mathbf{E}^{(3)} = [e^{-ik_3(z-d)} + r e^{ik_3(z-d)}] e^{iqx} \hat{y} \end{cases}. \quad (2.80)$$

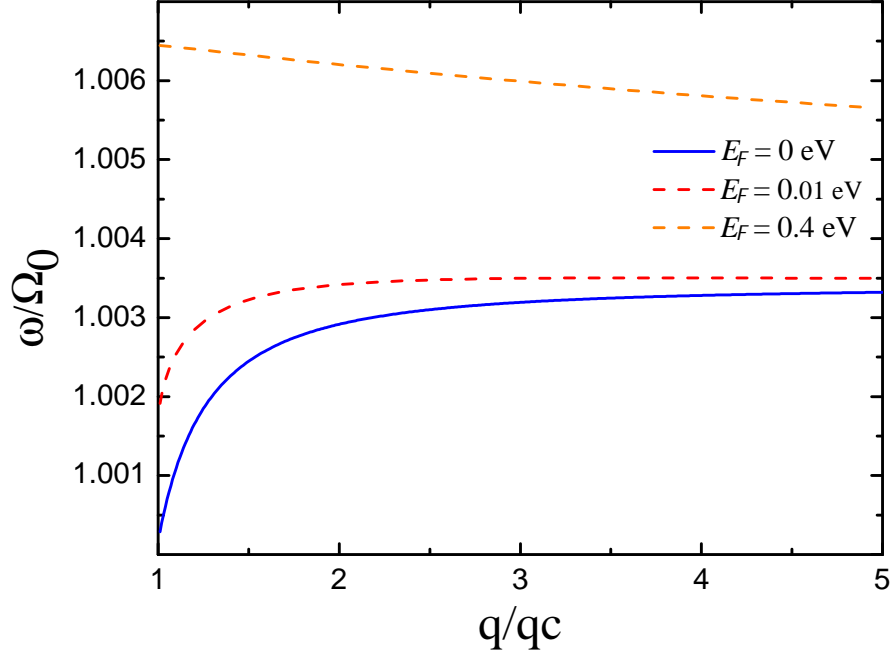


Figure 2.3: Dispersion relation for evanescent TE waves generated by surface magnon-plasmon polaritons, for different values of the Fermi energy  $E_F$ .  $\Omega_0$  is the antiferromagnet resonance frequency (2.29).  $q_c$  is the corresponding wavenumber in vacuum  $q_c = \frac{\Omega_0}{c}$ . The level of doping of the graphene sheet affects the nature of the dispersion. The group velocity is negative for  $E_F = 0.4$  eV, shifting from the positive group velocity associated with lower  $E_F$ . These are the solutions to equation (2.79). The value of  $d$ , the separation between the graphene sheet and the antiferromagnet, is  $0.5 \mu\text{m}$ . For the antiferromagnet permeability function given by (2.27)-(2.29), the values of the quantities that determine it were given by Table I of [60] and can also be consulted in equations (2.33)-(2.35). The value of the loss coefficient in (2.59) is  $\gamma_e = 0$  eV. Ignoring losses at the graphene sheet is valid when dealing with low temperatures. [20]

All the wavenumber components have to obey the dispersion relations in each media:

$$\begin{cases} \omega^2 = \frac{c^2}{\mu_1}(q^2 + k_1^2) \\ \omega^2 = c^2(q^2 + k_2^2) = c^2(q^2 + k_3^2) \end{cases} \quad (2.81)$$

The magnetic fields are obtained by applying the appropriate Maxwell equation (Faraday's law of induction):

$$-\frac{1}{c}\partial_t \mathbf{B} = \nabla \times \mathbf{E}, \quad (2.82)$$

$$i\frac{\omega}{c}\mathbf{B} = -\partial_z E_y \hat{x} + \partial_x E_y \hat{z}. \quad (2.83)$$

Thus, the magnetic fields read:

$$\begin{cases} \mathbf{B}^{(1)} = t e^{-ik_1 z} e^{iqx} \frac{c}{\omega} [k_1 \hat{x} + q \hat{z}] \\ \mathbf{B}^{(2)} = -\frac{k_2 c}{\omega} [E^+ e^{ik_2 z} - E^- e^{-ik_2 z}] e^{iqx} \hat{x} + \frac{qc}{\omega} [E^+ e^{ik_2 z} + E^- e^{-ik_2 z}] e^{iqx} \hat{z} \\ \mathbf{B}^{(3)} = -\frac{k_3 c}{\omega} [r e^{ik_3(z-d)} - e^{-ik_3(z-d)}] e^{iqx} \hat{x} + \frac{qc}{\omega} [r e^{ik_3(z-d)} + e^{-ik_3(z-d)}] \hat{z} \end{cases} \quad (2.84)$$

To obtain the dispersion relation, boundary conditions must be applied at  $z = 0$  and  $z = d$ . Starting with  $z = 0$ , the conditions read [61]:

$$\hat{z} \cdot (\mathbf{B}^{(2)} - \mathbf{B}^{(1)})|_{z=0} = 0, \quad (2.85)$$

$$\hat{z} \times (\mathbf{E}^{(2)} - \mathbf{E}^{(1)})|_{z=0} = 0, \quad (2.86)$$

$$\hat{z} \times \left( \mathbf{B}^{(2)} - \frac{\mathbf{B}^{(1)}}{\mu_1} \right) |_{z=0} = 0. \quad (2.87)$$

These conditions become:

$$t = E^+ + E^-, \quad (2.88)$$

$$k_1 t = -k_2 \mu_1 (E^+ - E^-). \quad (2.89)$$

Using the transmission coefficient  $t$  from (2.88) in (2.89) yields:

$$k_1 (E^+ + E^-) = -k_2 \mu_1 (E^+ - E^-), \quad (2.90)$$

$$E^- (k_2 \mu_1 - k_1) = E^+ (k_2 \mu_1 + k_1). \quad (2.91)$$

Now it is convenient to define a variable  $\alpha$  to be able to write:

$$E^- = \alpha E^+, \quad (2.92)$$

with

$$\alpha = \frac{k_2 \mu_1 + k_1}{k_2 \mu_1 - k_1}. \quad (2.93)$$

The boundary conditions at  $z = d$  read:

$$\hat{z} \cdot (\mathbf{B}^{(3)} - \mathbf{B}^{(2)})|_{z=d} = 0, \quad (2.94)$$

$$\hat{z} \times (\mathbf{E}^{(3)} - \mathbf{E}^{(2)})|_{z=d} = 0, \quad (2.95)$$

$$\hat{z} \times (\mathbf{B}^{(3)} - \mathbf{B}^{(2)})|_{z=d} = \frac{4\pi}{c} \sigma(\omega) \mathbf{E}^{\parallel}|_{z=d}. \quad (2.96)$$

where  $\sigma(\omega)$  is the conductivity of the graphene sheet. These equations become:

$$1 + r = E^+ e^{ik_2 d} + E^- e^{-ik_2 d}, \quad (2.97)$$

$$k_2 [E^+ e^{ik_2 d} - E^- e^{-ik_2 d}] - k_3 [r - 1] = \omega \frac{4\pi}{c} \sigma(\omega) [1 + r]. \quad (2.98)$$

It is possible to use equation (2.97) together with (2.92) to obtain the factor  $E^+$  as a function of  $r$ :

$$E^+ = \frac{1 + r}{e^{ik_2 d} + \alpha e^{-ik_2 d}}. \quad (2.99)$$

Finally we insert this last equation in (2.98) to obtain:

$$r = \frac{\omega \frac{4\pi}{c^2} \sigma(\omega) - k_3 - A}{A - k_3 - \omega \frac{4\pi}{c^2} \sigma(\omega)}, \quad (2.100)$$

with

$$A = \frac{k_2 e^{ik_2 d} - k_2 \alpha e^{-ik_2 d}}{e^{ik_2 d} + \alpha e^{-ik_2 d}}, \quad (2.101)$$

$$\alpha = \frac{k_2 \mu_1 + k_1}{k_2 \mu_1 - k_1}. \quad (2.102)$$

The corresponding loss function ( $\Im(r)$ ) is plotted in figure (2.4). This helps confirm the validity of the calculations of the dispersion relations that were performed in the previous section (figure 2.3). Equation (2.99), along with (2.92), can be inserted into (2.88) to obtain the relation between  $t$  and  $r$ :

$$t = \frac{1 + r}{e^{ik_2 d} + \alpha e^{-ik_2 d}} (1 + \alpha). \quad (2.103)$$

Now, to obtain the transmittance, or transmission coefficient, we consider the ratio between the transmitted intensity (medium 1, fields terms in (2.80) and (2.84)) and the incident intensity (medium 3, field terms with no  $r$  in (2.80) and (2.84)).

$$T = \frac{|\mathbf{I}^{(1)}|}{|\mathbf{I}_i^{(3)}|}. \quad (2.104)$$

The reflectance is the ratio between the reflected intensity (medium 1, field terms in in (2.80) and (2.84)) and the incident intensity (medium 3, field terms with  $r$  in (2.80) and (2.84)).

$$R = \frac{|\mathbf{I}_r^{(3)}|}{|\mathbf{I}_i^{(3)}|}. \quad (2.105)$$

The relevant electromagnetic intensity (the one that interacts with the surfaces) in medium  $n$  ( $\mathbf{I}^{(n)}$ ) relates to the fields via the  $z$  (normal) component of the time-averaged Poynting vector [62]:

$$\mathbf{I}^{(n)} = \frac{c}{4\pi} \langle \mathbf{S}(t) \cdot \hat{z} \rangle = \frac{\omega}{2\pi} \int_0^{2\pi/\omega} (\mathbf{S}^{(n)}(t) \cdot \hat{z}) dt, \quad (2.106)$$

where  $\mathbf{S}^{(n)}(t)$  is the Poynting vector in medium  $n$ , defined as:

$$\mathbf{S}^{(n)}(t) = \Re(\mathbf{E}^{(n)}(t)) \times \Re(\mathbf{H}^{(n)}(t)). \quad (2.107)$$



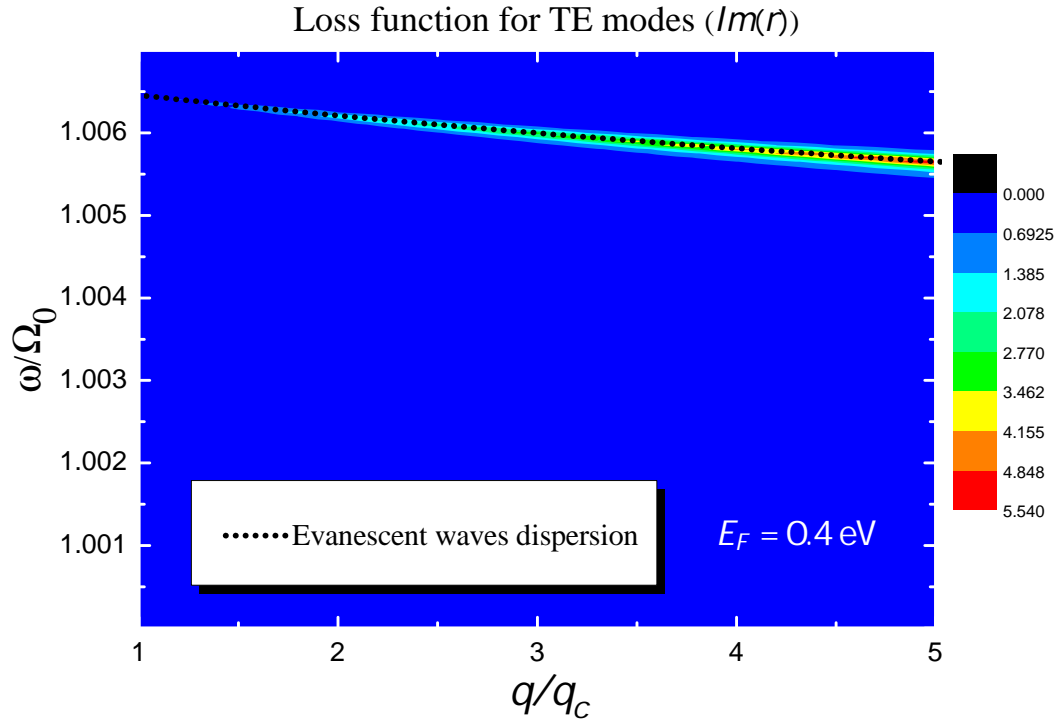


Figure 2.4: Comparison between the loss function ( $\Im(r)$ ) from (2.100) for propagating TE modes and the dispersion relation from (2.79) for evanescent TE waves generated by surface magnon-plasmon polaritons. The loss function is higher close to the energies of the evanescent modes.  $\Omega_0$  is the antiferromagnet resonance frequency (2.29).  $q_c$  is the corresponding wavenumber in vacuum  $q_c = \frac{\Omega_0}{c}$ . The value of  $d$ , the separation between the graphene sheet and the antiferromagnet, is  $0.5 \mu\text{m}$ . For the antiferromagnet permeability function given by (2.27)-(2.29), the values of the quantities that determine it were given by Table I of [60] and can also be consulted in equations (2.33)-(2.35). The value of the loss coefficient in (2.59) is  $\gamma_e = 0 \text{ eV}$ . Ignoring losses at the graphene sheet is valid when dealing with low temperatures. [20]

Now we can apply (2.107) and (2.106) to (2.104) and (2.105), using the fields (2.80) and (2.84) to obtain:

$$T = \left| \frac{t^2 k_1}{\mu_1 k_3} \right|, \quad (2.108)$$

and

$$R = |r|^2. \quad (2.109)$$

Figures 2.9-2.10 depict these quantities for different parts of the spectrum.

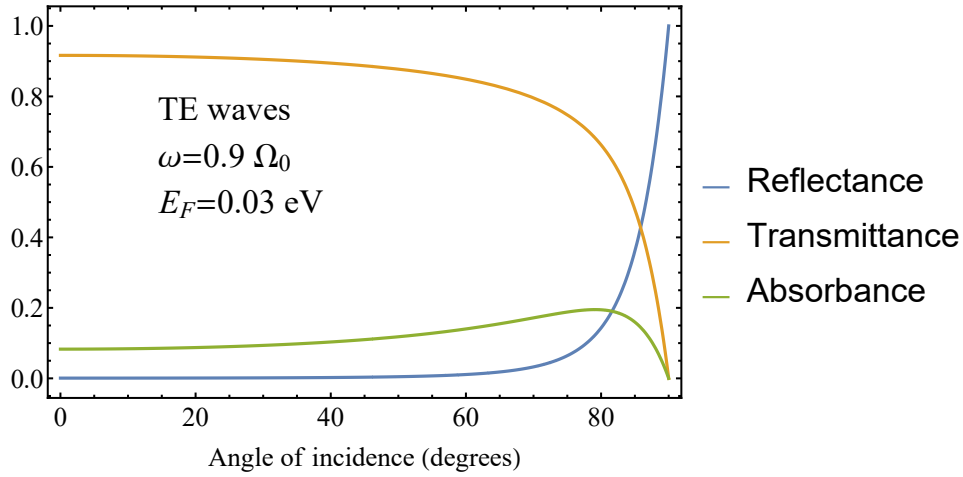


Figure 2.5: Reflectance, Transmittance and Absorbance, as defined by equations (2.109), (2.108) and  $A = 1 - R - T$  for propagating TE waves incident from medium 3 on the system depicted in figure 2.1, for the frequency  $\omega = 0.90 \Omega_0$ . For the antiferromagnet permeability function given by (2.27)-(2.29), the values of the quantities that determine it were given by Table I of [60] and can also be consulted in equations (2.33)-(2.35). The loss coefficient used in (2.59) was  $\gamma_e = 0.1 \text{ eV}$ .

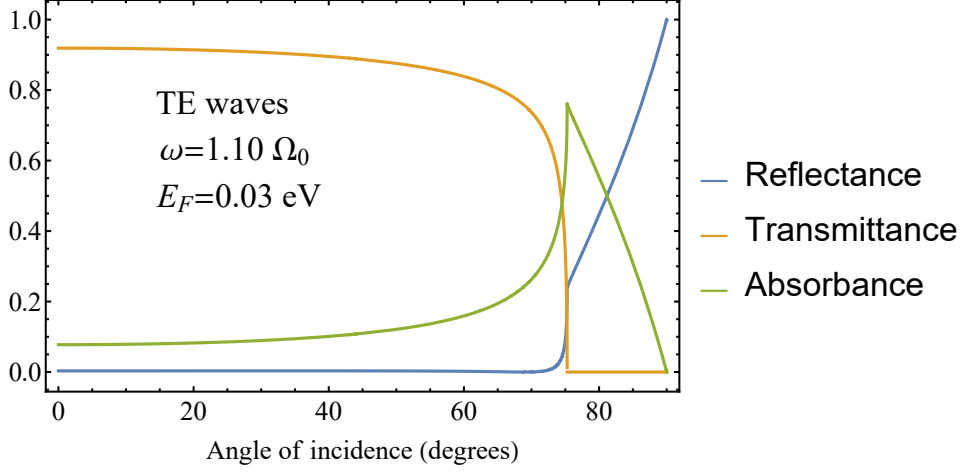


Figure 2.6: Reflectance, Transmittance and Absorbance, as defined by equations (2.109), (2.108) and  $A = 1 - R - T$  for propagating TE waves incident from medium 3 on the system depicted in figure 2.1, for the frequency  $\omega = 1.10 \Omega_0$ . For the antiferromagnet permeability function given by (2.27)-(2.29), the values of the quantities that determine it were given by Table I of [60] and can also be consulted in equations (2.33)-(2.35). The loss coefficient used in (2.59) was  $\gamma_e = 0.1$  eV. When the angle of incidence is higher than about 75 degrees, the value of  $q$ , the  $x$  component of the wave-vector, becomes so high that the wave cannot propagate inside the antiferromagnet, thus the sharp decline of the transmittance.

## 2.4.2 TM modes

### Evanescent waves

Transverse magnetic evanescent wave solutions to Maxwell's equations can be written in the form:

$$\begin{cases} \mathbf{B}^{(1)} = B_1 e^{\beta_1 z} e^{iqx} \hat{y} \\ \mathbf{B}^{(2)} = [B^+ e^{\beta_2 z} + B^- e^{-\beta_2 z}] e^{iqx} \hat{y} \\ \mathbf{B}^{(3)} = B_3 e^{-\beta_3(z-d)} e^{iqx} \hat{y} \end{cases} \quad (2.110)$$

To obtain the electric fields, we need to apply the relevant Maxwell equation (Ampère's law):

$$\frac{\epsilon\mu}{c} \partial_t \mathbf{E} = \nabla \times \mathbf{B}, \quad (2.111)$$

$$-i\epsilon\mu \frac{\omega}{c} \mathbf{E} = -\partial_z B_y \hat{x} + \partial_x B_y \hat{z}. \quad (2.112)$$

Which means the electric field can be written as:

$$\begin{cases} \mathbf{E}^{(1)} = -B_1 \frac{c}{\epsilon_1 \mu_1} e^{\beta_1 z} e^{iqx} \frac{1}{\omega} [i\beta_1 \hat{x} + q\hat{z}] \\ \mathbf{E}^{(2)} = -\frac{c}{\epsilon_2} i \frac{\beta_2}{\omega} [B^+ e^{\beta_2 z} - B^- e^{-\beta_2 z}] e^{iqx} \hat{x} - \frac{c}{\epsilon_2} \frac{q}{\omega} [B^+ e^{\beta_2 z} + B^- e^{-\beta_2 z}] e^{iqx} \hat{z} \\ \mathbf{E}^{(3)} = -B_3 \frac{c}{\epsilon_3} e^{-\beta_3(z-d)} e^{iqx} \frac{1}{\omega} [-i\beta_3 \hat{x} + q\hat{z}] \end{cases} \quad (2.113)$$

To obtain the dispersion relation we apply boundary conditions at  $z = 0$  and  $z = d$ . Starting by  $z = 0$ , these conditions read [61]:

$$\hat{z} \cdot (\mathbf{B}^{(2)} - \mathbf{B}^{(1)})|_{z=0} = 0, \quad (2.114)$$

$$\hat{z} \times (\mathbf{E}^{(2)} - \mathbf{E}^{(1)})|_{z=0} = 0, \quad (2.115)$$

$$\hat{z} \times \left( \mathbf{B}^{(2)} - \frac{\mathbf{B}^{(1)}}{\mu_1} \right)|_{z=0} = 0. \quad (2.116)$$

Equation (2.114) is always fulfilled. Equation (2.115) becomes:

$$\frac{\beta_1}{\epsilon_1 \mu_1} B_1 = \frac{\beta_2}{\epsilon_2} (B^+ - B^-), \quad (2.117)$$

and equation (2.116) becomes:

$$\frac{1}{\mu_1} B_1 = B^+ + B^-. \quad (2.118)$$

Cancelling  $B_1$ :

$$\frac{\beta_2}{\epsilon_2} (B^+ - B^-) = \frac{\beta_1}{\epsilon_1} (B^+ + B^-), \quad (2.119)$$

$$\left( \frac{\beta_2}{\epsilon_2} - \frac{\beta_1}{\epsilon_1} \right) B^+ = \left( \frac{\beta_2}{\epsilon_2} + \frac{\beta_1}{\epsilon_1} \right) B^-. \quad (2.120)$$

On the other hand, the boundary conditions at  $z = d$  read:

$$\hat{z} \cdot (\mathbf{B}^{(3)} - \mathbf{B}^{(2)})|_{z=d} = 0, \quad (2.121)$$

$$\hat{z} \times (\mathbf{E}^{(3)} - \mathbf{E}^{(2)})|_{z=d} = 0, \quad (2.122)$$

$$\hat{z} \times (\mathbf{B}^{(3)} - \mathbf{B}^{(2)})|_{z=d} = \frac{4\pi}{c} \sigma(\omega) \mathbf{E}^{\parallel}|_{z=d}. \quad (2.123)$$

where  $\sigma(\omega)$  is the conductivity of the graphene sheet, given by (2.59). Equation (2.121) is always fulfilled.

Equation (2.122) becomes:

$$\frac{\beta_3}{\epsilon_3} B_3 = -\frac{\beta_2}{\epsilon_2} (B^+ e^{\beta_2 d} - B^- e^{-\beta_2 d}) \quad (2.124)$$

and equation (2.123) becomes:

$$B_3 - (B^+ e^{\beta_2 d} + B^- e^{-\beta_2 d}) = -i B_3 \frac{\beta_3}{\omega \epsilon_3} 4\pi \sigma(\omega) \quad (2.125)$$

We can now cancel  $B_3$  to obtain:

$$(B^+ e^{\beta_2 d} + B^- e^{-\beta_2 d}) = -\left( i \frac{4\pi}{\omega} \sigma(\omega) + \frac{\epsilon_3}{\beta_3} \right) (B^+ e^{\beta_2 d} - B^- e^{-\beta_2 d}) \frac{\beta_2}{\epsilon_2}, \quad (2.126)$$

$$B^+ e^{2\beta_2 d} \left[ 1 + \frac{\epsilon_3 \beta_2}{\epsilon_2 \beta_3} + i \frac{\beta_2}{\epsilon_2 \omega} 4\pi \sigma(\omega) \right] = B^- \left[ i \frac{\beta_2}{\epsilon_2 \omega} 4\pi \sigma(\omega) + \frac{\epsilon_3 \beta_2}{\epsilon_2 \beta_3} - 1 \right]. \quad (2.127)$$

Combining equations (2.120) and (2.127) the dispersion relation is obtained:

$$e^{2\beta_2 d} \left[ 1 + \frac{\epsilon_3 \beta_2}{\epsilon_2 \beta_3} + i \frac{\beta_2}{\epsilon_2 \omega} 4\pi \sigma(\omega) \right] \left( \frac{\beta_2}{\epsilon_2} + \frac{\beta_1}{\epsilon_1} \right) = \left[ i \frac{\beta_2}{\epsilon_2 \omega} 4\pi \sigma(\omega) + \frac{\epsilon_3 \beta_2}{\epsilon_2 \beta_3} - 1 \right] \left( \frac{\beta_2}{\epsilon_2} - \frac{\beta_1}{\epsilon_1} \right). \quad (2.128)$$

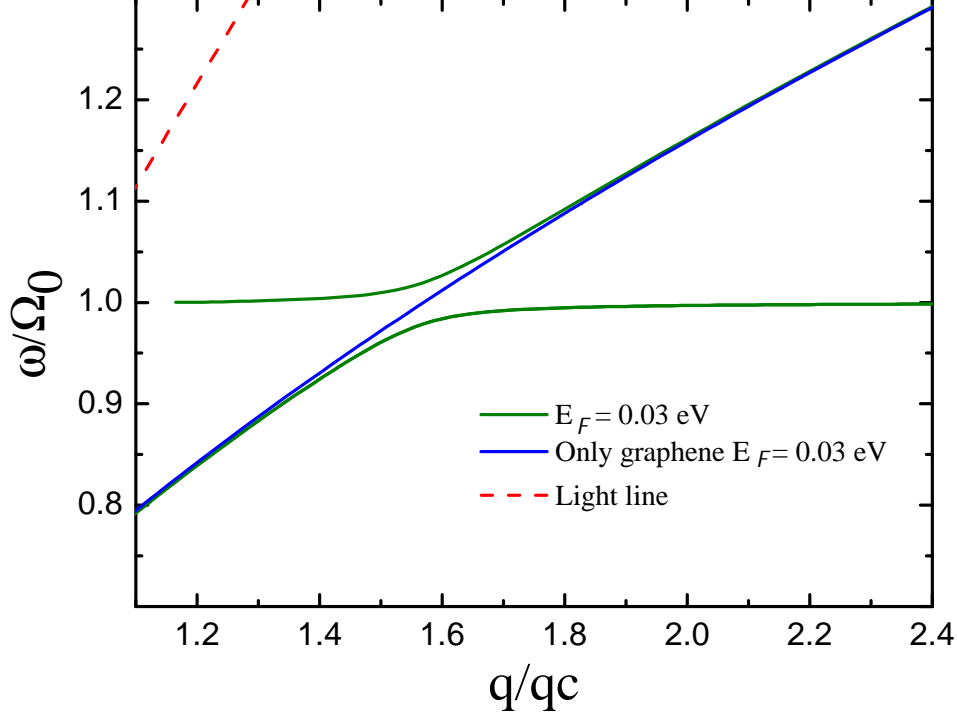


Figure 2.7: Dispersion relation for evanescent TM waves generated by surface magnon-plasmon polaritons, for the Fermi energy  $E_F = 0.03$  eV.  $\Omega_0$  is the antiferromagnet resonance frequency (2.29).  $q_c$  is the corresponding wavenumber in vacuum  $q_c = \frac{\Omega_0}{c}$ . The presence of the antiferromagnet splits the dispersion into a lower and upper branch. These are solutions to equation (2.128). The value of  $d$ , the separation between the graphene sheet and the antiferromagnet, is  $0.5 \mu\text{m}$ . For the antiferromagnet permeability function given by (2.27)-(2.29), the values of the quantities that determine it were given by Table I of [60] and can also be consulted in equations (2.33)-(2.35). The value of the loss coefficient in (2.59) is  $\gamma_e = 0$  eV. Ignoring losses at the graphene sheet is valid when dealing with low temperatures. [20]

### Propagating waves

As was done for TE modes, the scattering of propagating waves incident on the system depicted in figure 2.1 will be studied. For transverse magnetic propagating modes, the magnetic field can be written as:

$$\begin{cases} \mathbf{B}^{(1)} = t e^{-ik_1 z} e^{iqx} \hat{y} \\ \mathbf{B}^{(2)} = [B^+ e^{ik_2 z} + B^- e^{-ik_2 z}] e^{iqx} \hat{y} \\ \mathbf{B}^{(3)} = [e^{-ik_3(z-d)} + r e^{ik_3(z-d)}] e^{iqx} \hat{y} \end{cases} . \quad (2.129)$$

The electric fields are obtained by applying the appropriate Maxwell equation (Ampère's law):

$$\frac{\mu\epsilon}{c} \partial_t \mathbf{E} = \nabla \times \mathbf{B}, \quad (2.130)$$

$$-i\frac{\mu\epsilon}{c}\omega\mathbf{E} = -\partial_z B_y \hat{x} + \partial_x B_y \hat{z}. \quad (2.131)$$

Thus, the electric fields read:

$$\begin{cases} \mathbf{E}^{(1)} = -\frac{c}{\epsilon_1\mu_1}te^{-ik_1z}e^{iqx}\frac{1}{\omega}[k_1\hat{x} + q\hat{z}] \\ \mathbf{E}^{(2)} = \frac{c}{\epsilon_2}\frac{k_2}{\omega}[B^+e^{ik_2z} - B^-e^{-ik_2z}]e^{iqx}\hat{x} - \frac{c}{\epsilon_2}\frac{q}{\omega}[B^+e^{ik_2z} + B^-e^{-ik_2z}]e^{iqx}\hat{z} \\ \mathbf{E}^{(3)} = \frac{c}{\epsilon_3}\frac{k_3}{\omega}[re^{ik_3(z-d)} - e^{-ik_3(z-d)}]e^{iqx}\hat{x} - \frac{c^2}{\epsilon_3}\frac{q}{\omega}[re^{ik_3(z-d)} + e^{-ik_3(z-d)}]\hat{z} \end{cases}. \quad (2.132)$$

To obtain the dispersion relation, boundary conditions must be applied at  $z = 0$  and  $z = d$ . Starting with  $z = 0$ , the conditions read [61]:

$$\hat{z} \cdot (\mathbf{B}^{(2)} - \mathbf{B}^{(1)})|_{z=0} = 0, \quad (2.133)$$

$$\hat{z} \times (\mathbf{E}^{(2)} - \mathbf{E}^{(1)})|_{z=0} = 0, \quad (2.134)$$

$$\hat{z} \times \left( \mathbf{B}^{(2)} - \frac{\mathbf{B}^{(1)}}{\mu_1} \right)|_{z=0} = 0. \quad (2.135)$$

These conditions become:

$$\frac{k_1}{\epsilon_1\mu_1}t = -\frac{k_2}{\epsilon_2}(B^+ - B^-), \quad (2.136)$$

$$\frac{t}{\mu_1} = B^+ + B^-. \quad (2.137)$$

Cancelling the coefficient  $t$ :

$$\frac{k_1}{\epsilon_1}(B^+ + B^-) = -\frac{k_2}{\epsilon_2}(B^+ - B^-), \quad (2.138)$$

$$B^+\left(\frac{k_1}{\epsilon_1} + \frac{k_2}{\epsilon_2}\right) = B^-\left(\frac{k_2}{\epsilon_2} - \frac{k_1}{\epsilon_1}\right). \quad (2.139)$$

Now it is convenient to define a variable  $\alpha$  to quickly write:

$$B^- = \alpha B^+, \quad (2.140)$$

with

$$\alpha = \frac{k_2\epsilon_1 + k_1\epsilon_2}{k_2\epsilon_1 - k_1\epsilon_2}. \quad (2.141)$$

The boundary conditions at  $z = d$  read [61]:

$$\hat{z} \cdot (\mathbf{B}^{(3)} - \mathbf{B}^{(2)})|_{z=d} = 0, \quad (2.142)$$

$$\hat{z} \times (\mathbf{E}^{(3)} - \mathbf{E}^{(2)})|_{z=d} = 0, \quad (2.143)$$

$$\hat{z} \times (\mathbf{B}^{(3)} - \mathbf{B}^{(2)})|_{z=d} = \frac{4\pi}{c}\sigma(\omega)\mathbf{E}^{\parallel}|_{z=d}. \quad (2.144)$$

where  $\sigma(\omega)$  is the conductivity of the graphene sheet, give by (2.59). These equations become:

$$\frac{k_3}{\epsilon_3}(r - 1) = \frac{k_2}{\epsilon_2}(B^+e^{ik_2d} - B^-e^{-ik_2d}). \quad (2.145)$$

$$1 + r - (B^+e^{ik_2d} + B^-e^{-ik_2d}) = (1 - r)\frac{k_3}{\epsilon_3}\frac{4\pi}{\omega}\sigma(\omega) \quad (2.146)$$

It is possible to use equation (2.145) together with (2.140) to obtain the factor  $B^+$  as a function of  $r$ :

$$B^+ = \frac{r - 1}{e^{ik_2d} - \alpha e^{-ik_2d}} \frac{\epsilon_2 k_3}{\epsilon_3 k_2}. \quad (2.147)$$

Finally we insert this last equation in (2.146) to obtain:

$$r = \frac{A - B + 1}{A - B - 1}, \quad (2.148)$$

with

$$A = \frac{1 + \alpha e^{-2ik_2d}}{1 - \alpha e^{-2ik_2d}} \frac{\epsilon_2 k_3}{\epsilon_3 k_2}, \quad (2.149)$$

$$B = \frac{k_3}{\epsilon_3} \frac{4\pi}{\omega} \sigma(\omega), \quad (2.150)$$

$$\alpha = \frac{k_2 \epsilon_1 + k_1 \epsilon_2}{k_2 \epsilon_1 - k_1 \epsilon_2}. \quad (2.151)$$

The corresponding loss function ( $\Im(r)$ ) is plotted in figure (2.8).

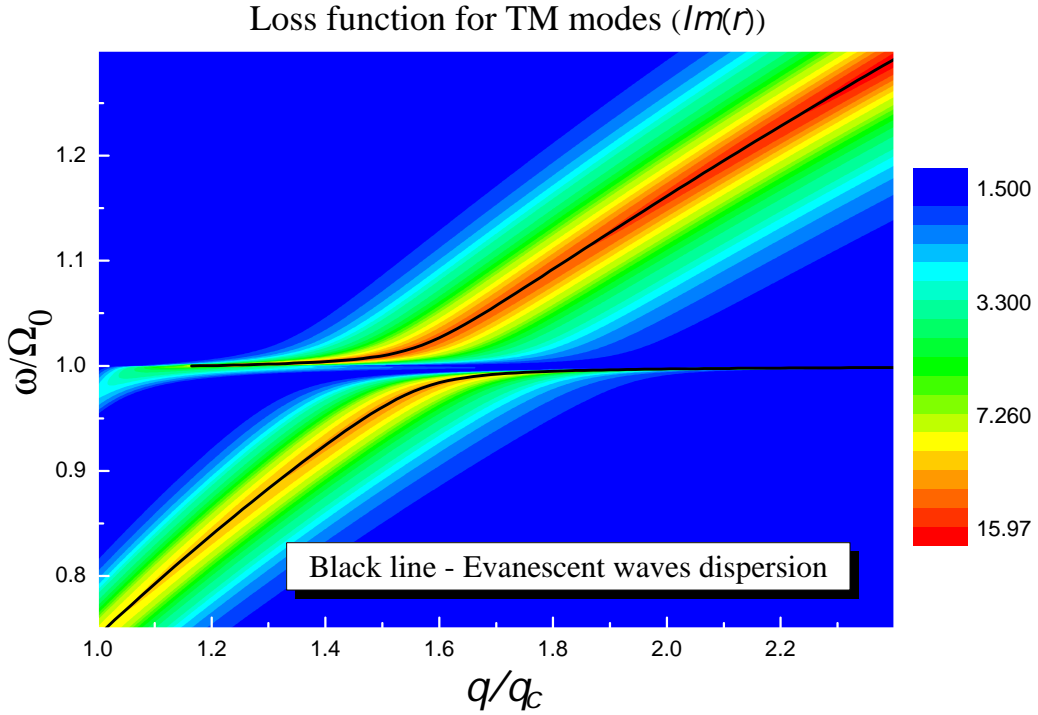


Figure 2.8: Comparison between the loss function ( $\Im(r)$ ) from (2.148) and the dispersion relation from (2.128) for TM modes generated by surface magnon-plasmon polaritons.  $\Omega_0$  is the antiferromagnet resonance frequency (2.29).  $q_c$  is the corresponding wavenumber in vacuum  $q_c = \frac{\Omega_0}{c}$ . The value of  $d$ , the separation between the graphene sheet and the antiferromagnet, is  $0.5 \mu\text{m}$ . For the antiferromagnet permeability function given by (2.27)-(2.29), the values of the quantities that determine it were given by Table I of [60] and can also be consulted in equations (2.33)-(2.35). The value of the loss coefficient in (2.59) is  $\gamma_e = 0 \text{ eV}$ . Ignoring losses at the graphene sheet is valid when dealing with low temperatures. [20]

Equation (2.147), along with (2.140), can be inserted into (2.137) to obtain the relation between  $t$  and  $r$ :

$$t = \frac{\epsilon_2 k_3}{\epsilon_3 k_2} \frac{r - 1}{e^{ik_2 d} - \alpha e^{-ik_2 d}} (1 + \alpha). \quad (2.152)$$

Now, to obtain the transmittance, or transmission coefficient, we consider the ratio between the transmitted intensity (medium 1, field terms in (2.129) and (2.132)) and the incident intensity (medium 3, field terms with no  $r$  in (2.129) and (2.132)).

$$T = \frac{|\mathbf{I}^{(1)}|}{|\mathbf{I}_i^{(3)}|}. \quad (2.153)$$

The reflectance is the ratio between the reflected intensity (medium 1, field terms in in (2.129) and (2.132)) and the incident intensity (medium 3, field terms with  $r$  in (2.129) and (2.132)).

$$R = \frac{|\mathbf{I}_r^{(3)}|}{|\mathbf{I}_i^{(3)}|}. \quad (2.154)$$

The relevant electromagnetic intensity (the one that interacts with the surfaces) in medium  $n$  ( $\mathbf{I}^{(n)}$ ) relates to the fields via the  $z$  (normal) component of the time-averaged Poynting vector [62]:

$$\mathbf{I}^{(n)} = \langle \mathbf{S}(t) \cdot \hat{z} \rangle = \frac{\omega}{2\pi} \int_0^{2\pi/\omega} (\mathbf{S}^{(n)}(t) \cdot \hat{z}) dt, \quad (2.155)$$

where  $\mathbf{S}^{(n)}(t)$  is the Poynting vector in medium  $n$ , defined as:

$$\mathbf{S}^{(n)}(t) = \Re(\mathbf{E}^{(n)}(t)) \times \Re(\mathbf{H}^{(n)}(t)). \quad (2.156)$$

Now we can apply (2.156) and (2.155) to (2.153) and (2.154), using the fields (2.129) and (2.132) to obtain:

$$T = \left| \frac{t^2 k_1}{\mu_1^2 k_3} \right|, \quad (2.157)$$

and

$$R = |r|^2. \quad (2.158)$$

Figures 2.9-2.10 depict these three quantities for different parts of the spectrum.



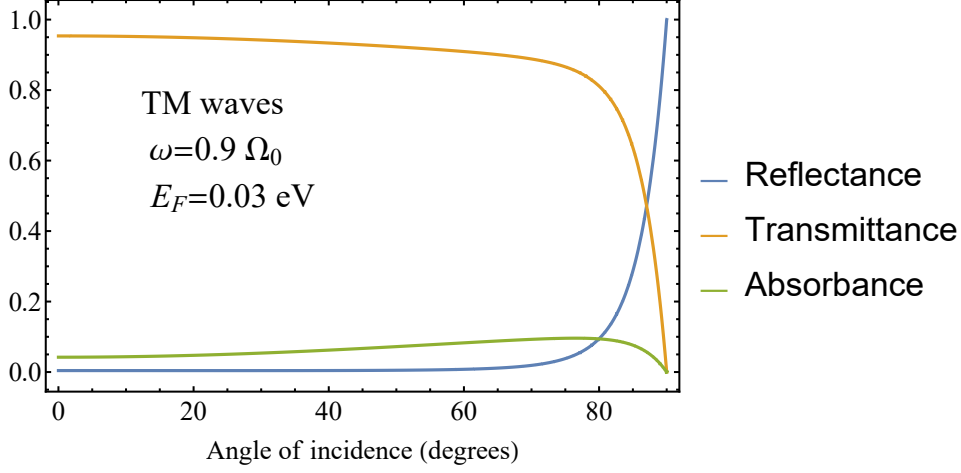


Figure 2.9: Reflectance, Transmittance and Absorbance, as defined by equations (2.158), (2.157) and  $A = 1 - T - R$  for propagating TM waves incident from medium 3 on the system depicted in figure 2.1.  $q_{lim} = \omega/c$  is the maximum value of  $q$  that maintains  $k_3$  real, for which we can say we have incident light from medium 3.  $k_1$  is always real for  $\omega < \Omega_0$  since  $\mu_1 > 1$ , which means the transmittance only goes to zero at the limit  $q = q_{lim}$  where  $k_3 = 0$ . The loss coefficient used in (2.59) was  $\gamma_e = 0.1 \text{ eV}$ .

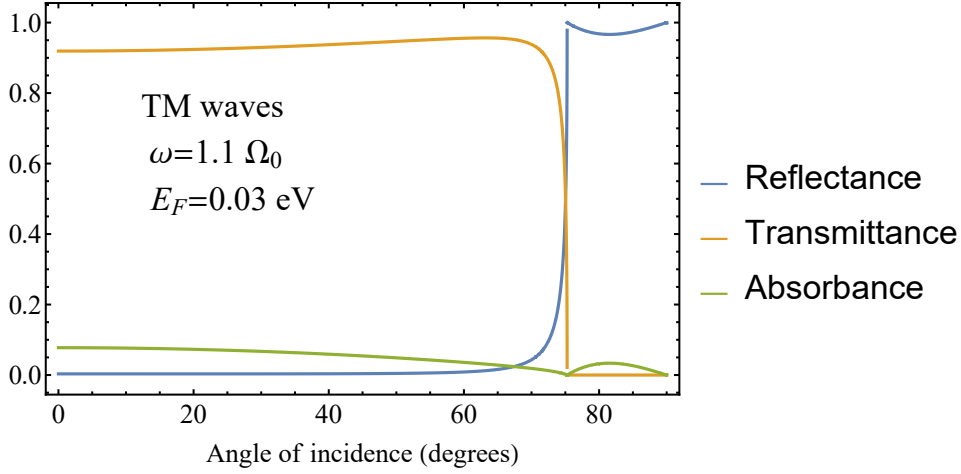


Figure 2.10: Reflectance, Transmittance and Absorbance, as defined by equations (2.109), (2.108) and  $A = 1 - T - R$  for propagating TM waves incident from medium 3 on the system depicted in figure 2.1.  $q_{lim} = \omega/c$  is the maximum value of  $q$  that maintains  $k_3$  real, for which we can say we have incident light from medium 3.  $k_1$  becomes zero when  $q = \omega/c\sqrt{\mu_1}$  and imaginary for higher values of  $q$ . From that point on the transmittance is zero since there is no propagating light in medium 1. The loss coefficient used in (2.59) was  $\gamma_e = 0.1 \text{ eV}$ .

## 2.5 Adding a perfect metal

It could be of interest to study a system with more confinement. For that, a perfect metal can be added either to the bottom of the system or to the top. The system depicted in figure 2.11, with a metal on the bottom, will be studied. The boundary conditions on the interface with a perfect metal are [61]:

$$\hat{z} \times \mathbf{E} = 0, \quad (2.159)$$

and

$$\hat{z} \cdot \mathbf{B} = 0. \quad (2.160)$$

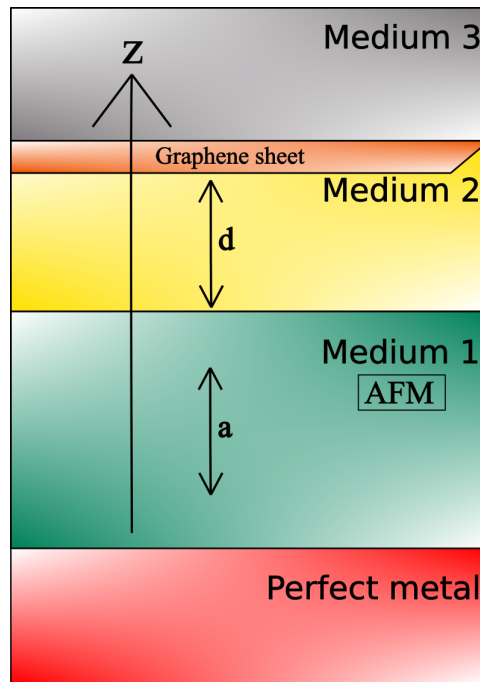


Figure 2.11: Scheme of the system with a graphene sheet a distance  $d$  from the antiferromagnet, of thickness  $a$  over a perfect metal. Evanescent waves decaying in the  $z$  direction, and propagating parallel to the graphene sheet will be studied, as well as propagating waves incident from medium 3, which generally is the vacuum or air.

### 2.5.1 TE modes

#### Evanescent waves

The electric field profiles in the different media are:

$$\begin{cases} \mathbf{E}^{(1)} = E_1 [e^{\beta_1 z} + \alpha e^{-\beta_1 z}] e^{iqx} \hat{y} \\ \mathbf{E}^{(2)} = [E^+ e^{\beta_2(z-a)} + E^- e^{-\beta_2(z-a)}] e^{iqx} \hat{y} \\ \mathbf{E}^{(3)} = E_3 e^{-\beta_3(z-a-d)} e^{iqx} \hat{y} \end{cases} . \quad (2.161)$$

It is now possible to determine the magnetic field from Faraday's law:

$$-\frac{1}{c}\partial_t\mathbf{B} = \nabla \times \mathbf{E}, \quad (2.162)$$

$$i\frac{\omega}{c}\mathbf{B} = -\partial_z E_y \hat{x} + \partial_x E_y \hat{z}. \quad (2.163)$$

With this equation, one can write the magnetic fields as:

$$\begin{cases} \mathbf{B}^{(1)} = E_1 e^{iqx} c \left( [e^{\beta_1 z} - \alpha e^{-\beta_1 z}] \frac{i\beta_1}{\omega} \hat{x} + [e^{\beta_1 z} + \alpha e^{-\beta_1 z}] \frac{q}{\omega} \hat{z} \right) \\ \mathbf{B}^{(2)} = i\frac{\beta_2}{\omega} c [E^+ e^{\beta_2(z-a)} - E^- e^{-\beta_2(z-a)}] e^{iqx} \hat{x} + \frac{q}{\omega} c [E^+ e^{\beta_2(z-a)} + E^- e^{-\beta_2(z-a)}] e^{iqx} \hat{z} \\ \mathbf{B}^{(3)} = E_3 e^{-\beta_3(z-a-d)} e^{iqx} \frac{c}{\omega} [-i\beta_3 \hat{x} + q\hat{z}] \end{cases} \quad (2.164)$$

Starting with condition (2.160),  $\alpha$  is determined:

$$B_z^{(1)}|_{z=0} = 0, \quad (2.165)$$

$$1 + \alpha = 0, \quad (2.166)$$

$$\alpha = -1. \quad (2.167)$$

As such, the fields can be written as:

$$\begin{cases} \mathbf{E}^{(1)} = E_1 \sinh(\beta_1 z) e^{iqx} \hat{y} \\ \mathbf{E}^{(2)} = [E^+ e^{\beta_2(z-a)} + E^- e^{-\beta_2(z-a)}] e^{iqx} \hat{y} \\ \mathbf{E}^{(3)} = E_3 e^{-\beta_3(z-a-d)} e^{iqx} \hat{y} \end{cases} \quad (2.168)$$

$$\begin{cases} \mathbf{B}^{(1)} = E_1 e^{iqx} c \left( \cosh(\beta_1 z) \frac{i\beta_1}{\omega} \hat{x} + \sinh(\beta_1 z) \frac{q}{\omega} \hat{z} \right) \\ \mathbf{B}^{(2)} = i\frac{\beta_2}{\omega} c [E^+ e^{\beta_2(z-a)} - E^- e^{-\beta_2(z-a)}] e^{iqx} \hat{x} + \frac{q}{\omega} c [E^+ e^{\beta_2(z-a)} + E^- e^{-\beta_2(z-a)}] e^{iqx} \hat{z} \\ \mathbf{B}^{(3)} = E_3 e^{-\beta_3(z-a-d)} e^{iqx} \frac{c}{\omega} [-i\beta_3 \hat{x} + q\hat{z}] \end{cases} \quad (2.169)$$

The next step is the application of boundary conditions at  $z = a$  and  $z = d + a$ . Starting with  $z = a$ , the boundary conditions are [61]:

$$\hat{z} \cdot (\mathbf{B}^{(2)} - \mathbf{B}^{(1)})|_{z=a} = 0, \quad (2.170)$$

$$\hat{z} \times (\mathbf{E}^{(2)} - \mathbf{E}^{(1)})|_{z=a} = 0, \quad (2.171)$$

$$\hat{z} \times \left( \mathbf{B}^{(2)} - \frac{\mathbf{B}^{(1)}}{\mu_1} \right)|_{z=a} = 0. \quad (2.172)$$

Equations (2.170) and (2.171) both yield:

$$E_1 \sinh(\beta_1 a) = E^+ + E^-, \quad (2.173)$$

whereas condition (2.172) gives:

$$\frac{\beta_1}{\mu_1} \cosh(\beta_1 a) E_1 = \beta_2 (E^+ - E^-). \quad (2.174)$$

Cancelling  $E_1$  from these equations, one gets:

$$\frac{\beta_1}{\mu_1} \coth(\beta_1 a) (E^+ + E^-) = \beta_2 (E^+ - E^-). \quad (2.175)$$

$$\left(\beta_2 + \frac{\beta_1}{\mu_1} \coth(\beta_1 a)\right) E^- = \left(\beta_2 - \frac{\beta_1}{\mu_1} \coth(\beta_1 a)\right) E^+. \quad (2.176)$$

Now for the boundary conditions at  $z = a + d$  [61]:

$$\hat{z} \cdot (\mathbf{B}^{(3)} - \mathbf{B}^{(2)})|_{z=a+d} = 0, \quad (2.177)$$

$$\hat{z} \times (\mathbf{E}^{(3)} - \mathbf{E}^{(2)})|_{z=a+d} = 0, \quad (2.178)$$

$$\hat{z} \times (\mathbf{B}^{(3)} - \mathbf{B}^{(2)})|_{z=a+d} = \frac{4\pi}{c} \sigma(\omega) \mathbf{E}^{\parallel}|_{z=a+d}. \quad (2.179)$$

$\sigma(\omega)$  is the conductivity of the graphene sheet, given by (2.59). Equations (2.177) and (2.178) both yield:

$$E_3 = E^+ e^{\beta_2 d} + E^- e^{-\beta_2 d}, \quad (2.180)$$

and equation (2.179) gives:

$$\beta_3 E_3 + \beta_2 (E^+ e^{\beta_2 d} - E^- e^{-\beta_2 d}) = i\omega \frac{4\pi}{c^2} \sigma(\omega) E_3. \quad (2.181)$$

Inputting (2.180) into (2.181):

$$\beta_2 (E^+ e^{\beta_2 d} - E^- e^{-\beta_2 d}) = \left(i\omega \frac{4\pi}{c^2} \sigma(\omega) - \beta_3\right) (E^+ e^{\beta_2 d} + E^- e^{-\beta_2 d}) \quad (2.182)$$

$$E^+ e^{2\beta_2 d} (\beta_2 + \beta_3 - i\omega \frac{4\pi}{c^2} \sigma(\omega)) = E^- (\beta_2 - \beta_3 + i\omega \frac{4\pi}{c^2} \sigma(\omega)). \quad (2.183)$$

Finally, one can combine equations (2.176) and (2.183) to solve the dispersion relation:

$$e^{2\beta_2 d} \left(\beta_2 + \beta_3 - i\omega \frac{4\pi}{c^2} \sigma(\omega)\right) \left(\beta_2 + \frac{\beta_1}{\mu_1} \coth(\beta_1 a)\right) = \left(\beta_2 - \beta_3 + i\omega \frac{4\pi}{c^2} \sigma(\omega)\right) \left(\beta_2 - \frac{\beta_1}{\mu_1} \coth(\beta_1 a)\right). \quad (2.184)$$

The effect of decreasing the distance of the graphene sheet to the AFM ( $d$ ) in the dispersion relations is to very slightly increase the effect of the graphene sheet on the modes of the system. The effect of making the AFM smaller (bringing the metal closer or decreasing  $a$ ) is to lower the energies of all the modes. There is a peak separation for a given  $a$ , depending slightly on  $d$ . A plot of the 'Mode distances' between modes of  $E_F = 0.4$  eV and modes of  $E_F = 0$  eV defined by:

$$\sum_n (\omega_n|_{E_F=0.4} - \omega_n|_{E_F=0}), \quad (2.185)$$

is presented in figure 2.12.

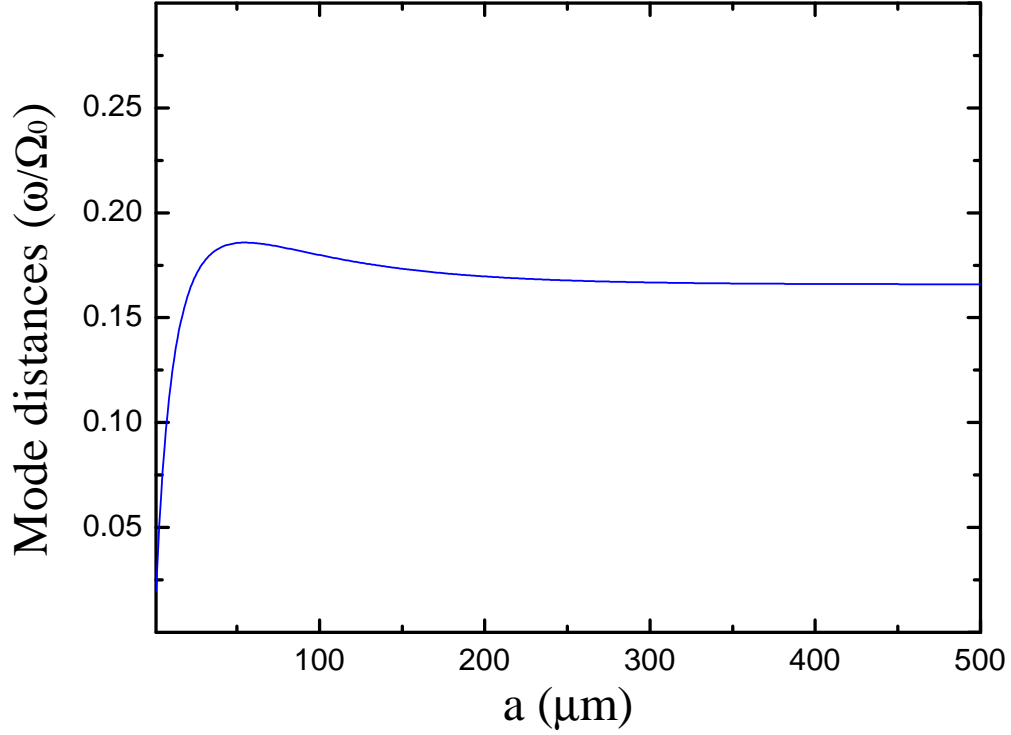


Figure 2.12: Plot of the result of (2.185), which measures the overall difference between the energies of the modes with a graphene sheet of Fermi energy  $E_F = 0.4$  eV and the energies of modes with a graphene sheet of Fermi energy  $E_F = 0$  eV. The distance between the graphene sheet and the antiferromagnet is  $d = 0.05$   $\mu\text{m}$ . The 'mode distances' between the modes are measured as a function of  $a$ , the width of the antiferromagnet. This is a way to find the value of  $a$  which maximizes the effect of the graphene sheet on the energies of the modes of the system.  $\Omega_0$  is the antiferromagnet resonance frequency (2.29). For the antiferromagnet permeability function given by (2.27)-(2.29), the values of the quantities that determine it were given by Table I of [60] and can also be consulted in equations (2.33)-(2.35). The value of the loss coefficient in (2.59) is  $\gamma_e = 0$  eV. Ignoring losses at the graphene sheet is valid when dealing with low temperatures. [20]

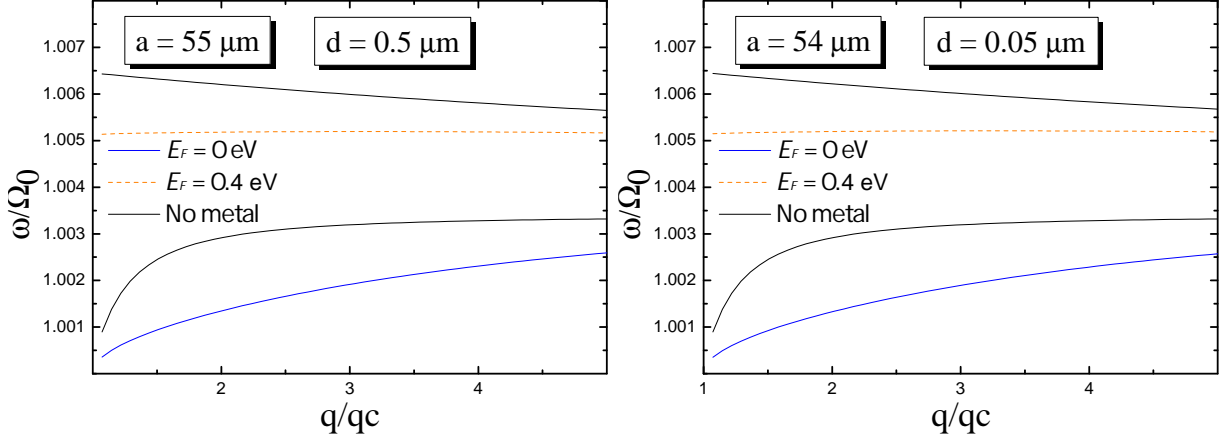


Figure 2.13: Dispersion relation for TE modes (2.184) solved for the values of  $a$  and  $d$  that maximize the 'mode distance' between the  $E_F = 0$  eV scenario and the  $E_F = 0.4$  eV scenario. The definition of 'mode difference' used was  $\sum_n \Delta\omega_n$  where  $\Delta\omega_n$  is the difference between the solution number  $n$  with  $E_F = 0.4$  and the solution number  $n$  with  $E_F = 0$ , and the sum is over all solutions plotted. For these values of  $a$  and  $d$ , the effect of the graphene sheet on the dispersion relation is maximized.  $\Omega_0$  is the antiferromagnet resonance frequency (2.29).  $q_c$  is the corresponding wavenumber in vacuum  $q_c = \frac{\Omega_0}{c}$ . For the antiferromagnet permeability function given by (2.27)-(2.29), the values of the quantities that determine it were given by Table I of [60] and can also be consulted in equations (2.33)-(2.35). The value of the loss coefficient in (2.59) is  $\gamma_e = 0$  eV. Ignoring losses at the graphene sheet is valid when dealing with low temperatures. [20]

### Propagating waves

For propagating waves, the field profiles will be:

$$\begin{cases} \mathbf{E}^{(1)} = t [e^{-ik_1z} + \alpha e^{ik_1z}] e^{iqx} \hat{y} \\ \mathbf{E}^{(2)} = [E^+ e^{ik_2(z-a)} + E^- e^{-ik_2(z-a)}] e^{iqx} \hat{y} \\ \mathbf{E}^{(3)} = [e^{-ik_3(z-a-d)} + r e^{ik_3(z-a-d)}] e^{iqx} \hat{y} \end{cases} \quad (2.186)$$

It is now possible to determine the magnetic field from Maxwell's equations:

$$-\frac{1}{c} \partial_t \mathbf{B} = \nabla \times \mathbf{E}, \quad (2.187)$$

$$i \frac{\omega}{c} \mathbf{B} = -\partial_z E_y \hat{x} + \partial_x E_y \hat{z}. \quad (2.188)$$

Thus,

$$\begin{cases} \mathbf{B}^{(1)} = t e^{iqx} c [ [e^{-ik_1z} - \alpha e^{ik_1z}] \frac{k_1}{\omega} \hat{x} + [e^{-ik_1z} + \alpha e^{ik_1z}] \frac{q}{\omega} \hat{z} ] \\ \mathbf{B}^{(2)} = -\frac{k_2}{\omega} c [E^+ e^{ik_2(z-a)} - E^- e^{-ik_2(z-a)}] e^{iqx} \hat{x} + \frac{q}{\omega} c [E^+ e^{ik_2(z-a)} + E^- e^{-ik_2(z-a)}] \hat{z} \\ \mathbf{B}^{(3)} = -\frac{k_3}{\omega} c [r e^{ik_3(z-a-d)} - e^{-ik_3(z-a-d)}] e^{iqx} \hat{x} + \frac{q}{\omega} c [r e^{ik_3(z-a-d)} + e^{-ik_3(z-a-d)}] \hat{z} \end{cases} \quad (2.189)$$

With condition (2.171) one can determine  $\alpha$ :

$$B_z^{(1)}|_{z=0} = 0, \quad (2.190)$$

$$\alpha = -1. \quad (2.191)$$

Thus, the fields can be written as:

$$\begin{cases} \mathbf{E}^{(1)} = t \sin(k_1 z) e^{iqx} \hat{y} \\ \mathbf{E}^{(2)} = [E^+ e^{ik_2(z-a)} + E^- e^{-ik_2(z-a)}] e^{iqx} \hat{y} \\ \mathbf{E}^{(3)} = [e^{-ik_3(z-a-d)} + r e^{ik_3(z-a-d)}] e^{iqx} \hat{y} \end{cases}. \quad (2.192)$$

$$\begin{cases} \mathbf{B}^{(1)} = t e^{iqx} \left( \cos(k_1 z) \frac{ik_1}{\omega} \hat{x} + \sin(k_1 z) \frac{q}{\omega} \hat{z} \right) \\ \mathbf{B}^{(2)} = -\frac{k_2}{\omega} [E^+ e^{ik_2(z-a)} - E^- e^{-ik_2(z-a)}] e^{iqx} \hat{x} + \frac{q}{\omega} [E^+ e^{ik_2(z-a)} + E^- e^{-ik_2(z-a)}] \hat{z} \\ \mathbf{B}^{(3)} = -\frac{k_3}{\omega} [r e^{ik_3(z-a-d)} - e^{-ik_3(z-a-d)}] e^{iqx} \hat{x} + \frac{q}{\omega} [r e^{ik_3(z-a-d)} + e^{-ik_3(z-a-d)}] \hat{z} \end{cases}. \quad (2.193)$$

The boundary conditions at  $z = a$  are [61]:

$$\hat{z} \cdot (\mathbf{B}^{(2)} - \mathbf{B}^{(1)})|_{z=a} = 0, \quad (2.194)$$

$$\hat{z} \times (\mathbf{E}^{(2)} - \mathbf{E}^{(1)})|_{z=a} = 0, \quad (2.195)$$

$$\hat{z} \times \left( \mathbf{B}^{(2)} - \frac{\mathbf{B}^{(1)}}{\mu_1} \right)|_{z=a} = 0. \quad (2.196)$$

These conditions yield:

$$t \sin(k_1 a) = E^+ + E^-, \quad (2.197)$$

$$-ik_1 t \cos(k_1 a) = k_2 \mu_1 (E^+ - E^-). \quad (2.198)$$

Combining these two equations:

$$-ik_1 \cot(k_1 a) (E^+ + E^-) = k_2 \mu_1 (E^+ - E^-), \quad (2.199)$$

$$E^- (k_2 \mu_1 - ik_1 \cot(k_1 a)) = E^+ (k_2 \mu_1 + ik_1 \cot(k_1 a)). \quad (2.200)$$

For simplicity of writing, a variable  $\eta$  will be defined as such:

$$E^- = \eta E^+, \quad (2.201)$$

$$\eta = \frac{k_2 \mu_1 + ik_1 \cot(k_1 a)}{k_2 \mu_1 - ik_1 \cot(k_1 a)}. \quad (2.202)$$

Now for the boundary conditions at  $z = a + d$  [61]:

$$\hat{z} \cdot (\mathbf{B}^{(3)} - \mathbf{B}^{(2)})|_{z=a+d} = 0, \quad (2.203)$$

$$\hat{z} \times (\mathbf{E}^{(3)} - \mathbf{E}^{(2)})|_{z=a+d} = 0, \quad (2.204)$$

$$\hat{z} \times (\mathbf{B}^{(3)} - \mathbf{B}^{(2)})|_{z=d} = \frac{4\pi}{c} \sigma(\omega) \mathbf{E}^{\parallel}|_{z=a+d}. \quad (2.205)$$

$\sigma(\omega)$  is the conductivity of the graphene sheet, given by (2.59). These equations yield:

$$1 + r = E^+ e^{ik_2 d} + E^- e^{-ik_2 d}, \quad (2.206)$$

$$k_2 [E^+ e^{ik_2 d} - E^- e^{-ik_2 d}] - k_3 [r - 1] = \omega \frac{4\pi}{c^2} \sigma(\omega) [1 + r]. \quad (2.207)$$

Now using equation (2.206) together with (2.201) one can obtain the factor  $E^+$  as a function of  $r$ :

$$E^+ = \frac{1+r}{e^{ik_2d} + \eta e^{-ik_2d}}. \quad (2.208)$$

Finally, this equation can be inserted in (2.207) to yield:

$$r = \frac{\omega \frac{4\pi}{c^2} \sigma(\omega) - k_3 - A}{A - k_3 - \omega \frac{4\pi}{c^2} \sigma(\omega)}, \quad (2.209)$$

with

$$A = \frac{k_2 e^{ik_2d} - k_2 \eta e^{-ik_2d}}{e^{ik_2d} + \eta e^{-ik_2d}}, \quad (2.210)$$

$$\eta = \frac{k_2 \mu_1 + ik_1 \cot(k_1 a)}{k_2 \mu_1 - ik_1 \cot(k_1 a)}. \quad (2.211)$$

## 2.5.2 TM modes

### Evanescent waves

The magnetic field for TM modes can be written as:

$$\begin{cases} \mathbf{B}^{(1)} = B_1 [e^{\beta_1 z} + \alpha e^{-\beta_1 z}] e^{iqx} \hat{y} \\ \mathbf{B}^{(2)} = [B^+ e^{\beta_2(z-a)} + B^- e^{-\beta_2(z-a)}] e^{iqx} \hat{y} \\ \mathbf{B}^{(3)} = B_3 e^{-\beta_3(z-a-d)} e^{iqx} \hat{y} \end{cases} \quad (2.212)$$

It is now possible to determine the electric field from Ampère's law:

$$\frac{\epsilon \mu}{c} \partial_t \mathbf{E} = \nabla \times \mathbf{B}, \quad (2.213)$$

$$-i\epsilon \mu \frac{\omega}{c} \mathbf{E} = -\partial_z B_y \hat{x} + \partial_x B_y \hat{z}. \quad (2.214)$$

With this equation, one can write the electric fields as:

$$\begin{cases} \mathbf{E}^{(1)} = -B_1 e^{iqx} \frac{c}{\epsilon_1 \mu_1 \omega} ([e^{\beta_1 z} - \alpha e^{-\beta_1 z}] i\beta_1 \hat{x} + [e^{\beta_1 z} + \alpha e^{-\beta_1 z}] q\hat{z}) \\ \mathbf{E}^{(2)} = -\frac{c}{\epsilon_2} i \frac{\beta_2}{\omega} [B^+ e^{\beta_2(z-a)} - B^- e^{-\beta_2(z-a)}] e^{iqx} \hat{x} - \frac{c}{\epsilon_2} \frac{q}{\omega} [B^+ e^{\beta_2(z-a)} + B^- e^{-\beta_2(z-a)}] e^{iqx} \hat{z} \\ \mathbf{E}^{(3)} = -B_3 \frac{c}{\epsilon_3} e^{-\beta_3(z-a-d)} e^{iqx} \frac{1}{\omega} [-i\beta_3 \hat{x} + q\hat{z}] \end{cases} \quad (2.215)$$

Applying condition (2.159),  $\alpha$  can be determined:

$$E_x^{(1)}|_{z=0} = 0, \quad (2.216)$$

$$\alpha = 1. \quad (2.217)$$

Thus, the fields can be written as:

$$\begin{cases} \mathbf{B}^{(1)} = B_1 \cosh(\beta_1 z) e^{iqx} \hat{y} \\ \mathbf{B}^{(2)} = [B^+ e^{\beta_2(z-a)} + B^- e^{-\beta_2(z-a)}] e^{iqx} \hat{y} \\ \mathbf{B}^{(3)} = B_3 e^{-\beta_3(z-a-d)} e^{iqx} \hat{y} \end{cases} \quad (2.218)$$



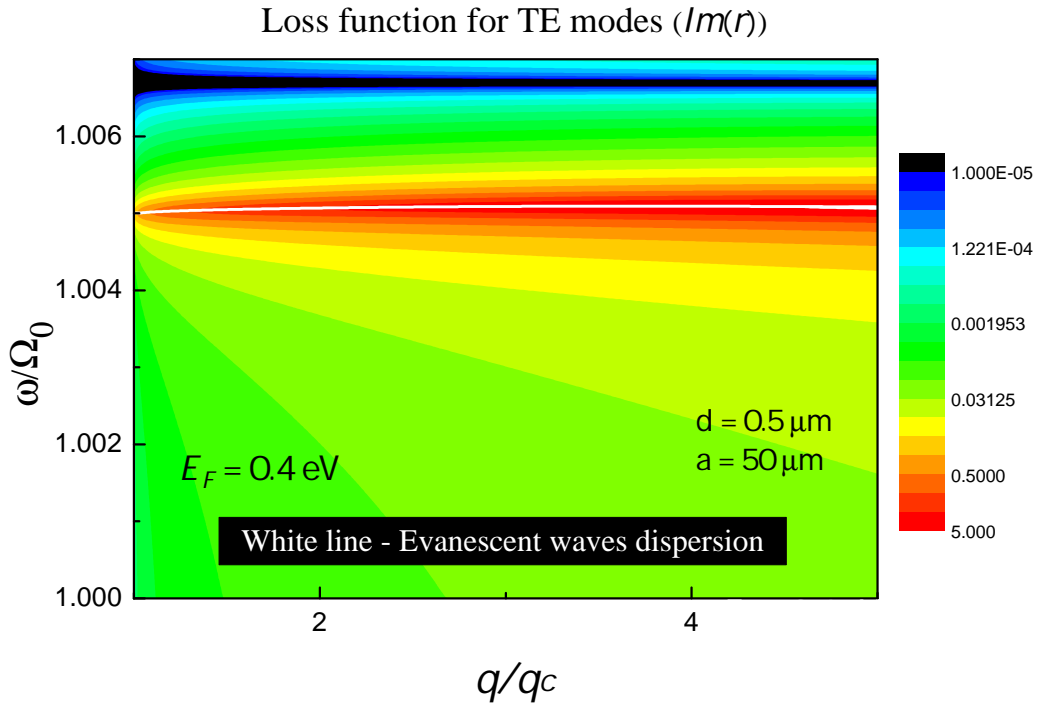


Figure 2.14: Comparison between the loss function ( $\Im(r)$ ) from (2.209) and the dispersion relation from (2.184) for TE modes generated by surface magnon-plasmon polaritons.  $\Omega_0$  is the antiferromagnet resonance frequency (2.29).  $q_c$  is the corresponding wavenumber in vacuum  $q_c = \frac{\Omega_0}{c}$ . The value of  $d$ , the separation between the graphene sheet and the antiferromagnet, is  $0.5 \mu\text{m}$ . The value of  $a$ , the thickness of the antiferromagnet, is  $50 \mu\text{m}$ . For the antiferromagnet permeability function given by (2.27)-(2.29), the values of the quantities that determine it were given by Table I of [60] and can also be consulted in equations (2.33)-(2.35). The value of the loss coefficient in (2.59) is  $\gamma_e = 0 \text{ eV}$ . Ignoring losses at the graphene sheet is valid when dealing with low temperatures. [20]

$$\begin{cases} \mathbf{E}^{(1)} = -B_1 e^{iqx} \frac{c}{\epsilon_1 \mu_1 \omega} (\sinh(\beta_1 z) i \beta_1 \hat{x} + \cosh(\beta_1 z) q \hat{z}) \\ \mathbf{E}^{(2)} = -\frac{c}{\epsilon_2} i \frac{\beta_2}{\omega} [B^+ e^{\beta_2(z-a)} - B^- e^{-\beta_2(z-a)}] e^{iqx} \hat{x} - \frac{c}{\epsilon_2} \frac{q}{\omega} [B^+ e^{\beta_2(z-a)} + B^- e^{-\beta_2(z-a)}] e^{iqx} \hat{z} \\ \mathbf{E}^{(3)} = -B_3 \frac{c}{\epsilon_3} e^{-\beta_3(z-a-d)} e^{iqx} \frac{1}{\omega} [-i \beta_3 \hat{x} + q \hat{z}] \end{cases} \quad (2.219)$$

Boundary conditions at  $z = a$  read [61]:

$$\hat{z} \cdot (\mathbf{B}^{(2)} - \mathbf{B}^{(1)})|_{z=a} = 0, \quad (2.220)$$

$$\hat{z} \times (\mathbf{E}^{(2)} - \mathbf{E}^{(1)})|_{z=a} = 0, \quad (2.221)$$

$$\hat{z} \times \left( \mathbf{B}^{(2)} - \frac{\mathbf{B}^{(1)}}{\mu_1} \right) |_{z=a} = 0. \quad (2.222)$$

These equations yield:

$$\frac{\beta_1}{\epsilon_1 \mu_1} \sinh(\beta_1 a) B_1 = \frac{\beta_2}{\epsilon_2} (B^+ - B^-), \quad (2.223)$$

$$\frac{\cosh(\beta_1 a)}{\mu_1} B_1 = B^+ + B^-. \quad (2.224)$$

Combining these two equations:

$$\frac{\beta_2}{\epsilon_2} \coth(\beta_1 a) (B^+ - B^-) = \frac{\beta_1}{\epsilon_1} (B^+ + B^-), \quad (2.225)$$

$$\left( \frac{\beta_2}{\epsilon_2} \coth(\beta_1 a) - \frac{\beta_1}{\epsilon_1} \right) B^+ = \left( \frac{\beta_2}{\epsilon_2} \coth(\beta_1 a) + \frac{\beta_1}{\epsilon_1} \right) B^-. \quad (2.226)$$

Now for the boundary conditions at  $z = a + d$  [61]:

$$\hat{z} \cdot (\mathbf{B}^{(3)} - \mathbf{B}^{(2)})|_{z=a+d} = 0, \quad (2.227)$$

$$\hat{z} \times (\mathbf{E}^{(3)} - \mathbf{E}^{(2)})|_{z=a+d} = 0, \quad (2.228)$$

$$\hat{z} \times (\mathbf{B}^{(3)} - \mathbf{B}^{(2)})|_{z=d} = \frac{4\pi}{c} \sigma(\omega) \mathbf{E}^{\parallel}|_{z=a+d}. \quad (2.229)$$

$\sigma(\omega)$  is the conductivity of the graphene sheet, given by (2.59). These equations yield:

$$\frac{\beta_3}{\epsilon_3} B_3 = -\frac{\beta_2}{\epsilon_2} (B^+ e^{\beta_2 d} - B^- e^{-\beta_2 d}) \quad (2.230)$$

$$B_3 - (B^+ e^{\beta_2 d} + B^- e^{-\beta_2 d}) = -i B_3 \frac{\beta_3}{\omega \epsilon_3} 4\pi \sigma(\omega), \quad (2.231)$$

which implies:

$$(B^+ e^{\beta_2 d} + B^- e^{-\beta_2 d}) = -\left( i \frac{1}{\omega} 4\pi \sigma(\omega) + \frac{\epsilon_3}{\beta_3} \right) (B^+ e^{\beta_2 d} - B^- e^{-\beta_2 d}) \frac{\beta_2}{\epsilon_2}, \quad (2.232)$$

$$B^+ e^{2\beta_2 d} \left[ 1 + \frac{\epsilon_3 \beta_2}{\epsilon_2 \beta_3} + i \frac{\beta_2}{\epsilon_2 \omega} 4\pi \sigma(\omega) \right] = B^- \left[ i \frac{\beta_2}{\epsilon_2 \omega} 4\pi \sigma(\omega) + \frac{\epsilon_3 \beta_2}{\epsilon_2 \beta_3} - 1 \right]. \quad (2.233)$$

Now, combining (2.226) with (2.233) the eigenmode equation is found:

$$\begin{aligned} e^{2\beta_2 d} \left[ 1 + \frac{\epsilon_3 \beta_2}{\epsilon_2 \beta_3} + i \frac{\beta_2}{\epsilon_2 \omega} 4\pi \sigma(\omega) \right] \left( \frac{\beta_2}{\epsilon_2} \coth(\beta_1 a) + \frac{\beta_1}{\epsilon_1} \right) = \\ \left[ i \frac{\beta_2}{\epsilon_2 \omega} 4\pi \sigma(\omega) + \frac{\epsilon_3 \beta_2}{\epsilon_2 \beta_3} - 1 \right] \left( \frac{\beta_2}{\epsilon_2} \coth(\beta_1 a) - \frac{\beta_1}{\epsilon_1} \right). \end{aligned} \quad (2.234)$$

Figure (2.15) shows the value of the gap between the first two modes as a function of  $a$  for a fixed  $d = 0.05 \mu\text{m}$ , for Fermi energies  $E_F = 0.03 \text{ eV}$  and  $E_F = 0.07 \text{ eV}$ . The values of  $a$  in figure (2.16) were chosen accordingly to maximize the gap size. These plots show that for a distance of the order of  $0.05 \text{ eV}$  maximum splitting is achieved up to three decimal places. Further narrowing of  $d$  will not increase the third decimal place of the splitting while quickly rendering this model inaccurate due to the distances of the order of a few nanometers becoming closer to the atomic radius of the carbon atoms, invalidating the classical electromechanical theory. Furthermore, increasing  $d$  has a very small effect on the dispersion. Also, increasing  $a$  (bringing the metal away from the AFM surface, thus increasing the AFM size) moves the dispersion to the left (the gap happens at smaller  $q$  values). Figure (2.7) shows the gap happening at  $q = 1.6 q_c$  for the system with  $a \rightarrow \infty$ , in contrast with the gap just before  $q = 1.8 q_c$  for  $a = 231 \mu\text{m}$  seen in figure (2.16).

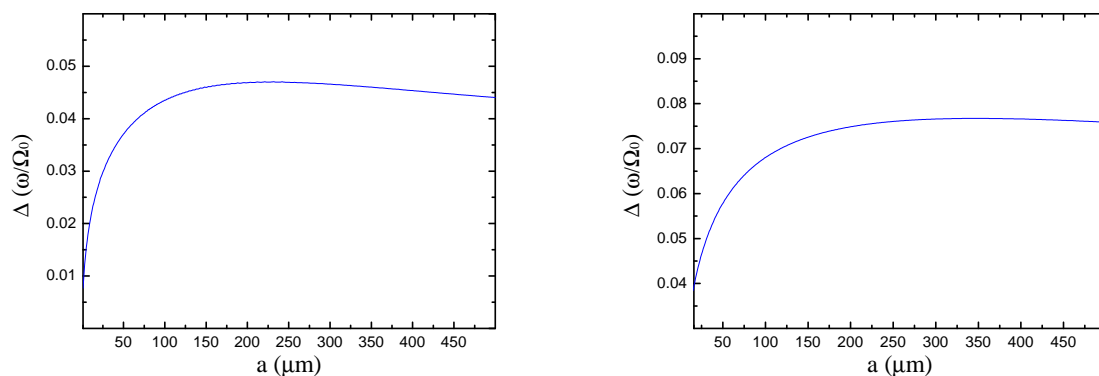


Figure 2.15: Values of the gap  $\Delta$  between between the lower and upper bands of TM modes for a separation between the antiferromagnet and the graphene sheet of  $d = 0.05 \mu\text{m}$ , as a function of  $a$ , for Fermi energies of  $E_F = 0.03 \text{ eV}$  and  $E_F = 0.07 \text{ eV}$ .  $\Omega_0$  is the antiferromagnet resonance frequency (2.29). For the antiferromagnet permeability function given by (2.27)-(2.29), the values of the quantities that determine it were given by Table I of [60] and can also be consulted in equations (2.33)-(2.35). The value of the loss coefficient in (2.59) is  $\gamma_e = 0 \text{ eV}$ . Ignoring losses at the graphene sheet is valid when dealing with low temperatures. [20]

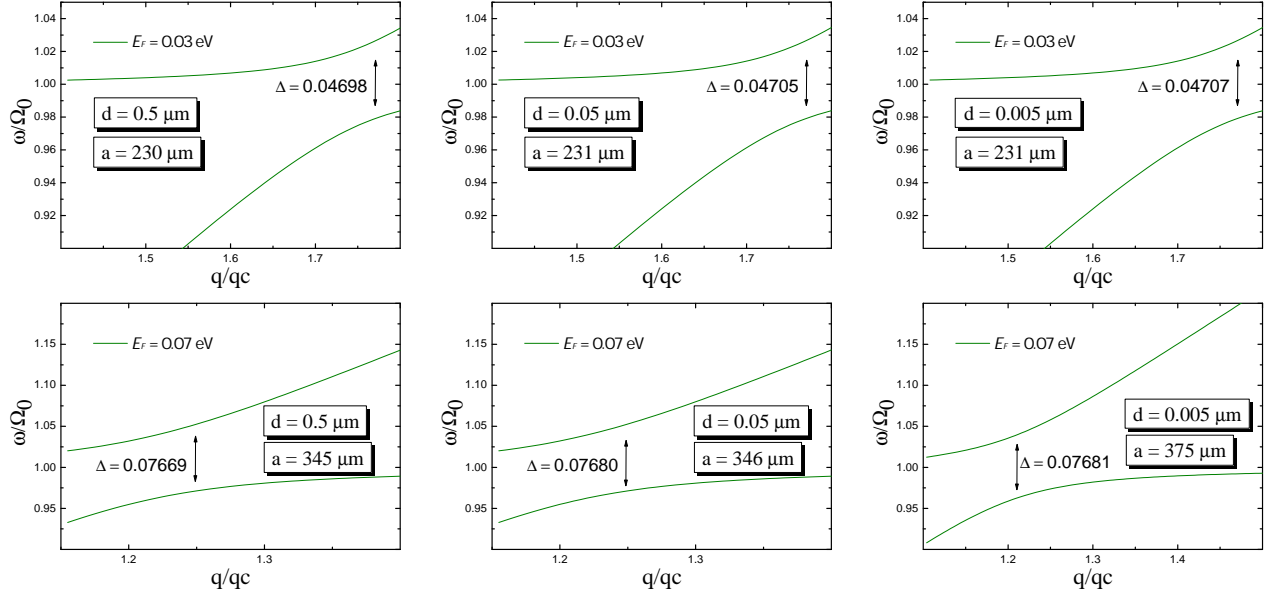


Figure 2.16: Dispersion relation for TM modes (2.184) solved for different values of AFM width  $a$ , different metal distances  $d$  and Fermi energy of the graphene sheet  $E_F = 0.03$  eV. The values of  $a$  are chosen to maximize the splitting energy  $\Delta$ .  $\Omega_0$  is the antiferromagnet resonance frequency (2.29).  $q_c$  is the corresponding wavenumber in vacuum  $q_c = \frac{\Omega_0}{c}$ . For the antiferromagnet permeability function given by (2.27)-(2.29), the values of the quantities that determine it were given by Table I of [60] and can also be consulted in equations (2.33)-(2.35). The value of the loss coefficient in (2.59) is  $\gamma_e = 0$  eV. Ignoring losses at the graphene sheet is valid when dealing with low temperatures. [20]

### Propagating waves

For propagating TM waves, the field profiles are:

$$\begin{cases} \mathbf{B}^{(1)} = t [e^{-ik_1 z} + \alpha e^{ik_1 z}] e^{iqx} \hat{y} \\ \mathbf{B}^{(2)} = [B^+ e^{ik_2(z-a)} + B^- e^{-ik_2(z-a)}] e^{iqx} \hat{y} \\ \mathbf{B}^{(3)} = [e^{-ik_3(z-a-d)} + r e^{ik_3(z-a-d)}] e^{iqx} \hat{y} \end{cases} \quad (2.235)$$

The electric field is obtained with Ampère's law:

$$\frac{\epsilon\mu}{c} \partial_t \mathbf{E} = \nabla \times \mathbf{B}, \quad (2.236)$$

$$-i\epsilon\mu \frac{\omega}{c} \mathbf{E} = -\partial_z B_y \hat{x} + \partial_x B_y \hat{z}. \quad (2.237)$$

Thus,

$$\begin{cases} \mathbf{E}^{(1)} = -\frac{c}{\epsilon_1 \mu_1 \omega} t e^{iqx} ([e^{-ik_1 z} - \alpha e^{ik_1 z}] k_1 \hat{x} + [e^{-ik_1 z} + \alpha e^{ik_1 z}] q \hat{z}) \\ \mathbf{E}^{(2)} = \frac{c}{\epsilon_2} \frac{k_2}{\omega} [B^+ e^{ik_2(z-a)} - B^- e^{-ik_2(z-a)}] e^{iqx} \hat{x} - \frac{c}{\epsilon_2} \frac{q}{\omega} [B^+ e^{ik_2(z-a)} + B^- e^{-ik_2(z-a)}] e^{iqx} \hat{z} \\ \mathbf{E}^{(3)} = \frac{c}{\epsilon_3} \frac{k_3}{\omega} [r e^{ik_3(z-a-d)} - e^{-ik_3(z-a-d)}] e^{iqx} \hat{x} - \frac{c}{\epsilon_3} \frac{q}{\omega} [r e^{ik_3(z-a-d)} + e^{-ik_3(z-a-d)}] \hat{z} \end{cases} \quad (2.238)$$

Applying condition (2.159) at  $z = 0$ ,  $\alpha$  is obtained:

$$E_x^{(1)}|_{z=0} = 0, \quad (2.239)$$

$$\alpha = 1. \quad (2.240)$$

So, the fields can be written as:

$$\begin{cases} \mathbf{B}^{(1)} = t \cos(k_1 z) e^{iqx} \hat{y} \\ \mathbf{B}^{(2)} = [B^+ e^{ik_2(z-a)} + B^- e^{-ik_2(z-a)}] e^{iqx} \hat{y} \\ \mathbf{B}^{(3)} = [e^{-ik_3(z-a-d)} + r e^{ik_3(z-a-d)}] e^{iqx} \hat{y} \end{cases}. \quad (2.241)$$

$$\begin{cases} \mathbf{E}^{(1)} = -\frac{c}{\epsilon_1 \mu_1 \omega} t e^{iqx} (-\sin(k_1 z) i k_1 \hat{x} + \cos(k_1 z) q \hat{z}) \\ \mathbf{E}^{(2)} = \frac{c}{\epsilon_2 \omega} \frac{k_2}{\omega} [B^+ e^{ik_2(z-a)} - B^- e^{-ik_2(z-a)}] e^{iqx} \hat{x} - \frac{c}{\epsilon_2 \omega} \frac{q}{\omega} [B^+ e^{ik_2(z-a)} + B^- e^{-ik_2(z-a)}] e^{iqx} \hat{z} \\ \mathbf{E}^{(3)} = \frac{c}{\epsilon_3 \omega} \frac{k_3}{\omega} [r e^{ik_3(z-a-d)} - e^{-ik_3(z-a-d)}] e^{iqx} \hat{x} - \frac{c}{\epsilon_3 \omega} \frac{q}{\omega} [r e^{ik_3(z-a-d)} + e^{-ik_3(z-a-d)}] e^{iqx} \hat{z} \end{cases}. \quad (2.242)$$

Boundary conditions at  $z = a$  read [61]:

$$\hat{z} \cdot (\mathbf{B}^{(2)} - \mathbf{B}^{(1)})|_{z=a} = 0, \quad (2.243)$$

$$\hat{z} \times (\mathbf{E}^{(2)} - \mathbf{E}^{(1)})|_{z=a} = 0, \quad (2.244)$$

$$\hat{z} \times \left( \mathbf{B}^{(2)} - \frac{\mathbf{B}^{(1)}}{\mu_1} \right)|_{z=a} = 0. \quad (2.245)$$

These conditions yield:

$$\frac{ik_1}{\epsilon_1 \mu_1} \sin(k_1 a) t = \frac{k_2}{\epsilon_2} (B^+ - B^-), \quad (2.246)$$

$$\frac{t}{\mu_1} \cos(k_1 a) = B^+ + B^-. \quad (2.247)$$

Combining these equations one obtains:

$$\frac{k_1}{\epsilon_1} (B^+ + B^-) = \frac{k_2}{\epsilon_2} \cot(k_1 a) (B^+ - B^-), \quad (2.248)$$

$$B^- \left( \frac{k_2}{\epsilon_2} \cot(k_1 a) - \frac{k_1}{\epsilon_1} \right) = B^+ \left( \frac{k_1}{\epsilon_1} + \frac{k_2}{\epsilon_2} \cot(k_1 a) \right). \quad (2.249)$$

We can write this as:

$$B^- = \eta B^+, \quad (2.250)$$

where

$$\eta = \frac{k_2 \epsilon_1 \cot(k_1 a) + k_1 \epsilon_2}{k_2 \epsilon_1 \cot(k_1 a) - k_1 \epsilon_2}. \quad (2.251)$$

Now, the boundary conditions at  $z = a + d$  read [61]:

$$\hat{z} \cdot (\mathbf{B}^{(3)} - \mathbf{B}^{(2)})|_{z=d} = 0, \quad (2.252)$$

$$\hat{z} \times (\mathbf{E}^{(3)} - \mathbf{E}^{(2)})|_{z=d} = 0, \quad (2.253)$$

$$\hat{z} \times (\mathbf{B}^{(3)} - \mathbf{B}^{(2)})|_{z=d} = \frac{4\pi}{c} \sigma(\omega) \mathbf{E}^{\parallel}|_{z=d}. \quad (2.254)$$

$\sigma(\omega)$  is the conductivity of the graphene sheet, given by (2.59). These equations yield:

$$\frac{k_3}{\epsilon_3} (r - 1) = \frac{k_2}{\epsilon_2} (B^+ e^{ik_2 d} - B^- e^{-ik_2 d}). \quad (2.255)$$

$$1 + r - (B^+ e^{ik_2 d} + B^- e^{-ik_2 d}) = (1 - r) \frac{k_3}{\epsilon_3} \frac{4\pi}{\omega} \sigma(\omega) \quad (2.256)$$

Now one can use equation (2.255) together with (2.250) to obtain the factor  $B^+$  as a function of  $r$ :

$$B^+ = \frac{r - 1}{e^{ik_2 d} - \alpha e^{-ik_2 d}} \frac{\epsilon_2 k_3}{\epsilon_3 k_2}. \quad (2.257)$$

Substituting this equation in (2.256) yields:

$$r = \frac{B - A - 1}{B - A + 1}, \quad (2.258)$$

with

$$A = \frac{1 + \eta e^{-2ik_2 d} \epsilon_2 k_3}{1 - \eta e^{-2ik_2 d} \epsilon_3 k_2}, \quad (2.259)$$

$$B = \frac{k_3}{\epsilon_3} \frac{4\pi}{\omega} \sigma(\omega), \quad (2.260)$$

$$\eta = \frac{k_2 \epsilon_1 \cot(k_1 a) + k_1 \epsilon_2}{k_2 \epsilon_1 \cot(k_1 a) - k_1 \epsilon_2}. \quad (2.261)$$

By placing a metal surface below the antiferromagnet, limiting the antiferromagnet to a width  $a$ , there is a value of  $a$  that maximizes the effect of the graphene sheet on the TE dispersion relation. Figure 2.12 shows the average separation of the  $E_F = 0$  eV and  $E_F = 0.4$  eV modes. At  $a \rightarrow \infty$  we get the result from the previous study, with a semi-infinite antiferromagnet. However, for the optimal value  $a = 55 \mu\text{m}$ , the negative group velocity at  $E_F = 0.4$  eV is no longer observed. The group velocity for  $E_F = 0.4$  eV is positive for smaller  $a$ , and becomes negative for larger  $a$ , being approximately zero at the  $a = 55 \mu\text{m}$  distance. As for the TM modes, the addition of the metal, at the right distance (figure 2.15), can slightly increase the gap between the lower and upper modes.

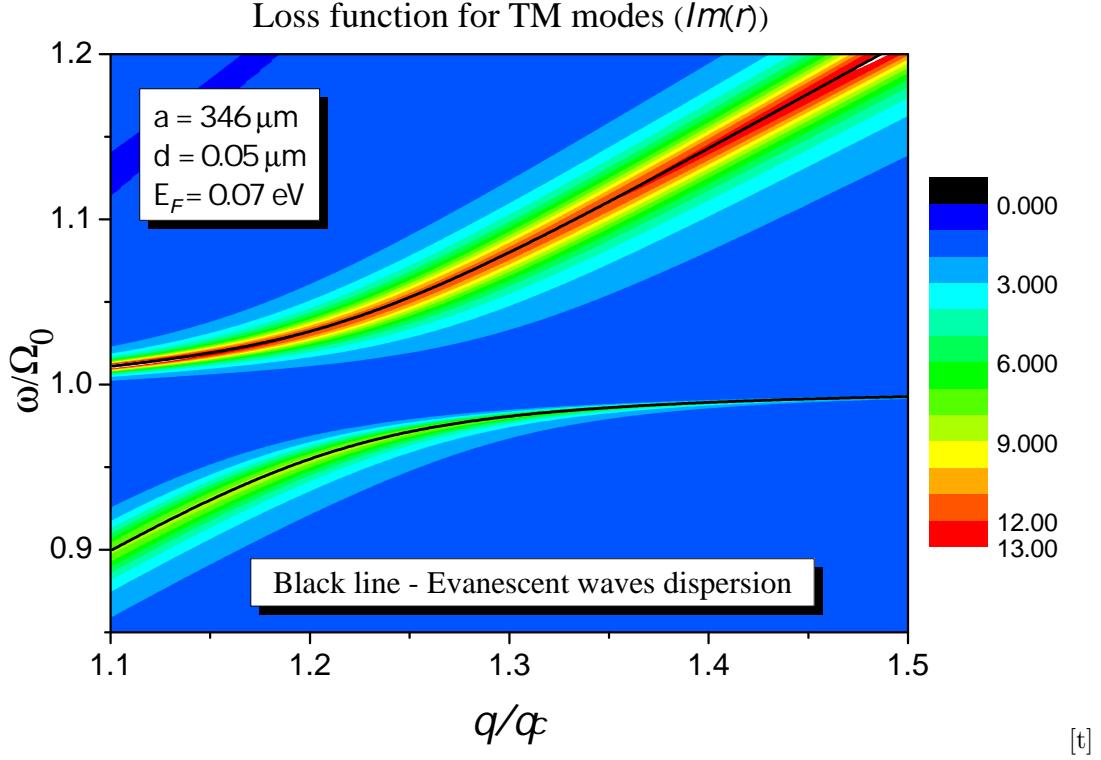


Figure 2.17: Comparing the imaginary part of the reflectivity (2.258) (Loss function) with the dispersion relation for evanescent TM modes calculated in the previous section (2.234) generated by surface magnon-plasmon polaritons.  $\Omega_0$  is the antiferromagnet resonance frequency (2.29).  $q_c$  is the corresponding wavenumber in vacuum  $q_c = \frac{\Omega_0}{c}$ . The value of  $d$ , the separation between the graphene sheet and the antiferromagnet, is  $0.5 \mu\text{m}$ . The value of  $a$ , the thickness of the antiferromagnet, is  $346 \mu\text{m}$ . The Fermi energy of the graphene sheet is  $E_F = 0.07 \text{ eV}$ . For the antiferromagnet permeability function given by (2.27)-(2.29), the values of the quantities that determine it were given by Table I of [60]. The value of the loss coefficient in (2.59) is  $\gamma_e = 0 \text{ eV}$ . Ignoring losses at the graphene sheet is valid when dealing with low temperatures. [20]. The loss function peaks at energies corresponding to the evanescent modes.

# 3

## Exciton-Polaritons of a 2D TMD layer embedded in a cylindrical microcavity

---

This chapter will study the formation of polaritons by adding a TMD semiconductor layer placed in the symmetry plane (perpendicular to the axis) of a perfect cylindrical microcavity, in order to enhance the excitonic coupling to the electromagnetic field. The system just described is depicted in figure (3.1). The exciton-polariton density of states projected onto the photonic subspace will be compared to the density of states of the empty cavity system (removing the TMD layer). For a cylinder of finite height with a dielectric interface on its surface, Maxwell's equations cannot be solved analytically. Thus, the focus will be on a cylindrical microcavity with perfect confinement. As such, the interface will be considered as perfectly conducting, as if the dielectric cylinder were covered by a thin perfectly metallic material. The validity of this approximation will be examined in the  $L \rightarrow \infty$  case. The exciton-polariton modes will be calculated exactly with a classical model, and with an approximate quantum model, the Hopfield coefficients [16] will be determined for each mode. These coefficients measure the fraction of exciton and photon in a polariton mode. Finally, the emission enhancement on a point emitter on the TMD plane will be studied for specific angular momenta as well as for the general case where all angular momenta are considered. For such an emitter, we shall assume a weak coupling regime and analyze how its emission is enhanced or inhibited (the Purcell effect [17]) due to the polaritonic background of the microcavity with embedded TMD layer.

In the next section we consider excitons confined to a 2D disk and derive the electric susceptibility of the TMD layer, which determines the coupling effects of the excitons with the electromagnetic field of the cavity modes. In section 3.3, we study coupled (polariton) modes in such a cavity using both semiclassical and quantum approaches. Employing these results, in section 3.4 we evaluate the total and projected densities of states (DOS) showing the possibility of strong enhancement of the local photonic DOS modified due to the presence of the TMD layer in the cavity. In addition, in section 3.5, we provide a theoretical analysis of the Purcell factor of a point emitter located in the vicinity of the TMD layer.



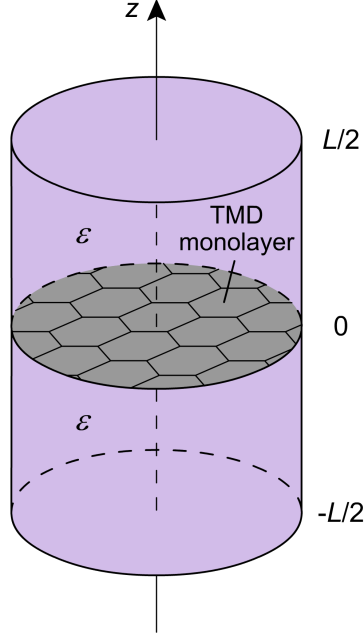


Figure 3.1: Sketch of the system under study in chapter 3: a TMD monolayer inserted in a dielectric cylindrical cavity of length  $L$  with relative permittivity  $\epsilon$ . The electrical permittivities of the materials in the cavity and their dimensions, as well as the TMD layer conductivity caused mainly by the formation of exciton-polaritons, will determine the optical spectra.

### 3.1 Excitonic susceptibility of the 2D semiconductor layer on the cavity

To calculate the eigenmodes of the system, it is necessary to model the susceptibility and conductivity of the embedded layer of TMD. For this, firstly the pure excitonic and photonic states must be characterized.

#### 3.1.1 Exciton confinement

For exciton states, the very small Bohr radius (of the order  $a_{ex} \sim 1$  nm [33], where the 2D disk's radius is  $R$  and is of the order  $1 \mu\text{m}$ ) means that it is a reasonable approximation to disregard the exciton's internal structure in what concerns its confinement in the radial direction, treating the exciton as a point-like particle confined in a circular potential well of radius  $R$ . Considering an infinite potential well, the point-like exciton will obey Schrödinger's equation:

$$-\frac{\hbar^2}{2M_{ex}} \nabla_{2D}^2 \Psi_{ex}(\mathbf{r}) = (E - E_{ex}) \Psi_{ex}(\mathbf{r}), \quad (3.1)$$

where  $\mathbf{r}$  is a 2D radius-vector,  $\nabla_{2D}$  is the Laplacian operator in the plane of the TMD,  $M_{ex}$  the excitonic mass and  $E_{ex}$  the binding energy for an infinite 2D layer cladded by the MC dielectric material. To solve this equation, we write it in polar coordinates as:

$$a \left( \frac{1}{r} \frac{\partial}{\partial r} + \frac{\partial^2}{\partial r^2} + \frac{1}{r^2} \frac{\partial^2}{\partial \phi^2} \right) \Psi_{ex}(\mathbf{r}) + \Delta E \Psi_{ex}(\mathbf{r}) = 0, \quad (3.2)$$

where  $a = \frac{\hbar^2}{2M_{ex}}$  and  $\Delta E = E - E_{ex}$ . Now multiplying by  $r^2$  and dividing by  $a$ , this equation takes the form:

$$\left( r \frac{\partial}{\partial r} + r^2 \frac{\partial^2}{\partial r^2} + \frac{\partial^2}{\partial \phi^2} \right) \Psi_{ex}(\mathbf{r}) + r^2 \frac{\Delta E}{a} \Psi_{ex}(\mathbf{r}) = 0. \quad (3.3)$$

It is noticeable that this equation is separable. Assuming a separable wavefunction

$$\Psi_{ex}(\mathbf{r}) = \Phi(\phi)\mathcal{R}(r), \quad (3.4)$$

and dividing the equation by the entire wavefunction on both sides, leads to:

$$\left( r \frac{\partial \mathcal{R}(r)}{\partial r} + r^2 \frac{\partial^2 \mathcal{R}(r)}{\partial r^2} \right) \frac{1}{\mathcal{R}(r)} + \frac{\partial^2 \Phi(\phi)}{\partial \phi^2} \frac{1}{\Phi(\phi)} + r^2 \frac{\Delta E}{a} = 0, \quad (3.5)$$

because the equation contains only separate terms that depend only on one variable. The part of the equation that only depends on  $\phi$  must be a constant of symmetric value to the rest of the equation (that depends only on  $r$ ). We attribute the value  $-m^2$  to this constant, effectively splitting this equation in two:

$$\frac{\partial^2 \Phi(\phi)}{\partial \phi^2} \frac{1}{\Phi(\phi)} = -m^2 \quad (3.6)$$

for  $\phi$ , and

$$\left( r \frac{\partial \mathcal{R}(r)}{\partial r} + r^2 \frac{\partial^2 \mathcal{R}(r)}{\partial r^2} \right) \frac{1}{\mathcal{R}(r)} - m^2 + r^2 \frac{\Delta E}{a} = 0 \quad (3.7)$$

for  $r$ . Now, equation (3.6) has the set of solutions:

$$\Phi(\phi) = e^{\pm im\phi}, \quad (3.8)$$

and equation (3.7) can be recognized as the Bessel differential equation [63], supporting Bessel functions of the first and second kinds as solutions:

$$\mathcal{R}_m(r) = C_m J_m(qr) + B Y_m(qr), \quad (3.9)$$

where

$$q = \sqrt{\frac{\Delta E}{a}}. \quad (3.10)$$

However, because the exciton is present inside the circular area, the point  $r = 0$  would present a divergence to infinity for the function of second kind  $Y_m$ . For this reason, solutions with  $B \neq 0$  are not valid and we are left with:

$$\mathcal{R}_m(r) = C_m J_m(qr). \quad (3.11)$$

Finally, applying the boundary condition  $\mathcal{R}(R) = 0$  (due to the infinite potential well) the values of  $q$  and, as a consequence, of the energy  $E$  become quantized:

$$q_{m,n} = \frac{\xi_{m,n}}{R}, \quad (3.12)$$

where  $\xi_{m,n}$  is the  $n$ -th zero of the Bessel function  $J_m$ . In conclusion the wavefunctions will be

$$\Psi_{\pm m,n}(\mathbf{r}) = C_{m,n} J_m(q_{m,n}r) e^{\pm im\phi}, \quad (3.13)$$

where  $m \geq 0$  is the angular momentum number and  $n \geq 0$  the radial quantum number.  $q_{m,n} = \frac{\xi_{m,n}}{R}$  is the radial wavenumber.  $C_{m,n}$  is the normalization constant, and it must be computed by ensuring the probability of finding the exciton somewhere inside the disk is 1. This is expressed as the integral over the disk:

$$\int_{disk} |\Psi_{\pm m,n}(\mathbf{r})|^2 r dr d\phi = 1, \quad (3.14)$$

$$2\pi |C_{m,n}|^2 \int_0^R J_m^2(\xi_{m,n} r/R) r dr = 1. \quad (3.15)$$

The integral's result is known to be  $\frac{R^2}{2} J'(\xi_{m,n})^2$  [?] and the expression becomes:

$$\pi |C_{m,n}|^2 R^2 J_m'(\xi_{m,n})^2 = 1 \quad (3.16)$$

The normalization constant is thus shown to be

$$C_{m,n} = 1/(\sqrt{\pi} R |J_m'(\xi_{m,n})|). \quad (3.17)$$

Finally, squaring both sides of (3.10) while using (3.12), the energies take the form

$$E_{m,n} = E_{ex} + \frac{\hbar^2 \xi_{m,n}^2}{2M_{ex} R^2}. \quad (3.18)$$

Due to the relatively high value of  $R$ , this can be approximated to:

$$E_{m,n} \simeq E_{ex}. \quad (3.19)$$

### 3.1.2 Empty cavity photon modes

The other part of the composite system in figure 3.1 is the empty cylindrical microcavity. This cavity harbours confined electromagnetic modes which must obey Maxwell's equations. As stated before, perfect confinement will be assumed as an approximation ('ideal cavity' approximation) which had been used by many authors, for example in Ref. [64]. A more elaborate treatment of photonic eigenmodes in a cylindrical microcavity considering a finite dielectric constant outside of the cavity (and, consequently, imperfect confinement of the fields inside it) has been presented in Ref. [65] using approximate decoupling of the degrees of freedom along and perpendicular to the  $z$  direction and the cavity modes are evaluated as a function of radius according to a self-consistent procedure. However, because we are interested in analytical solutions, we will stick to the 'ideal cavity' approximation, the validity of which is studied in appendix B, where the field profiles as well as the eigenfrequencies are compared with the exact solution, in the case of a very long cylinder ( $L \rightarrow \infty$ ). To determine these modes one must solve the Helmholtz equation in cylindrical coordinates:

$$\nabla^2 \mathbf{E} - k^2 \mathbf{E} = 0. \quad (3.20)$$

The method to find solutions will be to start by solving the  $z$  component of the equation:

$$\nabla^2 E_z = k^2 E_z. \quad (3.21)$$

This equation can be separated in the same way as in the solution to (3.1), with the addition of the  $z$  part, yielding:

$$\left( r \frac{\partial \mathcal{R}(r)}{\partial r} + r^2 \frac{\partial^2 \mathcal{R}(r)}{\partial r^2} \right) \frac{1}{\mathcal{R}(r)} + \frac{\partial^2 \Phi(\phi)}{\partial \phi^2} \frac{1}{\Phi(\phi)} + \frac{\partial^2 \mathcal{Z}(z)}{\partial z^2} \frac{r^2}{\mathcal{Z}(z)} + k^2 r^2 = 0, \quad (3.22)$$

with

$$E_z = E_0 \mathcal{R}(r) \mathcal{Z}(z) \Phi(\phi). \quad (3.23)$$

This leads to the same development of the previous section, except now we also have

$$\frac{\partial^2 \mathcal{Z}(z)}{\partial z^2} \frac{1}{\mathcal{Z}(z)} = -k_z^2, \quad (3.24)$$

leading to a solution of the form:

$$E_z = E_0 J_\mu(q_{\mu,\nu} r) (A e^{ik_z z} + B e^{-ik_z z}) e^{i(\mu\phi - \omega t)}, \quad (3.25)$$

where  $k^2 - k_z^2 = q_{\mu,\nu}^2$  and  $q_{\mu,\nu} = \frac{\xi_{\mu,\nu}}{R}$ . Now, Farady law and Ampère's law can be written for the transverse components:

$$-\frac{i\omega\epsilon}{c} \begin{pmatrix} E_r \\ E_\phi \end{pmatrix} = \begin{pmatrix} \frac{1}{r} \frac{\partial H_z}{\partial \phi} - \frac{\partial H_\phi}{\partial z} \\ \frac{\partial H_r}{\partial z} - \frac{\partial H_z}{\partial r} \end{pmatrix}, \quad (3.26)$$

$$\frac{i\omega}{c} \begin{pmatrix} H_r \\ H_\phi \end{pmatrix} = \begin{pmatrix} \frac{1}{r} \frac{\partial E_z}{\partial \phi} - \frac{\partial E_\phi}{\partial z} \\ \frac{\partial E_r}{\partial z} - \frac{\partial E_z}{\partial r} \end{pmatrix}. \quad (3.27)$$

Plugging (3.25) into the equations for the transverse components of  $\mathbf{H}$  (3.27):

$$\begin{pmatrix} H_r \\ H_\phi \end{pmatrix} = \frac{c}{i\omega} \begin{pmatrix} i\mu E_0 \frac{J_\mu(q_{\mu,\nu} r)}{r} (A e^{ik_z z} + B e^{-ik_z z}) e^{i\mu\phi} - \frac{\partial E_\phi}{\partial z} \\ \frac{\partial E_r}{\partial z} - E_0 q_{\mu,\nu} J'_\mu(q_{\mu,\nu} r) (A e^{ik_z z} + B e^{-ik_z z}) e^{i\mu\phi} \end{pmatrix}. \quad (3.28)$$

$J'(q_{\mu,\nu} r)$  denotes the derivative of the Bessel function with respect to its argument. Now, we will limit our scope to those solutions which are TM modes ( $H_z = 0$ ). This allows us to solve for the transverse components of  $\mathbf{E}$  (3.26) by plugging the results in (3.28) along with  $H_z = 0$ , yielding:

$$-\frac{i\omega^2\epsilon}{c^2} \begin{pmatrix} E_r \\ E_\phi \end{pmatrix} = \begin{pmatrix} i \frac{\partial^2 E_r}{\partial z^2} + E_0 k_z q_{\mu,\nu} J'_\mu(q_{\mu,\nu} r) (A e^{ik_z z} - B e^{-ik_z z}) e^{i\mu\phi} \\ i\mu E_0 k_z \frac{J_\mu(q_{\mu,\nu} r)}{r} (A e^{ik_z z} - B e^{-ik_z z}) e^{i\mu\phi} + i \frac{\partial^2 E_\phi}{\partial z^2} \end{pmatrix} \quad (3.29)$$

Now, in order for these to be self-consistent, the second derivatives in  $z$  of each of the components must match the component itself and the term  $A e^{ik_z z} - B e^{-ik_z z}$ . As such, this term must be the  $z$  dependence of these components. Applying this information and  $k^2 = \frac{\omega^2\epsilon}{c^2}$  the equations become:

$$(-ik^2 + ik_z^2) \begin{pmatrix} E_r \\ E_\phi \end{pmatrix} = \begin{pmatrix} E_0 k_z q_{\mu,\nu} J'_\mu(q_{\mu,\nu} r) (A e^{ik_z z} - B e^{-ik_z z}) e^{i\mu\phi} \\ i\mu E_0 k_z \frac{J_\mu(q_{\mu,\nu} r)}{r} (A e^{ik_z z} - B e^{-ik_z z}) e^{i\mu\phi} \end{pmatrix}. \quad (3.30)$$

Application of boundary conditions (2.159)-(2.160) at  $z = L/2$  and  $z = -L/2$  can now lead to:

$$\begin{cases} A e^{ik_z L} = B \\ A e^{-ik_z L} = B \end{cases}, \quad (3.31)$$

which means:

$$\begin{cases} e^{2ik_z L} = 1 \\ A = B \end{cases}. \quad (3.32)$$

With this, we conclude that the  $z$  dependence on these components is a sine wave because  $A = B$  and  $k_z = l\frac{\pi}{L}$  with  $l = 1, 2, 3, \dots$ . For reasons of convenience that will become clear in the section about exciton-polaritons, the shift  $z \rightarrow z - \frac{L}{2}$  will be introduced. Taking into account as well that  $k_z^2 - k^2 = -q_{\mu,\nu}^2$ , the components become:

$$\begin{pmatrix} E_r \\ E_\phi \end{pmatrix} = \begin{pmatrix} -\frac{k_z}{q_{\mu,\nu}} J'_\mu(q_{\mu,\nu}r) \\ -i\mu \frac{k_z}{q_{\mu,\nu}^2} \frac{J_\mu(q_{\mu,\nu}r)}{r} \end{pmatrix} E_0 \sin(k_z(z - L/2)) e^{i\mu\phi}. \quad (3.33)$$

Knowing the sine function is odd, we can express this as:

$$\begin{pmatrix} E_r \\ E_\phi \end{pmatrix} = \begin{pmatrix} \frac{k_z}{q_{\mu,\nu}} J'_\mu(q_{\mu,\nu}r) \\ i\mu \frac{k_z}{q_{\mu,\nu}^2} \frac{J_\mu(q_{\mu,\nu}r)}{r} \end{pmatrix} E_0 \sin(k_z(L/2 - z)) e^{i\mu\phi}. \quad (3.34)$$

Now it is necessary to return to equations (3.28) and plug the results from (3.34), along with the shift in  $z$ , which yields:

$$\begin{pmatrix} H_r \\ H_\phi \end{pmatrix} = \frac{c}{i\omega} \begin{pmatrix} i\mu \frac{J_\mu(q_{\mu,\nu}r)}{r} + i\mu \frac{k_z^2}{q_{\mu,\nu}^2} \frac{J_\mu(q_{\mu,\nu}r)}{r} \\ -\frac{k_z^2}{q_{\mu,\nu}} J'_\mu(q_{\mu,\nu}r) - q_{\mu,\nu} J'_\mu(q_{\mu,\nu}r) \end{pmatrix} E_0 \cos(k_z(L/2 - z)) e^{i\mu\phi}. \quad (3.35)$$

Now it is possible to use  $k_z^2 = \frac{\omega^2\epsilon}{c^2} - q_{\mu,\nu}^2$  in both equations to obtain:

$$\begin{pmatrix} H_r \\ H_\phi \end{pmatrix} = \begin{pmatrix} \mu \frac{\omega\epsilon}{cq_{\mu,\nu}^2} \frac{J_\mu(q_{\mu,\nu}r)}{r} \\ i\epsilon \frac{\omega}{cq_{\mu,\nu}} J'_\mu(q_{\mu,\nu}r) \end{pmatrix} E_0 \cos(k_z(L/2 - z)) e^{i\mu\phi}. \quad (3.36)$$

As such, the full EM fields (3.25),(3.34),(3.36) have been calculated and can be written as

$$E_z(r, \phi, z, \omega) = E_0 J_\mu(q_{\mu,\nu}r) \cos(k_z(L/2 - z)) e^{i(\mu\phi - \omega t)}, \quad (3.37)$$

$$E_r(r, \phi, z, \omega) = E_0 \frac{k_z}{q_{\mu,\nu}} J'_\mu(q_{\mu,\nu}r) \sin(k_z(L/2 - z)) e^{i(\mu\phi - \omega t)}, \quad (3.38)$$

$$E_\phi(r, \phi, z, \omega) = i\mu E_0 \frac{k_z}{q_{\mu,\nu}^2} \frac{J_\mu(q_{\mu,\nu}r)}{r} \sin(k_z(L/2 - z)) e^{i(\mu\phi - \omega t)}, \quad (3.39)$$

$$H_r(r, \phi, z, \omega) = \mu E_0 \frac{\omega\epsilon}{cq_{\mu,\nu}^2} \frac{J_\mu(q_{\mu,\nu}r)}{r} \cos(k_z(L/2 - z)) e^{i(\mu\phi - \omega t)} \quad (3.40)$$

$$H_\phi(r, \phi, z, \omega) = iE_0 \frac{\omega\epsilon}{cq_{\mu,\nu}} J'_\mu(q_{\mu,\nu}r) \cos(k_z(L/2 - z)) e^{i(\mu\phi - \omega t)}, \quad (3.41)$$

where:

$$\begin{cases} k_z = \pi l/L, & l = 1, 2, 3, \dots \\ q_{\mu,\nu} = \xi_{\mu,\nu}/R, \\ k^2 = \frac{\omega^2\epsilon}{c^2} = k_z^2 + q_{\mu,\nu}^2. \end{cases} \quad (3.42)$$

$\xi_{\mu,\nu}$  is the zero number  $n$  of the Bessel function  $J_{mu}$ . The eigenfrequencies are thus given by the formula:

$$\omega(\mu, \nu, k_z) = \frac{c}{\sqrt{\epsilon}} \sqrt{k_z^2 + q_{\mu,\nu}^2}. \quad (3.43)$$

For  $L \rightarrow \infty$  (a waveguide),  $k_z$  can be arbitrary, while for a cavity with perfectly reflecting bases  $k_z = \pi l/L$  ( $l = 1, 2, 3, \dots$ ). In order to completely characterize a single photon inside the empty microcavity,  $E_0$  must be calculated. The EM energy of this photon will be [3]:

$$\hbar\omega = \frac{1}{4\pi} \int d^3r (\epsilon \mathbf{E} \cdot \mathbf{E}^* + \mathbf{H} \cdot \mathbf{H}^*). \quad (3.44)$$

From this equation,  $E_0(\mu, \nu, k_z)$  can be expressed in a form analogous to that for a photon in vacuum as [3]:

$$E_0(\mu, \nu, k_z) = \sqrt{\frac{2\pi\hbar\omega(\mu, \nu, k_z)}{\epsilon\Omega(\mu, \nu, k_z)}}, \quad (3.45)$$

where  $\Omega(\mu, \nu, k_z)$  is generally referred to as the 'mode volume' and corresponds to:

$$\Omega(\mu, \nu, k_z) = \frac{1}{2\epsilon} \int d^3r \left( \epsilon \frac{\mathbf{E} \cdot \mathbf{E}^*}{E_0^2} + \frac{\mathbf{H} \cdot \mathbf{H}^*}{E_0^2} \right). \quad (3.46)$$

Inserting the fields (3.37)-(3.88) and omitting all indexes this takes the form:

$$\begin{aligned} \Omega(\mu, \nu, k_z) = & \frac{1}{2\epsilon} \int_0^R \int_{-L/2}^{L/2} \int_0^{2\pi} \left[ \cos^2(k_z(L/2 - z)) \left( \epsilon J^2(qr) + \mu^2 \frac{k_z^2 \epsilon}{q^4} \frac{J^2(qr)}{r^2} + \frac{k_z^2 \epsilon}{q^2} J'(qr)^2 \right) + \right. \\ & \left. \epsilon \sin^2(k_z(L/2 - z)) \left( \frac{k_z^2}{q^2} J'(qr)^2 + \mu^2 \frac{k_z^2}{q^4} \frac{J^2(qr)}{r^2} \right) \right] rd\phi dz dr. \end{aligned} \quad (3.47)$$

The integral in  $\phi$  is simply  $2\pi$  and the integrals in  $z$  are:

$$\begin{aligned} \int_{-L/2}^{L/2} \cos^2(k_z(L/2 - z)) dz &= \int_{-L/2}^{L/2} \frac{1 + \cos(k_z(L - 2z))}{2} dz = L/2 - \frac{\sin(k_z(L - 2z))}{4k_z} \Big|_{-L/2}^{L/2} \\ &= L/2 + \frac{\sin(2k_z L)}{4k_z} \end{aligned} \quad (3.48)$$

and

$$\begin{aligned} \int_{-L/2}^{L/2} \sin^2(k_z(L/2 - z)) dz &= \int_{-L/2}^{L/2} \frac{1 - \cos(k_z(L - 2z))}{2} dz = L/2 + \frac{\sin(k_z(L - 2z))}{4k_z} \Big|_{-L/2}^{L/2} \\ &= L/2 - \frac{\sin(2k_z L)}{4k_z} \end{aligned} \quad (3.49)$$

To simplify the writing, we will define

$$f_{(\pm)} = L/2 \pm \frac{\sin(2k_z L)}{4k_z}. \quad (3.50)$$

Finally, the integrals of  $J'(qr)^2 r$  can be modified by the use of integration by parts with  $v' = J'(qr)$  and  $u = J'(qr)r$ , which gives:

$$\int_0^R J'(qr)^2 r dr = \frac{1}{q^2} \int_0^{qR} J'(x)^2 x dx = \frac{1}{q^2} \left[ J'(x)J(x)x \Big|_0^{qR} - \int_0^{qR} J(x) (J''(x)x + J'(x)) dx \right]. \quad (3.51)$$

$q_{\mu, \nu} R = \xi_{\mu, \nu}$  which is a zero of the Bessel function. Also,

$$J''(x)x + J'(x) = \frac{\mu^2}{x} J(x) - xJ(x) \quad (3.52)$$

by Bessel's differential equation. Using these facts equation (3.51) becomes:

$$\int_0^R J'(qr)^2 r dr = -\frac{1}{q^2} \int_0^{qR} \left( \mu^2 \frac{J^2(x)}{x} - J^2(x)x \right) dx. \quad (3.53)$$

Inserting (3.48),(3.49) and (3.53) into equation (4.40), along with the integral in  $\phi$  being  $2\pi$ , yields

$$\Omega(\mu, \nu, k_z) = \frac{\pi}{q^2} \int_0^{qR} \left[ f_{(+)} \left( J^2(x)x + \mu^2 \frac{k^2}{q^2} \frac{J^2(x)}{x} - \frac{k^2}{q^2} \mu^2 \frac{J^2(x)}{x} + \frac{k^2}{q^2} J^2(x)x \right) + f_{(-)} \left( \frac{k_z^2}{q^2} J(x)^2 x - \frac{k_z^2 \mu^2}{q^2} \frac{J^2(x)}{x} + \mu^2 \frac{k_z^2}{q^2} \frac{J^2(x)}{x} \right) \right] dx, \quad (3.54)$$

where  $x = qr$ . This of course simplifies to

$$\Omega(\mu, \nu, k_z) = \frac{\pi}{q^2} \left( f_{(+)} \left( 1 + \frac{k^2}{q^2} \right) + f_{(-)} \frac{k_z^2}{q^2} \right) \int_0^{qR} J^2(x)x dx \quad (3.55)$$

The integral is the same as (3.15) in the previous section and the result is known [?]. It is also possible to simplify with  $k^2 = q^2 + k_z^2$  and obtain

$$\Omega(\mu, \nu, k_z) = \frac{\pi}{q^2} \left( f_{(+)} \left( 2 + \frac{k_z^2}{q^2} \right) + f_{(-)} \frac{k_z^2}{q^2} \right) q^2 \frac{R^2}{2} J'(qR)^2. \quad (3.56)$$

$$\Omega(\mu, \nu, k_z) = \pi \left( f_{(+)} \left( 2 + \frac{R^2 k_z^2}{\xi_{\mu, \nu}^2} \right) + f_{(-)} \frac{R^2 k_z^2}{\xi_{\mu, \nu}^2} \right) \frac{R^2}{2} J'(\xi_{\mu, \nu})^2. \quad (3.57)$$

This is the analytical form of the mode volume for a general  $k_z$ . Considering perfectly reflecting boundaries at  $z = \pm L/2$  the condition  $k_z = \frac{\pi l}{L}$  applies and this becomes:

$$\Omega(\mu, \nu, l) = \frac{\pi R^2 L}{2} \left[ 1 + \frac{\pi^2 l^2 R^2}{\xi_{\mu, \nu}^2 L^2} \right] J'(\xi_{\mu, \nu})^2. \quad (3.58)$$

Figure 3.2 depicts this mode volume for two different values of  $\mu$  and for  $l = 1$  as a function of the discrete values of energy  $\hbar\omega(\mu, \nu, 1)$  corresponding to the different modes (values of  $\nu$ ).

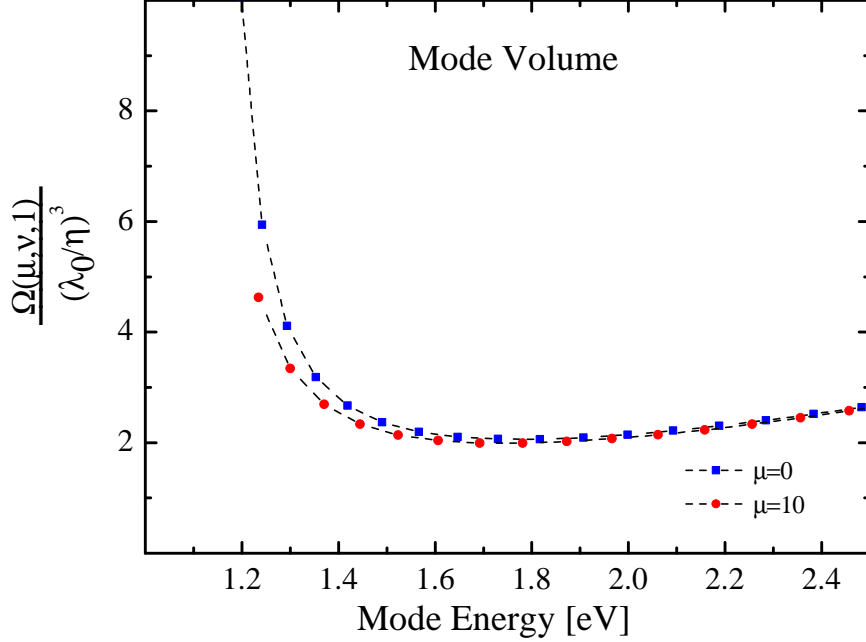


Figure 3.2: Mode volume (3.58) as a function of the energies of the modes for  $\mu = 0, 10$ . It is clear that for higher energy modes the angular momentum number  $\mu$  does not influence the mode volume as much as for lower energy modes. The cylinder radius is  $R = 3 \mu\text{m}$  and height  $L = 0.3 \mu\text{m}$ . Furthermore, these values are much smaller than for a planar cavity due to the field confinement in all directions.

### 3.1.3 Susceptibility and optical conductivity

The exciton-photon interaction can be modelled with the dipole approximation. This corresponds to assuming a potential of interaction of the form:

$$V_{int} = -(\mathbf{d}_{\mathbf{CV}} \cdot \mathbf{E}), \quad (3.59)$$

where  $\mathbf{d}_{\mathbf{CV}}$  is the dipole matrix element between the valence and conduction bands [66] and  $\mathbf{E}$  is the electric field associated with the empty cavity photon, whose constant is determined by equations (3.45) and (3.58). Assuming the most realistic case of having the dipole moment in the plane of the semiconductor material, we can write the basis of circular polarization:

$$\begin{cases} \mathbf{d}_{\mathbf{CV}} = \frac{d_{CV}}{\sqrt{2}} (\hat{x} \pm i\hat{y}); \\ d_{CV} = \frac{v_F \hbar e}{E_{ex}}. \end{cases} \quad (3.60)$$

The dipole moment  $d_{CV}$  is written in terms of the Fermi velocity  $v_F$  and the energy of the exciton level that is being considered.  $\pm$  apply to the  $K$  and  $K'$  points of the Brillouin zone [67]. This dipole moments



can be written in terms of the polar coordinates basis vectors  $\hat{r}$  and  $\hat{\phi}$ . Knowing that [?]

$$\begin{cases} \hat{x} = \hat{r} \cos(\phi) - \hat{\phi} \sin(\phi) \\ \hat{y} = \hat{r} \sin(\phi) + \hat{\phi} \cos(\phi) \end{cases} \quad (3.61)$$

$\mathbf{d}_{\mathbf{CV}}$  becomes

$$\mathbf{d}_{\mathbf{CV}} = \frac{d_{CV}}{\sqrt{2}} \left( \hat{r}(\cos(\phi) \pm i \sin(\phi)) + \hat{\phi}(-\sin(\phi) \pm i \cos(\phi)) \right) \quad (3.62)$$

$$\mathbf{d}_{\mathbf{CV}} = \frac{d_{CV}}{\sqrt{2}} e^{\pm i\phi} \left( \hat{r} \pm i\hat{\phi} \right) \quad (3.63)$$

The potential energy (3.59) is the operator that governs the transition from a vacuum state to the state corresponding to one exciton of angular momentum  $m$  and radial number  $n$  at the cost of one photon of angular momentum  $\mu$ , radial number  $n$  and  $z$  wavenumber  $k_z$ . This transition matrix element is then:

$$\mathcal{M}(\mu, \nu; m, n) = \langle m, n | -\mathbf{d}_{\mathbf{CV}} \cdot \mathbf{E}(\mu, \nu, k_z) | 0 \rangle. \quad (3.64)$$

$|0\rangle$  is the [68] state of excitonic vacuum which can be written as

$$|0\rangle = \delta(\mathbf{r}_e - \mathbf{r}_h), \quad (3.65)$$

where  $\mathbf{r}_e$  is the position of the electron and  $\mathbf{r}_h$  the position of the hole left by it on the valence band of the 2D TMD disk (see Fig. 3.1). The excitonic state  $|m, n\rangle$  can be written as:

$$|m, n\rangle = \Phi(\mathbf{r}_e - \mathbf{r}_h) \Psi_{m,n}(\mathbf{r}). \quad (3.66)$$

Here,  $\Phi(\vec{r}_e - \vec{r}_h)$  is the part of the excitonic wavefunction that represents its internal structure. Its magnitude in the origin can be evaluated using the hydrogen-like model [69] †

$$|\Phi(0)|^2 = \frac{2}{\pi a_{exc}^2}. \quad (3.67)$$

$\Psi_{m,n}(\mathbf{r})$  is the part of the wavefunction corresponding to the movement of the centre of mass of the exciton. This is given by equation (3.13). One can now use (3.63) and the electric fields given by (3.25) and (3.34) together with (3.58) to obtain:

$$\begin{aligned} (\mathbf{d}_{\mathbf{CV}} \cdot \mathbf{E}(\mu, \nu, k_z))|_{z=0} = \\ \frac{E_0(\mu, \nu, k_z) d_{CV}}{\sqrt{2}} \frac{k_z}{q_{\mu, \nu}} \sin(k_z L/2) e^{i(\mu \pm 1)\phi} \left( \hat{r} \pm i\hat{\phi} \right) \cdot \left( J'_\mu(q_{\mu, \nu} r) \hat{r} + i\mu \frac{J_\mu(q_{\mu, \nu} r)}{q_{\mu, \nu} r} \hat{\phi} \right) \end{aligned} \quad (3.68)$$

with  $E_0(\mu, \nu, k_z)$  given by (3.45) and (3.58). Thus,

$$(\mathbf{d}_{\mathbf{CV}} \cdot \mathbf{E}(\mu, \nu, k_z))|_{z=0} = \frac{E_0(\mu, \nu, k_z)}{\sqrt{2}} \frac{k_z}{q_{\mu, \nu}} d_{CV} \sin(k_z L/2) e^{i(\mu \pm 1)\phi} \left( J'_\mu(q_{\mu, \nu} r) \mp \mu \frac{J_\mu(q_{\mu, \nu} r)}{q_{\mu, \nu} r} \right). \quad (3.69)$$

† Excitons in TMDs are described by the electrostatic electron and hole interaction of  $V(\rho) = \pi e^2 r_0^{-1} [\mathcal{H}_0(\rho/r_0) - N_0(\rho/r_0)]$ , where  $H_0(x)$  and  $N_0(x)$  are the Struve and Neuman functions, respectively,  $\rho = |(\vec{r}_e - \vec{r}_h)|$  and  $r_0$  takes into account the non-local screened attractive interaction of two charges in the slab [68, 70]. Using the 2D effective mass approximation, this potential provides a non-hydrogenic Rydberg series for the exciton energies in correspondence with experimental results. [71] For the evaluation of Eq. (??) it is useful to approximate the exciton in the 2D TMD by a modified 2D Wannier-Mott model where the exciton Bohr radius for each state  $n$ , is chosen to fit the exciton energy values obtained from experiment, such that  $a_{exc} \mapsto a_n$ . [72]

Note that the Bessel function recurrence relations state

$$J'_\mu(x) \mp \mu \frac{J_\mu(x)}{x} = \mp J_{\mu\pm 1}(x) \quad (3.70)$$

Now we can use this and sum over the two possible polarizations,  $\pm$ , and write the total interaction potential as:

$$(\mathbf{d}_{\mathbf{CV}} \cdot \mathbf{E}(\mu, \nu, k_z))|_{z=0} = \frac{E_0(\mu, \nu, k_z)}{\sqrt{2}} \frac{k_z}{q_{\mu, \nu}} d_{CV} \sin(k_z L/2) \left( e^{i(\mu-1)\phi} J_{\mu-1}(q_{\mu, \nu} r) - e^{i(\mu+1)\phi} J_{\mu+1}(q_{\mu, \nu} r) \right). \quad (3.71)$$

With this we can go back to the equation for the matrix element we were looking for (3.64):

$$\mathcal{M}(\mu, \nu; m, n) = \frac{E_0(\mu, \nu, k_z)}{\sqrt{2}} \frac{k_z}{q_{\mu, \nu}} d_{CV} \sin(k_z L/2) \int_{\mathbf{r}_e - \mathbf{r}_h} \int_{\mathbf{r}} \delta(\mathbf{r}_e - \mathbf{r}_h) \Phi(\mathbf{r}_e - \mathbf{r}_h) \Psi_{m, n}(\mathbf{r}) \left( e^{i(\mu+1)\phi} J_{\mu+1}(q_{\mu, \nu} r) - e^{i(\mu-1)\phi} J_{\mu-1}(q_{\mu, \nu} r) \right) d(\mathbf{r}_e - \mathbf{r}_h) d\mathbf{r} \quad (3.72)$$

$$\mathcal{M}(\mu, \nu; m, n) = \frac{E_0(\mu, \nu, k_z)}{\sqrt{2}} \frac{k_z}{q_{\mu, \nu}} d_{CV} \sin(k_z L/2) \int_0^R \int_0^{2\pi} \Phi(0) \Psi_{m, n}(\mathbf{r}) \left( e^{i(\mu+1)\phi} J_{\mu+1}(q_{\mu, \nu} r) - e^{i(\mu-1)\phi} J_{\mu-1}(q_{\mu, \nu} r) \right) r dr d\phi \quad (3.73)$$

Now using the wavefunction of the exciton's centre of mass (3.13) we get

$$\mathcal{M}(\mu, \nu; m, n) = \Phi(0) \frac{E_0(\mu, \nu, k_z)}{\sqrt{2}} \frac{k_z}{q_{\mu, \nu}} d_{CV} \sin(k_z L/2) \int_0^R \int_0^{2\pi} \frac{1}{\sqrt{\pi} R |J'_m(\xi_{m, n})|} J_m(q_{m, n} r) \left( e^{i(m+\mu+1)\phi} J_{\mu+1}(q_{\mu, \nu} r) - e^{i(m+\mu-1)\phi} J_{\mu-1}(q_{\mu, \nu} r) \right) r dr d\phi \quad (3.74)$$

This simplifies to

$$\mathcal{M}(\mu, \nu; m, n) = d_{CV} \Phi(0) \frac{E_0(\mu, \nu, k_z)}{\sqrt{2\pi}} k_z \pi R^2 \sin(k_z L/2) I_{\mu, \nu; m, n} (\delta_{\mu+1, m} - \delta_{\mu-1, m}) \quad (3.75)$$

$I_{\mu, \nu; m, n}$  are coefficients defined by:

$$I_{\mu, \nu; m, n} = \frac{2}{\xi_{\mu, \nu} |J'_m(\xi_{m, n})|} \int_0^1 x J_m(\xi_{m, n} x) J_m(\xi_{\mu, \nu} x) dx. \quad (3.76)$$

The presence of  $\sin(k_z L/2)$  means that, for a perfectly confined cavity, only modes which are odd with respect to  $E_z$  (with the number  $l$  odd in  $k_z = \pi l/L$ ) can couple to the exciton. Angular momentum conservation is expressed by the kronecker symbols in (3.75). They guarantee that a transition is only possible if the resulting exciton has the spin of the photon absorbed (which is positive for left circular polarization and negative for right circular polarization) added to its angular momentum. The susceptibility tensor will have two equal components ( $xx$  and  $yy$ ) and no  $zz$  component because the dipole moment vector lies in the  $xy$  plane. It is convenient to consider two-dimensional (sheet) susceptibility defined as the dipole moment per unit area per unit field. The component that we want to calculate can be obtained using second order perturbation theory similar to the derivation of the atomic polarizability [73]. The energy of the semiconductor disk polarized by an electromagnetic mode  $(\mu, \nu, k_z)$  is:

$$E = \frac{1}{2} \chi_{2D} \int_{disk} (\mathbf{E}_\perp \cdot \mathbf{E}_\perp^*)|_{z=0} d\mathbf{r} = \sum_{m, n} \frac{|\mathcal{M}(\mu, \nu; m, n)|^2}{E_{m, n} - \hbar\omega}, \quad (3.77)$$

where  $\mathbf{E}_\perp$  refers to the in-plane components of the electric field (3.85) and (3.86). Notice this integral has been solved before as part of the mode volume calculation (3.58). It corresponds to the factor of  $f_{(-)}$  and as such its result is the same, removing the factor  $\frac{1}{2}f_{(-)}$ :

$$\int_{disk} (\mathbf{E}_\perp \cdot \mathbf{E}_\perp^*)|_{z=0} d\mathbf{r} = \frac{\epsilon\pi R^4 k_z^2}{2\xi_{\mu,\nu}^2} J_\mu'(\xi_{\mu,\nu})^2 \quad (3.78)$$

Solving equation (3.77) for the susceptibility thus yields

$$\chi_{2D} = \frac{2}{\pi R^2 B_{\mu,\nu,k_z}} \sum_{m,n} \frac{|\mathcal{M}(\mu,\nu,m,n)|^2}{E_{m,n} - \hbar\omega}, \quad (3.79)$$

where

$$B_{\mu,\nu,k_z} = |E_0(\mu,\nu,k_z)|^2 \left(\frac{k_z R}{\xi_{\mu,\nu}}\right)^2 [J_\mu'(\xi_{\mu,\nu} R)]^2. \quad (3.80)$$

From Green's function formalism, there would follow a non-resonant term [74] which is obtained by replacing  $\omega \rightarrow -\omega$ . Substitution of (3.75) yields:

$$\chi_{2D}(\omega; \mu, \nu) = \frac{|d_{CV}\Phi(0)|^2 \xi_{\mu,\nu}^2}{[J_\mu'(\xi_{\mu,\nu} R)]^2} \sum_{m,n} \frac{|I_{\mu,\nu;m,n}|^2}{E_{m,n} - \hbar\omega - i\delta} (\delta_{\mu+1,m} + \delta_{\mu-1,m}), \quad (3.81)$$

where a small imaginary part  $i\delta$  is added to avoid the singularity. In this equation we assume only one type of exciton with energy  $E_{m,n}$  that can be approximated to  $E_{ex}$  (3.19). Spin-orbit interaction in TMDs results in two types of excitons, A and B, with a splitting of 100-200 meV [33]. To consider these two types one would simply need to sum the contribution of the other type. However, the calculations done will be limited to the type A of energy  $E_{ex} = 1.9$  eV. The next section will apply the optical conductivity in Maxwell's boundary conditions. The optical conductivity is

$$\sigma_{2D}(\omega; \mu, \nu) = -i\omega\chi_{2D}(\omega; \mu, \nu). \quad (3.82)$$

## 3.2 Microcavity exciton-polaritons

### 3.2.1 Semiclassical theory

In order to determine the allowed states, given this interaction, it is necessary to plug in the following boundary conditions [5]

$$\begin{cases} H_r^+ - H_r^- = \frac{4\pi}{c} \sigma_{2D}(\omega; \mu, \nu) E_\phi|_{z=0} \\ H_\phi^+ - H_\phi^- = -\frac{4\pi}{c} \sigma_{2D}(\omega; \mu, \nu) E_r|_{z=0}. \end{cases} \quad (3.83)$$

Here the  $+(-)$  sign stands for the fields at  $z \geq 0$  ( $z \leq 0$ ). We write the fields above and below the TMD layer in the form:

$$E_z^\pm(r, \phi, z, \omega) = \pm E_0 J_\mu(q_{\mu,\nu} r) \cos\left[k_z(\omega)\left(\frac{L}{2} \mp z\right)\right] e^{i(\mu\phi - \omega t)}. \quad (3.84)$$

This is the reason for the shift  $z \rightarrow z - L/2$  in the last section. In this way, we can introduce the discontinuity needed to obey (3.83) and compare these modes to the corresponding empty cavity modes (3.37). Using (3.84) and looking at (3.85)-(3.88), the rest of the EM fields will become

$$E_r^\pm(r, \phi, z, \omega) = E_0 \frac{k_z}{q_{\mu,\nu}} J_\mu'(q_{\mu,\nu} r) \sin(k_z(L/2 \mp z)) e^{i(\mu\phi - \omega t)}, \quad (3.85)$$

$$E_{\phi}^{\pm}(r, \phi, z, \omega) = i\mu E_0 \frac{k_z}{q_{\mu, \nu}^2} \frac{J_{\mu}(q_{\mu, \nu} r)}{r} \sin(k_z(L/2 \mp z)) e^{i(\mu\phi - \omega t)}, \quad (3.86)$$

$$H_r^{\pm}(r, \phi, z, \omega) = \pm \mu E_0 \frac{\omega \epsilon}{c q_{\mu, \nu}^2} \frac{J_{\mu}(q_{\mu, \nu} r)}{r} \cos(k_z(L/2 \mp z)) e^{i(\mu\phi - \omega t)} \quad (3.87)$$

$$H_{\phi}^{\pm}(r, \phi, z, \omega) = \pm i E_0 \frac{\omega \epsilon}{c q_{\mu, \nu}} J'_{\mu}(q_{\mu, \nu} r) \cos(k_z(L/2 \mp z)) e^{i(\mu\phi - \omega t)}, \quad (3.88)$$

Equations (3.83) can thus be written as

$$2\mu E_0 \frac{\omega \epsilon}{c q_{\mu, \nu}^2} \cos(k_z L/2) = \frac{4\pi}{c} \sigma_{2D}(\omega; \mu, \nu) i\mu E_0 \frac{k_z}{q_{\mu, \nu}^2} \sin(k_z L/2) \quad (3.89)$$

$$2i E_0 \frac{\omega \epsilon}{c q_{\mu, \nu}} \cos(k_z L/2) = -\frac{4\pi}{c} \sigma_{2D}(\omega; \mu, \nu) E_0 \frac{k_z}{q_{\mu, \nu}} \sin(k_z L/2) \quad (3.90)$$

Note that modes for this system must have  $k_z \neq \pi l/L$  for if the  $k_z$  were the same as for the empty cavity these boundary conditions would not hold. Both these equations yield

$$2\pi \sigma_{2D}(\omega; \mu, \nu) k_z \tan(k_z \frac{L}{2}) = -i\omega \epsilon. \quad (3.91)$$

This equation is the polariton dispersion relation and, together with equation (3.43), permits to obtain the allowed values of  $k_z$  (they are, of course, different from those of the empty cavity, but will be labelled by the same index  $l$ ) and the corresponding  $\omega$  for each pair of quantum numbers  $\mu$  and  $\nu$

$$\omega(\mu, \nu, l) = \frac{c}{\sqrt{\epsilon}} \sqrt{k_z^2(\mu, \nu, l) + \left(\frac{\xi_{\mu, \nu}}{R}\right)^2}. \quad (3.92)$$

The polariton "dispersion curves" for two angular momentum values are shown in Fig. 3.3, which presents the eigenfrequencies calculated by Eqs. (3.91) and (3.92) *versus* the radial index,  $\nu$ , for the lowest  $k_z$  ( $l = 1$ ).

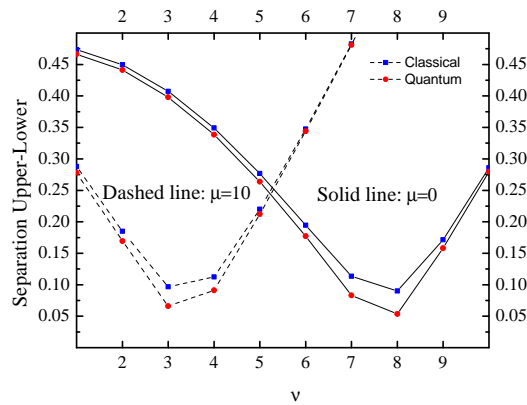


Figure 3.4: (Color online) Separations between the upper and lower polariton modes calculated within the classical picture, corresponding to Fig. 3.3 (red balls) and using the quantum formalism (blue squares), for  $\mu = 0$  (connected by solid lines) and 10 (connected by dashed lines). The parameters are the same as in Fig. 3.3.

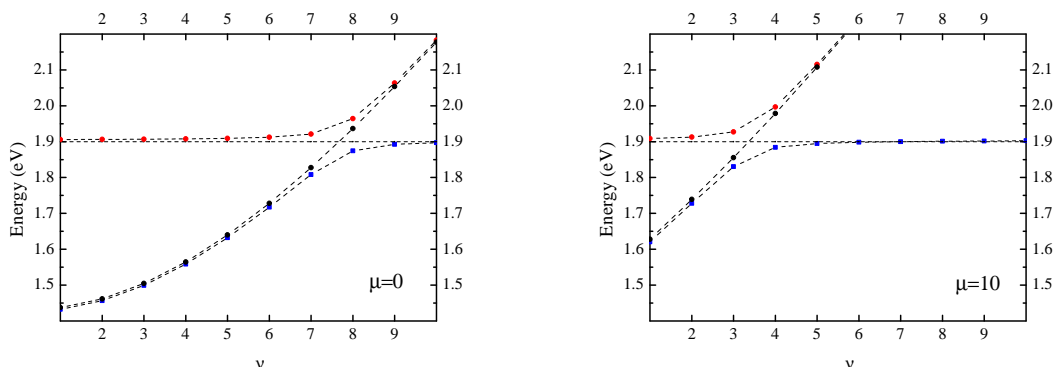


Figure 3.3: (Color online) Uncoupled exciton (dashed line), MC photon (dashed line with black balls) and polariton dispersion curves for  $\mu = 0$  and 10 (red balls and blue squares, respectively). The radial index takes only integer values but the points are connected to improve visibility. The parameters are: cylinder radius  $R = 2 \mu\text{m}$ , height  $L = 0.235 \mu\text{m}$ , dielectric constant of the MC material  $\epsilon = 3.4$ , Fermi velocity  $v_F = 5.5 \times 10^5 \text{ m/s}$ , exciton energy  $E_{ex} = 1.9 \text{ eV}$ , and Bohr radius  $a_{ex} = 0.8 \text{ nm}$ .

### 3.2.2 Quantum picture

Quantum-mechanical interaction between two bosonic fields can be considered by applying a unitary transformation proposed by Hopfield. As in Ref. [49], we denote by  $P_{(\dots)}$  ( $P_{(\dots)}^\dagger$ ) and  $A_{(\dots)}$  ( $A_{(\dots)}^\dagger$ ) the annihilation (creation) operators for photons and excitons, respectively, where  $(\dots)$  stands for the appropriate quantum numbers. The interaction term in the Hamiltonian is a sum over all these quantum numbers, with the interaction constant, in our case, equal to the matrix element (3.75). In a Fabry-Perot MC, the in-plane quantum numbers are replaced by  $m, n \rightarrow \vec{q}$  for excitons and  $\mu, \nu \rightarrow \vec{k}$  for photons. Because of the uniformity of the system in any direction perpendicular to  $z$ , the interaction matrix element in a planar microcavity contains the Kronecker symbol  $\delta_{\vec{k}, \vec{q}}$ . By virtue of this, the Hamiltonian of interacting excitons and MC photons, in the Fabry-Perot case reduces to the form [49]  $\hat{H} = \sum_{\vec{q}} \hat{H}_{\vec{q}}$  with

$$\hat{H}_{\vec{q}} = \hbar\omega(\vec{q})P_{\vec{q}}^\dagger P_{\vec{q}} + E_{ex}(\vec{q})A_{\vec{q}}^\dagger A_{\vec{q}} + g(\vec{q})P_{\vec{q}}^\dagger A_{\vec{q}} + \text{H.C.}, \quad (3.93)$$

where  $g(\vec{q})$  is the coupling constant for the cavity mode  $\vec{q}$  (for a certain  $l$ ). Therefore, the Hopfield transformation can be applied to diagonalize this Hamiltonian, for each  $\vec{q}$  separately.

Now, for the case of cylindrical cavity, the coupling constant (for a certain  $k_z$ ),  $g(\mu, \nu, k_z; m, n)$  is given by equation (3.75) and we have only Kronecker deltas involving the quantum numbers  $m$  and  $\mu$  and there are no restrictions on  $\nu$  and  $n$ . If we include all possible combinations of  $\nu$  and  $n$  in the Hamiltonian, we will not be able to write down a tractable Hopfield transformation. And even if we include only forms with  $|\nu - n| = 0, \pm 1$  there will be seven Hopfield coefficients and the diagonalization will become impossible to perform analytically. We shall make the following (seemingly crude) approximation,  $n = \nu$ . In appendix C, the calculation of  $I_{\mu, \nu; m, n}$  from (3.76) is performed to show that for a given  $\nu$  it is biggest for  $n = \nu$ . Later, the dispersion relation resulting from this approximation will be compared to the classical dispersion relation obtained in the last chapter in figure 3.3, in which the sum was performed from  $n = 1$  to  $n = 200$ . The values of  $k_z$  here will be pertaining to the empty cavity system only. As

such, they are back to being  $k_z = \pi l/L$ . In the following we will consider the lowest branch with  $l = 1$ . We can write the Hamiltonian as

$$\hat{H} = \sum_{\mu,\nu} \left[ \hbar\omega(\mu,\nu) P_{\mu,\nu}^\dagger P_{\mu,\nu} + E_{ex} A_{\mu\pm 1,\nu}^\dagger A_{\mu\pm 1,\nu} + (g_{\mu,\nu}^\pm A_{\mu\pm 1,\nu}^\dagger P_{\mu,\nu} + \text{H.C.}) \right] \equiv \sum_{\mu,\nu} \hat{H}_{\mu,\nu}, \quad (3.94)$$

where

$$g_{\mu,\nu}^\pm = \pm d_{CV} \Phi(0) \frac{\pi S}{L\sqrt{2\pi}} \sqrt{\frac{2\pi\hbar\omega(\mu,\nu,k_z)}{\epsilon\Omega(\mu,\nu,k_z)}} I_{\mu,\nu;\mu\pm 1,\nu}.$$

If we diagonalize the Hamiltonian  $\hat{H}_{\mu,\nu}$  using a  $3 \times 3$  Hopfield transformation, it will take the form

$$\hat{H}_{\mu,\nu} = \sum_{i=1}^3 E_i(\mu,\nu) \alpha_{\mu,\nu}^{(i)\dagger} \alpha_{\mu,\nu}^{(i)}, \quad (3.95)$$

where  $E_i$  ( $i = 1 - 3$ ) are the energies of the three polaritonic branches and the new operators  $\alpha^{(i)}$  are linear combinations of the operators  $A$  and  $P$ :

$$\alpha_{\mu,\nu}^{(i)} = \kappa_+^{(i)}(\mu,\nu) A_{\mu+1,\nu} + \kappa_-^{(i)}(\mu,\nu) A_{\mu-1,\nu} + \kappa_{ph}^{(i)} P_{\mu,\nu}, \quad (i = 1 - 3). \quad (3.96)$$

In (3.96),  $\kappa$  are the Hopfield coefficients, they constitute the  $3 \times 3$  Hopfield transformation matrix and are obtained by the diagonalization procedure of the Hamiltonian  $\hat{H}_{\mu,\nu}$ . To diagonalize the Hamiltonian (3.94) we write it in matrix form

$$\hat{H}_{\mu,\nu} = \begin{pmatrix} A_{\mu+1,\nu}^\dagger & A_{\mu-1,\nu}^\dagger & P_{\mu,\nu}^\dagger \end{pmatrix} \begin{pmatrix} E_{ex} & 0 & g_{\mu,\nu}^+ \\ 0 & E_{ex} & g_{\mu,\nu}^- \\ (g_{\mu,\nu}^+)^\dagger & (g_{\mu,\nu}^-)^\dagger & \hbar\omega(\mu,\nu) \end{pmatrix} \begin{pmatrix} A_{\mu+1,\nu} \\ A_{\mu-1,\nu} \\ P_{\mu,\nu} \end{pmatrix} \quad (3.97)$$

The eigenvalues are

$$E_1(\mu,\nu) = E_{ex};$$

$$E_{2,3}(\mu,\nu) = \frac{E_{ex} + \hbar\omega(\mu,\nu)}{2} \pm \sqrt{\frac{[E_{ex} - \hbar\omega(\mu,\nu)]^2}{4} + |g^-(\mu,\nu)|^2 + |g^+(\mu,\nu)|^2}, \quad (3.98)$$

Now we want to obtain the Hopfield coefficients, which will be the elements of the eigenvectors of each of the modes with the energies in (3.98). The equations to determine the eigenvectors will be

$$\begin{pmatrix} E_{ex} - E_i & 0 & g_{\mu,\nu}^+ \\ 0 & E_{ex} - E_i & g_{\mu,\nu}^- \\ (g_{\mu,\nu}^+)^\dagger & (g_{\mu,\nu}^-)^\dagger & \hbar\omega(\mu,\nu) - E_i \end{pmatrix} \begin{pmatrix} \kappa_+^{(i)} \\ \kappa_-^{(i)} \\ \kappa_{ph}^{(i)} \end{pmatrix} = 0 \quad (3.99)$$

This yields the Hopfield coefficients, which can be normalized such that  $|\kappa_+^{(i)}|^2 + |\kappa_-^{(i)}|^2 + |\kappa_{ph}^{(i)}|^2 = 1$  (skipping the indices  $\mu$  and  $\nu$  for clarity):

$$|\kappa_{ph}^{(1)}|^2 = 0, \quad |\kappa_\pm^{(1)}|^2 = \frac{|g^\mp|^2}{|g^+|^2 + |g^-|^2};$$

$$|\kappa_{ph}^{(2,3)}|^2 = \frac{(E_{ex} - E_{2,3})^2}{(E_{ex} - E_{2,3})^2 + |g^+|^2 + |g^-|^2}, \quad |\kappa_\pm^{(2,3)}|^2 = \frac{|g^\pm|^2}{(E_{ex} - E_{2,3})^2 + |g^+|^2 + |g^-|^2}. \quad (3.100)$$

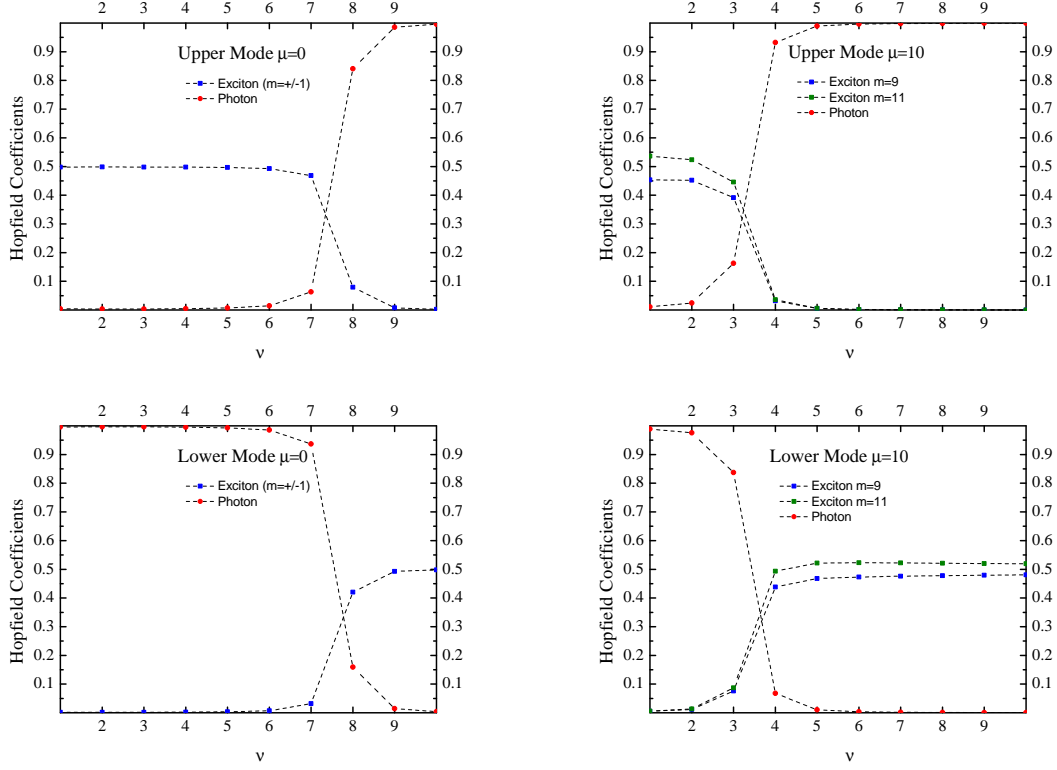


Figure 3.5: (Color online) Hopfield coefficients corresponding to the MC photon (red symbols and dash-lines) and two excitons ( $\mu \pm 1$ ) (green and blue symbols and dash-lines) for the upper and lower polariton modes with  $\mu = 0$  and 10. The parameters are the same as in Fig. 3.3.

As seen from Eqs. (3.98) and (3.100), the first mode is purely excitonic, while  $E_{2,3}(\mu, \nu)$  correspond to two polariton branches. As we can see from Fig. 3.4, the polariton eigenmode energies obtained within the reduced quantum model reproduce qualitatively quite well those calculated within the classical picture including all exciton-photon interactions, even though the former underestimates the separation between the upper and lower polariton branches. The minimum separation, i.e. the Rabi splitting is approximately equal to 100 mEv and almost independent of  $\mu$  (see Fig. 3.4). This is somewhat smaller than the value calculated for a TMD layer with the same parameters inserted in a planar MC [49] but closer to the experimentally measured values. [52]

The dependence of the Hopfield coefficients on  $\nu$  is shown in Fig. 3.5 for  $\mu = 0$  and 10. For  $\mu = 0$  the two Hopfield coefficients measuring the fraction of excitons with  $m = \pm 1$  are equal, while for  $\mu = 10$  the contributions of  $\mu = 9$  and  $\mu = 11$  are slightly different below the crossing point of the dispersion lines of the uncoupled photons and excitons.

### 3.3 Polariton Densities of States

#### 3.3.1 Total and Projected Densities of States

The angular momentum,  $\mu$ , still is a well-defined quantum number for polariton modes and, owing to our approximation, so is the radial number  $\nu$ . The density of polariton states (DOS) with a certain angular momentum  $\mu$  (and for the lowest  $k_z$ ) can be defined as

$$\rho^{(\mu)}(E) = \sum_{\nu, i} \delta(E_i(\mu, \nu) - E), \quad (3.101)$$

where  $i$  stands for the three polaritonic branches. The same definition (without sum over  $i$ ) can be used for purely photonic modes in empty cavity. It is interesting to compare the latter to the polariton DOS projected onto the photonic subspace, which is calculated by weighting each polariton mode by the corresponding (photon) Hopfield coefficient:

$$\rho_{ph}^{(\mu)}(E) = \sum_{\nu, i} |\kappa_{ph}^{(i)}(\mu, \nu)|^2 \delta(E_i(\mu, \nu) - E). \quad (3.102)$$

The projected density of states (PDOS),  $\rho_{\pm}^{(\mu)}(E)$ , for excitons with angular momenta  $\mu \pm 1$ , respectively, is defined similar to (3.102). Note that the sum of the three PDOS functions gives the total density of states, i.e.  $\rho^{(\mu)} = \rho_{ph}^{(\mu)} + \rho_{+}^{(\mu)} + \rho_{-}^{(\mu)}$ . The dependencies of the functions  $\rho_{ph}^{(\mu)}$ ,  $\rho_{\pm}^{(\mu)}$  (coinciding for  $\mu = 0$ ) on  $E$  are displayed in Figs. 3.6 along with the DOS for uncoupled cavity photons and excitons.

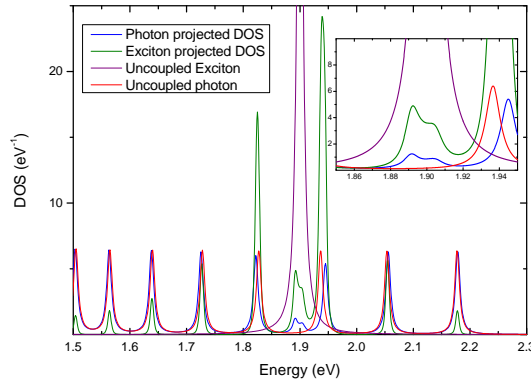


Figure 3.6: (Color online) Dependence of the DOS,  $\rho^{(\mu)}$ , for empty cavity (defined similar to Eq. (3.101) but without sum over  $i$ , red curve) and DOS for cavity with TMD layer projected over photonic ( $\rho_{ph}^{(\mu)}$ , Eq. (3.102), blue curve) and excitonic (green curve) subspaces for  $\mu = 0$ . Also shown is the uncoupled exciton peak. All densities of states are shown normalized to unity, i.e. divided by  $\int \rho^{(\mu)}(E)dE$ . The inset shows a zoom into the energy interval near the avoided crossing.

From Fig. 3.6 it can be seen that the function  $\rho_{ph}^{(0)}$  follows the trends of  $\rho^{(0)}$  for pure photons in a broad range of energy values below the crossing point ( $E < 1.8$  eV). Close to the crossing point (1.9 eV), the polaritons are an almost equal-fraction admixture of MC photons and two exciton species with angular



momenta  $\mu \pm 1$ . It results in a non-zero photonic PDOS within the "gap" of photon DOS with  $\mu = 0$ . For  $E > 2.0$  eV, the upper polariton branch is almost photon (see Fig. 3.5), therefore,  $\rho_{ph}^{(0)}$  and the empty cavity DOS again are similar.

### 3.3.2 Local Density of States

The local density of states (LDOS), i.e. space resolved DOS of photons is important since it determines the variation of the spontaneous decay rate of a point emitter placed in the cavity; it is defined by weighting each photon mode with squared local magnitude of the electric field. [1] Here we deal with mixed photon-exciton modes, therefore, it makes sense to consider the local density of states *projected onto the photon subspace* defined as follows:

$$\rho_{loc}^{(\mu)}(E; r, z) = \sum_{\nu, i} |\vec{\mathbb{E}}(\mu, \nu; r, \phi, z)|^2 |\kappa_{ph}^{(i)}(\mu, \nu)|^2 \delta(E_i(\mu, \nu) - E). \quad (3.103)$$

The electric field amplitude in (3.103) corresponds to one photon and is expressed through the mode volume according to Eq. (3.45). Employing Eq. (3.44) it follows that the integration of  $\rho_{loc}^{(\mu)}(E; r, \phi, z)$  over the MC volume yields the total energy of the photonic subsystem with angular momentum  $\mu$ , therefore, we have

$$\frac{\epsilon}{2\pi E} \int \rho_{loc}^{(\mu)}(E; r, z) d^3r = \rho_{ph}^{(\mu)}(E). \quad (3.104)$$

For the implementation that we have in mind, discussed below, it is particularly interesting to calculate LDOS at the TMD layer, i.e. for  $z = 0$ . In Fig. 3.7 it is shown the dependence of the LDOS,  $\pi R^2 \rho_{loc}^{(\mu)}(E; r, z = 0)$ , upon  $r$  and energy in the vicinity of the crossing point. As it can be seen from the plots, the local density of states depends strongly on both the energy and the radial position and it is redistributed owing to the presence of the TMD layer.

## 3.4 Point Emitter Attached to the TMD Layer: the Purcell effect

In the polariton framework, the exciton does not decay radiatively, instead, the strongly coupled system oscillates between the state with and without exciton and the energy is reversibly transferred from the exciton to photon and *vice versa*, the effect usually referred to as vacuum Rabi oscillations. [15] Yet, in a real cavity some photons escape (and, accordingly, some radiative decay of excitons does occur) giving rise to *polariton photoluminescence*, which can be observed experimentally. However, studies of MC-embedded semiconductor quantum wells (QWs) showed that this emission mechanism is inefficient and the luminescence is dominated by excitons bound to impurities or defects, with the QW emission line redshifted with respect to the polariton modes. [15]

Here we shall consider a point emitter (PE) located within the TMD layer or very close to it, however, without any direct interaction with the TMD excitons. We can think of a trapped exciton in TMD [75] or a point defect in an h-BN layer [76] attached to the TMD layer or even a nanocrystal quantum dot (QD) placed on top of it. [41, 77] We shall assume that it yields an optical transition at energy,  $\hbar\omega_0$ , sufficiently close but not coinciding with  $E_{ex}$ . The emitter interacts with the MC photon modes, which are affected by the strong coupling to the 2D excitons and it should influence emitter's properties. We shall assume that the PE is in the so called weak coupling regime. [13, 78]

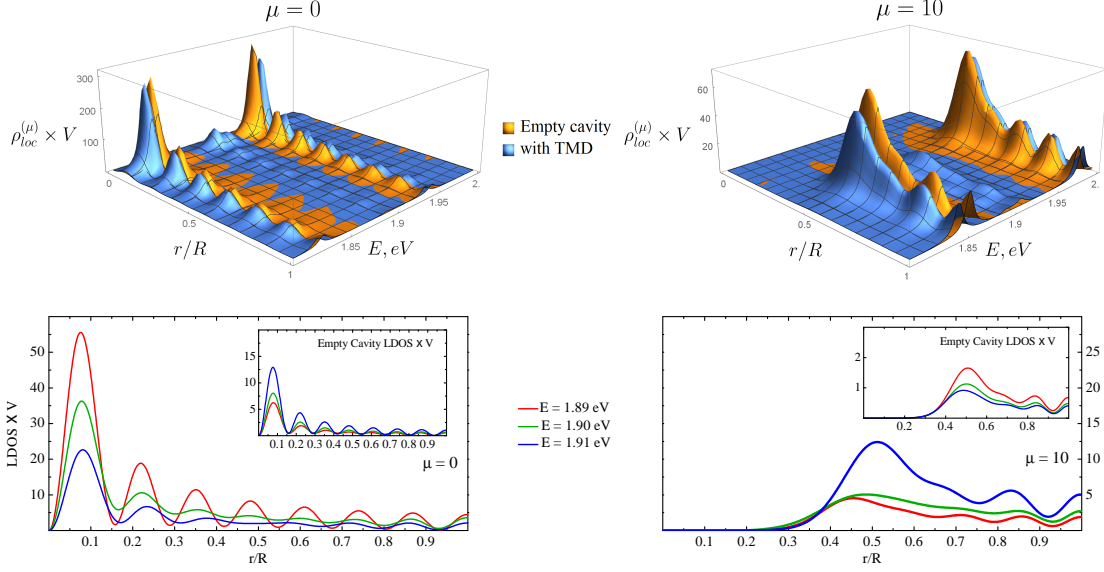


Figure 3.7: (Color online) Dependence of the local density of states,  $\rho_{loc}^{(\mu)}(E; r, z = 0) \times V$  (where  $V = \pi R^2 L$ ), on the normalized radius  $r/R$ , for empty cavity and for cavity with TMD [where it is the polariton photon-projected LDOS, Eq. (3.103)], for  $\mu = 0$  (left) and 10 (right). The lower panels highlight the redistribution of LDOS due to the TMD layer for the energies near the avoided crossing point. The parameters are the same as in Fig. 3.3.

The spontaneous emission rate of a point emitter located within a homogeneous infinite dielectric with refractive index  $\eta = \sqrt{\epsilon}$  is [1, 78]

$$\Gamma_0 = \frac{4\omega_0^3 d_0^2}{3\hbar c^3} \eta \quad (3.105)$$

where  $d_0$  is the dipole moment matrix element of the PE optical transition and  $\omega_0$  is the emission frequency. In the weak coupling regime, the spontaneous emission rate placed in an ideal photonic microcavity is enhanced or inhibited depending on the photonic LDOS value in the position of the emitter, [1]

$$\Gamma(\vec{r}) = \frac{4\pi^2 \omega_0 d_0^2}{\hbar} \rho_{loc}^{\parallel}(\hbar\omega_0, \vec{r}), \quad (3.106)$$

where  $\rho_0(\hbar\omega_0) = \omega_0^2 \eta^3 / (\pi^2 \hbar c^3)$  is the photon DOS in an infinite homogeneous dielectric medium and

$$\rho_{loc}^{\parallel}(E; \vec{r}) = \sum_{\mu, \nu} |\vec{u}(\mu, \nu; r, \phi, z) \cdot \vec{n}_d|^2 \delta(\hbar\omega(\mu, \nu) - E) \quad (3.107)$$

is the *local projected* density of photon states (LPDOS). Here  $\vec{n}_d$  is the unit vector along the emitter's dipole moment,  $\vec{d}_0$ ,  $\omega(\mu, \nu)$  is the frequency of the cavity mode with certain  $\mu$  and  $\nu$  (for simplicity we consider only modes with the lowest  $k_z$ ), and

$$\vec{u}(\mu, \nu; r, \phi, z) = \frac{\eta}{\sqrt{2\pi\hbar\omega(\mu, \nu)}} \vec{\mathbb{E}}(\mu, \nu; r, \phi, z)$$

(notice that it is normalized to unity). The electric field amplitude,  $\vec{\mathbb{E}}$  corresponds to one photon and is expressed through the mode volume according to Eq. (??). Note that we removed the factor 1/3 in Eq.

(3.106) and, correspondingly, the factor of 3 in the LDOS definition in Eq. (3.103), compared to Ref. [1] Taking average over possible orientations of the dipole moment yields:

$$\langle |\vec{u}(\mu, \nu; r, \phi, z) \cdot \vec{n}_d|^2 \rangle = \frac{\epsilon p^{-1}(\mu, \nu; r, \phi, z)}{2\pi \hbar \omega(\mu, \nu)} |\vec{\mathbb{E}}(\mu, \nu; r, \phi, z)|^2$$

where  $p$  is a numerical factor (e.g.  $p = 1$  if the dipole moment is aligned with the considered mode and  $p = 3$  if its orientation is isotropic in 3D space). Let  $\bar{p}^{-1} = \langle p^{-1}(\mu, \nu; r, \phi, z) \rangle$  be its average value over all its arguments, a number of the order of unity. Then we can express the local emission rate through the usual local density of states (LDOS) as follows:

$$\Gamma(\vec{r}) = \Gamma_0 \frac{3\epsilon \bar{p}^{-1} \rho_{loc}^{\parallel}(\hbar\omega_0, \vec{r})}{2\pi \hbar \omega_0 \rho_0(\hbar\omega_0)}. \quad (3.108)$$

Equation (3.108) expresses the so called the Purcell effect, [17] which can be controlled by manipulating the photonic LDOS in nanostructures. [79,80] Nowadays it finds applications in nano-optical spectroscopy, nanolasers, or broadband single-photon sources. [81]

If the emitter is located at  $z = 0$ , the relevant LDOS is written as follows:

$$\rho_{loc}^{\parallel}(\hbar\omega_0; r) = \frac{2\pi \hbar \omega_0}{\epsilon} \sum_{\mu, \nu} \Omega^{-1}(\mu, \nu) \left( \frac{k_z}{q_{\mu\nu}} \right)^2 \left\{ [J'_{\mu}(q_{\mu\nu}r)]^2 + [\mu J_{\mu}(q_{\mu\nu}r)/(q_{\mu\nu}r)]^2 \right\} \delta(\hbar\omega(\mu, \nu) - \hbar\omega_0), \quad (3.109)$$

( $\Omega$  is the EM mode volume). Taking into account losses due to imperfect mirrors (with the loss rate  $\gamma_{loss}$ ), the  $\delta$ -function in (3.109) is replaced by a Lorentzian function according to [78]

$$\delta(\hbar\omega(\mu, \nu) - \hbar\omega_0) \rightarrow \frac{2}{\pi} \frac{1}{\hbar\omega_0} \frac{Q}{1 + 4Q^2 [\omega(\mu, \nu)/\omega_0 - 1]^2}, \quad (3.110)$$

where  $Q = \gamma_{loss}/\omega_0$  and the  $\delta$ -function is recovered in the limit  $Q \rightarrow \infty$ .

Noting that

$$2\pi \hbar \omega_0 \rho_0(\hbar\omega_0) = 16\pi^2 \left( \frac{\eta}{\lambda_0} \right)^3 \quad (3.111)$$

where  $\lambda_0$  is the emission wavelength in vacuum, we can rewrite Eq. (3.108) as follows:

$$\frac{\Gamma(r)}{\Gamma_0} = \sum_{\bar{\mu}, \bar{\nu}} \left[ \frac{3Q}{4\pi^2} \Omega^{-1}(\bar{\mu}, \bar{\nu}) \left( \frac{\lambda_0}{\eta} \right)^3 \right] \bar{p}^{-1} \varphi(\bar{\mu}, \bar{\nu}; r), \quad (3.112)$$

where we have assumed exact resonance between the emission frequency and a cavity mode  $\bar{\mu}, \bar{\nu}$ , so that the sum is over all modes obeying the relation  $\omega(\bar{\mu}, \bar{\nu}) = \omega_0$ , and

$$\varphi(\bar{\mu}, \bar{\nu}; r) = \left( \frac{k_z}{q_{\bar{\mu}\bar{\nu}}} \right)^2 \left\{ [J'_{\bar{\mu}}(q_{\bar{\mu}\bar{\nu}}r)]^2 + [\bar{\mu} J_{\bar{\mu}}(q_{\bar{\mu}\bar{\nu}}r)/(q_{\bar{\mu}\bar{\nu}}r)]^2 \right\}.$$

Therefore, the emission rate is proportional to the quality factor,  $Q$ , and inversely proportional to the (resonance) mode volume, while its spatial dependence is determined by the function  $\varphi(\bar{\mu}, \bar{\nu}; r)$ . The factor  $\bar{p}^{-1}$  takes into account the emission polarization properties of the emitter. The term in square brackets in Eq. (3.112) is called the Purcell factor (originally introduced by Purcell [17] with the cavity volume,  $V$ , in place of the mode volume,  $\Omega$ ) and it measures the maximum spontaneous emission acceleration that can

be achieved by placing the emitter in a cavity, in the weak coupling regime. The Purcell factor has been generalized to take into account the effects such as photon confinement, absorption and MC material's dispersion, [81] so Eq. (3.112) can be seen as a generalization taking into account the cylindrical geometry.

For a cavity with embedded TMD layer, the local emission rate is expressed through the local polaritonic density density of states projected onto the photon subspace, defined in the previous section [Eq. (3.103)] as follows:

$$\Gamma(\vec{r}) = \Gamma_0 \frac{3\epsilon\bar{p}^{-1} \sum_{\mu} \rho_{loc}^{(\mu)}(\hbar\omega_0, \vec{r})}{2\pi\hbar\omega_0\rho_0(\hbar\omega_0)}. \quad (3.113)$$

Figure 3.8 illustrates how the local emission rates changes with energy and emitter's position within the  $z = 0$  plane inside either an empty cavity or a cavity with inserted TMD layer.

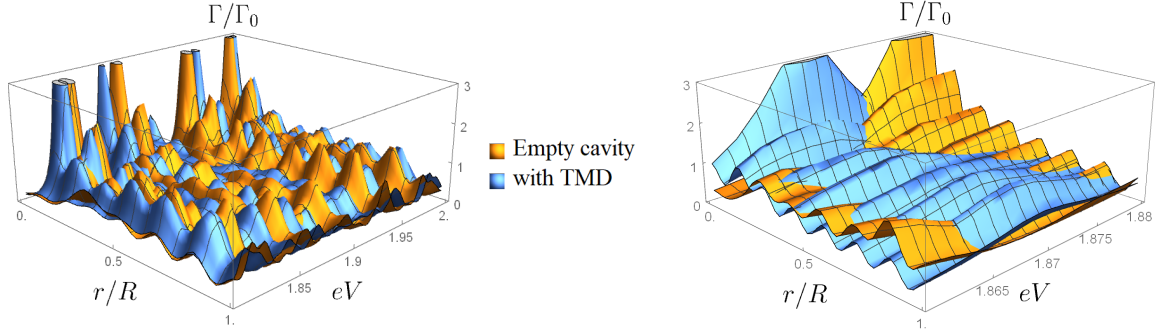


Figure 3.8: (Color online) Energy and position dependence of the local emission rate of a point emitter located in the  $z = 0$  plane calculated for empty cavity and for cavity with TMD. The right panel highlights the region near 1.87 eV where the Purcell effect enhancement due to the TMD layer is seen. We assumed  $\bar{p}^{-1} = 1$  and other parameters are the same as in Fig. 3.3.

From this figure we can see that local emission rate is redistributed both in energy and in space due to the presence of the TMD layer in the cavity. Such an engineering of  $\Gamma(\vec{r})$  can be useful for stimulating a point emitter tuned to a particular wavelength while pumping it through a cavity mode. If it is a trapped exciton in the TMD layer, the red shift of the photon-projected polariton LDOS with respect to the bare 2D exciton energy (1.9 eV in our example) is desirable indeed. Excitation can be performed through the upper polariton branch lying above 1.9 eV (see Fig. 3.3). The excitonic part of such a polariton can be trapped by a defect or impurity. Angular momentum is not conserved for trapped excitons and their emission, after being excited, can be proportional to the local photonic DOS irrespective of  $\mu$ . Yet, as Fig. 3.7 shows, LDOS, for the same energy, peaks at different distances from cavity's centre and it will enhance the emission of photons with certain angular momenta depending on the position of the emitter.

# 4

## Photonic states confined to a spherical microcavity

---

This chapter will consider the problem of electromagnetic modes in a microsphere with radius  $R$  of the order of a few  $\mu\text{ m}$ . This microsphere is a dielectric with relative permittivity  $\epsilon = 3.4$ . The goal is to find eigenmodes (solutions to Maxwell equations), and then study their spatial distribution through the photonic local density of states. This work was inspired by the nice observation by Prof. Adil Chahboun of the University of Tanger, figure 4.1. [82] This figure shows that dielectric microspheres of 10 to 20  $\mu\text{m}$  in size, uniformly doped with point emitters (dye molecules) during their growth, apparently emit light only from a relatively thin shell when the whole system is irradiated uniformly and (some of) the point emitters are excited. We attempted to explain this and other observations of this kind, presented in chapter 5 of Nizar Bchellaoui's thesis [83]. In short, the idea is that these molecules emit in resonance with certain electromagnetic eigenmodes of the sphere that have large orbital ( $l$ ) and radial ( $n$ ) numbers and  $l \sim n$ , the so called whispering-gallery (WG) modes [13]. Although this qualitative explanation can be plausible since the WG modes are said to be "quasiwaveguided" modes in spherical geometry [13], it is interesting to demonstrate it with calculations by analyzing the spherical cavity modes in the same way as we studied the cylindrical MC eigenmodes in the previous chapter.

The solutions to the Helmholtz scalar equation in spherical coordinates are well known (spherical Bessel functions). As such, these solutions will be used to arrive at general solutions for the vectorial Helmholtz equation. Calculations of dispersion and local density of states will be made for two types of cavity: ideal cavity modes, with a perfect conductor acting as the surface of the sphere, and real cavity modes, where the edge of the sphere is assumed to be a simple dielectric interface. The point emitters are excited by radiation of a considerably shorter wavelength than their emission wavelength and the absorption and emission events are separated in energy and in time and can be considered as independent. For simplicity, the excitation of the emitters will be analysed using geometrical optics. The absorption rate of such device will be estimated starting with results from Bohram and Huffman's book [19] and using some original calculations for a ray optics estimate of the distribution of rays in each part of the sphere. This allows us to map the absorption rate by molecules inside the sphere as it depends on its eigenmodes as well as on the characteristics of the incident light (direction, frequency, etc...). With this 'map' of absorption of the exiting radiation and the position-dependent Purcell factor evaluated from the calculated photonic DOS at the emission wavelength,, it is possible to estimate the

most efficient region for such a point emitter in order to maximize its emission rate.

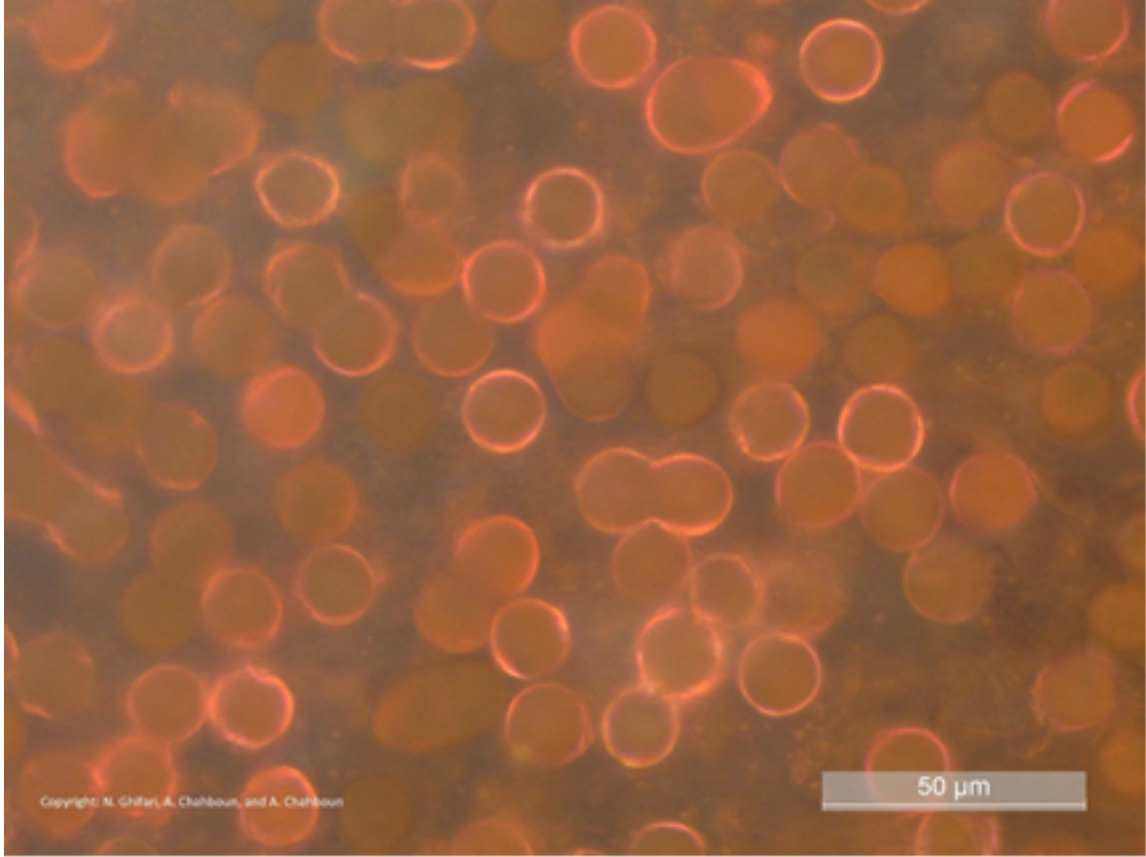


Figure 4.1: Photoluminescence of ZnO microspheres uniformly doped with point emitters (dye molecules Rhodamine B) under uniform illumination [82].

## 4.1 Determination of the eigenmodes

### 4.1.1 Scalar Helmholtz equation

The general vector equation solutions will be obtained from those of the scalar Helmholtz equation, which for a medium of relative permittivity  $\epsilon$  has the form:

$$\left(\nabla^2 - \frac{\epsilon}{c^2} \frac{\partial^2}{\partial t^2}\right)u(\mathbf{r}, t) = 0. \quad (4.1)$$

Assuming harmonic time dependence  $e^{-i\omega t}$  one obtains the Helmholtz equation:

$$\left(\nabla^2 + k^2\right)u(\mathbf{r}) = 0, \quad (4.2)$$

where  $k^2 = \epsilon\omega^2/c^2$ . Appendix D contains the detailed calculation of the solution, which is also done in literature [63], and can be written as:

$$u_{l,m}(\mathbf{r}, t) = u_{l,m}(\mathbf{r})e^{-i\omega t} = (Aj_l(kr) + By_l(kr))P_l^m(\cos\theta)e^{i(m\phi - \omega t)}, \quad (4.3)$$

where  $j_l$  and  $y_l$  are the spherical Bessel functions of first-kind and second-kind, respectively, of order  $l$ .  $A$  and  $B$  are constants generally determined by boundary conditions ( $B = 0$  if the medium contains the origin, because  $y_l(kr)$  diverges at  $r = 0$ ) and  $P_l^m$  is the associated Legendre polynomial.

### 4.1.2 Vectorial Helmholtz equation

Now, the focus is turned to the Helmholtz vectorial equation, which must be obeyed by both electric and magnetic fields:

$$\nabla^2 \mathbf{u}(\mathbf{r}) + k^2 \mathbf{u}(\mathbf{r}) = 0. \quad (4.4)$$

Knowing the scalar solutions, one may attempt to write  $\mathbf{u}(\mathbf{r})$  as a function of  $u(\mathbf{r})$ . Electric fields, for harmonic waves, can be written as the curl of the magnetic fields, and vice-versa. As such,  $\mathbf{u}(\mathbf{r})$  can be written as the curl of some vector function with scalar part  $\Psi(\mathbf{r})$  and direction  $\mathbf{A}(\mathbf{r})$ :

$$\mathbf{u}(\mathbf{r}) = \nabla \times [\Psi(\mathbf{r})\mathbf{A}(\mathbf{r})]. \quad (4.5)$$

Equation (4.4) becomes

$$\nabla^2 [\nabla \times [\Psi(\mathbf{r})\mathbf{A}(\mathbf{r})]] + k^2 \nabla \times [\Psi(\mathbf{r})\mathbf{A}(\mathbf{r})] = 0. \quad (4.6)$$

Now property (5.82) can be employed to obtain

$$\nabla \times [\nabla^2 [\Psi(\mathbf{r})\mathbf{A}(\mathbf{r})]] + k^2 \nabla \times [\Psi(\mathbf{r})\mathbf{A}(\mathbf{r})] = 0. \quad (4.7)$$

Using (5.83) this can be written as (the dependence on  $r$  will be omitted to save space)

$$\nabla \times [\mathbf{A}\nabla^2\Psi + 2[\nabla\Psi \cdot \nabla]\mathbf{A} + \Psi\nabla^2\mathbf{A}] + k^2 \nabla \times [\Psi\mathbf{A}] = 0. \quad (4.8)$$

With the clever choice of  $\mathbf{A} = \mathbf{r}$  the second and third terms become:

$$\nabla \times [2\nabla\Psi + \Psi(\nabla(\nabla \cdot \mathbf{r}) - \nabla \times (\nabla \times \mathbf{r}))], \quad (4.9)$$

and since  $\nabla \cdot \mathbf{r} = 3$  and  $\nabla \times \mathbf{r} = 0$  these terms are equal to

$$2\nabla \times \nabla\Psi = 0 \quad (4.10)$$

according to (5.84). With all this, equation (4.8) is simply

$$\nabla \times [\mathbf{r}(\nabla^2\Psi + k^2\Psi)] = 0. \quad (4.11)$$

Finally, if we choose the simple case of having  $\nabla^2\Psi + k^2\Psi = 0$ , then the solutions of equation (4.4) are determined by a potential function  $\Psi(\mathbf{r})$ , which is given by (4.3). In conclusion, the solutions found for the vectorial Helmholtz equation are of the form:

$$\mathbf{u}(\mathbf{r}) = \nabla \times (\Psi(\mathbf{r})\mathbf{r}), \quad (4.12)$$

where  $\Psi(\mathbf{r})$  are the solutions to the scalar equation given by (4.3).

### 4.1.3 Components of the electromagnetic fields

A general function  $f_l(kr)$  will be introduced,

$$f_l(kr) = A j_l(kr) + B y_l(kr). \quad (4.13)$$

Depending on the type of mode considered, either the electric or magnetic field will be proportional to

$$\mathbf{u}_{l,m}(\mathbf{r}) = \nabla \times [f_l(kr) P_l^m(\cos \theta) e^{im\phi} \mathbf{r}]. \quad (4.14)$$

Explicit calculation of the curl yields the components of this vector:

$$\begin{cases} u_{l,m}^{(r)} = 0 \\ u_{l,m}^{(\theta)} = im f_l(kr) \frac{P_l^m(\cos \theta)}{\sin \theta} e^{im\phi} \\ u_{l,m}^{(\phi)} = -f_l(kr) \partial_\theta P_l^m(\cos \theta) e^{im\phi} \end{cases}, \quad (4.15)$$

One of the fields (electric or magnetic) will be proportional to the vector  $\mathbf{u}(\mathbf{r})$  whereas the other field will be proportional to the curl of  $\mathbf{u}(\mathbf{r})$ . As such, it will be useful to define

$$\mathbf{c}_{l,m} = \frac{1}{k} \nabla \times \mathbf{u}_{l,m}. \quad (4.16)$$

Again, explicit calculation yields:

$$\begin{cases} c_{l,m}^{(r)} = \frac{f_l(kr)}{kr} l(l+1) P_l^m(\cos \theta) e^{im\phi}, \\ c_{l,m}^{(\theta)} = \frac{\partial_{kr}(kr f_l(kr))}{kr} \partial_\theta P_l^m(\cos \theta) e^{im\phi}, \\ c_{l,m}^{(\phi)} = i \frac{\partial_{kr}(kr f_l(kr))}{kr} m \frac{P_l^m(\cos \theta)}{\sin \theta} e^{im\phi} \end{cases}. \quad (4.17)$$

### 4.1.4 TM-type and TE-type modes

Two types of modes can be studied separately. Modes with zero radial component of the magnetic field are called electric or transverse magnetic (TM). If the same applies to the electric field, such modes are called magnetic or transverse electric (TE). With these considerations we have defined the fields:

$$\begin{cases} \mathbf{H}_{l,m}^{(TM)} = \sqrt{\epsilon} E_0^{(TM)} \mathbf{u}_{l,m}(\mathbf{r}) \\ \mathbf{E}_{l,m}^{(TE)} = E_0^{(TE)} \mathbf{u}_{l,m}(\mathbf{r}) \end{cases}, \quad (4.18)$$

with  $\mathbf{u}_{l,m}(\mathbf{r})$  being given by (4.15).  $E_0^{(TM)}$  and  $E_0^{(TE)}$  are the electric field amplitudes of 'TM-type' and 'TE-type' modes, respectively. Ampère's law and Faraday's equation read:

$$\begin{cases} \mathbf{E} = \frac{i}{\sqrt{\epsilon k}} \nabla \times \mathbf{H} \\ \mathbf{H} = -\frac{i\sqrt{\epsilon}}{k} \nabla \times \mathbf{E} \end{cases}. \quad (4.19)$$

Applying these two equations to (4.18) and using (4.16) yields the complete fields as:

$$\begin{cases} \mathbf{H}_{l,m}^{(TM)} = \sqrt{\epsilon} E_0^{(TM)} \mathbf{u}_{l,m}(\mathbf{r}) \\ \mathbf{E}_{l,m}^{(TM)} = i E_0^{(TE)} \mathbf{c}_{l,m}(\mathbf{r}) \\ \mathbf{H}^{(TE)} = -i\sqrt{\epsilon} E_0^{(TM)} \mathbf{c}_{l,m}(\mathbf{r}) \\ \mathbf{E}^{(TE)} = E_0^{(TE)} \mathbf{u}_{l,m}(\mathbf{r}) \end{cases}, \quad (4.20)$$



with  $\mathbf{u}_{l,m}^{(c)}$  being given by (4.17). By substitution of (4.15) and (4.14) into (4.20), the explicit form of the 'TM-type' modes will then read:

$$\begin{cases} (E_{l,m}^{(TM)})_r = E_0^{(TM)} \frac{f_l(kr)}{kr} l(l+1) P_l^m(\cos \theta) e^{im\phi} \\ (E_{l,m}^{(TM)})_\theta = iE_0^{(TM)} \frac{\partial_{kr}(kr f_l(kr))}{kr} \partial_\theta P_l^m(\cos \theta) e^{im\phi} \\ (E_{l,m}^{(TM)})_\phi = -E_0^{(TM)} \frac{\partial_{kr}(kr f_l(kr))}{kr} m \frac{P_l^m(\cos \theta)}{\sin \theta} e^{im\phi} \end{cases}, \quad (4.21)$$

$$\begin{cases} (H_{l,m}^{(TM)})_r = 0 \\ (H_{l,m}^{(TM)})_\theta = i\sqrt{\epsilon} E_0^{(TM)} m f_l(kr) \frac{P_l^m(\cos \theta)}{\sin \theta} e^{im\phi} \\ (H_{l,m}^{(TM)})_\phi = -\sqrt{\epsilon} E_0^{(TM)} f_l(kr) \partial_\theta P_l^m(\cos \theta) e^{im\phi} \end{cases}. \quad (4.22)$$

and the explicit form of the 'TE-type' modes will read:

$$\begin{cases} (E_{l,m}^{(TE)})_r = 0 \\ (E_{l,m}^{(TE)})_\theta = iE_0^{(TE)} f_l(kr) m \frac{P_l^m(\cos \theta)}{\sin \theta} e^{im\phi} \\ (E_{l,m}^{(TE)})_\phi = -E_0^{(TE)} f_l(kr) \partial_\theta P_l^m(\cos \theta) e^{im\phi} \end{cases}, \quad (4.23)$$

$$\begin{cases} (H_{l,m}^{(TE)})_r = -i\sqrt{\epsilon} E_0^{(TE)} \frac{f_l(kr)}{kr} l(l+1) P_l^m(\cos \theta) e^{im\phi}, \\ (H_{l,m}^{(TE)})_\theta = -i\sqrt{\epsilon} E_0^{(TE)} \frac{\partial_{kr}(kr f_l(kr))}{kr} \partial_\theta P_l^m(\cos \theta) e^{im\phi} \\ (H_{l,m}^{(TE)})_\phi = \sqrt{\epsilon} E_0^{(TE)} \frac{\partial_{kr}(kr f_l(kr))}{kr} m \frac{P_l^m(\cos \theta)}{\sin \theta} e^{im\phi} \end{cases}, \quad (4.24)$$

## 4.2 Ideal cavity modes

The simplest system involving a spherical microcavity made of a dielectric material would be to consider the microcavity to be surrounded by a spherical shell of a perfect metal ( $\epsilon \rightarrow -\infty$ ). This is the perfect confinement ideal cavity scenario. The field must then be equal to zero outside of the cavity (medium 2). Also, the tangential components of the electric field and radial component of the magnetic field must vanish at the interface. That is, the following boundary conditions must apply:

$$[\hat{r} \times \mathbf{E}_{l,m}]|_{r=R} = 0, \quad (4.25)$$

and

$$[\hat{r} \cdot \mathbf{H}_{l,m}]|_{r=R} = 0. \quad (4.26)$$

### 4.2.1 Dispersion relations

We can now apply conditions (4.25) and (4.26) to TM and TE-type modes to obtain their eigenenergies.

#### TM-type

According to (4.22), the condition for the magnetic field (4.26) is always met. So, only the application of condition (4.25) to (4.21) remains, which yields:

$$[\hat{r} \times \mathbf{E}_{l,m}]|_{r=R} = 0, \quad (4.27)$$

$$\begin{cases} (E_{l,m}^{(TM)})_{\theta}|_{r=R} = 0 \\ (E_{l,m}^{(TM)})_{\phi}|_{r=R} = 0 \end{cases} . \quad (4.28)$$

Both equations yield:

$$[\partial_{kr}(krj_l(kr))] |_{r=R} = 0, \quad (4.29)$$

which becomes:

$$j_l(kR) + kRj'_l(kR) = 0. \quad (4.30)$$

### TE-type

Now we can turn our attention to the TE-type modes. Firstly, using the expressions (4.23), the condition for the electric field (4.25) is:

$$\begin{cases} (E_{l,m}^{(TE)})_{\theta}|_{r=R} = 0 \\ (E_{l,m}^{(TE)})_{\phi}|_{r=R} = 0 \end{cases} , \quad (4.31)$$

and both equations yield

$$j_l(kR) = 0. \quad (4.32)$$

Secondly, with the expressions (4.24) the condition for the magnetic field (4.26) is:

$$(H_{l,m}^{(TE)})_r|_{r=R} = 0, \quad (4.33)$$

and this equation also yields

$$j_l(kR) = 0. \quad (4.34)$$

Figure 4.2 presents some solutions of both TM-type (4.30) and TE-type (4.34) with energies,  $\hbar\omega$ , in eV, for different  $l$ . The radial number  $n$  is simply the sequential number of the root of the corresponding dispersion equation. In the case of TE-type modes, the solutions are the  $n$ -th zeros of the spherical Bessel function. So, by definition, the eigenfrequencies always increase with the mode number.

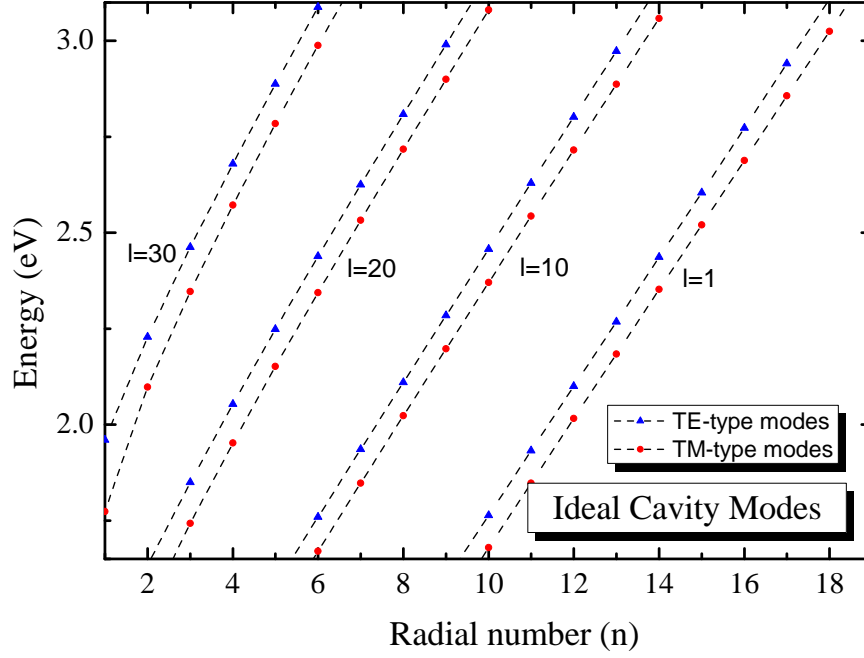


Figure 4.2: Solutions (for an ideal cavity) of equation (4.30) for TM-type modes and equation (4.34) for TE-type modes, with energy  $\hbar\omega$  in eV for different  $l$ . The energies presented correspond to the visible spectrum (1.65 to 3.1 eV). The radius of the sphere is  $R = 3 \mu\text{m}$ . The dielectric constant of the sphere's material is  $\epsilon = 3.4$ .

#### 4.2.2 Local density of states

The modes obtained in this work correspond to photonic distributions inside the cavity. The total density of states can be written as the sum of all the partial densities of states for a given angular momentum number  $l$ :

$$\varrho(E) = \sum_{l=1}^{\infty} \rho^{(l)}(E), \quad (4.35)$$

where

$$\rho^{(l)}(E) = (2l + 1) \sum_{n=1}^{\infty} \delta(E - E_{n,l}), \quad (4.36)$$

where  $E_{n,l}$  are the eigenenergies of the system given by either (4.30) for TM-type modes or (4.34) for TE-type modes, and depicted in figure 4.2. The factor  $2l + 1$  is the degeneracy of each mode of angular momentum  $l$ .

The spatial distribution of the photonic modes studied in this work is given by the modulus squared of the electric field. As such, one can define the local density of states as:

$$\rho_{loc}(r, E) = \sum_{n,l,m} \sum_{\sigma=TM,TE} |\mathbf{E}_{l,m}^{(\sigma)}(\mathbf{r}, E)|^2 \delta(E - E_{n,l}^{(\sigma)}). \quad (4.37)$$

As was done in the previous chapter, the electric field amplitude used in (4.37) must correspond to a single photon confined to the interior of the microcavity, which corresponds to quantifying the energy  $\hbar\omega$

pertaining to this photon:

$$\hbar\omega = \frac{1}{4\pi} \int d^3r (\epsilon \mathbf{E} \cdot \mathbf{E}^* + \mathbf{H} \cdot \mathbf{H}^*). \quad (4.38)$$

The electric field amplitude can be written as:

$$E_0(n, l, m) = \sqrt{\frac{2\pi\hbar\omega}{\epsilon\Omega_{n,l,m}}}, \quad (4.39)$$

where:

$$\Omega_{n,l,m} = \frac{1}{2\epsilon} \int d^3r \left( \epsilon \frac{\mathbf{E} \cdot \mathbf{E}^*}{E_0^2} + \frac{\mathbf{H} \cdot \mathbf{H}^*}{E_0^2} \right), \quad (4.40)$$

$\Omega$  is generally called the mode volume [3] and it is calculated in detail in appendix E. Its value for 'TM-type' modes is given by:

$$\Omega_{n,l,m}^{(TM)} = \frac{2\pi}{\left(k_{n,l,m}^{(TM)}\right)^3} \frac{2l(l+1)(l+m)!}{(2l+1)(l-m)!} \left[ z(j_l(z) + zj_l'(z))^2 + zj_l^2(z)[z^2 - l(l+1)] \right] \Bigg|_{z=0}^{k_{n,l,m}^{(TM)}R}, \quad (4.41)$$

where  $k_{n,l,m}^{(TM)} = \frac{\sqrt{\epsilon}}{\hbar c} E_{n,l,m}^{(TM)}$ , with  $E_{n,l,m}^{(TM)}$  representing the solutions to equation (4.30). The mode volume of 'TE-type' modes has a similar form:

$$\Omega_{n,l,m}^{(TE)} = \frac{2\pi}{\left(k_{n,l,m}^{(TE)}\right)^3} \frac{2l(l+1)(l+m)!}{(2l+1)(l-m)!} \left[ z(j_l(z) + zj_l'(z))^2 + zj_l^2(z)[z^2 - l(l+1)] \right] \Bigg|_{z=0}^{k_{n,l,m}^{(TE)}R}, \quad (4.42)$$

where  $k_{n,l,m}^{(TE)} = \frac{\sqrt{\epsilon}}{\hbar c} E_{n,l,m}^{(TE)}$ , with  $E_{n,l,m}^{(TE)}$  representing the solutions to equation (4.34). The integral only needs to be calculated in one medium (inside the sphere), because we are dealing with a perfect cavity. Notice the dispersion relations for both modes (equation (4.30) for TM-type modes and equation (4.34) for TE-type modes) both show up in the definitions of the mode volume (equations (4.41) and (4.42)), allowing for the simplification of both formulae:

$$\Omega_{n,l,m}^{(TM)} = 2\pi R^3 \frac{2l(l+1)(l+m)!}{(2l+1)(l-m)!} j_l'^2 \left( k_{n,l,m}^{(TM)} R \right) \left[ 1 - \frac{l(l+1)}{\left(k_{n,l,m}^{(TM)} R\right)^2} \right], \quad (4.43)$$

$$\Omega_{n,l,m}^{(TE)} = 2\pi R^3 \frac{2l(l+1)(l+m)!}{(2l+1)(l-m)!} j_l' \left( k_{n,l,m}^{(TE)} R \right)^2. \quad (4.44)$$

So, the following equations define the local densities of states of TM-type ( $\rho_{l,m}^{(TM)}$ ) and TE-type ( $\rho_{l,m}^{(TE)}$ ):

$$\left\{ \begin{array}{l} k \equiv k_{n,l,m}^{(TM)} = \frac{\sqrt{\epsilon}}{\hbar c} E_{n,l,m}^{(TM)} \\ |\mathbf{E}_{n,l,m}^{(TM)}|^2 = \\ |E_0^{(TM)}(n, l, m)|^2 \left[ \left[ \frac{j_l(kr)}{kr} l(l+1) P_l^m(\cos\theta) \right]^2 + \frac{[\partial_r(rj_l(kr))]^2}{(kr)^2} \left[ (\partial_\theta P_l^m(\cos\theta))^2 + \left( m \frac{P_l^m(\cos\theta)}{\sin\theta} \right)^2 \right] \right] \end{array} \right\}, \quad (4.45)$$

$$\left\{ \begin{array}{l} k \equiv k_{n,l,m}^{(TE)} = \frac{\sqrt{\epsilon}}{\hbar c} E_{n,l,m}^{(TE)} \\ |\mathbf{E}_{n,l,m}^{(TE)}|^2 = |E_0^{(TE)}(n, l, m)|^2 j_l^2(kr) \left[ (\partial_\theta P_l^m(\cos\theta))^2 + \left( m \frac{P_l^m(\cos\theta)}{\sin\theta} \right)^2 \right] \end{array} \right\}, \quad (4.46)$$

$$\begin{cases} E_0^{(TM)}(n, l, m) = \sqrt{\frac{2\pi E_{n,l,m}^{(TM)}}{\epsilon\Omega_{n,l,m}^{(TM)}}} \\ E_0^{(TE)}(n, l, m) = \sqrt{\frac{2\pi E_{n,l,m}^{(TE)}}{\epsilon\Omega_{n,l,m}^{(TE)}}} \end{cases}, \quad (4.47)$$

where the  $\Omega$  are given by (4.43) and (4.44) and finally, according to (4.37):

$$\begin{cases} \rho_{loc}^{(TM)}(\mathbf{r}, E) = \sum_{n,l,m} |\mathbf{E}_{n,l,m}^{(TM)}(\mathbf{r}, E_n)|^2 \delta(E - \hbar\omega_{n,l,m}^{(TM)}) \\ \rho_{loc}^{(TE)}(\mathbf{r}, E) = \sum_{n,l,m} |\mathbf{E}_{n,l,m}^{(TE)}(\mathbf{r}, E_n)|^2 \delta(E - \hbar\omega_{n,l,m}^{(TE)}) \end{cases}. \quad (4.48)$$

In figures 4.3 and 4.4 some terms of the sum in (4.48) are presented, to show the difference in the angular dependence of each different  $m$  value.

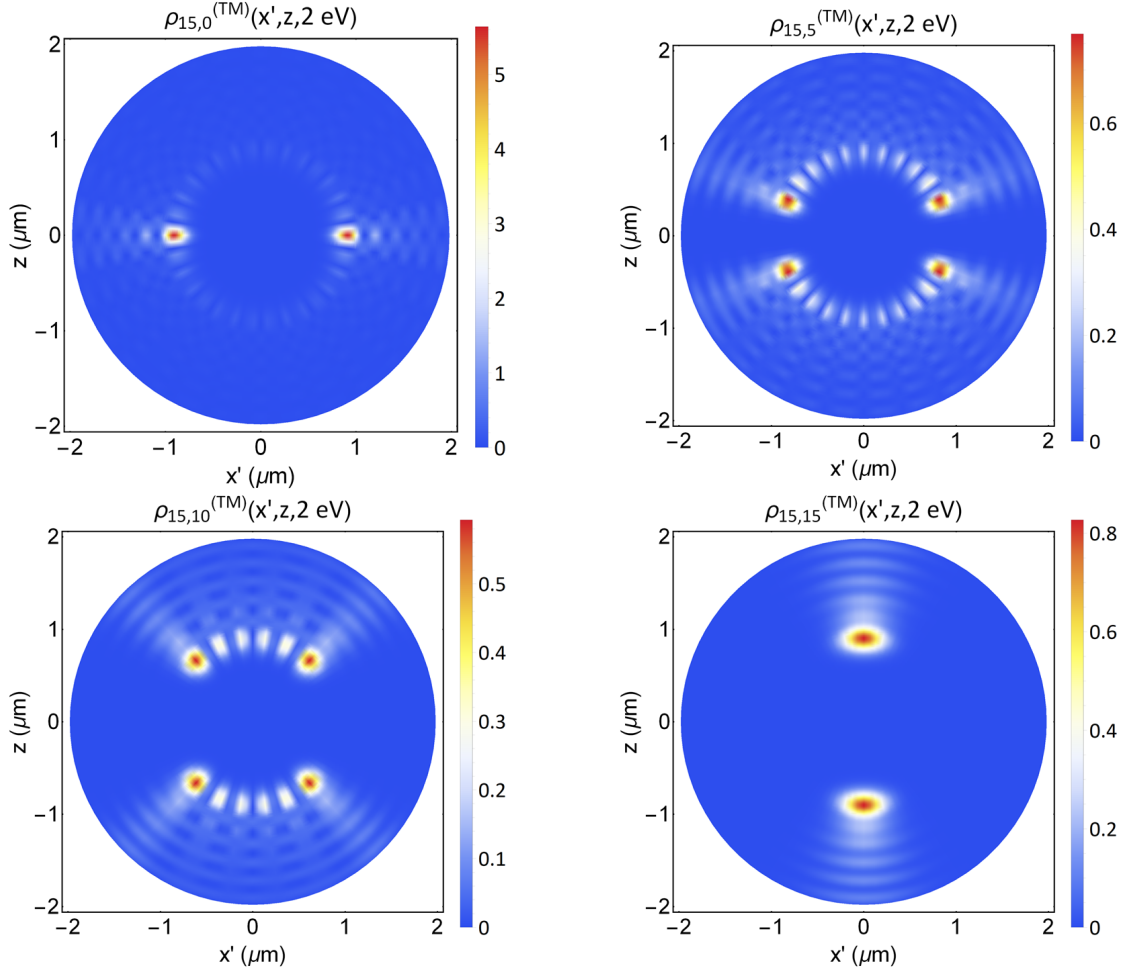


Figure 4.3: Evolution with respect to  $m$  of local densities of states for TM-type modes, given by the first equation in (4.48). The  $l$  value used is  $l = 15$  and the  $m$  values shown are, from left to right,  $m = 0$ ,  $m = 5$ ,  $m = 10$  and  $m = 15$ . The circle ( $x', z$ ) is any constant  $\phi$  cross-section of the sphere. The radius used was  $R = 2 \mu\text{m}$ , the energy at which the LDOS is calculated is 2 eV and only modes with  $0 < \hbar\omega < 4$  (eV) were considered.

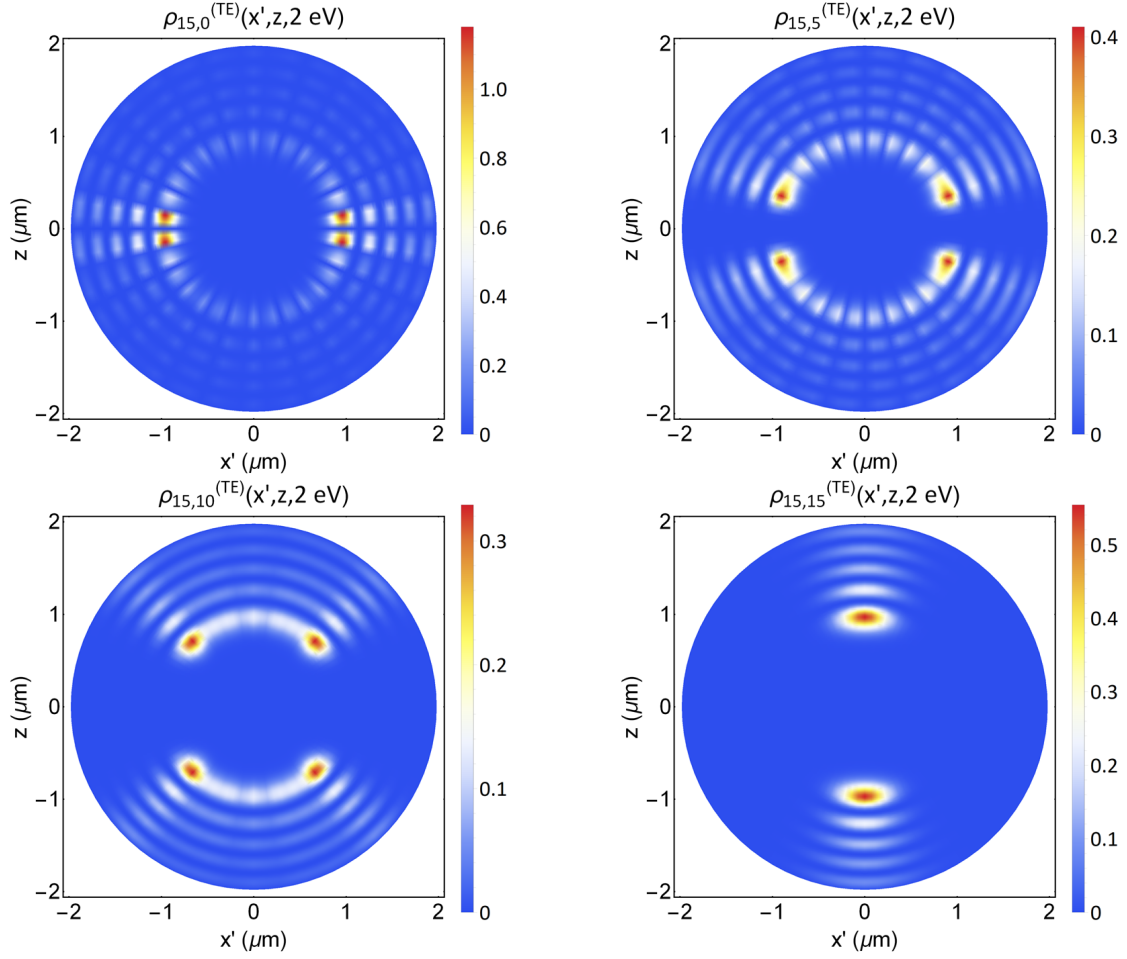


Figure 4.4: Evolution with relation to  $m$  of local densities of states for TE-type modes, given by the second equation in (4.48). The  $l$  value used is  $l = 15$  and the  $m$  values shown are, from left to right,  $m = 0$ ,  $m = 5$ ,  $m = 10$  and  $m = 15$ . The circle  $(x', z)$  is any constant  $\phi$  cross-section of the sphere. The radius used was  $R = 2 \mu\text{m}$ , the energy at which the LDOS is calculated is 2 eV and only modes with  $0 < E < 4$  (eV) were considered.

### 4.3 Modes for a real cavity with dielectric interface

The next step in the study is to consider a system where there is a spherical dielectric interface. The interior of the sphere will have permittivity  $\epsilon_1$  and the outside will have permittivity  $\epsilon_2$ , where  $\epsilon_2 = 1$  (vacuum) on all calculations performed. Propagative harmonic modes with real frequencies are not possible, because here the radial wavenumber is directly proportional to the frequency ( $k_1 = \sqrt{\epsilon_1} \frac{\omega}{c}$  and  $k_2 = \sqrt{\epsilon_2} \frac{\omega}{c}$ ) and as such one can not have  $k_1$  being real and  $k_2$  imaginary, unless  $\epsilon_2$  is negative. However, solutions to the eigenmode equations with complex frequencies were found. These solutions diverge with  $r$  due to the imaginary part of  $k$ , but also decay exponentially with  $t$ . All spherical Hankel functions of the first-kind, for complex arguments, grow slower than exponentially at infinity. [63] Precisely, the

amplitude squared at infinity decays with  $1/r^2$  as it should for a spherical wave. This means that any wave radiating from the interface, which has to be a superposition of these eigenmodes, will never have time to diverge with  $r$  because it will decay exponentially with time. As such, these modes are possible, but normalization to a single photon becomes complicated because the photon is not confined and the integration can not be made up to infinity. The integrations for the normalization of the EM field has been made up to a finite yet large radius  $R_L = 300 \mu\text{m}$ . This corresponds to assuming that the photon of the system is still inside this large volume of  $\frac{4}{3}\pi R_L^3$  at the precise moment one reads the density of states. Note that in this section the electric and magnetic fields will be labelled  $\mathbf{E}_{i,n,l,m}$  where  $i$  refers to either medium 1 or medium 2.

The complete electromagnetic boundary conditions, with no charges or currents, read:

$$\left\{ \begin{array}{l} [\hat{r} \times (\mathbf{E}_{2,n,l,m} - \mathbf{E}_{1,n,l,m})] |_{r=R} = 0 \\ [\hat{r} \cdot (\epsilon_2 \mathbf{E}_{2,n,l,m} - \epsilon_1 \mathbf{E}_{1,n,l,m})] |_{r=R} = 0 \\ [\hat{r} \cdot (\mathbf{B}_{2,n,l,m} - \mathbf{B}_{1,n,l,m})] |_{r=R} = 0 \\ [\hat{r} \times (\mathbf{B}_{2,n,l,m} - \mathbf{B}_{1,n,l,m})] |_{r=R} = 0 \end{array} \right. , \quad (4.49)$$

where  $\mathbf{E}_{2,l,m}$  and  $\mathbf{B}_{2,l,m}$  are the electric and magnetic fields outside the sphere (medium 2 with  $\epsilon = \epsilon_2$ ) and  $\mathbf{E}_{1,l,m}$  and  $\mathbf{B}_{1,l,m}$  are the electric and magnetic fields inside the sphere (medium 1 with  $\epsilon = \epsilon_1$ ).

### 4.3.1 Dispersion relations

The spherical Hankel function of the first-kind  $h_l \equiv h_l^{(1)} = j_l + iy_l$  is the function combination (4.3) with  $A = 1$  and  $B = i$  chosen for the modes outside the cavity. These combinations represent modes that propagate radially outwards. [63] The electric and magnetic fields for TM-type modes, inside and outside the sphere, are:

$$\left[ \begin{array}{l} (E_{1,n,l,m}^{(TM)})_r = E_1^{(TM)} \frac{j_l(k_1 r)}{k_1 r} \\ (E_{1,n,l,m}^{(TM)})_\theta = i E_1^{(TM)} \frac{\partial_r (r j_l(k_1 r))}{k_1 r} \\ (E_{1,n,l,m}^{(TM)})_\phi = -E_1^{(TM)} \frac{\partial_r (r j_l(k_1 r))}{k_1 r} \\ (H_{1,n,l,m}^{(TM)})_r = 0 \\ (H_{1,n,l,m}^{(TM)})_\theta = i \sqrt{\epsilon_1} E_1^{(TM)} j_l(k_1 r) \\ (H_{1,n,l,m}^{(TM)})_\phi = -\sqrt{\epsilon_1} E_1^{(TM)} j_l(k_1 r) \end{array} \right] \left[ \begin{array}{l} (E_{2,n,l,m}^{(TM)})_r = E_2^{(TM)} \frac{h_l(k_2 r)}{k_2 r} \\ (E_{2,n,l,m}^{(TM)})_\theta = i E_2^{(TM)} \frac{\partial_r (r h_l(k_2 r))}{k_2 r} \\ (E_{2,n,l,m}^{(TM)})_\phi = -E_2^{(TM)} \frac{\partial_r (r h_l(k_2 r))}{k_2 r} \\ (H_{2,n,l,m}^{(TM)})_r = 0 \\ (H_{2,n,l,m}^{(TM)})_\theta = i \sqrt{\epsilon_2} E_2^{(TM)} h_l(k_2 r) \\ (H_{2,n,l,m}^{(TM)})_\phi = -\sqrt{\epsilon_2} E_2^{(TM)} h_l(k_2 r) \end{array} \right] \left[ \begin{array}{l} l(l+1) P_l^m(\cos \theta) \\ \partial_\theta P_l^m(\cos \theta) \\ m \frac{P_l^m(\cos \theta)}{\sin \theta} \\ m \frac{P_l^m(\cos \theta)}{\sin \theta} \\ \partial_\theta P_l^m(\cos \theta) \end{array} \right], \quad (4.50)$$

and the explicit form of the 'TE-type' modes will read:

$$\begin{aligned}
 (E_{1,n,l,m}^{(TE)})_r &= 0 & (E_{2,n,l,m}^{(TE)})_r &= 0 \\
 \left[ (E_{1,n,l,m}^{(TE)})_\theta = iE_1^{(TE)} j_l(k_1 r) \right. & & \left. (E_{2,n,l,m}^{(TE)})_\theta = iE_2^{(TE)} h_l(k_2 r) \right] m \frac{P_l^m(\cos \theta)}{\sin \theta} \\
 \left[ (E_{1,n,l,m}^{(TE)})_\phi = -E_1^{(TE)} j_l(k_1 r) \right. & & \left. (E_{2,n,l,m}^{(TE)})_\phi = -E_2^{(TE)} h_l(k_2 r) \right] \partial_\theta P_l^m(\cos \theta) \\
 \left[ (H_{1,n,l,m}^{(TE)})_r = -i\sqrt{\epsilon_1} E_1^{(TE)} \frac{j_l(k_1 r)}{k_1 r} \right. & & \left. (H_{2,n,l,m}^{(TE)})_r = -i\sqrt{\epsilon_2} E_2^{(TE)} \frac{h_l(k_2 r)}{k_2 r} \right] l(l+1) P_l^m(\cos \theta) , \\
 \left[ (H_{1,n,l,m}^{(TE)})_\theta = -i\sqrt{\epsilon_1} E_1^{(TE)} \frac{\partial_r (r j_l(k_1 r))}{k_1 r} \right. & & \left. (H_{2,n,l,m}^{(TE)})_\theta = -i\sqrt{\epsilon_2} E_2^{(TE)} \frac{\partial_r (r h_l(k_2 r))}{k_2 r} \right] \partial_\theta P_l^m(\cos \theta) \\
 \left[ (H_{1,n,l,m}^{(TE)})_\phi = \sqrt{\epsilon_1} E_1^{(TE)} \frac{\partial_r (r j_l(k_1 r))}{k_1 r} \right. & & \left. (H_{2,n,l,m}^{(TE)})_\phi = \sqrt{\epsilon_2} E_2^{(TE)} \frac{\partial_r (r h_l(k_2 r))}{k_2 r} \right] m \frac{P_l^m(\cos \theta)}{\sin \theta}
 \end{aligned} \tag{4.51}$$

For TM-type modes (4.50), application of boundary conditions (4.49) yields the equations:

$$\begin{cases} \epsilon_1 E_1^{(TM)} j_l(k_1 R) = \epsilon_2 E_2^{(TM)} h_l(k_2 R) \\ E_1^{(TM)} (j_l(k_1 R) + k_1 R j_l'(k_1 R)) = E_2^{(TM)} (h_l(k_2 R) + k_2 R h_l'(k_2 R)) \end{cases} , \tag{4.52}$$

where  $h_l \equiv h_l^{(1)}$ . Thus, the dispersion relation for TM-type modes reads:

$$\epsilon_2 h_l(k_2 R) [j_l(k_1 R) + k_1 R j_l'(k_1 R)] = \epsilon_1 j_l(k_1 R) [h_l(k_2 R) + k_2 R h_l'(k_2 R)]. \tag{4.53}$$

For TE-type modes (4.51), application of boundary conditions (4.49) yields the equations:

$$\begin{cases} E_1^{(TE)} j_l(k_1 R) = E_2^{(TE)} h_l(k_2 R) \\ E_1^{(TE)} (j_l(k_1 R) + k_1 R j_l'(k_1 R)) = E_2^{(TE)} (h_l(k_2 R) + k_2 R h_l'(k_2 R)) \end{cases} . \tag{4.54}$$

Thus, the dispersion relation for TE-type modes reads:

$$h_l(k_2 R) [j_l(k_1 R) + k_1 R j_l'(k_1 R)] = j_l(k_1 R) [h_l(k_2 R) + k_2 R h_l'(k_2 R)] \tag{4.55}$$

The solutions  $\hbar\omega_{n,l}$  for TM-type modes (4.53) and TE-type modes (4.55) are shown in Figures 4.5 (real part) and 4.6 (imaginary part). As it can be observed in Figure 4.6, these radiative (i.e. not confined) modes are rather long lived, since the imaginary part of the eigenenergy is small for all of them. We also notice that TE modes with smaller  $l$  have shorter lifetimes, while for TM modes the dependence is more complex.



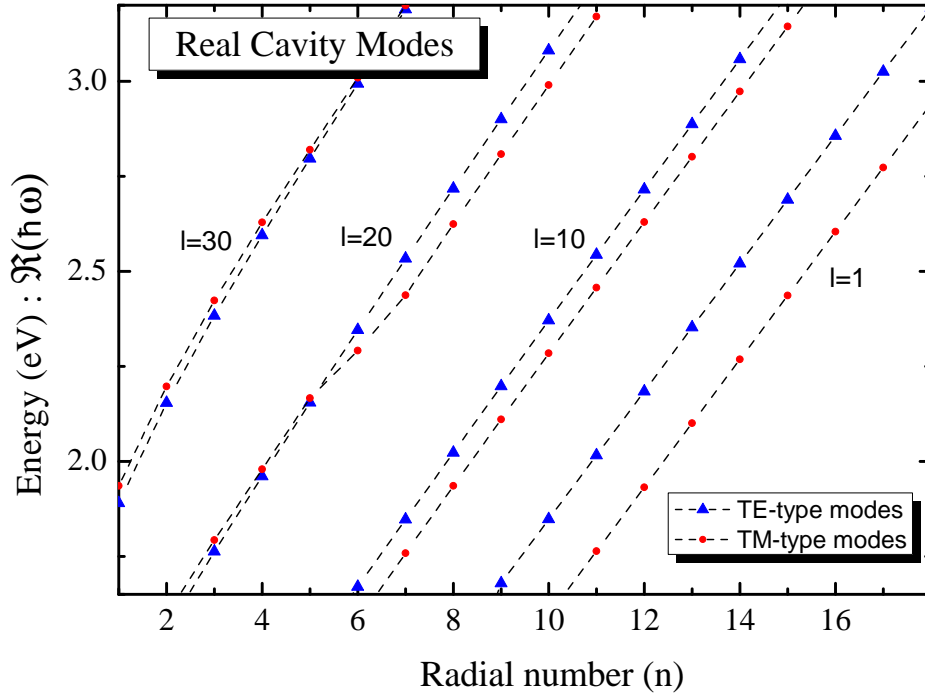


Figure 4.5: Real part of the solutions to equations for TM-type modes (4.53) and TE-type modes (4.55). The radius of the sphere is  $R = 2 \mu\text{m}$ ,  $\epsilon_1 = 3.4$  and  $\epsilon_2 = 1$ .

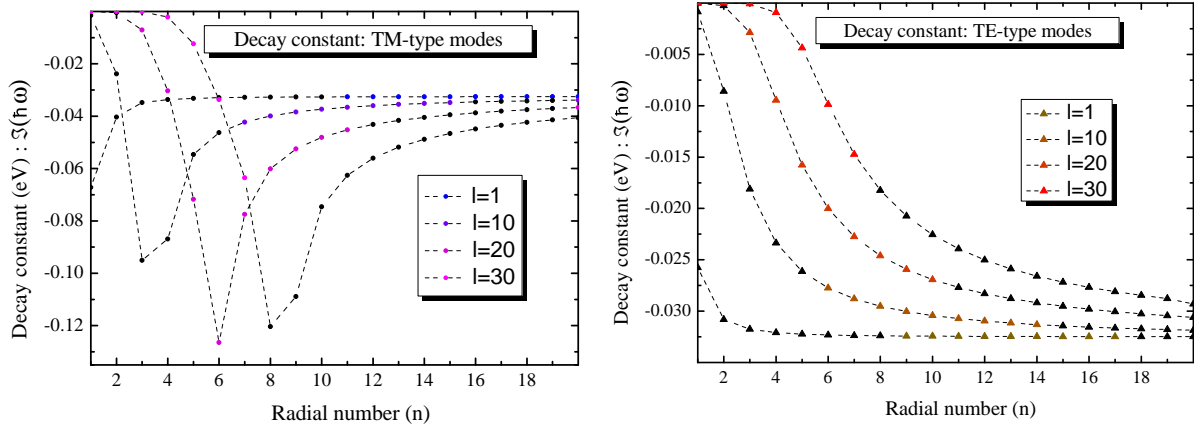


Figure 4.6: Imaginary parts of the solutions to the equation for TM-type modes (4.53) on the left and TE-type modes (4.55) on the right. Modes outside the visible range (1.65 to 3.1 eV) have been painted black. Note that the higher the angular momentum  $l$  of a mode, the higher its lifetime. The radius of the sphere is  $R = 2 \mu\text{m}$ ,  $\epsilon_1 = 3.4$  and  $\epsilon_2 = 1$ .

### 4.3.2 Local density of states

The local density of states for real cavity modes must take into account the mode volume for a photon that can be either inside or outside the cavity. The integration will be made up to  $R_I = 300 \mu\text{m}$ . Also, the approximation of considering only the real part of the eigenmodes will be made, to make  $k_1 \rightarrow \Re(k_1)$  and  $k_2 \rightarrow \Re(k_2)$ . As such, in this approximation:

$$\begin{cases} |h(z)|^2 = j^2(z) + y^2(z) \\ |h'(z)|^2 = j'(z)^2 + y'(z)^2 \end{cases} \quad (4.56)$$

The mode volume is then calculated by inputting equations (4.50) for TM modes and (4.51) for TE modes into (4.40), which, according to the calculations performed in appendix B, yields:

$$\Omega_{n,l,m}^{(TM)} = \Omega_{1,n,l,m}^{(TM)} + \left( \frac{\epsilon_1 j_l(k_1 R)}{\epsilon_2 h_l(k_2 R)} \right)^2 \Omega_{2,n,l,m}^{(TM)}, \quad (4.57)$$

$$\Omega_{n,l,m}^{(TE)} = \Omega_{1,n,l,m}^{(TE)} + \left( \frac{j_l(k_1 R)}{h_l(k_2 R)} \right)^2 \Omega_{2,l,m,n}^{(TE)}, \quad (4.58)$$

where

$$\Omega_{1,l,m,n}^{(TM/TE)} = \frac{2\pi}{k_1^3} \frac{2l(l+1)(l+m)!}{(2l+1)(l-m)!} \left[ z(j_l(z) + zj'_l(z))^2 + zj_l^2(z) [z^2 - l(l+1)] \right] \Big|_0^{k_1 R}, \quad (4.59)$$

where  $R$  is the radius of the cavity. And for the outside, the integral up to a radius  $R_I$  yields:

$$\begin{aligned} \Omega_{2,l,m,n}^{(TM/TE)} = \frac{2\pi}{k_2^3} \frac{2l(l+1)(l+m)!}{(2l+1)(l-m)!} & \left( \left[ z(j_l(z) + zj'_l(z))^2 + zj_l^2(z) [z^2 - l(l+1)] \right] \Big|_{k_2 R}^{k_2 R_I} + \right. \\ & \left. \left[ z(y_l(z) + zy'_l(z))^2 + zy_l^2(z) [z^2 - l(l+1)] \right] \Big|_{k_2 R}^{k_2 R_I} \right), \end{aligned} \quad (4.60)$$

with  $k_1 = k_{1,l,m,n}^{(TM)}$  and  $k_2 = k_{2,l,m,n}^{(TM)}$  or  $k_1 = k_{1,l,m,n}^{(TE)}$  and  $k_2 = k_{2,l,m,n}^{(TE)}$ . The local density of states will still be given by equation (4.37):

$$\rho_{loc}(r, E) = \sum_{n,l,m} \sum_{\sigma=TM,TE} |\mathbf{E}_{l,m}^{(\sigma)}(\mathbf{r}, E)|^2 \delta(E - E_{n,l}^{(\sigma)}). \quad (4.61)$$

but now the fields  $\mathbf{E}_{l,m}$  are the real cavity fields (4.50) and (4.51), with the real cavity mode volumes (4.57) and (4.58) used to determine the amplitude:

$$\begin{cases} E_1^{(TM)}(n, l, m) = \sqrt{\frac{2\pi E_{n,l}^{(TM)}}{\epsilon \Omega_{n,l,m}^{(TM)}}} \\ E_1^{(TE)}(n, l, m) = \sqrt{\frac{2\pi E_{n,l}^{(TE)}}{\epsilon \Omega_{n,l,m}^{(TE)}}} \end{cases}, \quad (4.62)$$

In figures 4.7 and 4.8 some terms of the sum in (4.61) are presented, to show the difference in the angular dependence of each different  $m$  value.

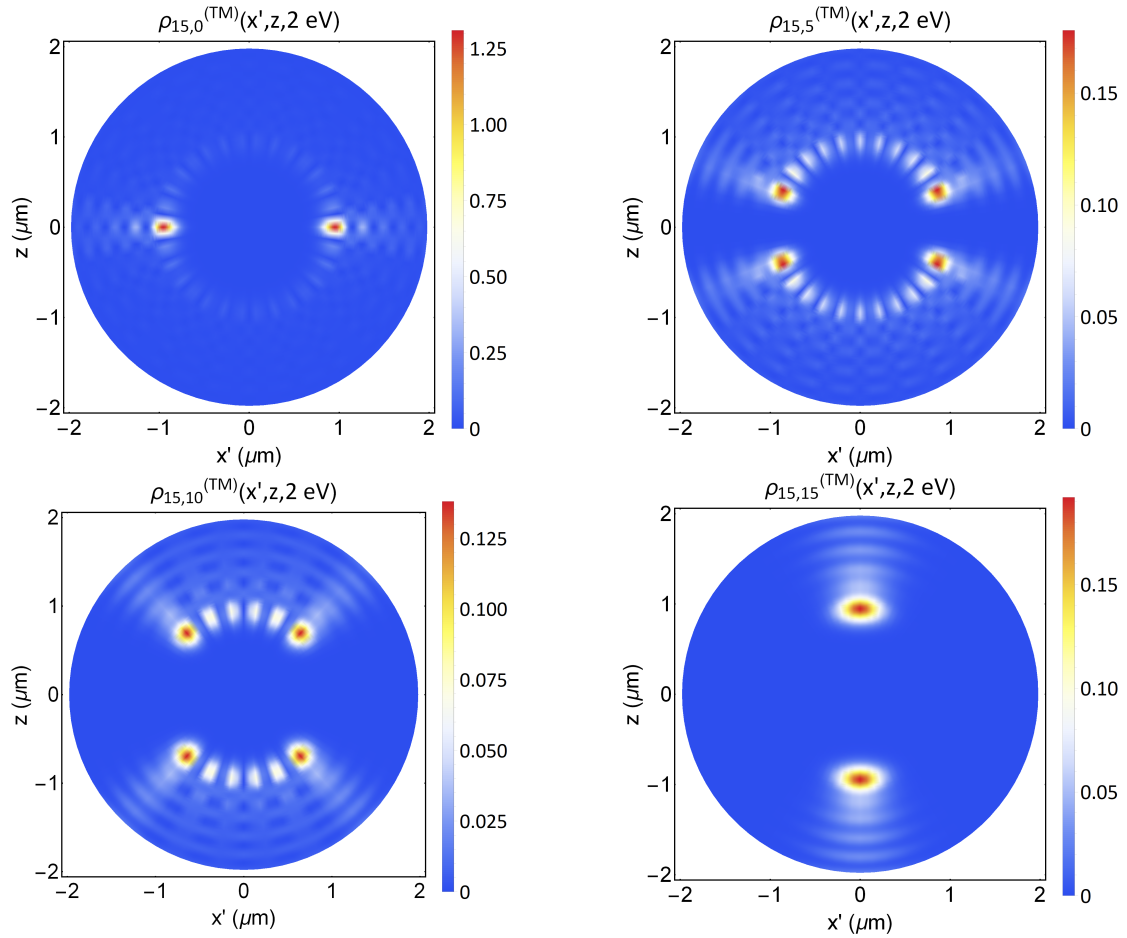


Figure 4.7: Evolution with respect to  $m$  of local densities of states for TM-type modes, real cavity with  $\epsilon_1 = 3.4$  inside the sphere and  $\epsilon_2 = 1$  outside. The local density of states ( $\rho_{l,m}$ ) is calculated according to equations (4.57)-(4.62) and using the electric field for real modes from equations (4.50). The  $l$  value used is  $l = 15$  and the  $m$  values shown are, from left to right,  $m = 0$ ,  $m = 5$ ,  $m = 10$  and  $m = 15$ . The circle  $(x', z)$  is any constant  $\phi$  cross-section of the sphere. The radius used was  $R = 2 \mu\text{m}$ , the energy at which the LDOS is calculated is 2 eV and only modes with  $0 < \hbar\omega < 4$  (eV) were considered.

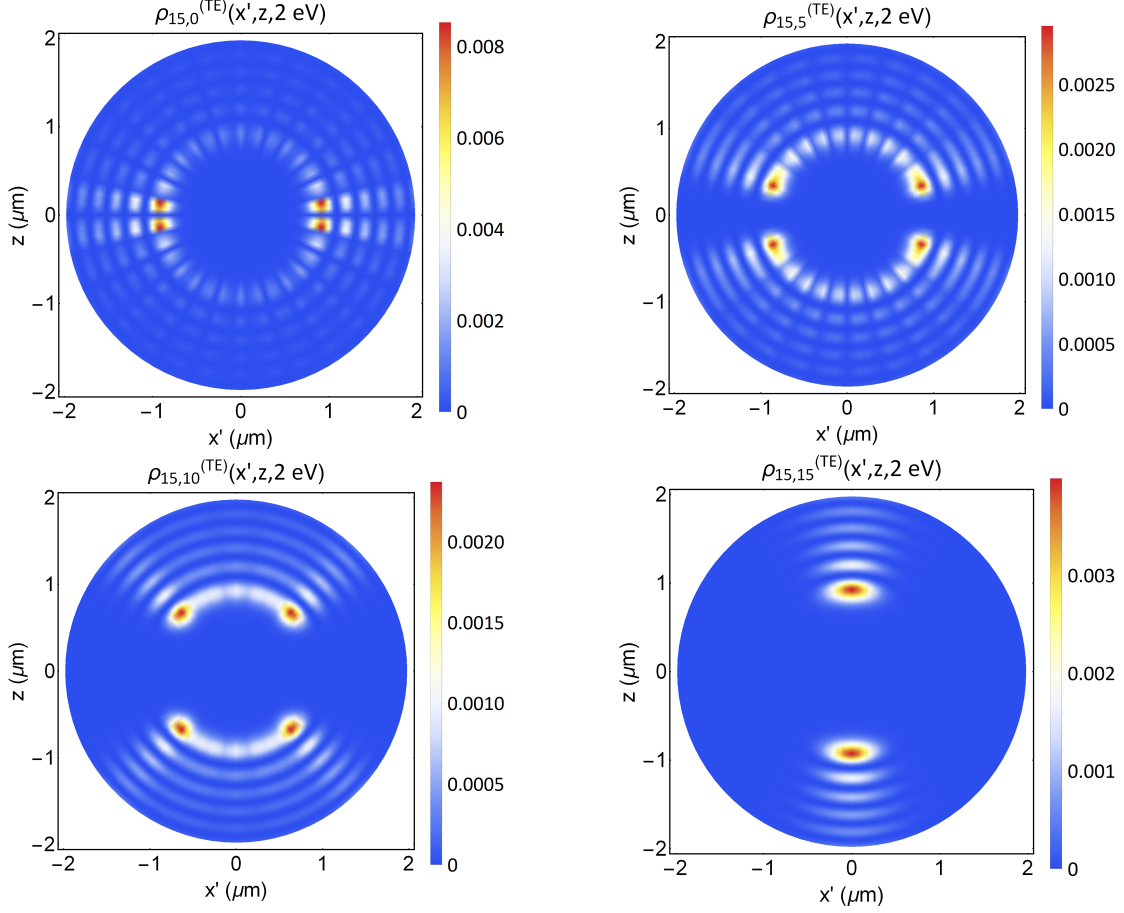


Figure 4.8: Evolution with respect to  $m$  of local densities of states for TE-type modes, real cavity with  $\epsilon_1 = 3.4$  inside the sphere and  $\epsilon_2 = 1$  outside. The local density of states ( $\rho_{l,m}$ ) is calculated according to equations (4.57)-(4.62) and using the electric field for real modes from equations (4.51). The  $l$  value used is  $l = 15$  and the  $m$  values shown are, from left to right,  $m = 0$ ,  $m = 5$ ,  $m = 10$  and  $m = 15$ . The circle  $(x', z)$  is any constant  $\phi$  cross-section of the sphere.  $x'$  is the value on the  $x$  axis rotated by the angle  $\phi$ . The radius used was  $R = 2 \mu\text{m}$ , the energy at which the LDOS is calculated is 2 eV and only modes with  $0 < \hbar\omega < 6$  (eV) were considered.

## 4.4 Microsphere with incorporated point emitters

### 4.4.1 Geometrical optics model for weakly absorbing sphere

The local density of states describes the spatial distribution of the EM fields of the cavity. This distribution influences spontaneous emission of a molecule which is already in an excited state (the Purcell effect). However, if one wishes to study how the system absorbs incident light and the molecules become excited, the distribution of these incident photons must also be taken into account. It will be assumed that the absorption is only due to the presence of the point emitters and these are evenly distributed among its volume. Let us assume that the molecules are excited at a frequency well above their emission spectrum.

This would be a typical situation with quantum dot emitters [84]. Absorbed photons create excitons in quantum dots or molecules that relax toward the ground state and then recombine. The absorbed light will then be re-emitted according to the density of states of the EM fields of the cavity. If the absorption and emission events were coherent, one would have to solve the scattering problem for a weakly absorbing sphere first and obtain the relevant cross-sections (the Mie problem [19]) rather than just finding the LDOS of cavity modes. However, since such coherence does not exist, because of the exciton relaxation, the absorption and emission processes may be considered separately and here we shall analyse the emitters' excitation by external light. If we assume further that the excitation wavelength is short enough, a simple model of geometrical optics can be used as an approximation as already mentioned in the introduction to this chapter. This should be valid for  $R \gg \lambda$  where  $R$  is the radius of the sphere and  $\lambda$  the wavelength of the incident light.

We begin by considering the result from Bohren and Huffman's book [19] for the total energy absorbed, per unit time, by a sphere of small absorption coefficient  $\alpha$ , which reads:

$$\frac{dW_{abs}}{d\Theta_i} = I_i 2\pi R^2 \mathcal{T}(\Theta_i, n) \sum_{j=0}^{\infty} [\mathcal{R}(\Theta_i, 1/n) e^{-\alpha\xi}]^j (1 - e^{-\alpha\xi}) \cos \Theta_i \sin \Theta_i. \quad (4.63)$$

Here,  $I_i$  is the incident beam intensity,  $\mathcal{T}(\Theta_i, n)$  and  $\mathcal{R}(\Theta_i, n)$  are the transmittance and reflectance, respectively, for unpolarized incident light,  $\Theta_i$  is the angle of incidence (see Fig. 4.9),  $\xi$  is the path length between any two points (1-2 or 2-3 in figure 4.9) and  $\alpha$  is the absorption coefficient. The infinite series in (4.63) is just the geometric series, and the result is:

$$\sum_{j=0}^{\infty} [\mathcal{R}(\Theta_i, 1/n) e^{-\alpha\xi}]^j = \frac{1}{1 - \mathcal{R}(\Theta_i, 1/n) e^{-\alpha\xi}}. \quad (4.64)$$

If we assume a weakly absorbing sphere, then  $1 - e^{-\alpha\xi} \simeq \alpha\xi$  and  $\frac{1}{1 - \mathcal{R}(\Theta_i, 1/n) e^{-\alpha\xi}} \simeq \frac{1}{\mathcal{T}(\Theta_i, 1/n)}$ , since  $\mathcal{R} + \mathcal{T} = 1$ . Considering the reciprocal relations:

$$\begin{cases} \mathcal{R}(\Theta_t, 1/n) = \mathcal{R}(\Theta_t, n) \\ \mathcal{T}(\Theta_t, 1/n) = \mathcal{T}(\Theta_t, n) \end{cases} \quad (4.65)$$

this means that  $\mathcal{T}(\Theta_i, n)$  cancels with the infinite series in equation (4.63), yielding:

$$\frac{dW_{abs}}{d\Theta_i} \simeq \frac{4\pi R^3 \alpha}{n} I_i \cos \Theta_i \sqrt{n^2 - \sin^2 \Theta_i} \sin \Theta_i, \quad (4.66)$$

where  $n = \sqrt{\epsilon}$  is the refractive index and  $I_i$  the incident irradiance. As we shall see, the absorption does not occur uniformly inside the sphere, in particular, because typical rays avoid the sphere's centre (notice the factor  $\sin \Theta_i \cos \Theta_i$  in 4.66). The absorption does not occur uniformly, since transmitted light inside the sphere will spend more time in some regions than in others. The plane of incidence formed by a representative ray and the normal to the spherical surface in the point of incidence makes a diametral cross-section of the sphere, a circle of sphere's radius  $R$ , described by the equation  $\phi = const$ , in spherical coordinates. This means one only needs to examine the circle shown in Figure 4.9b.

#### 4.4.2 Concentration of rays with respect to position

In this section, we will obtain the absorbed power with respect to positions in the circle of figure (4.9) and this density will depend on the angle of incidence  $\Theta_i$ . We start by tracing one of the partial paths of

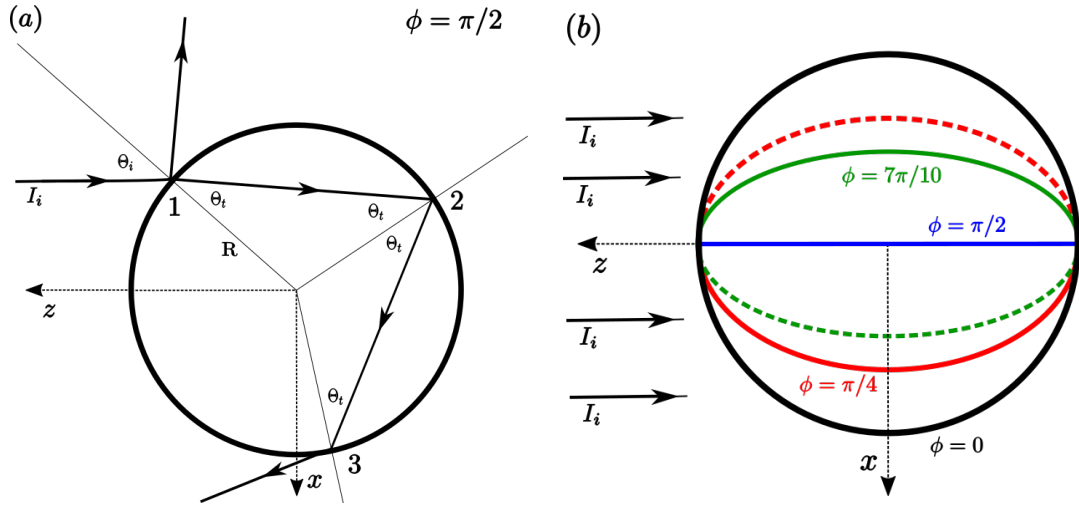


Figure 4.9: (a) Cross-section of a sphere with incident radiation of intensity  $I_i$ . The first two reflections are depicted, (but there are more). Equation (4.66) takes into account all reflections. (b) Side view of the sphere, showing projections of different diametric cross-sections onto  $zOx$  plane. All circles obeying equation  $\phi = \text{const}$  are similar and will exhibit the same distribution of transmitted radiation. This symmetry means that it is only necessary to study one of these circles.

a representative ray in polar coordinates.

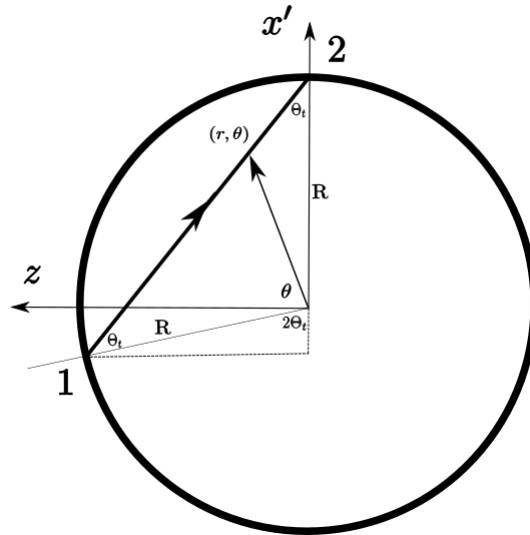


Figure 4.10: Schematic of the coordinate system used to determine the positions along the ray path.

In figure 4.10,  $x'$  is the  $x$  axis rotated around the  $z$  axis by the angle  $\phi$ . The ray travels at a constant speed from point 1 to point 2 in figure 4.10. Point 1's radius-vector is:

$$\vec{r}_1(\theta_t) = -R \cos(2\theta_t) \hat{x}' + R \sin(2\theta_t) \hat{z}, \quad (4.67)$$

and point 2's one is:

$$\vec{r}_2 = R\hat{x}'. \quad (4.68)$$

The radius-vector along the ray can therefore be written as:

$$\vec{r}(t, \Theta_t) = \vec{r}_1(\Theta_t) + \frac{\vec{r}_2 - \vec{r}_1(\Theta_t)}{t_{1,2}}t, \quad (4.69)$$

where  $t_{1,2}$  is the time it takes for the ray to travel between the two points. Now, the function we are looking for is the fraction of the time  $t_{1,2}$  that is spent in the interval  $dr$  of distances to the centre of the sphere. This is, by definition:

$$\frac{\delta t}{t_{1,2}} = \frac{1}{t_{1,2}} \frac{dt}{dr} dr. \quad (4.70)$$

Since the speed of the ray is constant,  $\frac{\delta t}{t_{1,2}} = \frac{\delta \xi}{\xi}$ . Therefore, the fraction of the path that lies in the interval  $dr$  is:

$$\frac{1}{\xi} \frac{d\xi}{dr} = \frac{1}{t_{1,2}} \frac{dt}{dr}. \quad (4.71)$$

The calculation of this quantity is presented in appendix F, the result is:

$$\Re\left[\frac{1}{\xi} \frac{d\xi}{dr}\right] = \begin{cases} \pm \frac{r}{2R \cos(\Theta_t) \sqrt{r^2 - R^2 \sin^2(\Theta_t)}}, & R \sin(\Theta_t) < r < R \\ 0, & r < R \sin(\Theta_t) \end{cases}. \quad (4.72)$$

The plus or minus signs have to do with whether the ray is on the first half (decreasing  $r$ ) or the second half (increasing  $r$ ) of the journey from point 1 to point 2 in Figure 4.10. For the purpose of defining this density this is irrelevant and we can sum the two cases to conclude that the density we are looking for is:

$$\mathcal{D}(r, \Theta_t) = 2 \left| \Re\left[\frac{1}{\xi} \frac{d\xi}{dr}\right] \right| \quad (4.73)$$

$$\mathcal{D}(r, \Theta_t) = \begin{cases} \frac{r}{R \cos(\Theta_t) \sqrt{r^2 - R^2 \sin^2(\Theta_t)}}, & r > R \sin(\Theta_t) \\ 0, & r < R \sin(\Theta_t) \end{cases}. \quad (4.74)$$

This quantity is such that:

$$\int_0^R \mathcal{D}(r, \Theta_t) dr = 1, \quad (4.75)$$

for each  $\Theta_i$ . Since this quantity is only concerned with the variations over  $r$  values, this term would factor out of the sum in (4.63). As such, the calculation for  $W_{abs}$  remains unaffected if we include this term in each of the successive reflections, and it can be stated from (4.66) that:

$$\frac{d\mathcal{W}_{abs}(r)}{d\Theta_i} = \frac{4\pi R^3 \alpha}{n} I_i \cos \Theta_i \sqrt{n^2 - \sin^2 \Theta_i} \sin \Theta_i \frac{1}{\xi} \mathcal{D}(r, \Theta_t) \quad (4.76)$$

where  $\mathcal{W}_{abs}(r)$  is the final distribution of energy absorbed, per unit time and unit length, that we are looking for. It is related to the total energy absorbed per unit time  $W_{abs}$  by:

$$\int_0^R \mathcal{W}_{abs}(r) dr = W_{abs}. \quad (4.77)$$

By Snell's law,

$$\sin \Theta_t = \frac{\sin \Theta_i}{n}. \quad (4.78)$$

We can perform the change of variable to the transmitted angle:

$$n \cos \Theta_t d\Theta_t = \cos \Theta_i d\Theta_i, \quad (4.79)$$

yielding:

$$\mathcal{W}_{abs}(r) = 4\pi n^2 R^3 \alpha I_i \int_0^{\sin^{-1} \frac{1}{n}} \cos^2 \Theta_t \sin \Theta_t \mathcal{D}(r, \Theta_t) d\Theta_t. \quad (4.80)$$

Inserting our calculated  $\mathcal{D}(r, \Theta_t)$  from (4.74) yields:

$$\mathcal{W}_{abs}(r) = 4\pi n^2 R^2 r \alpha I_i \int_0^{\sin^{-1} \frac{1}{n}} \frac{\cos \Theta_t \sin \Theta_t}{\sqrt{r^2 - R^2 \sin^2 \Theta_t}} H(r - R \sin \Theta_t) d\Theta_t. \quad (4.81)$$

$H(x)$  is the Heaviside function. Now, by changing variables to  $x = \sin \Theta_t$  and rearranging the Heaviside theta, this becomes:

$$\mathcal{W}_{abs}(r) = 4\pi n^2 R r \alpha I_i \int_0^{\frac{1}{n}} \frac{x}{\sqrt{\frac{r^2}{R^2} - x^2}} \Theta\left(\frac{r^2}{R^2} - x^2\right) dx. \quad (4.82)$$

$$\mathcal{W}_{abs}(r) = \begin{cases} 4\pi n^2 R r \alpha I_i \int_0^{\frac{r}{R}} \frac{x}{\sqrt{\frac{r^2}{R^2} - x^2}} dx, & r < \frac{R}{n} \\ 4\pi n^2 R r \alpha I_i \int_0^{\frac{1}{n}} \frac{x}{\sqrt{\frac{r^2}{R^2} - x^2}} dx. & r > \frac{R}{n} \end{cases} \quad (4.83)$$

The integral is easy to solve (substitution  $u = \frac{r^2}{R^2} - x^2$ ) and it yields either  $r/R$  or  $\frac{r}{R} - \sqrt{\frac{r^2}{R^2} - \frac{1}{n^2}}$ . The previous expression thus becomes:

$$\mathcal{W}_{abs}(r) = \begin{cases} 4\pi n^2 \alpha I_i r^2, & r < \frac{R}{n} \\ 4\pi n^2 \alpha I_i r \left( r - \sqrt{r^2 - \frac{R^2}{n^2}} \right), & r > \frac{R}{n} \end{cases}. \quad (4.84)$$

This is the distribution that we are looking for. This treatment is only concerned with the  $r$  distribution, and a more complete description would need to include the term  $\frac{1}{\xi} \frac{d\xi}{d\theta}$  to account for the different absorption rates at different  $\theta$ . It would be in this function that the information about the direction of the incident light would be contained. Namely, for smaller  $\theta$  the absorption would be stronger since it is the left side of the sphere ( $z$  axis in figure 4.9) that is receiving the incident light. In the weak absorption regime, the absorption probability is the same in any part of the segment  $\xi$  because terms of order  $(\alpha\xi)^2$  are neglected. Thus, assuming that the absorption is determined only by the 'time spent at some distance from the centre ( $r$ )', or, equivalently, by the fraction of path between points 1 and 2 (Fig. 4.10),  $\delta\xi(r)$ , the angular variation of the distribution of absorbed energy will only be affected by the losses from each reflection at the sphere's boundary. However, if we were to consider uniform incidence from all angles, this description remains accurate as it stands, since in that case the isotropic assumption would hold. In a real experiment done with multiple spheres like this one, the incident light scatters from all the spheres and on average the incidence in each of the individual spheres is isotropic. The radial distribution of the absorbed energy given by Eq. 4.84 is shown in Fig. 4.11. As it can be observed in the figure, the absorption peak shifts to a smaller  $r$  inside the sphere with the increase of its refractive index.



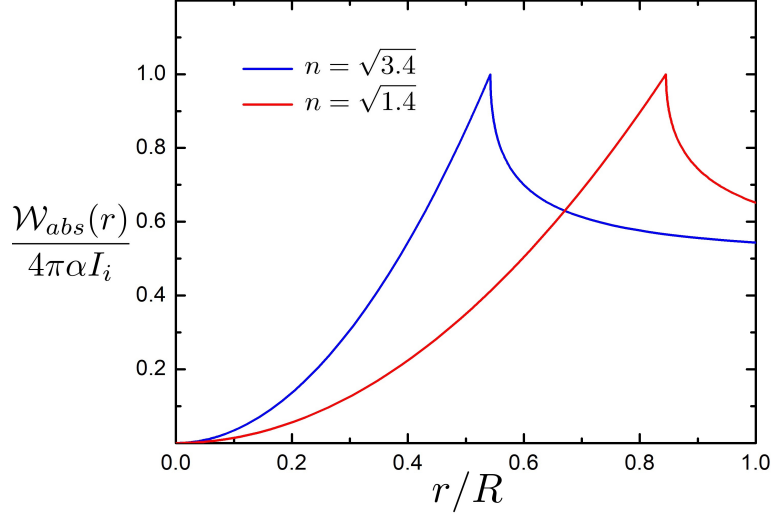


Figure 4.11: Plot of the density distribution of energy absorbed, per unit time and unit length, from equation (4.84) for two different  $n$  values. The point of maximum density occurs at  $r/R = 1/n$ . So, the index of refraction of the sphere determines this point. However, the value of this peak goes with  $1/n^2$ .

#### 4.4.3 Emission distribution inside the sphere

The combined effect on the overall intensity of light emitted will be proportional to both this distribution and the local density of states:

$$I(r) \propto \mathcal{W}_{abs}(r) \times \rho_{l,m}(r, x, E). \quad (4.85)$$

#### 4.4.4 Local emission rate

In order to excite the cavity modes studied a point emitter, like a Quantum Dot, can be placed at a point  $\mathbf{r}$  inside the sphere. Its transition dipole moment,  $\mathbf{d}$ , is oriented according to general angles  $\gamma$  and  $\psi$  in the local basis  $(x', y', z')$ . The electric field in the cavity is described by  $\mathbf{E}(\mathbf{r})$ , in the basis  $(x, y, z)$ . The vector of dipole moment  $\mathbf{d}$  can be cast in terms of these angles:

$$\begin{cases} d_x = d \sin \gamma \cos \psi \\ d_y = d \sin \gamma \sin \psi \\ d_z = d \cos \gamma \end{cases} . \quad (4.86)$$

The relevant matrix element is:

$$-(\mathbf{d} \cdot \mathbf{E}) = -(E_x \sin \gamma \cos \psi + E_y \sin \gamma \sin \psi + E_z \cos \gamma) d. \quad (4.87)$$

Averaging  $(\mathbf{d} \cdot \mathbf{E})^2$  over angles  $\gamma$  and  $\psi$  yields:

$$-\langle (\mathbf{d} \cdot \mathbf{E})^2 \rangle = \frac{1}{3} d^2 (E_x^2 + E_y^2 + E_z^2) = \frac{1}{3} d^2 E^2. \quad (4.88)$$

Therefore for any direction of local electric field the averaging gives the usual factor of 1/3. The local emission rate of an excited emitter is given by Eq. (3.113):

$$\Gamma(\vec{r}) = \Gamma_0 \frac{3\epsilon_1 \bar{p}^{-1} \sum_{n,l,m,\sigma} \rho_{n,l,m}^{(\sigma)}(\hbar\omega_0, \vec{r})}{2\pi \hbar\omega_0 \rho_0(\hbar\omega_0)}, \quad (4.89)$$

where  $\sigma = TM$  or  $TE$  and  $\bar{p}^{-1} = 1/3$ .  $\rho_0(\hbar\omega_0)$  is the local density of states for free space at the energy  $\hbar\omega_0$ . This has been shown, in chapter 3 (3.111), to be:

$$\rho_0(\hbar\omega_0) = \frac{8\pi}{\hbar\omega_0} \left( \frac{\eta}{\lambda_0} \right)^3 = \frac{\epsilon_1^{3/2} (\hbar\omega_0)^2}{\pi^2 (\hbar c)^3}. \quad (4.90)$$

A few chosen terms of the  $(l, m, \sigma)$  sums in the local densities of states were studied with three objectives: study the dependence of these modes on  $m$ , on the polarization  $\sigma$ , and most importantly the difference between the perfect cavity approximation and the study of a real cavity. The ideal cavity LDOS is studied in figures 4.3 and 4.4. The real cavity LDOS is studied in figures 4.7 and 4.8. From comparing the magnitudes in these figures we can conclude that the difference between real and ideal cavities is relevant and it is preferable to use the real cavity parameters, if possible. So, the attention will be turned to the complete local density of states for real cavity modes (4.61).

$$\rho_{loc}(r, E) = \rho_{loc}^{(TM)}(r, E) + \rho_{loc}^{(TE)}(r, E) = \sum_{n,l,m} \left( |\mathbf{E}_{l,m}^{(TM)}(\mathbf{r}, E)|^2 \delta(E - E_{n,l}^{(TM)}) + |\mathbf{E}_{l,m}^{(TE)}(\mathbf{r}, E)|^2 \delta(E - E_{n,l}^{(TE)}) \right). \quad (4.91)$$

For both polarizations, it will be useful to define a function from the mode volume (4.57)-(4.58) that does not depend on  $m$ :

$$\Lambda_{n,l}^{(\sigma)} \equiv \frac{(l-m)!}{(l+m)!} \Omega_{n,l,m}^{(\sigma)}. \quad (4.92)$$

Now we use (4.62) and the fields (4.50)-(4.51) to write the terms in (4.91) as:

$$\begin{aligned} \rho_{loc}^{(TM)}(r, E) &= \sum_{n,l,m} \frac{(l-m)!}{(l+m)!} \frac{2\pi E_{n,l}^{(TM)}}{\epsilon \Lambda_{n,l}^{(TM)}} \left[ \left( \frac{j_l(k_1 r)}{k_1 r} \right)^2 l^2 (l+1)^2 P_l^m(\cos x)^2 \right. \\ &\quad \left. + \left( \frac{\partial_r (r j_l(k_1 r))}{k_1 r} \right)^2 \left( (\partial_\theta P_l^m(\cos \theta))^2 + m^2 \left( \frac{P_l^m(\cos \theta)}{\sin \theta} \right)^2 \right) \right] \delta(E - E_{n,l}^{(TM)}). \end{aligned} \quad (4.93)$$

$$\begin{aligned} \rho_{loc}^{(TE)}(r, E) &= \\ &\sum_{n,l,m} \frac{(l-m)!}{(l+m)!} \frac{2\pi E_{n,l}^{(TE)}}{\epsilon \Lambda_{n,l}^{(TE)}} j_l^2(k_1 r) \left( (\partial_\theta P_l^m(\cos \theta))^2 + m^2 \left( \frac{P_l^m(\cos \theta)}{\sin \theta} \right)^2 \right) \delta(E - E_{n,l}^{(TE)}). \end{aligned} \quad (4.94)$$

The local density of states can not depend on the angle  $\theta$ , and thus on  $x = \cos \theta$ , because of the spherical symmetry of the system. We can therefore calculate  $\rho_{loc}$  for any given value of  $x$  and it must be the same regardless of the value of  $x$  we used. A convenient value is  $x \rightarrow 1-$ . This will allow us to solve the entire sum over all  $m$  analytically since it turns out that for  $x \rightarrow 1-$  only the  $m = -1, 1$  terms of the sums survive. In appendix H this is shown and the sums over  $m$  are determined analytically. Using the results from appendix H, (4.93) and (4.94) become:

$$\rho_{loc}^{(TM)}(r, E) = \sum_{n,l} \frac{2\pi E_{n,l}^{(TM)}}{\epsilon \Lambda_{n,l}^{(TM)}} \left[ \left( \frac{j_l(k_1 r)}{k_1 r} \right)^2 l^2 (l+1)^2 + \left( \frac{\partial_r (r j_l(k_1 r))}{k_1 r} \right)^2 l(l+1) \right] \delta(E - E_{n,l}^{(TM)}). \quad (4.95)$$

$$\rho_{loc}^{(TE)}(r, E) = \sum_{n,l} \frac{2\pi E_{n,l}^{(TE)}}{\epsilon \Lambda_{n,l}^{(TE)}} j_l^2(k_1 r) l(l+1) \delta(E - E_{n,l}^{(TE)}). \quad (4.96)$$

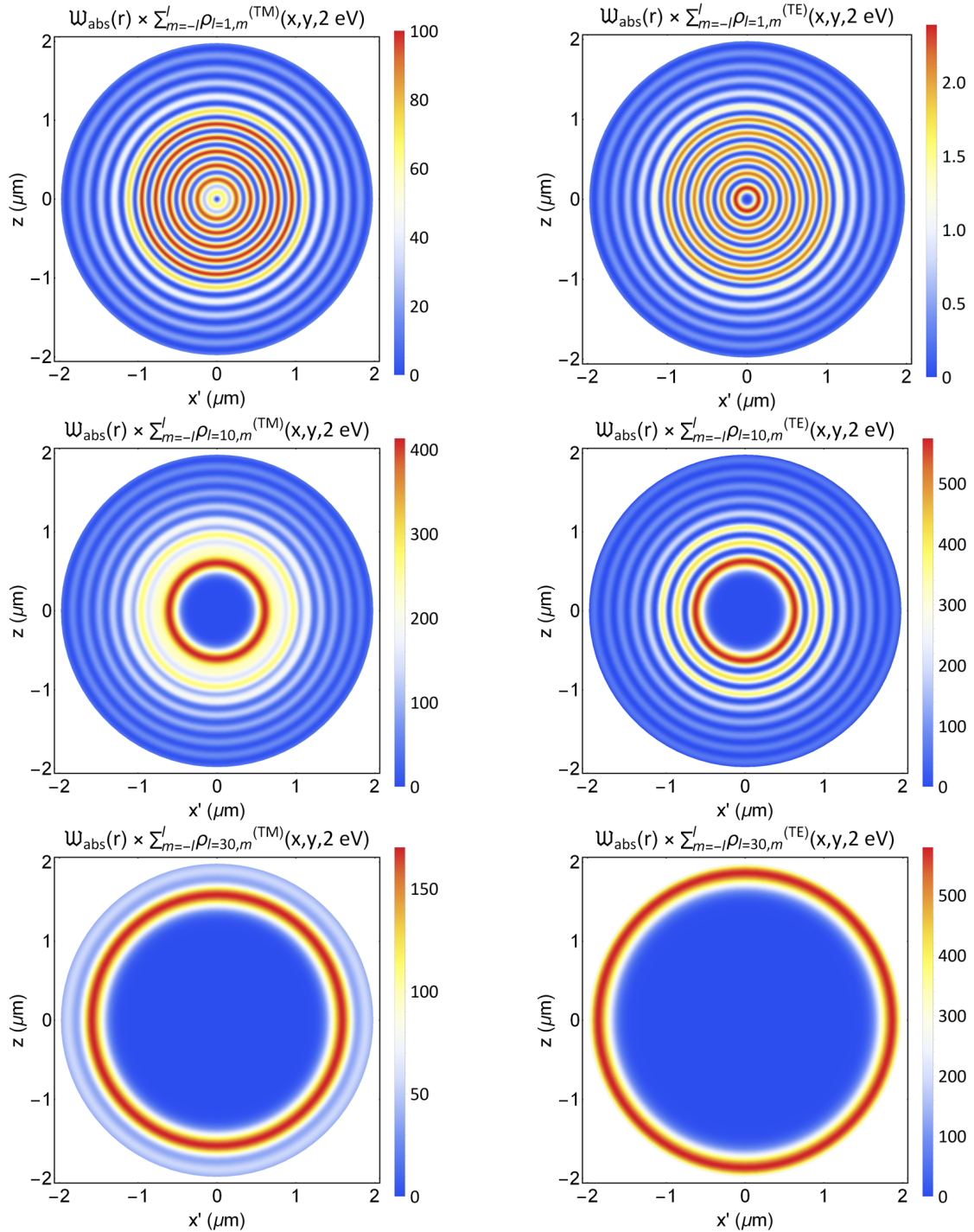


Figure 4.12: Evolution with relation to  $l$  of the sums of local densities of states multiplied by the intensity distribution  $\mathcal{W}_{abs}(r)$  for TE modes on the left and TM modes on the right. The  $l$  values shown are, from top to bottom,  $l = 1$ ,  $l = 10$  and  $l = 30$ . The circle  $(x', z)$  is any constant  $\phi$  cross-section of the sphere.  $x'$  is the value on the  $x$  axis rotated by the angle  $\phi$ . The radius used was  $R = 2 \mu\text{m}$ , the energy at which the LDOS is calculated is 2 eV and only modes with  $0 < \hbar\omega < 6$  (eV) were considered.

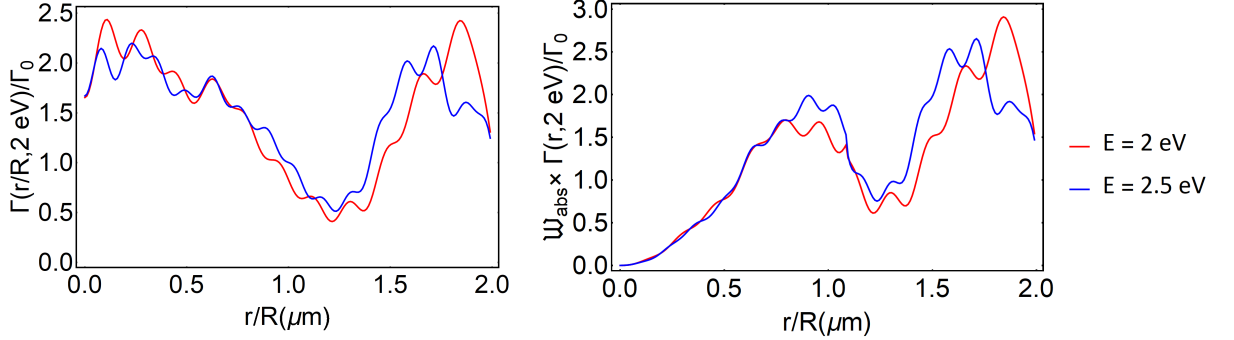


Figure 4.13: On the left, the normalized Purcell factor from (4.89), and on the right, the same factor multiplied by the intensity distribution  $\mathcal{W}_{abs}(r)$ . The  $l$  values used ranged from  $l = 1$  to  $l_{max} = 40$ . The criterion applied was to only use modes whose energies were smaller than  $\hbar\omega = 6$  eV. The radius used was  $R = 2 \mu\text{m}$ , the energies at which the LDOS is calculated are 2 and 2.5 eV.

From figure 4.13 we can conclude that, for a sphere of few microns in diameter one should expect an emission pattern consisting of two concentric rings, caused by smaller and larger values of  $l$ .

## 4.5 Continuous regime

If the size of the microspheres is large enough, the eigenmodes become compact in energy and tend to form a continuous spectrum where all the energies are allowed. At dimensions of about  $100 \mu\text{m}$ , as used in [83], this regime starts to apply virtually. We will study the densities of states for this continuous regimes. We wish to estimate the typical value of  $k$  for the modes in the continuous regime. If we consider an energy of 2 eV, then:

$$k = \frac{2 [\text{eV}]}{\hbar c}, \quad (4.97)$$

$$k = 10. [\mu\text{m}^{-1}] \quad (4.98)$$

For instance, for TE-type modes,  $k_{n,l} = \frac{\xi_{n,l}}{R\sqrt{\epsilon}}$ , where  $\xi_{n,l}$  are the zeros of the spherical Bessel function, and so, for  $R = 100 \mu\text{m}$ ,

$$\xi_{n,l} = 10^3 \sqrt{\epsilon} \gg 1. \quad (4.99)$$

So, the argument of the Bessel function, which can be written as  $\zeta \frac{r}{R}$  can be assumed to be large except near  $r = 0$ . The asymptotic behaviour of the Bessel functions [63] reads:

$$j_l(x) \simeq \frac{1}{x} \cos\left(x - (l+1)\frac{\pi}{2}\right), \quad (4.100)$$

for  $x \rightarrow \infty$ . And therefore the zeros can be approximated by the zeros of the sinusoidal function:

$$\xi_{n,l} \simeq \left(n + \frac{l}{2}\right)\pi. \quad (4.101)$$

Combining (4.99) and (4.101) we can conclude that modes with  $n$  and  $l$  values such that

$$\left(n + \frac{l}{2}\right)\pi \simeq 10^3 \sqrt{\epsilon} \quad (4.102)$$

yield energies close to 2 eV.

### 4.5.1 Total density of states

The total density of states is given in equations (4.35) and (4.36), and it reads:

$$\rho(E) = \sum_{n,l} (2l+1) \delta(E - E_{n,l}). \quad (4.103)$$

The Euler-MacLaurin formula can be used to evaluate nearly continuous sums [63]

$$\sum_{n=a}^b f(n) \simeq \int_a^b f(x) dx + \frac{f(a) + f(b)}{2}. \quad (4.104)$$

Applying this to equation (4.103) we can write:

$$\rho(E) \simeq \sum_n \int_1^\infty (2l+1) \delta(E - \alpha \xi_{n,l}) dl, \quad (4.105)$$

where  $\alpha = \frac{\hbar c}{\sqrt{\epsilon} R}$ . Using (4.101), this becomes:

$$\rho(E) = \sum_n \int_1^\infty (2l+1) \delta(E - \pi \alpha (n + l/2)) dl, \quad (4.106)$$

and using the Euler-MacLaurin formula again on  $n$ :

$$\rho(E) = \frac{2}{\pi \alpha} \int_1^N dn \left[ 4 \left( \frac{E}{\pi \alpha} - n \right) + 1 \right] + \frac{8}{\pi \alpha} \frac{E}{\pi \alpha} - \frac{4}{\pi \alpha} N - \frac{2}{\pi \alpha}, \quad (4.107)$$

Solving the integral yields:

$$\rho(E) = \frac{2}{\pi \alpha} \left[ 4 \left( \frac{E}{\pi \alpha} (N-1) - N^2/2 + 1/2 \right) + N - 1 \right] + \frac{8}{\pi \alpha} \frac{E}{\pi \alpha} - \frac{4}{\pi \alpha} N - \frac{2}{\pi \alpha}, \quad (4.108)$$

$$\rho(E) = -4 \frac{N^2}{\pi \alpha} + N \left( \frac{8E}{(\pi \alpha)^2} - \frac{2}{\pi \alpha} \right). \quad (4.109)$$

The maximum possible value of  $n$  is  $N = \frac{E}{\pi \alpha} - \frac{1}{2}$ , since it corresponds to the minimum value of  $l = 1$ . Using this:

$$\rho(E) = \frac{4E^2}{(\pi \alpha)^3} - \frac{2E}{(\pi \alpha)^2} + \frac{1}{\pi \alpha} \quad (4.110)$$

Since  $E \gg \pi \alpha$ , this is approximately equal to:

$$\rho(E) \simeq 4 \frac{E^2}{(\pi \alpha)^3} = 4 \frac{E^2}{\pi^3 c^3} \epsilon^{3/2} R^3. \quad (4.111)$$

Dividing by the volume:

$$\bar{\rho}(E) = \frac{1}{\frac{4\pi}{3} R^3} \rho(E) = \frac{3\epsilon^{3/2}}{\pi^4 c^3} E^2. \quad (4.112)$$

This approximation is off by a factor of  $\frac{6}{\pi^2}$  from the infinite space free density of states [10]:

$$\rho_0(E) = \frac{\epsilon^{3/2}}{2\pi^2 c^3} E^2, \quad (4.113)$$

but the approximation captures the  $E^2$  dependence.

### 4.5.2 Local density of states

Now we will attempt to determine the local density of states in the same continuous regime approximation. The mode volume (4.44) for TE-type modes reads:

$$\Omega_{l,m}^{(TE)} = 2\pi R^3 \frac{2l(l+1)(l+m)!}{(2l+1)(l-m)!} j_l'((n+l/2)\pi)^2. \quad (4.114)$$

Now, we can analyse the equations for the electric fields (4.46) together with (4.47) to find that they can be written as:

$$|\mathbf{E}_{l,m}^{(TE)}|^2 = \frac{\pi\alpha(n+\frac{l}{2})}{\epsilon R^3} \frac{(2l+1)(l-m)!}{2l(l+1)(l+m)!} \frac{j_l^2((n+l/2)\pi\frac{r}{R})}{j_l'((n+l/2)\pi)^2} \left[ (\partial_\theta P_l^m(\cos\theta))^2 + \left( m \frac{P_l^m(\cos\theta)}{\sin\theta} \right)^2 \right]. \quad (4.115)$$

Now, the local density of states (4.61) will be:

$$\rho_{loc}(E, r) = \sum_{n,l,m} \frac{\alpha(n+l/2)}{\epsilon R^3} \frac{(2l+1)}{2l(l+1)} \frac{j_l^2((n+l/2)\pi\frac{r}{R})}{j_l'((n+l/2)\pi)^2} \frac{(l-m)!}{(l+m)!} \left[ (\partial_\theta P_l^m(\cos\theta))^2 + \left( m \frac{P_l^m(\cos\theta)}{\sin\theta} \right)^2 \right] \delta(E - \pi\alpha(n+l/2)). \quad (4.116)$$

We will attempt to evaluate the angular term

$$\Theta_l^m(\theta) \equiv \frac{(l-m)!}{(l+m)!} \left[ (\partial_\theta P_l^m(\cos\theta))^2 + \left( m \frac{P_l^m(\cos\theta)}{\sin\theta} \right)^2 \right]. \quad (4.117)$$

We will change variables to  $x \equiv \cos(\theta)$ , so we can write this term as:

$$\Theta_l^m(x) \equiv \frac{(l-m)!}{(l+m)!} \left[ \left( -\sqrt{1-x^2} \partial_x P_l^m(x) \right)^2 + \frac{m^2}{1-x^2} P_l^m(x)^2 \right]. \quad (4.118)$$

The local density of states is not dependent on the angle  $\theta$ , because, due to the spherical symmetry of the system, no physical result can be asymmetric unless we had a source of asymmetry, such as incident light rays from a given direction, for instance. As such, we can choose the most convenient angle for the calculation. In appendix H, we choose to set  $\theta = 0$ , so  $x = 1$ , and using an asymptotic formula for  $x \rightarrow 1-$ , we concluded (5.159):

$$\sum_{m=-l}^{m=l} \Theta_l^m(x) = \frac{l(l+1)}{2}. \quad (4.119)$$

Using this result, the local density of states (4.116) will become:

$$\rho_{loc}(E, r) = \sum_{n,l} \frac{\hbar c(n+l/2)}{2\epsilon^{3/2} R^4} (2l+1) \frac{j_l^2((n+l/2)\pi\frac{r}{R})}{j_l'((n+l/2)\pi)^2} \delta(E - \pi\alpha(n+l/2)). \quad (4.120)$$

We evaluate this sum numerically using Lorentzian functions in place of the Dirac deltas for  $R = 100\mu m$ , which includes many terms. The only approximation we will be making is to consider only modes reasonably close to our chosen energy of  $E$ , such that, following from (4.102):

$$\frac{E}{\alpha} \left( 1 - \frac{\Gamma}{E} \right) < \left( n + \frac{l}{2} \right) \pi < \frac{E}{\alpha} \left( 1 + \frac{\Gamma}{E} \right), \quad (4.121)$$

where  $\Gamma$  is the width chosen for the Lorentzian functions, which will be  $\Gamma = 0.05$  eV and  $E = 2$  eV, and so:

$$10^3 \sqrt{\epsilon} \times 0.99 < \left(n + \frac{l}{2}\right) \pi < 10^3 \sqrt{\epsilon} \times 1.01. \quad (4.122)$$

Taking the same  $\epsilon$  as in [83], which was  $\epsilon = 1.33^2$ , we get the range:

$$419 < n + \frac{l}{2} < 428. \quad (4.123)$$

Also obeying the conditions  $l \geq 1$  and  $n \geq 0$ . From figure 4.13 we can conclude that, for a sphere of few

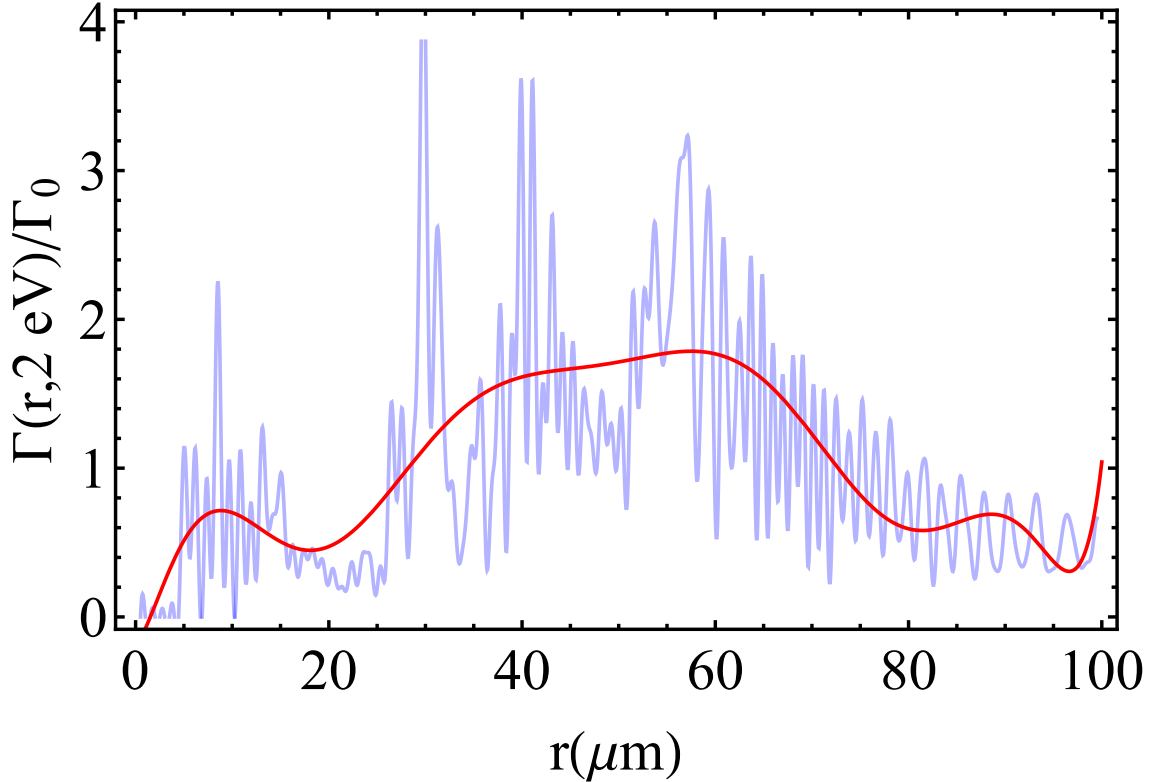


Figure 4.14: Variation of the Purcell factor defined by (4.89), which is a multiple of the complete local density of states, with the distance from the center of the sphere, in the approximation of a large sphere (4.120), for a constant  $E$  value of 2 eV. The total local density of states will be the sum of all possible  $n$  values, in this case, all 428 possible values. The radius of the sphere is  $R = 100 \mu\text{m}$ . The refractive index is  $n = \sqrt{\epsilon} = 1.33$ .

microns in diameter one should expect an emission pattern consisting of two concentric rings, caused by smaller and larger values of  $l$ . The results presented in 4.14 and 4.15 show that for spheres of the order of a hundred microns in size, where the EM eigenmodes distribution is nearly continuous, one can expect a single peak in the radial distribution of the emission intensity, which lies about half-way from the centre to the surface of the sphere. There are many spherical cavity modes contributing to this 'luminous ring', with large both orbital and radial numbers, i.e. the Whispering Gallery modes. The somewhat surprising result is that this ring is not attached to the sphere's surface.



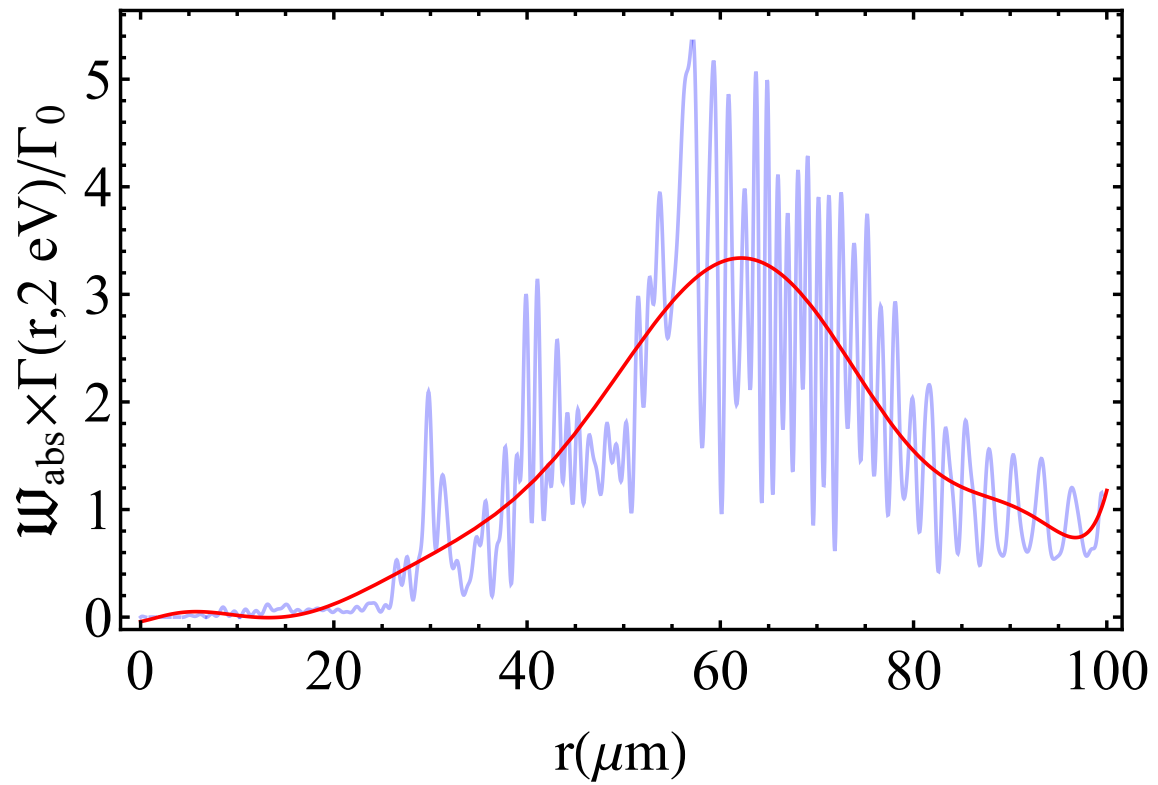


Figure 4.15: Variation of the Purcell factor defined by (4.89), multiplied by the incident ray distribution factor (4.84), with the distance from the center of the sphere, in the approximation of a large sphere (4.120), for a constant  $E$  value of 2 eV. The total local density of states will be the sum of all possible  $n$  values, in this case, all 428 possible values. The radius of the sphere is  $R = 100\mu\text{m}$ . The permittivity is  $\epsilon = 1.33$ .

# 5

## Conclusion

---

This thesis has been dedicated to the study of electromagnetic modes in different contexts, namely, in the form of plasmon-polaritons, magnon-polaritons, hybrid polaritons, exciton-polaritons, and pure photonic modes inside dielectric cavities. These modes arise from the collective electrical or magnetic excitations of multiple electrons. [4, 5] Graphene supports surface plasmons, which are oscillations of charge density in the sheet [9]. Antiferromagnets allow for the production of magnons, which are oscillations of the spin density. The spin carriers are affected by the magnetic field and when their spin changes direction it generates another magnetic field which influences the neighbouring spin carriers. Magnon-polaritons can be either bulk (inside the material) or surface (near the edge).

Interesting phenomena such as Rabi splitting or emission enhancement can be observed in microcavities, specially when combined with a material that allows for the formation of some type of excitation mentioned above. An optical micro-cavity is any closed space with partially or totally reflecting boundaries, with dimensions of the order of micro-meters, hence the name micro-cavity. [13] In chapter 2, a semiconductor is inserted (theoretically) into a microcavity in order to study its effect on the possible emission properties of the cavity. Semiconductors allow for the formation of excitons, which are pseudo-particles comprised of an electron in an excited state and the hole that it leaves behind in the valence band. The process of successive creation and destruction of excitons can be thought of as a particle called the exciton-polariton. [15, 16] Characteristic dispersion relations for these hybrid modes that combine photons and electrons were calculated in chapter 2, although involving different properties of the latter, for the system with graphene and antiferromagnet, and in chapter 3 for a cavity with a 2D semiconductor with exciton formation.

Firstly, in chapter 2, the properties of an antiferromagnetic material were combined with those of a nearby graphene sheet in order to theoretically study new types of hybrid polaritons, both TE and TM polarized, combining the effects of collective spin precession (magnons) inside the antiferromagnet with the effect of surface plasmon-polariton creation at the graphene sheet. It has been found that the doping of the graphene sheet can control the direction of propagation of the TE modes (negative group velocity in figure (2.3) for higher Fermi energies). Furthermore, when the scattering properties of this system were studied, it was found that the graphene sheet absorbs at high angles of incidence, as expected, but the absorption increases considerably for energies slightly above the antiferromagnet resonance (figure 2.6).

This can be explained by noting that waves with enough energy to cause resonance in the antiferromagnet allow the graphene sheet to receive more energy, and thus the two objects can work to enhance each other's properties. For TM modes, the addition of the graphene sheet causes the magnon-polariton fundamental mode to split into a lower mode and upper mode. The separation of these modes increases with the Fermi energy of graphene. As such, by doping the graphene sheet one can control the gap. When it comes to the scattering problem for TM modes, absorption at the graphene sheet remains low, both above and below the antiferromagnet energy (figures 2.9 and 2.10). Manipulating the properties of magnons can be useful for the purposes of spintronics, which is the creation of practical circuits through the manipulation of currents of spins instead of charges. [85, 86] Even though this study is performed with a bulk antiferromagnet, there have been discoveries of ferromagnetic and antiferromagnetic properties in 2D layers as well [87–91]. Combining these materials with 2D layers of graphene can lead to the observation of these effects but in the context of Van der Waals heterostructures. [20] The study of negative refraction is also possible for an antiferromagnet that also contains metallic properties (negative permeability). At energies lower than the resonance of the antiferromagnet the permeability can also be negative (2.27). Chapter 3 has been dedicated to the properties of exciton-polaritons that arise due to strong coupling of cylindrical cavity photon modes to 2D excitons confined in a TMD semiconductor layer placed inside the cavity. Such a system is feasible and may be used in on-chip optoelectronics, [52] and has advantages in comparison with planar MCs because of the lateral confinement of the EM field permitting to decrease the mode volume and therefore enhance light matter interaction. This exciton-mediated coupling is intrinsically strong enough for single- and few-layer TMDs and its enhancement by taking advantage of the MC effect can make these structure competitive with the traditional semiconductor materials used in optoelectronics. [35, 50, 51] The cylindrical geometry allows, in principle, for separate excitation of the cavity modes with different angular momenta ( $\mu$ ), which have distinct radial distribution of the EM field. For large  $\mu$ , so called whispering gallery modes can be formed with the field amplitude peaking near the lateral walls; such modes have been observed in semiconductor micropillars. [18, 92] The eigenfrequencies of polariton modes with different angular momenta and radial number  $\nu$  have been obtained and presented in the form of dispersion curves and DOS. Also, we showed that the simplified quantum model of the polariton modes taking into account coupling of a photon cavity mode with certain  $\mu$  and  $\nu$  only to two excitons with the (centre of mass) quantum numbers  $m = \mu \pm 1$  and the  $n = \nu$ , providing a reasonable description of them and yielding an explicit form of the Hopfield coefficients.

The coupling with the 2D layer causes a strong enhancement of the photonic density of states in the cavity, as we have demonstrated by calculating the photon-projected (i.e. weighted by the corresponding Hopfield coefficient) DOS for certain energies. In particular, it peaks near the exciton resonance energy (see Fig. 3.7) that, for a micrometer-diameter cavity is practically independent of  $m$  and  $n$ . The local photon-projected DOS shows a similar behaviour as a function of energy and it testifies the  $\mu$ -dependent spatial distribution of the photonic field outlined above. This quantity determines the spontaneous emission rate of a quantum emitter placed in the cavity, so the photoluminescence intensity of such an emitter will depend on its position or, seen from another point of view, on the direction of the light beam exciting the microcavity (by selecting cavity polariton modes with different  $\mu$ ). Such effects have been observed for micropillar cavities made of a bulk semiconductor, using either point defects [92] or QDs [18] as emitters. For 2D materials, such an emitter can be a trapped exciton in the TMD layer (emission energy below the free exciton one,  $E_{ex}$  or in a nearby h-BN layer [93] (emission above  $E_{ex}$ , in which case

an upconversion process [84, 94] is required for the excitation). We hope that the presented calculated results will help devising such experiments for microcavities with TMDs, in particular, aimed at building controllable single photon emitters. Single photon emission has been observed for various TMDs [75] and also from h-BN [93], presumably originated from the radiative recombination of excitons trapped on material defects. [93, 95] The location of such an emitter is random and, depending on the position it will couple to polariton modes with different angular momenta. This feature may be used to excite the emitters space-selectively. On the other hand, emitters with a relatively large absorption cross-section (such as QDs [84]) placed in the system in a controlled way may be used to create exciton-polaritons as suggested in Refs. [39, 77] or, in the case of cylindrical cavity, a particular class of them with certain angular momenta.

In chapter 3, the system under study is a simple spherical microcavity made of a dielectric material. Firstly, the dispersion relations for a perfect cavity (a dielectric sphere surrounded by a perfect metal, thus perfectly confined) and a 'real' cavity (a sphere of a dielectric material with another dielectric material surrounding it) were determined. It has been found, as expected, that higher energies arise from higher angular momenta of the modes. Furthermore, 'TE-type' modes (modes with no radial component of the electric field) have slightly higher energies than their 'TM-type' (modes with no radial component of the magnetic field) counterparts. This can be found in figure 4.2. As for real cavities, in the range of low radial numbers used (the first few solutions found for each angular momentum), the 'TE-type' modes have higher energies for low angular momenta but the 'TM-type' modes have higher energies for higher angular momenta. The crossover happens between angular momenta of about  $l = 25$ , depending on the radial number. This is found in figure 4.5. The real cavity modes have complex wavenumbers, and as such are subject to time decay. The study of the decay constants (figure 4.6) shows that the first few modes decay very slowly, and are thus more prevalent. For higher energy modes, the decay constant converges regardless of angular momentum at about 0.04 eV for 'TM-type' modes and 0.03 eV for 'TE-type' modes. The analysis of the local densities of states shows that in both cases the higher momentum modes are more concentrated near the surface and the low momentum modes near the center, and that the number  $m$  is responsible for the angular distribution of the modes. In fact, if we sum over all possible  $m$  we get a local density of states that is independent of the angular direction and only depends on the radial direction. Using methods similar to those used in chapter 2 (determination of eigenmodes, application of boundary conditions, determination of the local density of states and finally calculation of the Purcell factor) the expected distribution of light intensity inside the sphere, when illuminated by all sides, was calculated. The knowledge of the local densities of states, together with a simple ray optics calculation to determine the density of rays passing through a given area, allows us to determine the overall distribution of intensity of light, when the sphere is illuminated from the exterior. This calculation shows that the highest intensity is to be expected near the edge of the sphere, and the modes of higher angular momentum (whispering gallery modes) are the main contributors to this intensity. As with the cylindrical cavity, a quantum dot can be placed inside the sphere at the optimal location (calculated through the local Purcell factor) to enhance its emission with the help of the cavity confinement.

# Appendices

## A. Magnetization of an easy-axis antiferromagnet

In chapter 2, the system of equations (2.38)-(2.41) arises in the calculation of the magnetization of an easy-axis antiferromagnet in the presence of a static field. The system reads:

$$\frac{-i\omega}{\gamma}M_{1x} = M_{1y}(B_A + B_E + \mu_0 H_0) + M_{2y}B_E, \quad (5.1)$$

$$\frac{-i\omega}{\gamma}M_{1y} = M_S\mu_0 H_x - M_{2x}B_E - M_{1x}(B_A + B_E + \mu_0 H_0), \quad (5.2)$$

$$\frac{-i\omega}{\gamma}M_{2x} = -M_{2y}(B_A + B_E - \mu_0 H_0) - M_{1y}B_E, \quad (5.3)$$

$$\frac{-i\omega}{\gamma}M_{2y} = -M_S\mu_0 H_x + M_{1x}B_E + M_{2x}(B_A + B_E - \mu_0 H_0). \quad (5.4)$$

To simplify writing, we shall introduce the variables

$$\begin{cases} A = \frac{-i\omega}{\gamma} \\ B_- = B_A + B_E - \mu_0 H_0 \\ B_+ = B_A + B_E + \mu_0 H_0 \end{cases} . \quad (5.5)$$

We now reduce the system to two equations by writing only the equations for  $M_{1y}$  (5.2) and  $M_{2y}$  (5.4) multiplied by  $A$  and with  $AM_{1x}$  replaced by equation (5.1) and  $AM_{2x}$  replaced by equation (5.3):

$$A^2 M_{1y} = AM_S\mu_0 H_x - B_E(-M_{2y}B_- - B_E M_{1y}) - (M_{1y}B_+ + M_{2y}B_E)B_+, \quad (5.6)$$

$$A^2 M_{2y} = -AM_S\mu_0 H_x + (M_{1y}B_+ + M_{2y}B_E)B_E + (-M_{2y}B_- - M_{1y}B_E)B_-. \quad (5.7)$$

Organizing these equations:

$$M_{1y}(A^2 - B_E^2 + B_+^2) = AM_S\mu_0 H_x + M_{2y}B_E(B_- - B_+), \quad (5.8)$$

$$M_{2y}(A^2 - B_E^2 + B_-^2) = -AM_S\mu_0 H_x + M_{1y}B_E(B_+ - B_-). \quad (5.9)$$

Noting that  $B_- - B_+ = -2\mu_0 H_0$ , inserting (5.9) into (5.8) yields:

$$M_{1y}(A^2 - B_E^2 + B_+^2) = AM_S\mu_0 H_x - 2\mu_0 H_0 B_E \frac{-AM_S\mu_0 H_x + M_{1y}B_E 2\mu_0 H_0}{A^2 - B_E^2 + B_-^2}, \quad (5.10)$$

and this allows us to obtain  $M_{1y}$ :

$$M_{1y} \left( A^2 - B_E^2 + B_+^2 + \frac{(2\mu_0 H_0 B_E)^2}{A^2 - B_E^2 + B_-^2} \right) = AM_S \mu_0 H_x + \frac{2\mu_0^2 AM_S B_E H_0 H_x}{A^2 - B_E^2 + B_-^2}. \quad (5.11)$$

For  $M_{2y}$  we insert (5.8) into (5.9), which yields:

$$M_{2y} (A^2 - B_E^2 + B_-^2) = -AM_S \mu_0 H_x + 2\mu_0 H_0 B_E \frac{AM_S \mu_0 H_x - M_{2y} B_E 2\mu_0 H_0}{A^2 - B_E^2 + B_+^2}, \quad (5.12)$$

and now we isolate  $M_{2y}$ :

$$M_{2y} \left( A^2 - B_E^2 + B_-^2 + \frac{(2\mu_0 H_0 B_E)^2}{A^2 - B_E^2 + B_+^2} \right) = -AM_S \mu_0 H_x + \frac{2\mu_0^2 AM_S B_E H_0 H_x}{A^2 - B_E^2 + B_+^2}. \quad (5.13)$$

Now, multiplying (5.11) by  $A^2 - B_E^2 + B_-^2$  and (5.13) by  $A^2 - B_E^2 + B_+^2$  makes the factors of  $M_{1y}$  and  $M_{2y}$  become equal:

$$M_{1y} \left( (A^2 - B_E^2 + B_+^2) (A^2 - B_E^2 + B_-^2) + (2\mu_0 H_0 B_E)^2 \right) = (A^2 - B_E^2 + B_-^2) AM_S \mu_0 H_x + 2\mu_0^2 AM_S B_E H_0 H_x. \quad (5.14)$$

$$M_{2y} \left( (A^2 - B_E^2 + B_-^2) (A^2 - B_E^2 + B_+^2) + (2\mu_0 H_0 B_E)^2 \right) = - (A^2 - B_E^2 + B_+^2) AM_S \mu_0 H_x + 2\mu_0^2 AM_S B_E H_0 H_x. \quad (5.15)$$

Now we can sum (5.14) and (5.15) to obtain the total magnetization in  $y$ : ( $M_y = M_{1y} + M_{2y}$ )

$$M_y = \frac{\gamma^4 (B_-^2 - B_+^2) AM_S \mu_0 H_x + 4\gamma^4 \mu_0^2 AM_S B_E H_0 H_x}{\gamma^4 (A^2 + B_+^2 - B_E^2) (A^2 + B_-^2 - B_E^2) + (2\gamma^2 \mu_0 H_0 B_E)^2}. \quad (5.16)$$

Now to simplify the expression, we start by the calculating  $B_-^2 - B_+^2$ :

$$B_-^2 - B_+^2 = (B_A + B_E - \mu_0 H_0)^2 - (B_A + B_E + \mu_0 H_0)^2 \quad (5.17)$$

$$B_-^2 - B_+^2 = -4(B_A + B_E) \mu_0 H_0. \quad (5.18)$$

Now we use this to simplify the numerator of (5.16):

$$N(M_y) = \gamma^4 AM_S \mu_0 H_x (-4(B_A + B_E) \mu_0 H_0 + 4\mu_0 H_0 B_E), \quad (5.19)$$

$$N(M_y) = 4\gamma^3 i\omega M_S \mu_0 H_x B_A \mu_0 H_0, \quad (5.20)$$

$$N(M_y) = 4i\gamma\omega H_x \mu_0 H_0 \Omega_S^2, \quad (5.21)$$

where  $\Omega_S = \gamma\sqrt{\mu_0 M_S B_A}$ . Now we note that

$$\begin{cases} B_+^2 - B_E^2 = (B_A + B_E + \mu_0 H_0)^2 - B_E^2 \\ B_-^2 - B_E^2 = (B_A + B_E - \mu_0 H_0)^2 - B_E^2, \end{cases} \quad (5.22)$$

$$\begin{cases} B_+^2 - B_E^2 = (B_A + B_E)^2 - B_E^2 + \mu_0^2 H_0^2 + 2(B_A + B_E) \mu_0 H_0 \\ B_-^2 - B_E^2 = (B_A + B_E)^2 - B_E^2 + \mu_0^2 H_0^2 - 2(B_A + B_E) \mu_0 H_0, \end{cases} \quad (5.23)$$

$$\begin{cases} \gamma^2 (B_+^2 - B_E^2) = \Omega_0^2 + \gamma^2 \mu_0 H_0 (\mu_0 H_0 + 2B_A + 2B_E) \\ \gamma^2 (B_-^2 - B_E^2) = \Omega_0^2 + \gamma^2 \mu_0 H_0 (\mu_0 H_0 - 2B_A - 2B_E), \end{cases} \quad (5.24)$$

where  $\Omega_0 = \gamma \sqrt{2B_E B_A + B_A^2}$ . As such

$$\gamma^4 (B_+^2 - B_E^2) (B_-^2 - B_E^2) = (\Omega_0^2 + \gamma^2 \mu_0^2 H_0^2)^2 - 4\gamma^4 \mu_0^2 H_0^2 (B_A + B_E)^2 \quad (5.25)$$

and

$$\gamma^2 (B_+^2 - B_E^2) + \gamma^2 (B_-^2 - B_E^2) = 2\Omega_0^2 + 2\gamma^2 \mu_0^2 H_0^2. \quad (5.26)$$

Therefore, the denominator of (5.16) is:

$$D(M_y) = \omega^4 - \omega^2 \gamma^2 (B_+^2 - B_E^2) - \omega^2 \gamma^2 (B_-^2 - B_E^2) + \gamma^4 (B_+^2 - B_E^2) (B_-^2 - B_E^2) + 4\gamma^4 \mu_0^2 H_0^2 B_E^2, \quad (5.27)$$

$$D(M_y) = \omega^4 - 2\omega^2 (\Omega_0^2 + \gamma^2 \mu_0^2 H_0^2) + (\Omega_0^2 + \gamma^2 \mu_0^2 H_0^2)^2 - 4\gamma^4 \mu_0^2 H_0^2 (B_A + B_E)^2 + 4\gamma^4 (\mu_0 H_0 B_E)^2, \quad (5.28)$$

$$D(M_y) = \Omega_0^2 (\Omega_0^2 + 2\gamma^2 \mu_0^2 H_0^2 - 2\omega^2) + \omega^4 - 2\omega^2 \gamma^2 \mu_0^2 H_0^2 - 4\gamma^2 \mu_0^2 H_0^2 \Omega_0^2 + \gamma^4 \mu_0^4 H_0^4, \quad (5.29)$$

$$D(M_y) = \Omega_0^2 (\Omega_0^2 - 2\gamma^2 \mu_0^2 H_0^2 - 2\omega^2) + \omega^4 - 2\omega^2 \gamma^2 \mu_0^2 H_0^2 + \gamma^4 \mu_0^4 H_0^4, \quad (5.30)$$

$$D(M_y) = \Omega_0^2 (\Omega_0^2 - 2\gamma^2 \mu_0^2 H_0^2 - 2\omega^2) + (\omega^2 - \gamma^2 \mu_0^2 H_0^2)^2. \quad (5.31)$$

Now we complete the square of the second and third terms and separate the square difference of the last term:

$$D(M_y) = \Omega_0^2 \left( \Omega_0^2 - 2(\omega + \gamma B_0)^2 + 4\gamma B_0 \omega \right) + (\omega + \gamma B_0)^2 (\omega - \gamma B_0)^2, \quad (5.32)$$

$$D(M_y) = \Omega_0^2 \left( \Omega_0^2 - (\omega + \gamma B_0)^2 \right) - \Omega_0^2 (\omega + \gamma B_0)^2 + 4\Omega_0^2 \omega \gamma B_0 + (\omega + \gamma B_0)^2 (\omega - \gamma B_0)^2, \quad (5.33)$$

$$D(M_y) = \Omega_0^2 \left( \Omega_0^2 - (\omega + \gamma B_0)^2 \right) - \Omega_0^2 (\omega - \gamma B_0)^2 + (\omega + \gamma B_0)^2 (\omega - \gamma B_0)^2, \quad (5.34)$$

and thus

$$D(M_y) = \left( \Omega_0^2 - (\omega - \gamma B_0)^2 \right) \left( \Omega_0^2 - (\omega + \gamma B_0)^2 \right). \quad (5.35)$$

Now, with the knowledge of (5.21) and (5.35), the  $y$  magnetization can be written as

$$M_y = iH_x \Omega_S^2 \frac{4\gamma \omega B_0}{\left( \Omega_0^2 - (\omega - \gamma B_0)^2 \right) \left( \Omega_0^2 - (\omega + \gamma B_0)^2 \right)}, \quad (5.36)$$

and this can be separated into two fractions, by creating the square differences in the numerator, as such:

$$M_y = iH_x \Omega_S^2 \frac{4\gamma \omega B_0 + \Omega_0^2 - \Omega_0^2 - \omega^2 + \omega^2 + \gamma^2 B_0^2 - \gamma^2 B_0^2}{\left( \Omega_0^2 - (\omega - \gamma B_0)^2 \right) \left( \Omega_0^2 - (\omega + \gamma B_0)^2 \right)}, \quad (5.37)$$

$$M_y = iH_x \Omega_S^2 \frac{\left( \Omega_0^2 - (\omega - \gamma B_0)^2 \right) - \left( \Omega_0^2 - (\omega + \gamma B_0)^2 \right)}{\left( \Omega_0^2 - (\omega - \gamma B_0)^2 \right) \left( \Omega_0^2 - (\omega + \gamma B_0)^2 \right)}, \quad (5.38)$$

$$M_y = iH_x \Omega_S^2 \left( \frac{1}{\Omega_0^2 - (\omega + \gamma B_0)^2} - \frac{1}{\Omega_0^2 - (\omega - \gamma B_0)^2} \right). \quad (5.39)$$

Now we turn to  $M_x$ . The system (5.1)-(5.4) can be reduced to two equations (5.1) and (5.3) multiplied by  $A$ , with the values of  $AM_{1y}$  and  $AM_{2y}$  given by equations (5.2) and (5.4), respectively. Equations (5.1) and (5.3) then become:

$$A^2 M_{1x} = B_+ (M_S \mu_0 H_x - M_{2x} B_E - M_{1x} B_+) + B_E (-M_S \mu_0 H_x + M_{1x} B_E + M_{2x} B_-), \quad (5.40)$$

$$A^2 M_{2x} = -B_- (-M_S \mu_0 H_x + M_{1x} B_E + M_{2x} B_-) - B_E (M_S \mu_0 H_x - M_{2x} B_E - M_{1x} B_+). \quad (5.41)$$

Organizing these equations:

$$M_{1x} (A^2 + B_+^2 - B_E^2) = M_S \mu_0 H_x (B_+ - B_E) + B_E M_{2x} (B_- - B_+), \quad (5.42)$$

$$M_{2x} (A^2 + B_-^2 - B_E^2) = M_S \mu_0 H_x (B_- - B_E) + B_E M_{1x} (B_+ - B_-). \quad (5.43)$$

Now we can insert (5.43) into (5.42) to obtain ( $B_0 = \mu_0 H_0$ ):

$$M_{1x} (A^2 + B_+^2 - B_E^2) = M_S \mu_0 H_x (B_A + B_0) - 2B_E B_0 \frac{M_S \mu_0 H_x (B_A - B_0) + 2B_0 B_E M_{1x}}{A^2 + B_-^2 - B_E^2}, \quad (5.44)$$

$$M_{1x} \left( A^2 + B_+^2 - B_E^2 + 4 \frac{(B_E B_0)^2}{A^2 + B_-^2 - B_E^2} \right) = M_S \mu_0 H_x (B_A + B_0) - \frac{2B_E B_0 M_S \mu_0 H_x (B_A - B_0)}{A^2 + B_-^2 - B_E^2} \quad (5.45)$$

$$M_{1x} = \frac{\gamma^4 (A^2 + B_-^2 - B_E^2) M_S \mu_0 H_x (B_A + B_0) - 2\gamma^4 B_E B_0 M_S \mu_0 H_x (B_A - B_0)}{\gamma^4 (A^2 + B_+^2 - B_E^2) (A^2 + B_-^2 - B_E^2) + 4\gamma^4 B_E^2 B_0^2}, \quad (5.46)$$

Now we turn to  $M_{2x}$ , inserting (5.42) into (5.43) to obtain:

$$M_{2x} (A^2 + B_-^2 - B_E^2) = M_S \mu_0 H_x (B_A - B_0) + 2B_0 B_E \frac{M_S \mu_0 H_x (B_A + B_0) - 2B_0 B_E M_{2x}}{A^2 + B_+^2 - B_E^2}, \quad (5.47)$$

$$M_{2x} \left( A^2 + B_-^2 - B_E^2 + 4 \frac{(B_E B_0)^2}{A^2 + B_+^2 - B_E^2} \right) = M_S \mu_0 H_x (B_A - B_0) + 2B_0 B_E M_S \mu_0 H_x \frac{B_A + B_0}{A^2 + B_+^2 - B_E^2}, \quad (5.48)$$

$$M_{2x} = \frac{\gamma^4 (A^2 + B_+^2 - B_E^2) M_S \mu_0 H_x (B_A - B_0) + 2\gamma^4 B_0 B_E M_S \mu_0 H_x (B_A + B_0)}{\gamma^4 (A^2 + B_-^2 - B_E^2) (A^2 + B_+^2 - B_E^2) + 4\gamma^4 B_E^2 B_0^2}. \quad (5.49)$$

The  $x$  component of the total magnetization is

$$M_x = M_{1x} + M_{2x} \quad (5.50)$$

$$M_x = \gamma^4 M_S \mu_0 H_x \frac{2(A^2 - B_E^2) B_A + B_A (B_-^2 + B_+^2) + B_0 (B_-^2 - B_+^2) + 4B_0^2 B_E}{\gamma^4 (A^2 + B_+^2 - B_E^2) (A^2 + B_-^2 - B_E^2) + 4\gamma^4 B_E^2 B_0^2}. \quad (5.51)$$

The denominator is the same as in (5.16) and it has been calculated, resulting in (5.35). The numerator can be simplified further:

$$N(M_x) = B_A \left( 2A^2 - 2B_E^2 + 2(B_A + B_E)^2 + 2B_0^2 \right) - 4B_0^2 (B_A + B_E) + 4B_0^2 B_E, \quad (5.52)$$

$$N(M_x) = 2B_A (A^2 + B_A^2 + 2B_A B_E + B_0^2) - 4B_0^2 B_A, \quad (5.53)$$

$$N(M_x) = 2 \frac{B_A}{\gamma^2} (-\omega^2 + \Omega_0^2 - \gamma^2 B_0^2) \quad (5.54)$$



$$N(M_x) = \frac{B_A}{\gamma^2} \left( -(\omega - \gamma B_0)^2 + 2\omega\gamma B_0 + \Omega_0^2 - (\omega + \gamma B_0)^2 - 2\omega\gamma B_0 + \Omega_0^2 \right), \quad (5.55)$$

$$N(M_x) = \frac{B_A}{\gamma^2} \left( \Omega_0^2 - (\omega - \gamma B_0)^2 + \Omega_0^2 - (\omega + \gamma B_0)^2 \right). \quad (5.56)$$

Now we write  $M_x$  using (5.56) and (5.35):

$$M_x = H_x \Omega_S^2 \frac{\Omega_0^2 - (\omega - \gamma H_0)^2 + \Omega_0^2 - (\omega + \gamma H_0)^2}{\left( \Omega_0^2 - (\omega + \gamma B_0)^2 \right) \left( \Omega_0^2 - (\omega - \gamma B_0)^2 \right)}, \quad (5.57)$$

which finally becomes:

$$M_x = H_x \Omega_S^2 \left( \frac{1}{\Omega_0^2 - (\omega + \gamma B_0)^2} + \frac{1}{\Omega_0^2 - (\omega - \gamma B_0)^2} \right). \quad (5.58)$$

In conclusion, in this appendix we obtained (5.58) and (5.39):

$$M_y = iH_x \Omega_S^2 \left( \frac{1}{\Omega_0^2 - (\omega + \gamma B_0)^2} - \frac{1}{\Omega_0^2 - (\omega - \gamma B_0)^2} \right), \quad (5.59)$$

## B. Comparison of cylindrical cavity field profiles: ideal cavity *vs* exact solution for infinite cylinder

The EM fields used in this work correspond to an ideal cavity with its boundaries being perfect mirrors. However, in reality the contrast of the dielectric constant at the boundaries is finite. We shall compare these field profiles obtained within the ideal cavity model to exact solution of Maxwell's equations in the case of infinite cylinder where analytical solution is possible considering finite dielectric constant (and therefore non-zero field amplitudes) outside of the cylinder.

The equations that relate the transverse to the longitudinal components of the vector fields are

$$-\frac{i\omega\epsilon}{c} \vec{\mathbb{E}}_T = \left( \frac{1}{r} \frac{\partial H_z}{\partial \phi} - \frac{\partial H_\phi}{\partial z} \right); \quad \frac{i\omega}{c} \vec{\mathbb{H}}_T = \left( \frac{1}{r} \frac{\partial E_z}{\partial \phi} - \frac{\partial E_\phi}{\partial z} \right). \quad (5.60)$$

Due to the translational and axial symmetry of the cylindrical microcavity in Fig. 3.1, the electromagnetic fields  $\vec{\mathbb{E}}$  and  $\vec{\mathbb{H}}$  can be cast as

$$\vec{\mathbb{E}}(r, \phi, z) = \vec{E}(r)\Psi(\phi, z); \quad \vec{\mathbb{H}}(r, \phi, z) = \vec{H}(r)\Psi(\phi, z), \quad (5.61)$$

with  $\Psi(\phi, z) = e^{i(m\phi + k_z z)}$ . For the  $z$ -components it is possible to choose the solutions

$$E_z^{(j)} = A^{(j)} f_\mu^{(j)}(q_j r)\Psi(\phi, z); \quad H_z^{(j)} = B^{(j)} f_\mu^{(j)}(q_j r)\Psi(\phi, z); \quad (j = 1, 2), \quad (5.62)$$

where  $q_j^2 = \epsilon_i \omega^2 / c^2 - k_z^2$ ,  $\epsilon_1(\epsilon_2)$  is the inner (outer) dielectric constant. In Eq. (5.62)  $f_\mu^{(1)}$  is the Bessel function  $J_\mu(q_1 r)$  for  $0 \leq r \leq R$  and if  $q_2^2 > 0$  ( $q_2^2 = -\kappa^2 < 0$ ),  $f_\mu^{(2)}$  is the Hankel function of the first kind,  $\mathcal{H}_\mu^{(1)}(q_2 r)$  (MacDonald function  $K_\mu(|q_2| r)$ ) for  $r \geq R$ , both defined in Ref. [96].

Using Eqs. (5.60), the field transverse components are given by

$$\left[ E_r^{(j)}(r), E_\phi^{(j)}(r) \right] = \frac{1}{q_i^2 - k_z^2} \left[ -\frac{\omega\mu}{cr} B^{(j)} f_\mu^{(j)} + ik_z q_j A^{(j)} f_\mu^{(j)}, -i\frac{\omega q_j}{c} B^{(j)} f_\mu^{(j)} - \frac{\mu k_z}{r} A^{(j)} f_\mu^{(j)} \right]; \quad (5.63)$$

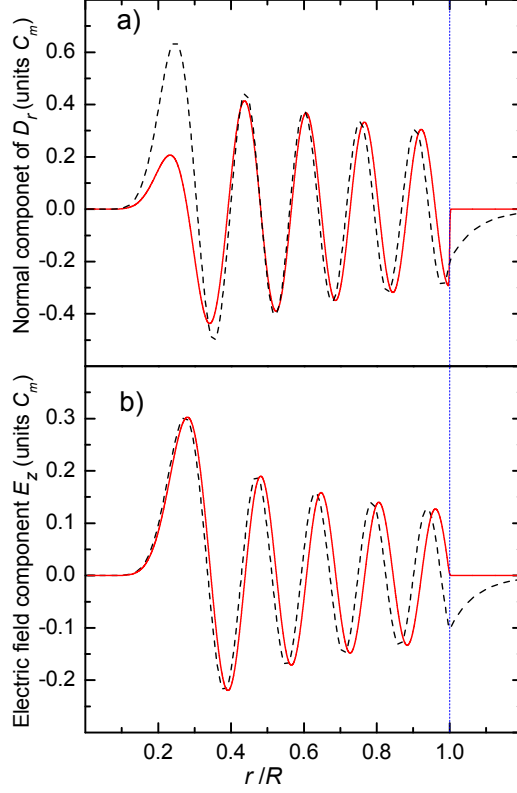


Figure 5.1: Comparison of the field components' profiles  $E_z$  and  $D_r$  from exact solution, Eq. (5.65) (dashed lines) and from the ideal cavity model, Eq. (5.66) (full red lines) for  $ck_z = 4$  eV. The radius of the cylinder  $R = 3 \mu\text{m}$ ,  $\epsilon_1 = 1$ ,  $\epsilon_2 = 3.4$ , and the height  $L = 0.3 \mu\text{m}$ .

$$\left[ H_r^{(j)}(r), H_\phi^{(j)}(r) \right] = \frac{1}{q_j^2 - k_z^2} \left[ \frac{\epsilon_j \omega \mu}{cr} A^{(j)} f_\mu^{(j)} + ik_z q_j B^{(j)} f_\mu^{\prime(j)}, i \frac{\epsilon_j \omega q_j}{c} A^{(j)} f_\mu^{\prime(j)} - \frac{\mu k_z}{r} B^{(j)} f_\mu^{(j)} \right]. \quad (5.64)$$

It is possible now to determine the eigenmodes by imposing appropriate boundary conditions. The normal component of the electric induction vector,  $\vec{\mathbb{D}}$ , the electric field components  $[E_r, E_\phi]$  and the magnetic field vector,  $\vec{\mathbb{H}}$ , should be continuous at the interface  $r = R$ , i.e.  $\epsilon_1 E_r^{(1)}(R) = \epsilon_2 E_r^{(2)}(R)$ ,  $E_\phi^{(1)}(R) = E_\phi^{(2)}(R)$ ,  $E_z^{(1)}(R) = E_z^{(2)}(R)$  and  $\vec{H}^{(1)}(R) = \vec{H}^{(2)}(R)$ . Using Eqs. (5.63) and (5.64) and assuming  $q_j^2 = -\kappa^2$ , we obtain the dispersion relation

$$(q\kappa R)^2 [\kappa K_\mu J'_\mu + q J_\mu K'_\mu] [\epsilon_1 \kappa K_\mu J'_\mu + q \epsilon_2 J_\mu K'_\mu] = (\mu K_\mu J_\mu)^2 \frac{\omega^2 k_z^2}{c^2} (\epsilon_1 - \epsilon_2)^2. \quad (5.65)$$

For a given  $\mu$  and  $k_z$ , Eq. (5.65) provides a set of solutions, which we wish to compare to those of our "ideal cavity" model. An ideal cavity mode is one where the tangential components of the electric field and  $H_r$  vanish at the interface. We can imagine that the walls of the ideal cavity are made of a perfect metal. Then  $E_r$  is discontinuous at the interface and so are  $H_z$  and  $H_\phi$ . Therefore, an ideal cavity TM

mode has the components that are non-zero only inside the cavity:

$$\begin{aligned} E_{z_1} &= C_\mu J_\mu(qr) , \\ E_{r_1} &= \frac{k_z}{q_1} C_\mu J'_\mu(q_1 r) . \end{aligned} \quad (5.66)$$

So, the boundary conditions reduce to  $J_\mu(q_1 R) = 0$ . In Fig. 5.1 we compare the exact field profiles  $E_z$  and  $D_r$  with fields (5.66). As an example, it shows the  $\nu = 9$  mode, which corresponds to  $\hbar\omega = 1.866$  eV for ideal cavity of  $R = 3\mu\text{m}$  and demonstrates a reasonable qualitative agreement between the field distributions inside the cylinder. where the excitons are confined.

### C. Semiconductor on a cylindrical cavity: exciton-photon matrix elements $I_{\mu,\nu;m,n}$

The integral  $I_{\mu,\nu;m,n}$  in the matrix element (??) is written as

$$I_{\mu,\nu;m,n} = \frac{2}{\xi_{\mu,\nu} |J'_m(\xi_{m,n})|} \int_0^1 x J_m(\xi_{m,n} x) J_m(\xi_{\mu,\nu} x) dx . \quad (5.67)$$

Using the Bessel functions' properties, [96] the integral is equal to:

$$I_{\mu,\nu;m,n} = \frac{2}{\xi_{\mu,\nu} |J'_m(\xi_{m,n})|} \frac{\xi_{m,n} J_{m+1}(\xi_{m,n}) J_m(\xi_{\mu,\nu}) - \xi_{\mu,\nu} J_m(\xi_{m,n}) J_{m+1}(\xi_{\mu,\nu})}{\xi_{m,n}^2 - \xi_{\mu,\nu}^2}, \quad (5.68)$$

and, since the second term is zero, we obtain:

$$\begin{aligned} I_{\mu,\nu;m,n} &= \frac{2}{\xi_{\mu,\nu} |J'_m(\xi_{m,n})|} \frac{\xi_{m,n} J_{m+1}(\xi_{m,n}) J_m(\xi_{\mu,\nu})}{\xi_{m,n}^2 - \xi_{\mu,\nu}^2} \\ &= - \frac{2}{\xi_{\mu,\nu} |J'_m(\xi_{m,n})|} \frac{\xi_{m,n} J'_m(\xi_{m,n}) J_m(\xi_{\mu,\nu})}{\xi_{m,n}^2 - \xi_{\mu,\nu}^2}. \end{aligned} \quad (5.69)$$

Therefore, the integral squared is given by:

$$|I_{\mu,\nu;m,n}|^2 = 4 \frac{\xi_{m,n}^2}{\xi_{\mu,\nu}^2} \frac{J_m^2(\xi_{\mu,\nu})}{(\xi_{m,n}^2 - \xi_{\mu,\nu}^2)^2}. \quad (5.70)$$

As an example, the squared values of the integrals (5.70) for  $\mu = 0$  and  $m = 1$  are given in Table 1.

Table 1. Values of  $|I_{0,\nu;1,n}|^2$ .

$\nu/n$	1	2	3	4
1	$3.5 \times 10^{-2}$	$4.8 \times 10^{-3}$	$2.0 \times 10^{-3}$	$1.1 \times 10^{-3}$
2	$9.0 \times 10^{-4}$	$2.1 \times 10^{-3}$	$2.9 \times 10^{-4}$	$1.2 \times 10^{-4}$
3	$1.6 \times 10^{-5}$	$2.9 \times 10^{-4}$	$5.0 \times 10^{-4}$	$6.6 \times 10^{-5}$
4	$1.5 \times 10^{-6}$	$9.5 \times 10^{-6}$	$1.2 \times 10^{-4}$	$1.8 \times 10^{-4}$

## D. Solution of the Helmholtz equation with spherical coordinates

Expressing the Helmholtz equation (4.2) in spherical coordinates leads to:

$$\frac{1}{r^2} \partial_r [r^2 \partial_r u(\mathbf{r})] + \frac{1}{r^2 \sin^2 \theta} \left[ \sin \theta \partial_\theta [\sin \theta \partial_\theta u(\mathbf{r})] + \partial_\phi^2 u(\mathbf{r}) \right] + k^2 u(\mathbf{r}) = 0. \quad (5.71)$$

Applying the method of separation of variables we can express the solution as:

$$u(\mathbf{r}) = R(r)\Theta(\theta)\Phi(\phi). \quad (5.72)$$

Multiplying (5.71) by  $\sin^2(\theta)r^2/(R\Theta\Phi)$  yields:

$$\frac{\sin^2 \theta}{R} \partial_r [r^2 \partial_r R] + \frac{\sin \theta}{\Theta} \partial_\theta [\sin \theta \partial_\theta \Theta] + \frac{1}{\Phi} \partial_\phi^2 \Phi + \sin^2(\theta)k^2 r^2 = 0. \quad (5.73)$$

There is a term that only depends on  $\phi$  and others that involve  $r$  and  $\theta$ . As such, the term that only depends on  $\phi$  must be a constant. We call this constant  $-m^2$  and thus are able to write:

$$\frac{1}{\Phi} \partial_\phi^2 \Phi = -m^2, \quad (5.74)$$

$$\Phi(\phi) = e^{im\phi}. \quad (5.75)$$

The number  $m$  must be an integer to allow the solution to be periodic for  $\phi \rightarrow \phi + 2\pi$ . Equation (5.73) can be written as:

$$\frac{1}{R} \partial_r [r^2 \partial_r R] + k^2 r^2 + \frac{1}{\Theta \sin \theta} \partial_\theta [\sin \theta \partial_\theta \Theta] - \frac{m^2}{\sin^2 \theta} = 0. \quad (5.76)$$

Now there is one term that varies only with  $\theta$  and another that varies only with  $r$ . As such, both terms must be constant. The constant for the  $\theta$  term will be defined according to:

$$\frac{1}{\Theta \sin \theta} \partial_\theta [\sin \theta \partial_\theta \Theta] - \frac{m^2}{\sin^2 \theta} = -l(l+1). \quad (5.77)$$

Thus, using  $x \equiv \cos \theta$  this equation is:

$$\partial_x [(1-x^2)\partial_x \Theta(x)] + [l(l+1) - \frac{m^2}{1-x^2}] \Theta(x) = 0 \quad (5.78)$$

This is the associated Legendre equation, whose solutions are the associated Legendre polynomials:

$$\Theta(x) = P_l^m(x), \quad (5.79)$$

or,

$$\Theta(\theta) = P_l^m(\cos \theta). \quad (5.80)$$

$m$  takes values in the range  $-l < m < l$ , and must also be an integer. Finally, we deal with the radial part of equation (5.76), which becomes:

$$\partial_r [r^2 \partial_r R] + [k^2 r^2 - l(l+1)] R = 0. \quad (5.81)$$

This is the spherical Bessel equation, whose solutions are spherical Bessel functions of first and second kind.

## E. Properties of vectorial calculus

The following properties are useful in chapter 3 and can be consulted in [97]:

$$\nabla^2 [\nabla \times \mathbf{A}] = \nabla \times [\nabla^2 \mathbf{A}], \quad (5.82)$$

$$\nabla^2 [\Psi \mathbf{A}] = \mathbf{A} \nabla^2 \Psi + 2 [\nabla \Psi \cdot \nabla] \mathbf{A} + \Psi \nabla^2 \mathbf{A}, \quad (5.83)$$

$$\nabla \times \nabla \Psi = 0, \quad (5.84)$$

$$\nabla \times (\Psi \mathbf{A}) = \Psi (\nabla \times \mathbf{A}) + \nabla \Psi \times \mathbf{A}, \quad (5.85)$$

$$\begin{cases} (\nabla \times \mathbf{A})_r = \frac{1}{r \sin \theta} (A_\phi \sin \theta)^\theta - \frac{1}{r \sin \theta} A_\theta^\phi \\ (\nabla \times \mathbf{A})_\theta = \frac{1}{r \sin \theta} A_r^\phi - \frac{1}{r} (r A_\phi)^r \\ (\nabla \times \mathbf{A})_\phi = \frac{1}{r} (r A_\theta)^r - \frac{1}{r} A_r^\theta \end{cases}, \quad (5.86)$$

where superscripts indicate partial differentiation and subscripts indicate the component of a vector.

## F. Mode volume for a spherical cavity

To normalize the spherical photon field to a single photon, it is necessary to determine the integral (4.40), given by:

$$\Omega = \frac{1}{2\epsilon} \int d^3r \left( \epsilon \frac{\mathbf{E} \cdot \mathbf{E}^*}{E_0^2} + \frac{\mathbf{H} \cdot \mathbf{H}^*}{E_0^2} \right). \quad (5.87)$$

### TM-type

The electromagnetic fields for TM-type modes are given by equations (4.21)-(4.22):

$$\begin{cases} (E_{l,m}^{(TM)})_r = E_0^{(TM)} \frac{f_l(kr)}{kr} l(l+1) P_l^m(\cos \theta) e^{im\phi} \\ (E_{l,m}^{(TM)})_\theta = i E_0^{(TM)} \frac{\partial_{kr}(kr f_l(kr))}{kr} \partial_\theta P_l^m(\cos \theta) e^{im\phi} \\ (E_{l,m}^{(TM)})_\phi = -E_0^{(TM)} \frac{\partial_{kr}(kr f_l(kr))}{kr} m \frac{P_l^m(\cos \theta)}{\sin \theta} e^{im\phi} \end{cases}, \quad (5.88)$$

$$\begin{cases} (H_{l,m}^{(TM)})_r = 0 \\ (H_{l,m}^{(TM)})_\theta = i \sqrt{\epsilon} E_0^{(TM)} m f_l(kr) \frac{P_l^m(\cos \theta)}{\sin \theta} e^{im\phi} \\ (H_{l,m}^{(TM)})_\phi = -\sqrt{\epsilon} E_0^{(TM)} f_l(kr) \partial_\theta P_l^m(\cos \theta) e^{im\phi} \end{cases}. \quad (5.89)$$

$k$  will be taken to be a real number, because the imaginary parts of the frequencies have been neglected in this study. Several indexes will be removed to facilitate reading. The integral  $\Omega_{l,m}^{(TM)}$  will be calculated over a general spherical shell ranging from  $R_1$  to  $R_2$ , and for now  $f_l(kr)$  will be assumed to be a real function:

$$\begin{aligned} \Omega = \int_0^{2\pi} \int_0^\pi \int_{R_1}^{R_2} r^2 \sin(\theta) & \left( \left| \frac{f(kr)}{kr} \right|^2 l^2 (l+1)^2 P(\cos \theta)^2 + \left[ \left| \frac{f(kr) + r \partial_r f(kr)}{kr} \right|^2 + |f(kr)|^2 \right] \right. \\ & \left. \left[ (\partial_\theta P(\cos \theta))^2 + \frac{m^2}{\sin^2 \theta} P(x)^2 \right] \right) dr d\theta d\phi, \end{aligned} \quad (5.90)$$

$$\Omega = \frac{2\pi}{k^3} \int_{-1}^1 \int_{kR_1}^{kR_2} \left[ f^2(z) l^2 (l+1)^2 P(x)^2 + \left( (f(z) + zf'(z))^2 + z^2 f^2(z) \right) \left( (1-x^2) (\partial_x P(x))^2 + \frac{m^2}{1-x^2} P(x)^2 \right) \right] dz dx. \quad (5.91)$$

The orthogonality relations for Associated Legendre Polynomials of the same  $m$  and  $l$  read:

$$\int_{-1}^1 P(x)^2 dx = \frac{2(l+m)!}{(2l+1)(l-m)!}, \quad (5.92)$$

$$\int_{-1}^1 \frac{P(x)^2}{1-x^2} dx = \frac{(l+m)!}{m(l-m)!}. \quad (5.93)$$

Looking back at  $\Omega$  (5.91), the only integral in  $x$  not in these forms is:

$$\int_{-1}^1 (1-x^2) (\partial_x P(x))^2 dx. \quad (5.94)$$

However, integration by parts can simplify this integral if one considers  $u = (1-x^2)\partial_x P(x)$  and  $v' = \partial_x P(x)$  to obtain:

$$\begin{aligned} \int_{-1}^1 (1-x^2) (\partial_x P(x))^2 dx &= \\ &= [(1-x^2)P(x)\partial_x P(x)] \Big|_{-1}^1 - \int_{-1}^1 P(x) [-2x\partial_x P(x) + (1-x^2)\partial_x^2 P(x)]. \end{aligned} \quad (5.95)$$

The first term is null and in the second term is part of the Associated Legendre differential equation, which reads:

$$(1-x^2)\partial_x^2 P(x) - 2x\partial_x P(x) = \left( \frac{m^2}{1-x^2} - l(l+1) \right) P(x). \quad (5.96)$$

Plugging this relation into (5.95) one gets:

$$\int_{-1}^1 (1-x^2) (\partial_x P(x))^2 dx = \int_{-1}^1 \left[ l(l+1)P(x)^2 - \frac{m^2}{1-x^2} P(x)^2 \right] dx. \quad (5.97)$$

Going back to (5.91), substitution of this integral along with usage of the orthogonality relation (5.92) simplifies the result to:

$$\Omega = \frac{2\pi}{k^3} \frac{2l(l+1)(l+m)!}{(2l+1)(l-m)!} \int_{kR_1}^{kR_2} \left[ l(l+1)f^2(z) + (f(z) + zf'(z))^2 + z^2 f(z)^2 \right] dx. \quad (5.98)$$

Now only the spherical Bessel integrals remain. The spherical Bessel differential equation reads:

$$z^2 f''(z) + 2zf'(z) + (z^2 - l(l+1)) f(z) = 0. \quad (5.99)$$

It is noticeable that the  $l(l+1)$  part of this equation is present in the integrand of (5.98). Writing only the integral of (5.98) and expanding the square, one has to solve:

$$I_f = \int_{kR_1}^{kR_2} \left[ l(l+1)f^2(z) + f^2(z) + 2zf(z)f'(z) + z^2 f'(z)^2 + z^2 f(z)^2 \right] dx \quad (5.100)$$

The terms with derivatives can be transformed with integration by parts. The first term, with  $u = 2zf(z)$  and  $v' = f'(z)$ , becomes:

$$\int_{kR_1}^{kR_2} 2zf(z)f'(z)dz = 2zf^2(z)|_{kR_1}^{kR_2} - 2 \int_{kR_1}^{kR_2} f(z)[f(z) + zf'(z)] \quad (5.101)$$

$$\int_{kR_1}^{kR_2} 2zf(z)f'(z)dz = zf^2(z)|_{kR_1}^{kR_2} - \int_{kR_1}^{kR_2} f^2(z)dz. \quad (5.102)$$

The second term, with  $u = z^2f'(z)$  and  $v' = f'(z)$ , becomes:

$$\int_{kR_1}^{kR_2} z^2f'(z)^2dz = [z^2f'(z)f(z)]|_{kR_1}^{kR_2} - \int_{kR_1}^{kR_2} f(z)[2zf'(z) + z^2f''(z)]dz, \quad (5.103)$$

where part of the spherical Bessel equation (5.99) shows up in the last integral. Using (5.99) it is possible to write this integral as:

$$\int_{kR_1}^{kR_2} z^2f'(z)^2dz = [z^2f'(z)f(z)]|_{kR_1}^{kR_2} + \int_{kR_1}^{kR_2} [z^2 - l(l+1)]f^2(z)dz. \quad (5.104)$$

Now it is a simple matter to substitute equations (5.102) and (5.104) into the integral (5.100), which yields:

$$I_f = [zf(z)(f(z) + zf'(z))]|_{kR_1}^{kR_2} + 2 \int_{kR_1}^{kR_2} z^2f^2(z)dz. \quad (5.105)$$

Finally, the last integral has the simple analytical solution:

$$\int z^2f^2(z)dz = \frac{z^3}{2} (f^2(z) - f_{l-1}(z)f_{l+1}(z)). \quad (5.106)$$

The spherical Bessel recurrence relations are:

$$\begin{cases} f'(z) = f_{l-1}(z) - \frac{l+1}{z}f(z) \\ f'(z) = -f_{l+1}(z) + \frac{l}{z}f(z) \end{cases}. \quad (5.107)$$

So, the solution (5.106) can be written as:

$$\int z^2f^2(z)dz = \frac{z}{2} [f^2(z)[z^2 - l(l+1)] + zf'(z)[f(z) + zf'(z)]]. \quad (5.108)$$

So,

$$I_f = [zf(z)(f(z) + zf'(z)) + z(f^2(z)[z^2 - l(l+1)] + zf'(z)[f(z) + zf'(z)])]|_{kR_1}^{kR_2}. \quad (5.109)$$

$$I_f = [z(f(z) + zf'(z))^2 + zf^2(z)[z^2 - l(l+1)]]|_{kR_1}^{kR_2}. \quad (5.110)$$

The original integral (5.87) that needed to be solved can be written as:

$$\Omega = \frac{2\pi}{k^3} \frac{2l(l+1)(l+m)!}{(2l+1)(l-m)!} [z(f(z) + zf'(z))^2 + zf^2(z)[z^2 - l(l+1)]]|_{kR_1}^{kR_2}. \quad (5.111)$$

## TE-type

Again, the mode volume integral is:

$$\Omega = \frac{1}{2\epsilon} \int d^3r \left( \epsilon \frac{\mathbf{E} \cdot \mathbf{E}^*}{E_0^2} + \frac{\mathbf{H} \cdot \mathbf{H}^*}{E_0^2} \right). \quad (5.112)$$

For TE-type modes the fields (4.23)-(4.24) read:

$$\begin{cases} (E_{l,m}^{(TE)})_r = 0 \\ (E_{l,m}^{(TE)})_\theta = iE_0^{(TE)} f_l(kr) m \frac{P_l^m(\cos\theta)}{\sin\theta} e^{im\phi} \\ (E_{l,m}^{(TE)})_\phi = -E_0^{(TE)} f_l(kr) \partial_\theta P_l^m(\cos\theta) e^{im\phi} \end{cases}, \quad (5.113)$$

$$\begin{cases} (H_{l,m}^{(TE)})_r = -i\sqrt{\epsilon} E_0^{(TE)} \frac{f_l(kr)}{kr} l(l+1) P_l^m(\cos\theta) e^{im\phi}, \\ (H_{l,m}^{(TE)})_\theta = -i\sqrt{\epsilon} E_0^{(TE)} \frac{\partial_{kr}(kr f_l(kr))}{kr} \partial_\theta P_l^m(\cos\theta) e^{im\phi} \\ (H_{l,m}^{(TE)})_\phi = \sqrt{\epsilon} E_0^{(TE)} \frac{\partial_{kr}(kr f_l(kr))}{kr} m \frac{P_l^m(\cos\theta)}{\sin\theta} e^{im\phi} \end{cases}, \quad (5.114)$$

Inserting (5.113) and (5.114) into (5.112) yields:

$$\Omega = \int_0^{2\pi} \int_0^\pi \int_{R_1}^{R_2} r^2 \sin(\theta) \left( \left| \frac{f(kr)}{kr} \right|^2 l^2 (l+1)^2 P(\cos\theta)^2 + \left[ \left| \frac{f(kr) + r \partial_r f(kr)}{kr} \right|^2 + |f(kr)|^2 \right] \right. \\ \left. \left[ (\partial_\theta P(\cos\theta))^2 + \frac{m^2}{\sin^2\theta} P(x)^2 \right] \right) dr d\theta d\phi, \quad (5.115)$$

which is of the same form as (5.115). The difference between TE and TM will be the different  $k$  values corresponding to their eigenenergies. Finally, if  $f_l = h_l^{(1)} = j_l + iy_l$ , then:

$$|f|^2 = j^2 + y^2, \quad (5.116)$$

and

$$|f + kr f'|^2 = |h + kr h'|^2 = |j + iy + kr(j' + iy')|^2, \quad (5.117)$$

$$|f + kr f'|^2 = (j + kr j')^2 + (y + kr y')^2. \quad (5.118)$$

As such, equation (5.115) can be separated into the sum of the  $f = j$  case and the  $f = y$  case, each of the terms yielding the result (5.111).

## General mode volume

Summarising, the total expression for the mode volume integral for the inside of the sphere reads:

$$\Omega_1 = \frac{2\pi}{k_1^3} \frac{2l(l+1)(l+m)!}{(2l+1)(l-m)!} \left[ z(j_l(z) + z j_l'(z))^2 + z j_l^2(z) [z^2 - l(l+1)] \right] \Big|_0^{k_1 R}, \quad (5.119)$$

where  $R$  is the radius of the cavity. And for the outside, the integral up to a radius  $R_I$  yields:

$$\Omega_2 = 2\pi \frac{2l(l+1)(l+m)!}{(2l+1)(l-m)!} \left( \frac{1}{k_2^3} \left[ z(j_l(z) + z j_l'(z))^2 + z j_l^2(z) [z^2 - l(l+1)] \right] \Big|_{k_2 R}^{k_2 R_I} + \right. \\ \left. \frac{1}{k_2^3} \left[ z(y_l(z) + z y_l'(z))^2 + z y_l^2(z) [z^2 - l(l+1)] \right] \Big|_{k_2 R}^{k_2 R_I} \right). \quad (5.120)$$



For a real cavity, the  $E_0$  in (5.112) will be taken to be  $E_1$ , the constant of the interior of the sphere, as such, the mode volume for a real cavity will be:

$$\Omega = \Omega_1 + \frac{|E_2|^2}{|E_1|^2} \Omega_2. \quad (5.121)$$

Applying conditions (4.52) and (4.54), the mode volumes for TM-type modes and TE-type modes become:

$$\Omega^{(TM)} = \Omega_1^{(TM)} + \left| \frac{\epsilon_1 j_l(k_1 R)}{\epsilon_2 h_l(k_2 R)} \right|^2 \Omega_2^{(TM)}, \quad (5.122)$$

$$\Omega^{(TE)} = \Omega_1^{(TE)} + \left| \frac{j_l(k_1 R)}{h_l(k_2 R)} \right|^2 \Omega_2^{(TE)}. \quad (5.123)$$

## G. Distribution of light rays inside a sphere according to geometrical optics

The quantity that describes the density of transmitted radiation in a section  $dr$  of the sphere is:

$$\frac{1}{\xi} \frac{d\xi}{dr} = \frac{1}{t_{1,2}} \frac{dt}{dr}. \quad (5.124)$$

It is shown on section 1.1, that the radius-vector of the ray inside the sphere is:

$$\vec{r}(t, \Theta_t) = \vec{r}_1(\Theta_t) + \frac{\vec{r}_2 - \vec{r}_1(\Theta_t)}{t_{1,2}} t. \quad (5.125)$$

Using (4.67) and (4.68), this can be written as:

$$\vec{r}(t, \Theta_t) = -R \cos(2\Theta_t) \hat{x}' + R \sin(2\Theta_t) \hat{z} + \frac{R \hat{x}' + R \cos(2\Theta_t) \hat{x}' - R \sin(2\Theta_t) \hat{z}}{t_{1,2}} t \quad (5.126)$$

$$\vec{r}(t, \Theta_t) = R \left[ \left(1 + \cos(2\Theta_t)\right) \frac{t}{t_{1,2}} - \cos(2\Theta_t) \right] \hat{x}' + R \left[ -\sin(2\Theta_t) \frac{t}{t_{1,2}} + \sin(2\Theta_t) \right] \hat{z} \quad (5.127)$$

The distance from the centre  $r$  will be the modulus of this vector:

$$r = |\vec{r}| = R \sqrt{\left[ \left(1 + \cos(2\Theta_t)\right) \frac{t}{t_{1,2}} - \cos(2\Theta_t) \right]^2 + \left[ -\sin(2\Theta_t) \frac{t}{t_{1,2}} + \sin(2\Theta_t) \right]^2}. \quad (5.128)$$

Developing the squares, this equals:

$$r = R \sqrt{\left[ (1 + \cos(2\Theta_t))^2 + \sin^2(2\Theta_t) \right] \frac{t^2}{t_{1,2}^2} - 2 [1 + \cos(2\Theta_t)] \frac{t}{t_{1,2}} + 1}, \quad (5.129)$$

$$r = R \sqrt{2 [1 + \cos(2\Theta_t)] \frac{t^2}{t_{1,2}^2} - 2 [1 + \cos(2\Theta_t)] \frac{t}{t_{1,2}} + 1}, \quad (5.130)$$

$$r = R \sqrt{4 \cos^2(\Theta_t) \left[ \frac{t^2}{t_{1,2}^2} - \frac{t}{t_{1,2}} \right] + 1}. \quad (5.131)$$

To obtain  $\frac{1}{t_{1,2}} \frac{dt}{dr}$  we can calculate  $t_{1,2} \frac{dr}{dt}$ :

$$t_{1,2} \frac{dr}{dt} = \frac{R^2}{2r(t, \Theta_t)} 4 \cos^2(\Theta_t) \left[ 2 \frac{t}{t_{1,2}} - 1 \right]. \quad (5.132)$$

Evidently, we are forced to invert equation (5.131) to obtain  $\frac{t}{t_{1,2}}(r)$ . From (5.131) we write:

$$\frac{r^2}{R^2} = 4 \cos^2(\Theta_t) \left[ \frac{t^2}{t_{1,2}^2} - \frac{t}{t_{1,2}} \right] + 1, \quad (5.133)$$

$$\frac{t^2}{t_{1,2}^2} - \frac{t}{t_{1,2}} + \frac{1 - r^2/R^2}{4 \cos^2(\Theta_t)} = 0, \quad (5.134)$$

$$\frac{t}{t_{1,2}} = \frac{1}{2} \pm \sqrt{\frac{1}{4} - \frac{1 - r^2/R^2}{4 \cos^2(\Theta_t)}}. \quad (5.135)$$

Inserting this expression into (5.132) we obtain:

$$t_{1,2} \frac{dr}{dt} = \pm \frac{2R^2}{r} \cos^2(\Theta_t) \sqrt{1 - \frac{1 - r^2/R^2}{\cos^2(\Theta_t)}}, \quad (5.136)$$

$$t_{1,2} \frac{dr}{dt} = \pm \frac{2R^2 \cos(\Theta_t)}{r} \sqrt{\cos^2(\Theta_t) - 1 + r^2/R^2}, \quad (5.137)$$

$$t_{1,2} \frac{dr}{dt} = \pm \frac{2R \cos(\Theta_t)}{r} \sqrt{r^2 - R^2 \sin^2(\Theta_t)}, \quad (5.138)$$

Thus, the quantity in equation (5.124) will be:

$$\frac{1}{\xi} \frac{d\xi}{dr} = \frac{1}{t_{1,2}} \frac{dt}{dr} = \frac{1}{t_{1,2}} \frac{dt}{dt} \frac{dt}{dr}, \quad (5.139)$$

$$\frac{1}{\xi} \frac{d\xi}{dr} = \pm \frac{r}{2R \cos(\Theta_t) \sqrt{r^2 - R^2 \sin^2(\Theta_t)}}. \quad (5.140)$$

This is only valid as a description of the density of transmitted radiation in values of  $r$  where the ray in Figure 4.10 passes. Values where the ray does not pass will result in a negative argument in the square root of equation (5.140). The minimum value of  $r$  is obtained by setting this argument to zero.

$$r_{min}^2 - R^2 \sin^2(\Theta_t) = 0, \quad (5.141)$$

$$r_{min} = R \sin(\Theta_t). \quad (5.142)$$

This can be seen geometrically from Figure (4.10) since this corresponds to the mid-point of the ray's path, where the  $r$ -vector must be perpendicular to the path, causing a right triangle to form with  $\sin(\Theta_t) = r/R$ . Thus, the real valued density is  $\Re[\frac{1}{\xi} \frac{d\xi}{dr}]$ :

$$\Re\left[\frac{1}{\xi} \frac{d\xi}{dr}\right] = \begin{cases} \pm \frac{r}{2R \cos(\Theta_t) \sqrt{r^2 - R^2 \sin^2(\Theta_t)}}, & r > R \sin(\Theta_t) \\ 0, & r < R \sin(\Theta_t) \end{cases}. \quad (5.143)$$

## H. Study of the angular term in the local density of states

### Term in TE modes

We wish to study the behaviour of (4.118)

$$\Theta_l^m(x) \equiv \frac{(l-m)!}{(l+m)!} \left[ (1-x^2) (\partial_x P_l^m(x))^2 + \frac{m^2}{1-x^2} P_l^m(x)^2 \right]. \quad (5.144)$$

The function  $\Theta_l^m(x)$ , which is the angular part of the density of states, obeys the relation  $\Theta_l^{-m} = \Theta_l^m$ . This is to be expected since nothing in the system studied breaks the symmetry  $z \rightarrow -z$  and the  $m$  angular momentum number represents the projection of angular momentum on the  $z$  axis. Therefore we can consider only positive values of  $m$  and then multiply by 2 to add the contribution of the  $-m$  modes. Furthermore, the density of states can not depend on the angle  $\theta$ , and thus on  $x = \cos\theta$ , because of the spherical symmetry of the system. We can therefore calculate  $\Theta_l^m(x)$  for any given value of  $x$  and its sum over all  $m$  must be the same regardless of the value of  $x$  we used. This will hopefully allow us to solve the entire sum over all  $m$  analytically. A convenient value is  $x \rightarrow 1-$ . The starting point is to apply the following asymptotic relation, valid for when  $x \rightarrow 1-$  [98, Eq. 14.8.2]

$$P_l^m(x) \sim (-1)^m \frac{(l-m+1)_{2m}}{m!} \left( \frac{1-x}{2} \right)^{m/2}, \quad (5.145)$$

where  $(l-m+1)_{2m}$  denotes the Pochhammer's symbol, or shifted factorial, defined by:

$$(a)_n = a(a+1)(a+2)\dots(a+n-1). \quad (5.146)$$

Now, taking just the bracketed part of (5.144) and using (5.145) we get, for  $x \rightarrow 1-$ :

$$p\Theta_l^m(x) \equiv (1-x^2) (\partial_x P_l^m(x))^2 + \frac{m^2}{1-x^2} P_l^m(x)^2 \quad (5.147)$$

$$p\Theta_l^m(x) \sim \frac{m^2(l-m+1)_{2m}^2}{2^m m!^2} \left( \frac{1}{4} (1-x)^{m-2} (1-x^2) + \frac{(1-x)^m}{1-x^2} \right). \quad (5.148)$$

Analysing (5.148) we can already conclude that for  $m = 2$ :

$$p\Theta_l^2(x) \propto \frac{1}{4}(1-x^2) + \lim_{x \rightarrow 1} \frac{(1-x)^2}{1-x^2}, \quad (5.149)$$

$$p\Theta_l^2(x) \propto \frac{1}{4}(1-x^2) + \lim_{x \rightarrow 1} \frac{(1-x)^2}{(1-x)(1+x)} = 0 \quad (5.150)$$

$$p\Theta_l^2(x) \propto \frac{1}{4}(1-x^2) + \lim_{x \rightarrow 1} \frac{(1-x)}{(1+x)} = 0 \quad (5.151)$$

Simply looking at the  $(1-x)$  terms in (5.148) allows us to further conclude that:

$$p\Theta_l^m(x) = 0, \quad m \geq 2. \quad (5.152)$$

Now we only need to determine  $p\Theta_l^m(x)$  for  $m = 0, 1$ . For  $m = 0$ , the leading factor of (5.148), with  $m^2$ , will be exactly 0, which ensures

$$p\Theta_l^0(x) = 0. \quad (5.153)$$

Finally, for the only surviving term  $m = 1$ :

$$p\Theta_l^1(x) = \frac{l^2}{2} \left( \frac{1}{4} \lim_{x \rightarrow 1} \frac{1-x^2}{1-x} + \lim_{x \rightarrow 1} \frac{1-x}{1-x^2} \right), \quad (5.154)$$

and by using L'Hôpital's rule:

$$p\Theta_l^1(x) = \frac{l^2}{2} \left( \frac{1}{2} + \frac{1}{2} \right), \quad (5.155)$$

$$p\Theta_l^1(x) = \frac{l^2}{2}, \quad (5.156)$$

$$p\Theta_l^1(x) = \frac{l^2(l+1)^2}{2}. \quad (5.157)$$

Taking this all together, we can conclude that:

$$\sum_{m=-l}^{m=l} \Theta_l^m(x) = \Theta_l^1(x) + \Theta_l^{-1}(x) = 2\Theta_l^1(x) = \frac{(l-1)!}{(l+1)!} l^2(l+1)^2, \quad (5.158)$$

$$\sum_{m=-l}^{m=l} \Theta_l^m(x) = l(l+1). \quad (5.159)$$

### Extra term in TM modes

In the local density of states for *TM* modes, we have the additional term:

$$\Phi_l^m(x) \equiv \frac{(l-m)!}{(l+m)!} P_l^m(x)^2, \quad (5.160)$$

Again, using (5.145), this becomes, for  $x \rightarrow 1-$ :

$$\Phi_l^m(x) \sim \frac{(l-m)!}{(l+m)!} \frac{(l-m+1)_{2m}^2}{m!^2} \left( \frac{1-x}{2} \right)^m. \quad (5.161)$$

This term will be 0 for all  $m$  except  $m = 0$ , in which case it will be:

$$\Phi_l^0(x) \sim \frac{(l-0)!}{(l+0)!} \frac{(l+1)_0^2}{0!^2}. \quad (5.162)$$

$$\Phi_l^0(x) \sim 1. \quad (5.163)$$

Thus,

$$\sum_{m=-l}^l \Phi_l^m(x) = 1. \quad (5.164)$$

## Bibliography

- [1] Lukas Novotny and Bert Hecht. *Principles of Nano-Optics*. Cambridge University Press, 2012.
- [2] Itai Epstein, Bernat Terrés, André J Chaves, Varun-Varma Pusapati, Daniel A Rhodes, Bettina Frank, Valentin Zimmermann, Ying Qin, Kenji Watanabe, Takashi Taniguchi, and Others. Near-unity light absorption in a monolayer WS<sub>2</sub> van der Waals heterostructure cavity. *Nano Letters*, 20(5):3545–3552, 2020.
- [3] V B Berestetskii, L P Pitaevskii, and E M Lifshitz. *Quantum Electrodynamics: Volume 4 (Course of Theoretical Physics)*. Butterworth-Heinemann, Oxford, UK, 1982.
- [4] A Kavokin and G Malpeuch. *Cavity Polaritons*. Elsevier, Amsterdam, 2003.
- [5] Yu. V Bludov, A Ferreira, N M R Peres, and M I Vasilevskiy. A Primer on Surface Plasmon-Polaritons in Graphene. *Int. J. Mod. Phys. B*, 27:1341001, 2013.
- [6] Takashi Kita, Yukihiro Harada, and Shigeo Asahi. *Fundamentals of Semiconductors*. Springer, 2019.
- [7] Andre K Geim and K S Novoselov. The rise of graphene. *Nature materials*, 6 3:183–191, 2007.
- [8] Stefan Alexander Maier. *Plasmonics: fundamentals and applications*. Springer Science & Business Media, 2007.
- [9] Paulo André Dias Gonçalves and Nuno M R Peres. *An introduction to graphene plasmonics*. World Scientific, 2016.
- [10] Michael P Marder. *Condensed matter physics*. John Wiley & Sons, 2010.
- [11] C Kittel. Magnons and their interactions with phonons and photons. 1959.
- [12] José Nuno S Gomes, Carlos Trallero-Giner, Nuno M R Peres, and Mikhail I Vasilevskiy. Exciton-polaritons of a 2D semiconductor layer in a cylindrical microcavity. *Journal of Applied Physics*, 127(13):133101, 2020.
- [13] A V Kavokin, J J Baumberg, G Malpuech, and F P Laussy. *Microcavities*. Oxford University Press, Oxford, UK, 2008.
- [14] Babu V Suresh. *Solid State Devices and Technology*. Pearson Education India, 2010.
- [15] L Andreani. Exciton-polaritons in bulk semiconductors and in confined electron and photon systems. In Leong-Chuan Kwek, Alexia Auffeves, Dario Gerace, Maxime Richard, Stefano Portolan, Marcelo Franca Santos, and Christian Miniature, editors, *Strong light-matter Coupling: from atoms to solid state systems*, chapter 2, pages 37–82. World Scientific, Singapore, 2014.

- [16] J J Hopfield. Theory of the contribution of excitons to the complex dielectric function in crystals. *Phys. Rev.*, 112:1555, 1958.
- [17] E M Purcell. Spontaneous emission probability at radio frequencies. *Phys. Rev.*, 69:681, 1946.
- [18] T Jakubczyk, W Pacuski, T Smoleński, A Golnik, M Florian, F Jahnke, C Kruse, D Hommel, and P Kossacki. Pronounced Purcell enhancement of spontaneous emission in CdTe/ZnTe quantum dots embedded in micropillar cavities. *Applied Physics Letters*, 101:132105, 2012.
- [19] Craig F Bohren and Donald R Huffman. *Absorption and scattering of light by small particles*. John Wiley & Sons, 2008.
- [20] Y V Bludov, J N Gomes, G A Farias, J Fernández-Rossier, M I Vasilevskiy, and N M R Peres. Hybrid plasmon-magnon polaritons in graphene-antiferromagnet heterostructures. *2D Materials*, 6(4):45003, jul 2019.
- [21] A H Castro Neto, F Guinea, N M R Peres, K S Novoselov, and A K Geim. The electronic properties of graphene. *Reviews of Modern Physics*, 81(1):109–162, jan 2009.
- [22] Brian Thomas Kelly. *Physics of graphite*. 1981.
- [23] M O Goerbig. Electronic properties of graphene in a strong magnetic field. *Reviews of Modern Physics*, 83(4):1193, 2011.
- [24] Beidou Guo, Liang Fang, Baohong Zhang, and Jian Ru Gong. Graphene doping: a review. *Insciences J.*, 1(2):80–89, 2011.
- [25] Philip Richard Wallace. The band theory of graphite. *Physical review*, 71(9):622, 1947.
- [26] Byoung-ho Lee, Il-Min Lee, Seyoon Kim, Dong-Ho Oh, and Lambertus Hesselink. Review on sub-wavelength confinement of light with plasmonics. *Journal of Modern Optics*, 57(16):1479–1497, 2010.
- [27] Jon A Schuller, Edward S Barnard, Wenshan Cai, Young Chul Jun, Justin S White, and Mark L Brongersma. Plasmonics for extreme light concentration and manipulation. *Nature materials*, 9(3):193, 2010.
- [28] R E Camley and D L Mills. Surface polaritons on uniaxial antiferromagnets. *Physical Review B*, 26(3):1280, 1982.
- [29] F Keffer and Ch Kittel. Theory of antiferromagnetic resonance. *Physical Review*, 85(2):329, 1952.
- [30] Supriyo Bandyopadhyay and Marc Cahay. *Introduction to spintronics*. CRC press, 2015.
- [31] Hailong Wang, Chunhui Du, P Chris Hammel, and Fengyuan Yang. Spin transport in antiferromagnetic insulators mediated by magnetic correlations. *Physical Review B*, 91(22):220410, 2015.
- [32] R Lebrun, A Ross, S A Bender, A Qaiumzadeh, L Baldrati, J Cramer, A Brataas, R A Duine, and M Kläui. Electrically controlled long-distance spin transport through an antiferromagnetic insulator. *arXiv preprint arXiv:1805.02451*, 2018.

- [33] Gang Wang, Alexey Chernikov, Mikhail M Glazov, Tony F Heinz, Xavier Marie, Thierry Amand, and Bernhard Urbaszek. Colloquium: Excitons in atomically thin transition metal dichalcogenides. *Rev. Mod. Phys.*, 90:21001, 2018.
- [34] L Britnell, R M Ribeiro, A Eckmann, R Jalil, B D Belle, A Mishchenko, Y.-J. Kim, R V Gorbachev, T Georgiou, S V Morozov, A N Grigorenko, A K Geim, C Casiraghi, A H Castro Neto, and K S Novoselov. Strong Light-Matter Interactions in Heterostructures of Atomically Thin Films. *Science*, 340:1311, 2013.
- [35] Xiaoze Liu, Tal Galfsky, Zheng Sun, Fengnian Xia, Erh-chen Lin, Yi-Hsien Lee, S Kéna-Cohen, and Vinod M Menon. Strong light-matter coupling in two-dimensional atomic crystals. *Nature Photonics*, 9:30, 2015.
- [36] M Koperski, K Nogajewski, A Arora, V Cherkez, P Mallet, J.-Y. Veullen, J Marcus, P Kossacki, and M Potemski. Single photon emitters in exfoliated WSe<sub>2</sub> structures. *Nature Nanotechnology*, 10:503, 2015.
- [37] Sajedeh Manzeli, Dmitry Ovchinnikov, Diego Pasquier, Oleg V Yazyev, and Andras Kis. 2D transition metal dichalcogenides. *Nature Reviews Materials*, 2(8):17033, 2017.
- [38] A K Geim and I V Grigorieva. Van der Waals Heterostructures. *Nature*, 499:419, 2013.
- [39] Yuri N Gartstein, Xiao Li, and Chuanwei Zhang. Exciton polaritons in transition-metal dichalcogenides and their direct excitation via energy transfer. *Phys. Rev. B*, 92:75445, 2015.
- [40] Vasilios D Karanikolas, Cristian A Marocico, Paul R Eastham, and A Louise Bradley. Near-field relaxation of a quantum emitter to two-dimensional semiconductors: Surface dissipation and exciton polaritons. *Phys. Rev. B*, 94:195418, 2016.
- [41] Archana Raja, Andrés Montoya-Castillo, Johanna Zultak, Xiao-Xiao Zhang, Ziliang Ye, Cyrielle Roquelet, Daniel A Chenet, Arend M van der Zande, Pinshane Huang, Steffen Jockusch, James Hone, David R Reichman, Louis E Brus, and Tony F Heinz. Energy Transfer from Quantum Dots to Graphene and MoS<sub>2</sub>: The Role of Absorption and Screening in Two-Dimensional Materials Dichalcogenides. *Nano Letters*, 16:2328, 2016.
- [42] Sina Najmaei, Adnen Mlayah, Arnaud Arbouet, Christian Girard, Jean Léotin§, and Jun Lou. Plasmonic Pumping of Excitonic Photoluminescence in Hybrid MoS<sub>2</sub>-Au Nanostructures. *ACS Nano*, 8:12682, 2014.
- [43] Wenjing Liu, Bumsu Lee, Carl H Naylor, Ho-Seok Ee, Joohee Park, A T Charlie Johnson, and Ritesh Agarwal. Strong Exciton-Plasmon Coupling in MoS<sub>2</sub> Coupled with Plasmonic Lattice. *Nano Letters*, 16:1262, 2016.
- [44] I Abid, W Chen, J Yuan, A Bohloul, S Najmaei, C Avendano, R Péchou, A Mlayah, and J Low. Temperature-Dependent Plasmon-Exciton Interactions in Hybrid Au/MoSe<sub>2</sub> Nanostructures. *ACS Photonics*, 4:1653, 2017.

- [45] W Liu, Y Wang, C Naylor, B Lee, B Zheng, G Liu, A T C Johnson, A Pan, and R Agarwal. Understanding the Different Exciton–Plasmon Coupling Regimes in Two-Dimensional Semiconductors Coupled with Plasmonic Lattices: A Combined Experimental and Unified Equation of Motion Approach. *ACS Photonics*, 5:192, 2018.
- [46] Thomas P Lyons, Scott Dufferwiel, Matthew Brooks, Freddie Withers, T Taniguchi, Kenji Watanabe, K S Novoselov, Guido Burkard, and Alexander I Tartakovskii. The valley Zeeman effect in inter- and intra-valley trions in monolayer WSe<sub>2</sub>. *Nature communications*, 10(1):1–8, 2019.
- [47] D S Dovzhenko, S V Ryabchuk, Yu. P Rakovich, and I R Nabiev. Light-matter interaction in the strong coupling regime: configurations, conditions and applications. *Nanoscale*, 10:3589–3605, 2018.
- [48] S Dufferwiel, S Schwarz, F Withers, A A P Trichet, M Sich F. Li, O Del Pozo-Zamudio, C Clark, A Nalitov, D D Solnyshkov, G Malpuech, K S Novoselov, J M Smith, M S Skolnick, D N Krizhanovskii, and A I Tartakovskii. Exciton–polaritons in van der Waals heterostructures embedded in tunable microcavities. *Nature Communications*, 6:8579, 2015.
- [49] M I Vasilevskiy, D G Santiago-Perez, C Trallero-Giner, N M R Peres, and A Kavokin. Exciton-polaritons in 2D dichalcogenide layers placed in a planar microcavity: tuneable interaction between two Bose-Einstein condensates. *Phys. Rev. B*, 92:245435, 2015.
- [50] L C Flatten, Z He, D M Coles, A A P Trichet, A W Powell, R A Taylor, J H Warner, and J M Smith. Room-temperature exciton-polaritons with two-dimensional WS<sub>2</sub>. *Scientific Reports*, 6:33134, 2016.
- [51] Nils Lundt, Sebastian Klemmt, Evgeniia Cherotchenko, Simon Betzold, Oliver Iff, Anton V Nalitov, Martin Klaas, Christof P Dietrich, Alexey V Kavokin, Sven Höfling, and Christian Schneider. Room-temperature Tamm-plasmon exciton-polaritons with a WSe<sub>2</sub> monolayer. *Nature Communications*, 7:13328, 2016.
- [52] Yu Ye, Zi Jing Wong, Xiufang Lu, Hanyu Zhu, Xianhui Chen, Yuan Wang, and Xiang Zhang. Monolayer Excitonic Laser. *Nature Photonics*, 9:733, 2015.
- [53] Changhua Liu, Jiajiu Zheng, Yueyang Chen, Taylor Fryett, and Arka Majumda. Van der Waals materials integrated nanophotonic devices. *Optical Materials Express*, 9:384–399, 2019.
- [54] J D Jackson. *Classical Electrodynamics*. J. Wiley, New York, 1998.
- [55] Evgeny Vinogradov. Semiconductor microcavity polaritons. *Physics-Uspeski*, 45:1213–1250, 2002.
- [56] K Kajiyama, Y Mizushima, and S Sakata. Schottky barrier height of n-In<sub>x</sub>Ga<sub>1-x</sub>As diodes. *Applied Physics Letters*, 23(8):458–459, 1973.
- [57] Vladimir Moiseevich Agranovich. *Surface polaritons*. Elsevier, 2012.
- [58] Thomas Dumelow. *Negative Refraction and Imaging from Natural Crystals with Hyperbolic Dispersion*. 2016.
- [59] Herbert Goldstein, Charles Poole, and John Safko. *Classical mechanics*, 2002.
- [60] Rair Macêdo. Tunable hyperbolic media: Magnon-polaritons in canted antiferromagnets, 2017.



- [61] Liudmila Nickelson. Maxwell's Equations and Boundary Conditions. In *Electromagnetic Theory and Plasmonics for Engineers*, pages 195–268. Springer, 2019.
- [62] David J Griffiths. Introduction to electrodynamics, 2005.
- [63] George B Arfken and Hans J Weber. Mathematical methods for physicists, 1999.
- [64] T Gutbrod, M Bayer, A Forchel, J P Reithmaier, T L Reinecke, S Rudin, and P A Knipp. Weak and strong coupling of photons and excitons in photonic dots. *Phys. Rev. B*, 57:9950, 1998.
- [65] G Panzarini and L C Andreani. Quantum theory of exciton-polaritons in cylindrical semiconductor cavities. *Phys. Rev. B*, 60:16799, 1999.
- [66] Di Xiao, Gui-Bin Liu, Wanxiang Feng, Xiaodong Xu, and Wang Yao. Coupled Spin and Valley Physics in Monolayers of MoS<sub>2</sub> and Other Group-VI Dichalcogenides. *Phys. Rev. Lett.*, 108:196802, 2012.
- [67] Fengcheng Wu, Fanyao Qu, and A H MacDonald. Absorption of light by excitons and trions in monolayers of metal dichalcogenide MoS<sub>2</sub>: Experiments and theory. *Phys. Rev. B*, 91:75310, 2015.
- [68] Pierluigi Cudazzo, Ilya V Tokatly, and Angel Rubio. Dielectric screening in two-dimensional insulators: Implications for excitonic and impurity states in graphane. *Phys. Rev. B*, 84:85406, 2011.
- [69] C Ciuti, V Savona, C Piermarocchi, A Quattropani, and P Schwendimann. Role of the exchange of carriers in elastic exciton-exciton scattering in quantum wells. *Phys. Rev. B*, 58:7926, 1998.
- [70] L V Keldysh. Coulomb interaction in thin semiconductor and semimetal films. *JETP Letters*, 29:658, 1979.
- [71] Z Ye, T Cao, K O'Brien, H Zhu, X Yin, Y Wang, S G Louie, and X Zhang. Probing excitonic dark states in single-layer tungsten disulphide. *Nature*, 513:214, 2014.
- [72] A Chernikov, T C Berkelbach, H M Hill, A Rigosi, Y Li, O B Aslan, D R Reichman, M S Hybertsen, and T F Heinz. Exciton Binding Energy and Nonhydrogenic Rydberg Series in Monolayer WS<sub>2</sub>. *Phys. Rev. Lett.*, 113:76802, 2014.
- [73] L D Landau and E M Lifshitz. *Quantum Mechanics: Volume 3 (Course of Theoretical Physics)*. Pergamon Press, Oxford, UK, 1965.
- [74] H Haug and S W Koch. *Quantum Theory of the Optical and Electronic Properties of Semiconductors*. World Scientific, 2004.
- [75] Philipp Tonndorf, Robert Schmidt, Robert Schneider, Johannes Kern, Michele Buscema, Gary A Steele, Andres Castellanos-Gomez, Herre S J van der Zant, Steffen Michaelis de Vasconcellos, and Rudolf Bratschitsch. Single-photon emission from localized excitons in an atomically thin semiconductor. *Optica*, 2:347, 2015.
- [76] Toan Trong Tran, Kerem Bray, Michael J Ford, Milos Toth, and Igor Aharonovich. Quantum emission from hexagonal boron nitride. *Nature Nanotechnology*, 11:37, 2016.

- [77] Ferry Prins, Aaron J Goodman, and William A Tisdale. Reduced dielectric screening and Enhanced Energy Transfer in Single- and Few-Layer MoS<sub>2</sub>s. *Nano Letters*, 14:6087, 2014.
- [78] Pierre Meystre and Murray Sargent III. *Elements of Quantum Optics*. Springer, Berlin, 2007.
- [79] S Noda, M Fujita, and T Asano. Spontaneous emission control by photonic crystals and microcavities. *Nature Photonics*, 1:449–458, 2007.
- [80] M Pelton. Modified spontaneous emission in nanophotonic structures. *Nature Photonics*, 9:427–435, 2015.
- [81] C Sauvan, J P Hugonin, I S Maksymov, and P Lallane. Theory of the spontaneous optical emission of nanosize photonic and plasmonic resonators. *Phys. Rev. Lett.*, 110:237401, 2013.
- [82] private communication A. Chahboun.
- [83] Nizar Bchellaoui. *Elaboration par voie microfluidique de microcapsules monodisperses de verre de silice à caractéristiques morphologiques et optiques contrôlées*. PhD thesis, 2017.
- [84] Yu. P Rakovich, John F Donegan, Mikhail I Vasilevskiy, and Andrey L Rogach. Anti-Stokes cooling in semiconductor nanocrystal quantum dots: A feasibility study. *Phys. Status Solidi A*, 206:2497–2509, 2009.
- [85] L J Cornelissen, J Liu, B J Van Wees, and R A Duine. Spin-current-controlled modulation of the magnon spin conductance in a three-terminal magnon transistor. *Physical review letters*, 120(9):97702, 2018.
- [86] Joel Cramer, Felix Fuhrmann, Ulrike Ritzmann, Vanessa Gall, Tomohiko Niizeki, Rafael Ramos, Zhiyong Qiu, Dazhi Hou, Takashi Kikkawa, Jairo Sinova, and Others. Ferroic collinear multilayer magnon spin valve. *arXiv preprint arXiv:1706.07592*, 2017.
- [87] Bevin Huang, Genevieve Clark, Efrén Navarro-Moratalla, Dahlia R Klein, Ran Cheng, Kyle L Seyler, Ding Zhong, Emma Schmidgall, Michael A McGuire, David H Cobden, and Others. Layer-dependent ferromagnetism in a van der Waals crystal down to the monolayer limit. *Nature*, 546(7657):270–273, 2017.
- [88] B Huang, G Clark, E Navarro-Moratalla, D R Klein, R Cheng, and K L Seyler. Zhong D, Schmidgall E, McGuire MA, Cobden DH, Yao W, Xiao D, Jarillo-19 Herrero P and Xu X 2017 Layer-dependent ferromagnetism in a van der Waals 2D crystal down to the monolayer limit. *Nature*, 546:270–273, 18.
- [89] Johanna L Miller. Ferromagnetism found in two-dimensional materials. *Physics today*, 70(7):16–19, 2017.
- [90] Lin Hao, D Meyers, Hidemaro Suwa, Junyi Yang, Clayton Frederick, Tamene R Dasa, Gilberto Fabbri, Lukas Horak, Dominik Kriegner, Yongseong Choi, and Others. Giant magnetic response of a two-dimensional antiferromagnet. *Nature Physics*, 14(8):806–810, 2018.
- [91] Zaiyao Fei, Bevin Huang, Paul Malinowski, Wenbo Wang, Tiancheng Song, Joshua Sanchez, Wang Yao, Di Xiao, Xiaoyang Zhu, Andrew F May, and Others. Two-dimensional itinerant ferromagnetism in atomically thin Fe<sub>3</sub>GeTe<sub>2</sub>. *Nature materials*, 17(9):778–782, 2018.

- 
- [92] Liaoxin Sun, Zhanghai Chen, Qijun Ren, Ke Yu, Lihui Bai, Weihang Zhou, Hui Xiong, Z Q Zhu, and Xuechu Shen. Direct Observation of Whispering Gallery Mode Polaritons and their Dispersion in a ZnO Tapered Microcavity. *Physical Review Letters*, 100:156403, 2008.
- [93] Toan Trong Tran, Kerem Bray, Michael J Ford, Milos Toth, and Igor Aharonovich. Quantum emission from hexagonal boron nitride monolayers. *Nature Nanotechnology*, 11:37–41, 2016.
- [94] J R Santos, Mikhail I Vasilevskiy, and Sergey A Filonovich. Cascade upconversion of photoluminescence in quantum dot ensembles. *Phys. Rev. B*, 78:245422, 2008.
- [95] Y J Zheng, Y Chen, Y L Huang, P K Gogoi, M Y Li, L.-J. Li, P E Trevisanutto, Q Wang, S J Pennycook, A T S Wee, and S Y Quek. The Origin of Single Photon Emission in 2D WSe<sub>2</sub>. *ArXiv181100221 Cond-Mat*, 2018.
- [96] M Abramowitz and I A Stegun, editors. *Handbook of Mathematical Functions*. Dover, New York, 1972.
- [97] Jerrold E Marsden and A Tromba. Vector Calculus. W. H. *Freedman and Company, Nova York*, 2003.
- [98] \it NIST Digital Library of Mathematical Functions. <http://dlmf.nist.gov/>, Release 1.0.26 of 2020-03-15.

